# Effect of Support Conditions on the Behavior of Elastomeric Bearings

# EFFECT OF SUPPORT CONDITIONS ON THE BEHAVIOR OF ELASTOMERIC BEARINGS

BY

SAMAN RASTGOO MOGHADAM, M.Sc.

A THESIS

SUBMITTED TO THE DEPARTMENT OF CIVIL ENGINEERING

AND THE SCHOOL OF GRADUATE STUDIES

OF MCMASTER UNIVERSITY

IN PARTIAL FULFILMENT OF THE REQUIREMENTS

FOR THE DEGREE OF

DOCTOR OF PHILOSOPHY

Doctor of Philosophy (2017) McMaster University

(Civil Engineering) Hamilton, Ontario, Canada

| | |
|---|---|
| TITLE: | Effect of Support Conditions on the Behavior of Elastomeric Bearings |
| AUTHOR: | Saman Rastgoo Moghadam<br>B.Sc., M.Sc., (Civil Engineering)<br>University of Tehran, Tehran, Iran |
| SUPERVISOR: | Dr. Dimitrios Konstantinidis |
| NUMBER OF PAGES: | xx, 229 |

*To my beloved parents...*

# Abstract

Many seismic protection techniques have been proposed over the years to mitigate the damaging effects of earthquake shaking. Seismic isolation is an earthquake-resistant design approach where a horizontally flexible layer is introduced at the base of a structure to decouple the structure from the motion of the ground. The concept of using isolation as a practical method has evolved into reality with the development of multilayer elastomeric bearings.

Elastomeric bearings usually feature thick steel end plates and are connected to the superstructure and substructure by mechanical means; that is referred to herein as a bonded application. In buildings, traditional practice places the isolation system at the foundation level and calls for the construction of rigid diaphragms above and below. The flexural rigidity of these diaphragms prevents the isolators from experiencing rotations. However, in some application such as bridge applications, isolation of high–rise buildings and mid–height isolation, it is possible for elastomeric bearings to experience rotation. In another application, the bearings do not have steel end plates, and shear forces are transferred from the bearing to the superstructure and substructure by the frictional force that develops along the rubber–to–concrete or rubber–to–steel interface; this referred to herein as unbonded application.

The main objective of this study is to investigate the effect of support conditions

on the behavior of elastomeric bearings; more specifically the effect of support rotation on the horizontal behavior and stability of bonded elastomeric bearings and the effect of slip on the vertical behavior of unbonded bearings. To provide a better understanding and quantitative characterization of the behavior of elastomeric bearings under combined loading, an extensive nonlinear 3D Finite Element Analysis (FEA) study was undertaken. Moreover, three mechanical models available in the literature were modified to capture the effect of rotation on the lateral behavior of elastomeric bearings. In addition, a new macro model to predict the lateral stability limit was proposed and the results based on the mechanical models were compared against FEA. In order to study the axial–shear–rotation interaction in elastomeric bearings, an experimental investigation was carried out on a 1/4-scale circular bearing. It was shown that, in general, support rotation has a minimal effect on the critical displacement, but it does affect the critical shear force. This observation was confirmed by experimental tests and modeled by the proposed mechanical models. Finally, to study the effect of slip on the vertical behavior of unbonded bearings, a closed–form solution including the effects of the elastomer's bulk compressibility was provided and compared against FEA results.

# Acknowledgments

First and foremost I would like to thank my supervisor Dr. Dimitrios Konstantinidis for his support, guidance and encouragement throughout this research. I am also extremely grateful to the members of my supervisory committee, Dr. Michael Tait and Dr. Peidong Wu, for their valuable comments and suggestions throughout the course of this research work.

I would like to thank the technical staffs at the ADL: Mr. Kent Wheeler and Mr. Paul Heerema and the summer student, Mr. Zachary Van Galen. Their assistance and advice in conducting the experimental tests have been greatly appreciated. I want to thank Dr. Tracy Becker for providing equipment including the elastomeric bearing to conduct the experimental tests and Mr. Adrian Crowder for his valuable experiences to build the experimental setup.

I would also like to thank my friends and colleagues for their support helpful discussion and encouragement.

Finally and most importantly, this work would not have been possible without the love and support of my parents to whom this thesis is dedicated.

# Contents

# List of Tables

# List of Figures

# Co–Authorship

This thesis has been prepared in accordance with the regulations for a "sandwich" thesis format as stipulated by the School of Graduate Studies at McMaster University. The thesis has been co–authored as:

**Chapter 2: Finite Element Study of the Effect of Support Rotation on the Horizontal Behavior of Elastomeric Bearings**

Authors: S. Rastgoo Moghadam and D. Konstantinidis

The 3–D finite element model was developed by S. Rastgoo Moghadam under the supervision of D. Konstantinidis. The manuscript was prepared by S. Rastgoo Moghadam under the supervision of D. Konstantinidis. This chapter has been published in the journal of Composite Structures.

**Chapter 3: Study of the Horizontal Behavior of Elastomeric Bearings by Simple Mechanical Models Including the Effect of Support Rotation**

Authors: S. Rastgoo Moghadam and D. Konstantinidis

The analytical solution using three mechanical models was conducted by S. Rastgoo Moghadam under the supervision of D. Konstantinidis. The modifications applied on these models were conducted by S. Rastgoo Moghadam under the supervision of D. Konstantinidis. The proposed modified model was developed by S. Rastgoo

Moghadam under the supervision of D. Konstantinidis. The 3–D finite element model was developed by S. Rastgoo Moghadam under the supervision of D. Konstantinidis. The manuscript was prepared by S. Rastgoo Moghadam under the supervision of D. Konstantinidis. This chapter has been submitted for publication in the journal of Engineering Structures.

**Chapter 4: Experimental and Analytical Studies on the Horizontal Behavior of Elastomeric Bearings under Support Rotation**

Authors: S. Rastgoo Moghadam and D. Konstantinidis

The experimental setup was designed and built by S. Rastgoo Moghadam under the supervision of D. Konstantinidis. The experimental tests were carried out by S. Rastgoo Moghadam under the supervision of D. Konstantinidis. The 3–D finite element model was developed by S. Rastgoo Moghadam under the supervision of D. Konstantinidis. The proposed modified model was developed by S. Rastgoo Moghadam under the supervision of D. Konstantinidis. The manuscript was prepared by S. Rastgoo Moghadam under the supervision of D. Konstantinidis. This chapter will be submitted for publication in the Journal of Structural Engineering.

**Chapter 5: Compression of Unbonded Rubber Layers Taking into Account Bulk Compressibility and Contact Slip at the Supports**

Authors: D. Konstantinidis and S. Rastgoo Moghadam

The original idea of compression of unbonded rubber layers including bulk compressibility belongs to D. Konstantinidis. The formulations for infinite strip pad was derived by S. Rastgoo Moghadam and D. Konstantinidis and for circular bearing was derived by S. Rastgoo Moghadam under the supervision of D. Konstantinidis. The

2–D finite element model was developed by S. Rastgoo Moghadam under the supervision of D. Konstantinidis. The manuscript was prepared by S. Rastgoo Moghadam and D. Konstantinidis. This chapter has been published in the International Journal of Solids and Structures.

# Chapter 1

# Introduction

## 1.1 Background

Seismic isolation is an earthquake-protection strategy aimed to uncouple a structure from the ground motion so as to reduce the damaging effects of earthquake shaking on the structure and its contents (see Fig. 1.1). The basic concept of using seismic isolation is not new, and many devices have been proposed over the years (Buckle and Mayes, 1990). The first known use of seismic isolation goes back to 6th century BC in Persia, where the foundation layers of a mausoleum could slide on each other during earthquake (Saiful Islam et al., 2011). Seismic isolation research in the middle and late 1970s grew out of the observation that the spectral accelerations of most recorded strong earthquake motions were very low in the long-period range (Jangid and Kelly, 2001). This observation played a key role in the development of isolation systems. In fact, isolation shifts the fundamental natural period of the system to the long period range through installation of horizontally flexible elements called isolators, or bearings at the base of a structure (Kelly, 1997) (see Fig. 1.2).

Rubber bearings are also used in other applications beside isolation. They are currently used widely to accommodate deformations associated with thermal expansion/contraction, traffic loads and construction misalignment in bridges (Stanton and Roeder, 1982; Constantinou et al., 2011), to isolate equipment and structures from vibration and shock (Snowdon, 1979).

## 1.2 Elastomeric Bearings

Elastomeric bearings which consist of rubber layers interleaved with steel reinforcing plates, are one of the most popular seismic isolation system (Fig. 1.3). They

are made by bonding rubber sheets to steel reinforcing-plates (shims). The shims are surrounded all-around by rubber to prevent corrosion. The shims restrict the bulging of the rubber and provide vertical and rotational stiffness. The thickness of an individual rubber layer is the most important factor that affects the vertical and bending stiffness of the isolator. Under horizontal loads, e.g. seismic loading, the high horizontal flexibility of the bearings isolates the structure from earthquake ground motion, while under vertical loads, i.e. gravity loading, the high vertical stiffness resulting from the restraint of the shims adequately supports the weight of the structure. The ratio of vertical to horizontal stiffness must be large so as to prevent rocking of the building during earthquake shaking. These bearings usually feature thick steel end plates and are connected to the superstructure and substructure by mechanical means; this is referred to as a *bonded* application (Fig. 1.4a). Sometimes elastomeric bearings do not have end plates, and shear forces are transferred from the bearing to the superstructure and substructure by frictional force; this is referred to as an *unbonded* application (Fig. 1.4b).

The idea of multilayer rubber bearings reinforced by thin steel plates was introduced by the famous French engineer Eugene Freyssinet to provide a flexible connection between relatively rigid parts of a structure (Kelly and Konstantinidis, 2011). Rubber bearings will inevitably experience such displacement during an earthquake. A comprehensive experimental study on their behavior under seismic loading conditions showed that these bearings can accommodate shear strains up to 200 percent (or more, depending on their height-to-width ratio) without damage (Konstantinidis et al., 2008).

## 1.3 Motivation

Past studies have shown that elastomeric bearings under combined axial and horizontal loading behave nonlinearly, and an individual bearing undergoing large lateral displacements may experience a decrease in its axial load capacity. Therefore, one of the important aspects of bearing design is stability of the individual bearing. Although many investigators have suggested nonlinear mechanical models (Koh and Kelly, 1987; Koo et al., 1999; Nagarajaiah and Ferrell, 1999; Iizuka, 2000; Yamamoto et al., 2009; Kikuchi et al., 2010; Forcellini and Kelly, 2014; Han and Warn, 2014; Vemuru et al., 2014, 2016; Maureira et al., 2017) for elastomeric bearings in previous theoretical studies, the effects of rotation at the top or the bottom of the bearing have been overlooked. In reality, however, it is possible for an isolator to experience rotation. There are many cases in which bearing's supports can rotate during an earthquake. For example in tall buildings, the center of mass is not close to the ground level (base) and during an earthquake large overturning moments can develop and makes the bearing rotates as well. Oshaki et al. (2015), who investigated the dynamic response of a base-isolated 10-story RC frame building using 3D finite element analysis (FEA), noted that the elastomeric isolators experienced rotation at their supports. In applications such as isolation of high-rise buildings or mid-height isolation, the effect of rotation may be significant. Recently, Japanese researchers (Kawamura et al., 2000; Murakami et al., 2000) proposed using bearings at the mid-storey instead of at the base level in a building. Use of mid-storey isolation systems may eliminate the construction cost associated with the stiff elements above and below the isolation system, when that is located at the base of the building. In this

approach, the columns under the bearings can deform during the earthquake, consequently the bearing rotates (Crowder and Becker , 2016). The effect of rotation may also be important in bridge applications, where the seismic isolators are placed between the bridge deck and the piers or abutments and can experience rotation due to flexure of the deck above the isolator or the piers below(Constantinou et al., 2011).

As mentioned earlier, unbonded bearings do not feature thick steel end plates, and they are not bonded to the supports. Shear forces are transferred from the bearing to the superstructure and substructure by the frictional force that develops along the rubber–to–concrete or rubber–to–steel interface. Although the frictional resistance of rubber is relatively high, it is possible that it may be reduced by the introduction of lubrication, either intentional or accidental. As a result, the frictional resistance that develops between the rubber layers is reduced significantly. In unbonded bearings with only a few rubber layers, this reduction may result in a notable reduction in vertical stiffness.

## 1.4 Literature Review

In this introductory chapter, a general overview of the pertinent literature is presented. Subsequent chapters of this sandwich thesis offer a more focused and detailed literature review. The stability of elastomeric bearings was studied by Haringx (1948) assuming the bearing to be a homogenous isotropic column that behaves as a rubber rod, following Euler buckling load theory. Stanton et al. (1990) extended the theory to account for the effect of axial shortening and provided experimental verification. Experimental tests on the stability of modern elastomeric bearings by Buckle and Kelly (1986) and Buckle and Liu (1993), have led to the development of a simple

formula, namely, the Overlapping Area Method, for estimating the critical load. Further experimental studies showed that this formula is overly conservative, especially at lateral displacements equal to the bearing diameter or width (Buckle et al., 2002; Cardone and Perrone, 2012; Sanchez et al., 2013). Recently Sanchez et al. (2013) carried out a comprehensive experimental program to examine the stability of bearings under quasi-static and dynamic loading. The advantage of dynamic testing is realistic simulation of seismic loadings conditions and quantification of the response of elastomeric bearings beyond their stability limit.

To decrease the construction cost of bearings, the use of fiber instead of steel in traditional elastomeric bearings has been suggested in recent years. De Raaf et al. (2011) investigated the stability of fiber reinforced elastomeric isolators (FREIs) using dynamic and monotonic lateral testing. The behavior of unbonded FREIs that feature geometric modifications was experimentally investigated under pure compression in (Van Engelen et al., 2014) and combined compression and shear in (Osgooei et al., 2015). An extensive experimental tests on fiber reinforced elastomeric bridge bearings were conducted by Konstantinidis et al. (2008) and Al-Anany and Tait (2017). Moreover, to improve the lateral behavior of bearings, Han et al. (2016) proposed a new unbonded elastomeric bearings reinforced by high-strength steel mesh. It was shown that friction introduced in the steel mesh can enhance the damping energy dissipation. As an alternative to FREIs, Van Engelen et al. (2015) proposed partially-bonded FREIs, which aim to take advantage of the benefits of both bonded and unbonded isolators; most notably resistance against slipping while still reducing tensile stresses that would develop if the bearing was fully bonded.

In order to model the lateral behavior of elastomeric bearings, several mechanical models have been proposed. The first model proposed was by Koh and Kelly (1987), to study the stability of elastomeric isolators. They showed that the model provides an acceptable error in comparison with experimental tests. Koo et al. (1999) modified the Koh-Kelly model by using an instantaneous apparent shear modulus obtained from test results instead of a constant shear modulus value. In this model the shear modulus is a function of the shear strain and can be presented by a polynomial equation obtained by least-squares fitting of test results. The advantage of this modification is elimination of imprecision associated with in the constant shear modulus. Nagarajaiah and Ferrell (1999) extended the Koh-Kelly model to include large displacements. The model was capable of modeling the critical point in elastomeric bearings. However, Han et al. (2013) experimentally showed that the model proposed by Nagarajaiah and Ferrell (1999) does not provide accurate results for three different bearings. Iizuka (2000) developed a model by introducing finite deformation and nonlinear springs into the Koh-Kelly model. From experimental and analytical results, this model accurately captures various characteristics of elastomeric bearings, including hardening, load deterioration, and buckling phenomena. The nonlinear parameters of the rotational and shear springs in the model are determined through experimental testing. The advantage of this model is that it can easily handle a variable axial force.

Han and Warn (2014) conducted sensitivity analysis on previous models using FEA and proposed an alternative model which does not rely on experimentally calibrated parameters. This model includes a series of vertical springs with simple bilinear constitutive relationship. These vertical springs replace the rotational spring which

was used in the Koh-Kelly model. Vemuru et al. (2014) modified the Nagarajaiah-Ferrell model by incorporating higher order displacement terms in the rotational spring in an effort to characterize the dynamic behavior of bearings more accurately than previous models, particularly beyond the instability point.

A three dimensional model which includes multiple shear springs at the mid-height and a series of axial springs at the top and bottom of an isolator was proposed by Yamamoto et al. (2009) and Kikuchi et al. (2010) for circular and rectangular isolators, respectively. Ishii et al. (2016) extended the previous model by Yamamoto et al. (2009) to account for the effect of rotation on the horizontal behavior of elastomeric bearings. It was shown that end rotations do not affect the critical displacement.

The use of FEA is a common approach to understand the behavior of rubber isolators. Recently, studies using this approach have evaluated the behavior of isolation bearings under compression and shear, as well as their stability. Mordini and Strauss (2008) presented an isolation system consisting of high damping rubber bearings reinforced with glass fiber fabric. This parametric study using FEA examined the vertical and horizontal behavior of bearings with Neo-Hookean and Ogden rubber material models. Toopchi-Nezhad et al. (2011) compared the behavior of FREIs in unbonded and bonded applications. Osgooei et al. (2014a) used 3D FEA to study the behavior of circular fiber-reinforced elastomeric bearings under compression. Osgooei et al. (2014b) investigated the lateral response of unbonded FREIs when loaded in different directions.

Warn and Weisman (2011) conducted a parametric study to investigate the effect of geometry on the critical load of rubber bearings using 2D FEA. Their results showed that the critical load is more sensitive to the bearing width and the individual rubber

layer thickness than it is to the number of rubber layers. Weisman and Warn (2012) used experimental testing and FEA to investigate the critical load capacities of an elastomeric bearing and a lead-rubber bearing with shape factor values of 10 and 12, respectively. The results of this investigation showed that the lead core does not have a significant effect on the critical load over a range 150–280 percent shear strain in comparison with elastomeric bearings without a lead core. Another FEA study by Kalfas et al. (2017) showed that when a bearing is subjected to axial and horizontal load and the endplate is allowed to rotate, the development of local tensile stresses changes the stiffness and damping ratio.

## 1.5 Objectives

The main objectives of this study were to

- Investigate the effects of rotation on the horizontal behavior and stability of bonded elastomeric bearings using FEA and experimental testing,
- Compare available hyperelastic material models and their effects on the stresses, strains and lateral behavior of bearings,
- Modify the mechanical models available in the literature and propose a new simple mechanical model to account for the effect of rotation on the lateral behavior of bearings,
- Provide a closed-form solution for the behavior of an unbonded rubber layer, including the effects of the elastomer's bulk compressibility and the contact slip at the supports, and verified by FEA.

## 1.6 Organization of the Thesis

This thesis was prepared in accordance with the regulations of a "sandwich" thesis format. Therefore, each chapter contains its own introduction, conclusion and references.

In the second chapter of this thesis (Paper #1), to investigate the effect of rotation on the lateral behavior of bearings, 3D FEA was carried out using ABAQUS (2010) on bearing similar to the one studied by Weisman and Warn (2012). The FEA model was first validated using an available analytical solution presented by Karbakhsh Ravari et al. (2012). To investigate the effect of rubber description on the FEA results, three material models (Neo-Hookean, Mooney-Rivlin and Yeoh) were considered and the bearing was analyzed under different rotation angles and axial loads. Furthermore, the effect of rotation on the stress and strain distribution was studied. The effect of rotation on the critical point of the bearing was investigated. In order to examine the instability in elastomeric bearings used in practice, five bearings with large shape factor and second shape factor were analyzed using ABAQUS (2010) under different conditions.

In the third chapter of this thesis (Paper #2), the performance of simple mechanical models was evaluated in capturing the effect of rotation on the lateral behavior of bearings. Three existing models were considered: the Nagarajiah-Ferrell (Nagarajaiah and Ferrell, 1999), the Iizuka (Iizuka, 2000), and the Han-Warn models (Han and Warn, 2014). First, these three models were examined by comparing their predictions with results of FEA, assuming no rotation at the supports. Subsequently, the models were modified to account for the effect of rotation. The modified models

were evaluated using results from FEA under prescribed rotation values for the elastomeric bearing. In order to investigate the effect of geometry on the results, bearings with different second shape factors (2, 4 and 6) were considered. Finally, the study proposed a new model that includes the effect of rotation. This model was used to predict the lateral stability limit, and the results were compared against those from FEA.

In Chapter 4 of this thesis (Paper #3), experimental tests of a 1/4–scale circular bearing with the shape factor of 20 and second shape factor of 4 were conducted at the Applied Dynamic Laboratory (ADL) at McMaster University. The results of the tests were compared against FEA results. Furthermore, the experimental results were used to evaluate the ability of the mechanical model proposed in the previous chapter. Two experimental procedures were employed. The first investigated the behavior of the bearing under lateral quasi-static cyclic displacement tests, constant axial and constant rotation. The second investigated the lateral behavior of the bearing through monotonic lateral displacement tests under constant axial load and rotation angle. The experimental setup used in the study was explained in this chapter.

Chapter 5 of this thesis (Paper #4) investigates a closed-form solution using theoretical analysis for the behavior of an unbonded rubber layer, including the effects of the elastomer's bulk compressibility and contact slip at the supports. The theoretical solution was compared against a FEA solution using MSC Marc (2011).

## 1.7 References

Al-Anany Y.M., Tait M.J. (2017). Experimental assessment of utilizing fiber reinforced elastomeric isolators as bearings for bridge applications. *Composites Part*

*B: Engineering*. 114: 373–385.

Bridgestone. (1999). *Base isolation manual.* Bridgestone Engineered Products Company, Inc., Nashville.

Buckle I.G., Kelly J.M. (1986). Properties of slender elastomeric isolation bearings during shake table studies of a large-scale model bridge deck. *ACI Special Publication*. 94: 247–270.

Buckle I.G., Liu H. (1993). Stability of elastomeric seismic isolation systems. *Seminar on Seismic Isolation, Passive Energy Dissipation and Control.* Applied Technology Council (ATC), Redwood City, CA.

Buckle, I.G., Mayes, R.L. (1990). Seismic isolation: history, application, and performance–a world view. *Earthquake Spectra*. 6(2): 161–201.

Buckle I.G., Nagarajaiah S, Ferrell K. (2002). Stability of elastomeric isolation bearings: experimental Study. *Journal of Structural Engineering*. 128(1): 3–11.

Cardone D., Perrone G. (2012). Critical load of slender elastomeric seismic isolators: an experimental perspective. *Engineering Structures*. 40: 198–204.

Constantinou, M.C., Kalpakidis, I., Filiatrault, A., Ecker Lay, R.A. (2011). LRFD-based analysis and design procedures for bridge bearings and seismic isolators. *Technical Report MCEER-11-0004.* Multidisciplinary Center for Earthquake Engineering Research. University at Buffalo, State University of New York.

Crowder A.P., Becker T.C. (2016) Effects of non-traditional isolator placement for seismic retrofit. *Canadian Society of Civil Engineering.* Resilient Infrastructure. London, ON, June 1–4.

Dassault Systèmes Simulia Corp. (2010). *ABAQUS/CAE Version 6.10-1.* Providence, RI.

De Raaf M.G.P., Tait M.J., Toopchi-Nezhad, H. (2011). Stability of fiber-reinforced elastomeric bearings in an unbonded application. *Journal of Composite materials.* 5(18): 1873–1884.

Forcellini D., Kelly J.M. (2014). Analysis of the large deformation stability of elastomeric bearings. *Journal of Engineering Mechanics.* 140(6): 04014036.

Han L., Shengze T., Xinzhi D., Wancheng Y., Kai W. (2016) Performance of steel mesh reinforced elastomeric isolation bearing: Experimental study. *Construction and Building Materials.* 121: 60–68.

Han X., Kelleher C.A., Warn G.P., Wagener T. (2013). Identification of the controlling mechanism for predicting critical loads in elastomeric bearings. *Journal of Structural Engineering.* 139(12): 04013016.

Han X., Warn G.P. (2014). Mechanistic model for simulating critical behavior in elastomeric bearings. *Journal of Structural Engineering.* 141(5): 04014140.

Haringx J.A. (1948). On highly compressible helical springs and rubber rods and their application for vibration-free mountings. *Philips Research Reports.* 13(6): 401–449.

Iizuka M. (2000). A macroscopic model for predicting large-deformation behaviors of laminated rubber bearings. *Engineering Structures.* 22(4): 323–334.

Ishii K., Kikuchi M., Nishimura T., Black C.J. (2016). Coupling behavior of shear

deformation and end rotation of elastomeric seismic isolation bearings. *Earthquake Engineering & Structural Dynamics*. In press.

Jangid R.S., Kelly J.M. (2001). Base isolation for near-fault motions. *Earthquake Engineering & Structural Dynamics*. 30(5): 691–707.

Karbakhsh Ravari A., Othman I.B., Ibrahim Z.B., Ab-Malek K. (2012). P-$\Delta$ and end rotation effects on the influence of mechanical properties of elastomeric isolation bearings. *Journal of Structural Engineering*. 138(6): 669–675.

Kawamura S., Sugisaki R., Ogura K., Maezawa K., Tanaka S., Yajima A. (2000). Seismic isolation retrofit in Japan. *12th World Conference of Earthquake Engineering*. Auckland, New Zealand, Jan 30–Feb 4.

Kalfas K.N., Mitoulis S.A., Katakalos K. (2017) Numerical study on the response of steel-laminated elastomeric bearings subjected to variable axial loads and development of local tensile stresses. *Engineering Structures*. 134: 346–357.

Kelly, J.M. (1997). *Earthquake-Resistant Design with Rubber*. 2nd ed. London: Springer-Verlag Telos.

Kelly, J.M., Konstantinidis, D. (2011). *Mechanics of Rubber Bearings for Seismic Isolation and Vibration Isolation*. Chichester, UK: John Wiley & Sons.

Kikuchi M., Nakamura T., Aiken I.D. (2010). Three-dimensional analysis for square seismic isolation bearings under large shear deformations and high axial loads. *Earthquake Engineering & Structural Dynamics*. 39(13): 1513–1531.

Koh C.G., Kelly J.M. (1987). Effects of axial load on elastomeric isolation bearings.

*Report UCB/EERC-86/12*. Earthquake Engineering Research Center. University of California, Berkeley.

Konstantinidis, D., Kelly, J.M., Makris, N. (2008). Experimental investigation on the seismic response of bridge bearings. *Technical Report EERC 2008-02*. Earthquake Engineering Research Center, University of California, Berkeley.

Koo G., Lee J., Yoo B., Ohtori Y. (1999). Evaluation of laminated rubber bearings for seismic isolation using modified macro-model with parameter equations of instantaneous apparent shear modulus. *Engineering Structures*. 21(7): 594–602.

Maureira N., de la Llera J., Oyarzo C., Miranda S. (2016). A nonlinear model for multilayered rubber isolators based on a co-rotational formulation. *Engineering Structures*. 131: 1–13.

Mordini A., Strauss A. (2008). An innovative earthquake isolation system using fiber reinforced rubber bearings. *Engineering Structures*.30(10): 2739–2751.

Murakami K., Kitamura K., Ozaki H., Teramoto T. (2000). Design and analysis of a building with the middle-story isolation structural stystem. *12th World Conference of Earthquake Engineering*. Auckland, New Zealand, Jan 30–Feb 4.

MSC Marc. (2011). *MSC Marc and Mentat*. [computer software]. Santa Ana, California: MSC Software Corporation.

Nagarajaiah S., Ferrell F. (1999). Stability of elastomeric seismic isolation bearings. *Journal of Structural Engineering*. 125(9): 946–954.

Ohsaki M., Miyamura T., Kohiyama M., Yamashita T., Yamamoto M., Nakamura, N. (2015). Finite-element analysis of laminated rubber bearing of building frame

under seismic excitation. *Earthquake Engineering & Structural Dynamics*. 44(11): 1881–1898.

Osgooei P.M., Tait M.J., Konstantinidis D. (2014). Finite element analysis of unbonded square fiber-reinforced elastomeric isolators (FREIs) under lateral loading in different directions. *Composite Structures*. 113: 164–173.

Osgooei P.M., Tait M.J., Konstantinidis D. (2014). Three-dimensional finite element analysis of circular fiber-reinforced elastomeric bearings under compression. *Composite Structures*. 108: 191–204.

Osgooei P.M., Van Engelen N.C., Konstantinidis D., Tait M.J. (2015). Experimental and finite element study on the lateral response of modified rectangular fiber-reinforced elastomeric isolators (MR-FREIs). *Engineering Structures*. 85: 293–303.

Saiful Islam, A.B.M., Jameel, M., Jumaat, M.Z. (2011). Seismic isolation in buildings to be a practical reality: behavior of structure and installation technique. *Journal of Engineering and Technology Research*. 3(4): 99–117.

Sanchez J., Masroor A., Mosqueda G., Ryan K.L., (2013). Static and dynamic stability of elastomeric bearings for seismic protection of structures. *Journal of Structural Engineering*. 139(7): 1149–1159.

Snowdon, J.C. (1979). Vibration isolation: use and characterization. *The Journal of the Acoustical Society of America*. 66(5), 1245–1274.

Stanton, J.F., Roeder, C.W. (1982). Elastomeric bearings design, construction, and materials. *NCHRP Report 248*. National Cooperative Highway Research Program (NCHRP). Transportation Research Board, Washington, DC.

Stanton J.F., Scroggins G., Taylor A., Roeder C.W. (1990). Stability of laminated elastomeric bearings. *Journal of Engineering Mechanics*. 116(6): 1351–1371.

Toopchi-Nezhad H, Tait M.J., Drysdale R.G. (2011). Bonded versus unbonded strip fiber reinforced elastomeric isolators: Finite element analysis. *Composite Structures*. 93(2): 850–859.

Van Engelen N.C., Osgooei P.M., Tait M.J., Konstantinidis D. (2014). Experimental and finite element study on the compression properties of modified rectangular fiber-reinforced elastomeric isolators (MR-FREIs). *Engineering Structures*. 74: 52–64.

Van Engelen N.C., Osgooei P.M., Tait M.J., Konstantinidis D. (2015). Partially bonded fiber-reinforced elastomeric isolators (PB-FREIs). *Structural Control and Health Monitoring*. 22(3): 417–432.

Vemuru V.S.M., Nagarajaiah S., Masroor A., Mosqueda G. (2014). Dynamic lateral stability of elastomeric seismic isolation bearings. *Journal of Structural Engineering*. 140(8): A4014014.

Vemuru V.S.M., Nagarajaiah S., Mosqueda G. (2016). Coupled horizontal–vertical stability of bearings under dynamic loading. *Earthquake Engineering & Structural Dynamics*. 45(6): 913–934.

Warn G.P., Weisman J. (2011). Parametric finite element investigation of the critical load capacity of elastomeric strip bearings. *Engineering Structures*. 33(12): 3509–3515.

Weisman J., Warn G.P. (2012). Stability of elastomeric and lead-rubber seismic isolation bearings. *Journal of Structural Engineering.* 128(2): 215–223.

Yamamoto S., Kikuchi M., Ueda M., Aiken I.D. (2009). A mechanical model for elastomeric seismic isolation bearings including the influence of axial load. *Earthquake Engineering & Structural Dynamics.* 38(2): 157–180.

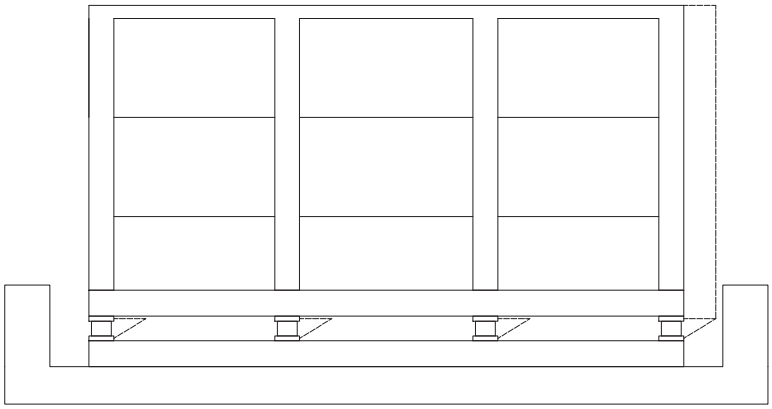

Figure 1.1: Deformation of a structure with seismic isolation system.

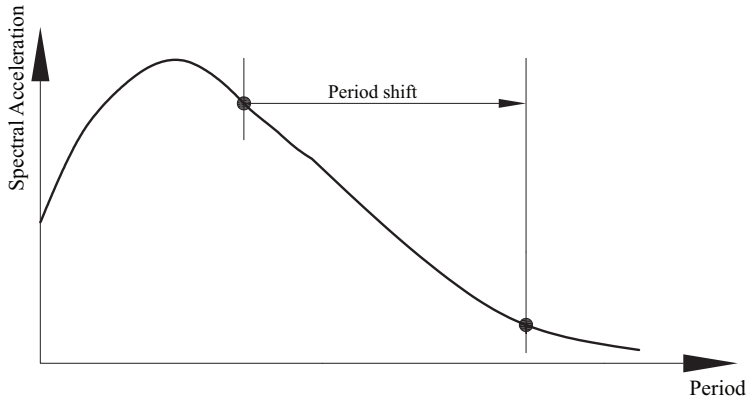


Figure 1.2: Reduction in spectral acceleration at long periods.

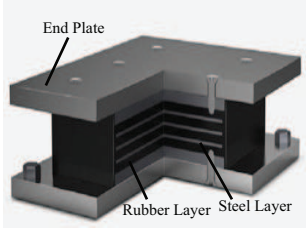


Figure 1.3: A typical elastomeric bearing (Bridgestone, 1999).

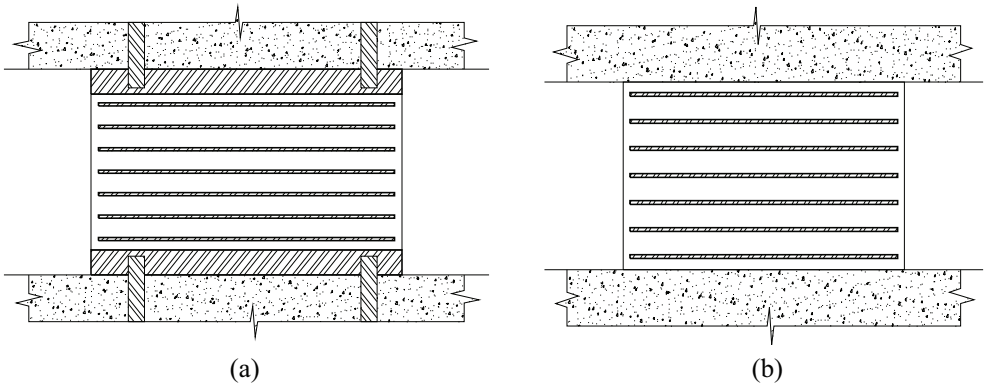


Figure 1.4: Elastomeric bearing (a) Bonded application (b) Unbonded application (Konstantinidis et al., 2008).

# Chapter 2

# Finite Element Study of the Effect of Support Rotation on the Horizontal Behavior of Elastomeric Bearings



Rastgoo Moghadam S, Konstantinidis D. Finite element study of the effect of support rotation on the horizontal behavior of elastomeric bearings. *Composite Structures*, 2017; 163: 474–490.

## 2.1 Abstract

Laminated elastomeric bearings are used widely in both seismic and non-seismic structural engineering applications. The behavior of these bearings under pure loading (compression, shear, or bending) and under combined compression–shear loading has been studied at various levels in previous studies. However, very few studies have considered the behavior of elastomeric bearings under combined loading that includes rotation, and, to the best of the authors' knowledge, there has been no previous study on the effect of rotation on the lateral stability of elastomeric bearings. In bridge applications and some novel seismic isolation applications, e.g., isolation of high-rise buildings and mid-height isolation, it is possible for elastomeric bearings to experience rotation, the effect of which is not well understood. This paper studies the effect of rotation on the horizontal behavior of elastomeric bearings using 3D Finite Element Analysis (FEA). It is observed that constitutive modeling assumptions can have a notable influence on the results, especially at low vertical pressure where the critical shear strain is large. Support rotation does not affect the critical displacement appreciably, but it significantly affects the critical shear force. It is observed that support rotation becomes important for bearings with low second shape factor, even if their first shape factor is large.

## 2.2 Introduction

Multilayer elastomeric bearings are used extensively in bridge applications [1-4] to accommodate deformations associated with thermal expansion/contraction, traffic loads and construction misalignment, and to reduce the effects of earthquake loads on the

bridge. This type of bearing is also the most commonly used seismic isolation device in building applications [5-8, among others and references reported herein]. Isolation involves the introduction of a horizontally flexible layer that in effect decouples the superstructure from the horizontal seismic excitation. Conventional elastomeric bearings are made of layers of natural or synthetic rubber (often filled with various additives to enhanced their damping properties) interleaved with steel reinforcing plates (shims). Thick steel end plates are used to bolt the bearing to to the superstructure and substructure. The horizontal shims restrict the lateral bulging of the rubber and provide vertical and rotational stiffness but do not affect the bearing's large horizontal flexibility. Early studies [9,10] showed that elastomeric bearings under combined axial and horizontal loads behave nonlinearly and, when they undergo large lateral displacements, they may experience a significant decrease in critical axial-load capacity. The behaviour of elastomeric bearings of various geometries subjected to pure bending was studied by Stanton and Roeder [1], Chalhoub and Kelly [11], Stanton et al. [12], and Kelly and Konstantinidis [7], among others, who developed expressions for the bending rigidity, a property that plays an important role in the estimate of the buckling load of a bearing. However, nearly all previous experimental and analytical studies investigating the behavior of elastomeric bearings under combined shear and compression were conducted under the assumption of zero top and bottom support rotation. This assumption is in many cases reasonable because the presence of rigid structural elements above and below the bearing prevent it from experiencing rotation at the supports. There are, however, several scenarios where it is possible for an elastomeric bearing to experience rotation at its supports, together with compression

and shear. Ohsaki et al. [13], who investigated the dynamic response of a base-isolated 10-story reinforced-concrete frame building using 3D FEA, noted that the elastomeric bearings experienced rotation at their supports. In applications such as isolation of high-rise buildings or mid-height isolation [14], the effect of rotation may be significant. The effect of rotation may also be important in bridge applications, where the bearings can experience rotation due to flexure of the bridge deck above the bearing or the piers below. Because of its geometric nonlinearity, the problem of an elastomeric bearing under combined shear, axial and bending actions is not amenable to superposition of existing solutions for simple shear, pure axial and pure bending—even under the assumption of linear elasticity. This study aims to fill in the knowledge gap that currently exists by better understanding and quantifying the response of elastomeric bearings under combined loading that includes rotation.

The determination of the lateral stability limit of elastomeric bearings is based on an extension of Euler buckling load theory proposed by Haringx [15]. This linear theory assumes a bearing to be a homogenous, isotropic column that behaves as a rubber rod. Gent [16] investigated the decrease in the horizontal stiffness of rubber bearings with increasing axial load. Stanton et al. [17] extended the theory to account for the effect of axial shortening and provided experimental verification. Experimental tests on the stability of seismic isolation elastomeric bearings under quasi-static loading were conducted by Buckle and Kelly [9]. Buckle and Liu [18] carried out an experimental investigation to determine the critical buckling load of elastomeric bearings and proposed a formula based on the so-called *overlapping area method* to estimate the critical load, which is used in practice nowadays; although further experimental investigation showed this formula to be overly conservative, especially at

lateral displacements equal to the bearing diameter, or width [19-21]. Sanchez et al. [21] carried out an experimental study on the stability of elastomeric bearings under quasi-static and dynamic loading. Two quasi-static and one dynamic methods were used. The first method followed the conventional method, where a bearing is held at a fixed horizontal displacement while the axial load is increased until the critical load is obtained. In the second method, the bearing was loaded under a constant axial load, while the horizontal displacement was increased until the instability point was observed. It was noted that the second method proved to be accurate and more direct in obtaining the critical load. The third method evaluated the dynamic stability of a group of elastomeric bearings supporting a rigid frame using shake table testing.

Besides experimental investigations, there have been several analytical studies on the stability of elastomeric bearings. Koh and Kelly [22] proposed a simple mechanical model including both shear and flexural deformations to study the stability of elastomeric bearings. They compared the results of the model to experimental results for natural rubber bearings and showed that the model captured the behavior with good accuracy. Koo et al. [23] modified the Koh-Kelly model by using an instantaneous apparent shear modulus obtained from test results instead of a constant shear modulus value. Nagarajaiah and Ferrell [24] extended the Koh-Kelly model to include large displacements. They showed that the critical load and horizontal stiffness decreases with increasing lateral displacement. Iizuka [25] developed a model by introducing finite deformation and nonlinear springs into the Koh-Kelly model. The model is shown to accurately capture the characteristics of elastomeric bearings, such as hardening, load deterioration, and buckling phenomena, by comparison to experimental results. Three-dimensional models using multiple shear springs at mid-height

and a series of axial springs at the top and bottom were proposed by Yamamoto et al. [26] for circular bearings and Kikuchi et al. [27] for rectangular bearings. Han and Warn [28] conducted sensitivity analysis on prior models using FEA and proposed an alternative model which does not rely on experimentally calibrated parameters. This model includes a series of vertical springs with a simple bilinear constitutive relationship. These vertical springs replace the rotational spring that was used in the Koh-Kelly model. Vemuru et al. [29] showed that the Nagarajaiah-Ferrell model, which was based on quasi-static tests, over-predicts the stiffness degradation beyond the stability point. They modified the Nagarajaiah-Ferrell model by incorporating higher order displacement terms in the rotational spring. The resulting model was shown to be able to characterize the dynamic behavior of bearings more accurately than previous models, particularly beyond the instability point. In another study by Vemuru et al. [30], a 3-DOF variant of the Nagarajaiah-Ferrell model was introduced, capable of capturing the vertical behavior more accurately.

FEA has become a common approach for understanding various aspects of the behavior of rubber bearings. The first study on the stability of elastomeric bearings using FEA was conducted by Simo and Kelly [31]. Recently, Warn and Weisman [32] conducted a parametric study to investigate the effect of geometry on the critical load of rubber bearings using 2D FEA. Their results showed that the critical load is more sensitive to the bearing width and the individual rubber layer thickness than it is to the number of rubber layers. Weisman and Warn [33] used experimental testing and FEA to investigate the critical load capacity of an elastomeric bearing and a lead-rubber bearing with shape factor values of 10 and 12, respectively. The results of this investigation showed that the lead core does not have a significant effect on

the critical load over the 150–280 percent range of shear strain in comparison with elastomeric bearings without a lead core. Montuori et al. [34] studied the effect of the second shape factor on the stability of elastomeric bearings, confirming that the second shape factor significantly affects the stability of the bearing. Nguyen and Tassoulas [35] modeled a square and a rectangular unbonded steel-reinforced elastomeric bridge bearing in 3D under compression and shear in various lateral directions. A constitutive model based on the Yeoh strain energy density function was used to represent the behavior of the rubber. Their results showed that there was no significant effect of the shear direction on the stiffness at 50 percent shear displacement.

Mordini and Strauss [36] carried out FEA to study the vertical and horizontal behavior of fiber-reinforced high-damping rubber bearings, with the rubber modeled using Neo-Hookean and Ogden hyperelastic material models. Toopchi-Nezhad et al. [37] compared the behaviour of fiber-reinforced elastomeric isolators (FREIs) in unbonded and bonded applications. Osgooei et al. [38] used 3D FEA to study the behavior of circular fiber-reinforced elastomeric bearings under compression. In another study, Osgooei et al. [39] investigated the lateral response of unbonded rectangular FREIs when loaded in different directions. The behavior of unbonded FREIs that feature geometric modifications was investigated under pure compression [40] and combined compression and shear in [41]. Al-Anany and Tait [42] modeled bonded and unbonded FREI to study the effect of rotation on the vertical behavior of FREIs. Their results showed that Unbonded FREIs in comparison with Bonded FREIs experience lower normal stresses and shear strains in the elastomer. Osgooei et al. [43] investigated the variation in vertical stiffness of strip FREIs under lateral loading. Their results revealed that for bonded FREIs, the vertical stiffness decreases

monotonically with increase of lateral displacement; while, for unbonded FREIs, the vertical stiffness decreases up to particular shear deformation and then it increases. A FEA investigation on the compression of unbonded rubber pads including contact slip at the supports can be found in [44].

This paper presents the results of a study investigating the effect of rotation on the horizontal behavior of steel-reinforced elastomeric bearings. For these bearings, depending on the structural application, the rotation may be constant or vary while the bearing is sheared. This is the first systematic FEA study on the behavior of bearings under combined compression, lateral displacement and support rotation. As such, the discussion is limited to the simpler case of constant rotation. First, a 3D finite element model of a circular elastomeric bearing is developed in ABAQUS [45] and validated by comparing the results of the FEA with an analytical solution presented by Karbakhsh Ravari et al. [46], which is applicable for studying the behavior of elastomeric bearings before the instability point. Subsequently, in order to examine the effect of material modeling assumptions, the rubber is characterized using three different hyperelastic material models. To the best of the authors' knowledge, this study is the first of its kind to provide an in-depth comparison of local and global behaviour predictions using different hyperelastic material models in finite element modeling of steel-reinforced elastomeric bearings under combined loading. Subsequently, the paper investigates the effects of support rotation on the stress and strain distributions, and lateral response and stability of elastomeric bearings with various geometric characteristics, subject to different levels of average vertical stress.

## 2.3 Analytical Solution

The theory for the buckling of multilayer elastomeric bearings is an outgrowth of the work of Haringx on the stability of solid elastomeric rods [15]. This theory was later applied by Gent [16] to the stability of multilayer rubber compression springs. Haringx's theory is basically an extension of elastomeric column buckling theory to take into account shear deformation. This theory predicts the reduction of apparent lateral stiffness due to the presence of an axial load; however, for a fixed axial load, the theory is unable to capture the reduction in lateral stiffness that occurs as lateral displacement increases [31]. Consequently, while Haringx's theory achieves relatively good predictions at low to moderate levels of shear, as observed by Gent [16] by comparison to experimental results, it is not capable of capturing the lateral stiffness reduction and the critical lateral displacement (i.e., the value of lateral displacement at which the tangent lateral stiffness becomes zero), which is known to decrease as axial load increases [31].

The theory treats an individual bearing as a homogenous isotropic column with its properties geometrically modified to account for the presence of the steel, which is assumed to be rigid. Nearly all works on the subject have focused on the case with zero rotation boundary conditions at the top and bottom supports of the bearing. Chang [47] and Karbakhsh Ravari et al. [46] applied the theory to the case where the supports experience rotation to study its effect on the behavior of the elastomeric bearings under vertical and lateral forces. In this section, we review the analytical formulation from Karbakhsh Ravari et al. [46], the results of which will be used in the following section to validate the results of FEA.

Fig. 4.1(a) shows a deformed bearing where the upper and lower supports experience a rotation angle of $\theta_h$ and $\theta_0$, respectively. The deformation pattern is defined by two quantities: $u(y)$ is the horizontal displacement of the midline of the bearing, and $\theta(y)$ is the rotation of a plane originally normal to the $y$ axis. Plane sections normal to the undeformed midline are assumed to remain plane but not necessarily normal to the deformed midline. The overall shear deformation, $\gamma$, is the difference between the slope of the midline, $u'(y)$, and $\theta(y)$. The shear force, $H_0$, and the axial force, $P$, are shown parallel and perpendicular, respectively, to the rotated surface. The bending moment, $M(y)$, and the shear force, $H(y)$, at a cross section at height $y$, as shown in Fig. 4.1(b), can be expressed as

$$M(y) = EI_s\theta'(y) \tag{2.1}$$

$$H(y) = GA_s\gamma = GA_s\left(u'(y) - \theta(y)\right) \tag{2.2}$$

where $E$ is the Young's modulus, $G$ is the shear modulus of the rubber material, $A_s = A\left(h/t_r\right)$ is the shear area of the elastomeric bearing, in which $h$ is the total height of the multilayer elastomeric bearing (including the steel), $t_r$ is the total height of rubber material, and $A$ is the cross sectional area. $EI_s$ is the bending rigidity of the rubber-steel composite system computed from $EI_s = EI_{eff}\left(h/t_r\right)$, where $EI_{eff}$ is the effective bending stiffness of an individual rubber layer, expressions for which can be found in [7] for bearings with various geometric shapes, both with and without compressibility included in the analysis. The bending stiffness of a circular elastomeric

bearing (incompressible rubber material) is obtained from

$$EI_s = 2GS^2 \frac{h}{t_r} \left( \frac{\pi R^4}{4} \right) \tag{2.3}$$

where $S = R/2t$ is the shape factor of the circular bearing with radius $R$ and rubber layers each of thickness $t$.

The equations of equilibrium for the shear force and bending moment in the deformed state, shown in Fig. 4.1(b), using Eqs. (2.1) and (2.2), are

$$P \sin(\theta_0) - H_0 \cos(\theta_0) + GA_s (u' - \theta) \cos(\theta) - P \sin(\theta) = 0 \tag{2.4}$$

$$EI_s \theta' + M_0 + [P \cos(\theta_0) + H_0 \sin(\theta_0)] u + [H_0 \cos(\theta_0) - P \sin(\theta_0)] y = 0 \tag{2.5}$$

where the argument $(y)$ of the variables has been dropped for brevity. When $\theta$, $\theta_0$ and $\theta_h$ are small, Eqs. (2.4) and (2.5) are [46]

$$GA_s (u' - \theta) - P\theta = H_0 - P\theta_0 \tag{2.6}$$

$$EI_s \theta' + (P + H_0\theta_0) u = (P\theta_0 - H_0) y - M_0 \tag{2.7}$$

The derivative of Eq. (2.7) gives [46]

$$EI_s \theta'' + (P + H_0\theta_0) u' = P\theta_0 - H_0 \tag{2.8}$$

Differentiating Eq. (2.6) and rearranging gives

$$\theta' = \beta u'' \tag{2.9}$$

where

$$\beta = \frac{GA_s}{GA_s + P} \tag{2.10}$$

Also, rearranging Eq. (2.6) gives

$$u' = \frac{1}{\beta}\theta - \frac{P}{GA_s}\left(\theta_0 - \frac{H_0}{P}\right) \tag{2.11}$$

Substituting Eq. (2.9) into Eq. (2.7) and Eq. (2.11) into Eq. (2.8) and rearranging gives the following two differential equations

$$u'' + \alpha^2 u = \frac{\alpha^2}{1 + \frac{H_0}{P}\theta_0}\left[\left(\theta_0 - \frac{H_0}{P}\right)y - \frac{M_0}{P}\right] \tag{2.12}$$

$$\theta'' + \alpha^2 \theta = \frac{\alpha^2 \beta}{1 + \frac{H_0}{P}\theta_0}\left(\theta_0 - \frac{H_0}{P}\right)\left[1 + \frac{P}{GA_s}\left(1 + \frac{H_0}{P}\theta_0\right)\right] \tag{2.13}$$

where $\alpha$ is defined by

$$\alpha^2 = \frac{1}{\beta}\frac{P}{EI_s}\left(1 + \frac{H_0}{P}\theta_0\right) \tag{2.14}$$

The solutions of Eqs. (2.12) and (2.13) are, respectively,

$$u = C_1 \cos(\alpha y) + C_2 \sin(\alpha y) + \frac{\theta_0 - \frac{H_0}{P}}{1 + \frac{H_0}{P}\theta_0} y - \frac{M_0}{P}\frac{1}{1 + \frac{H_0}{P}\theta_0} \tag{2.15}$$

$$\theta = \alpha\beta C_2 \cos(\alpha y) - \alpha\beta C_1 \sin(\alpha y) + \frac{\beta}{1 + \frac{H_0}{P}\theta_0}\left(\theta_0 - \frac{H_0}{P}\right)\left[1 + \frac{P}{GA_s}\left(1 + \frac{H_0}{P}\theta_0\right)\right] \tag{2.16}$$

where Eq. (2.11) has been used to obtain the constants multiplying the eigenfunctions in Eq. (2.16). The constants $C_1$ and $C_2$ can be determined from the boundary conditions. The general boundary conditions are: $\theta(0) = \theta_0$, $\theta(h) = \theta_h$, $u(0) = 0$,

$u(h) = u_h$. $u_h$ is the lateral displacement at the top of the bearing. From Eq. (2.16),

$$\theta(0) = \theta_0 \Rightarrow C_2 = \frac{1}{\alpha}\left[\frac{1}{\beta}\theta_0 - \frac{\theta_0 - \frac{H_0}{P}}{1 + \frac{H_0}{P}\theta_0}\left[1 + \frac{P}{GA_s}\left(1 + \frac{H_0}{P}\theta_0\right)\right]\right] \tag{2.17}$$

$$\theta(h) = \theta_h \Rightarrow C_1 = C_2\cot(\alpha h) - \frac{\csc(\alpha h)}{\alpha}\left[\frac{1}{\beta}\theta_h - \frac{\theta_0 - \frac{H_0}{P}}{1 + \frac{H_0}{P}\theta_0}\left[1 + \frac{P}{GA_s}\left(1 + \frac{H_0}{P}\theta_0\right)\right]\right] \tag{2.18}$$

and from Eq. (2.15),

$$u(0) = 0 \Rightarrow M_0 = P\left(1 + \frac{H_0}{P}\theta_0\right)C_1 \tag{2.19}$$

$$u(h) = u_h \Rightarrow u_h = C_1(\cos(\alpha h) - 1) + C_2\sin(\alpha h) + \frac{\theta_0 - \frac{H_0}{P}}{1 + \frac{H_0}{P}\theta_0}h \tag{2.20}$$

The lateral displacement at the top of the bearing due to the lateral load, $H_o$, axial load, $P$, and rotation angles, $\theta_0$ and $\theta_h$, is calculated from Eq. (2.20). This value is used to validate the FE model, which will be discussed in the next section.

## 2.4 Validation of Finite Element Analysis

In order to validate the FEA approach, the circular elastomeric bearing shown in Fig. 4.2 (which is similar to the bearing studied in [46]) was modeled in 3D using ABAQUS [45], and the results of the analysis were compared against the results of the analytical solution presented in the previous section. The bearing had a radius of $R = 140$ mm and consisted of 20 rubber layers ($n_r = 20$). The thickness of each layer was $t = 10$ mm, amounting to a total thickness of rubber of $t_r = 200$ mm. The thickness of the steel shims was $t_s = 2$ mm, and the top and bottom end plates were

21 mm thick with a radius of 160 mm.

Fig. 4.3 shows the 3D mesh of the circular bearing. The rubber layers were discretized with a combination of 8-node linear brick, hybrid, constant pressure elements (C3D8H), used nearly throughout, and 6-node linear triangular prism, hybrid, constant pressure elements (C3D6H), used around the central axis of the bearing. To avoid volumetric locking issues associated with nearly incompressible rubber-like materials, ABAQUS [45] uses a hybrid formulation, where the pressure and displacement fields are treated independently. The steel shims and end-plates were discretized with 8-node linear brick elements with incompatible modes (C3D8I). Elements with incompatible modes were used to deal with potential shear locking issues, which could result in spurious shear stresses.

As the rubber layers experience large deformations and displacements during the analysis, a hyperelastic material model was used for the rubber. The stresses in such a model are derived from a stored strain energy density function. In this model, the compressible Neo-Hookean material [48] was used for the rubber material. This material model is defined by two material constants: the shear modulus, $G$, and the bulk modulus, $K$. For the compressible Neo-Hookean model used in this study, the strain energy density function is

$$W = C_{10}\left(\bar{I}_1 - 3\right) + \frac{1}{D_1}\left(J-1\right)^2 \tag{2.21}$$

where $C_{10} = G/2$, $D_1 = 2/K$, $\bar{I}_1$ is the the first modified invariant of the deviatoric part of the Cauchy-Green deformation tensor, and $J$ is the elastic volume ratio. In the model developed for this study, $C_{10} = 0.31$ MPa and $D_1 = 2 \times 10^{-6}$ MPa$^{-1}$, which corresponds to nearly incompressible material. The steel shims and end plates

were modeled using a linear elastic material with Young's modulus of 200 GPa and Poisson's ratio of 0.3.

In the model, all nodes at the top end plate were constrained to a point located at the centroid of the end plate, and the displacement and force boundary conditions were assigned to this point. The control node was free to move vertically and laterally in one direction, and, in the case of support rotation, this node could rotate in the specified direction. Similar to the top end plate, all nodes at the bottom end plate were constrained to a control node. This point was restrained in all degrees of freedom except for rotation. The analysis was performed in two stages: in the first stage, the axial load and rotation were simultaneously applied to the top control node gradually until the desired values are achieved; in the second stage, the lateral force was applied gradually to the top control node until the desired value was achieved, while the axial load and rotation at the end of the first stage were kept constant. The applied axial and lateral load followed the nodal rotation (at the control node), i.e, the lateral load was parallel to the top rotated surface of the bearing, and the axial load was perpendicular to the surface. The analysis included nonlinear geometry, large displacements, and large strains. The incremental nonlinear analysis was conducted using an updated Lagrangian formulation and Newton-Raphson iteration method.

Four boundary condition cases were considered to compare the FEA with the analytical solution,

(1) No rotation of the end plates,

(2) Rotation of the top end plate only (control node at the top end plate),

(3) Rotation of the top and bottom end plates (control node at the top and bottom

end plates), and,

(4) Rotation of the bottom end plate only (control node at the bottom end plate).

The rotation angle in this analysis was 0.02 rad (1.15°), and the horizontal force was 5 kN. A series of analyses with different values of average vertical stress ($\bar{p} = P/A$) was performed. Fig. 4.4(a) shows the deformed shape of the bearing at the end of the first stage of the analysis, at which the axial force is 200 kN and the rotation angle is 0.02 rad at the top of the bearing, while Fig. 4.4(b) shows the bearing at the end of the second stage of the analysis, where the horizontal force is 5 kN. Fig. 4.5 shows a comparison between the FEA and the analytical solution results for the four aforementioned cases under a constant average vertical stress in the range of 0 to 5 MPa. The figure shows that there is good agreement between the results for all cases, thus providing confidence that the finite element model developed in ABAQUS can be used for further analysis. The figure also shows that for the different rotation cases, the maximum value of the shear strain ($u_{max}/t_r$) varies, and this variation becomes more pronounced under larger values of average vertical stress. As can be seen, the case of rotation at the top of the bearing causes the largest apparent shear strain, $u_h/t_r$.

## 2.5 Method for Determining the Critical Point

The *critical point* is defined as the point where the shear force reaches a maximum value in the lateral force–lateral displacement curve; the tangent lateral stiffness beyond this point becomes negative. For a given bearing, three quantities are associated with the critical point: the axial load, $P$, the lateral displacement, $u$, and the lateral (shear) force, $F$. To obtain this point by FEA, the constant-axial force method [32]

was used. Sanchez et al. [21] conducted experimental tests based on this method and showed that it is reliable for capturing the critical point. In this method, the $u$ and $F$ associated with the critical point are determined from the shear force–lateral displacement curve for a given constant $P$. In the loading part, the axial load is applied first, and then the horizontal displacement is applied incrementally, while the axial load is kept constant, until the horizontal tangent stiffness becomes zero, and the shear force attains its maximum value.

The loading history for the FEA in this study follows a similar approach, differing only by the application of rotation. During the first stage, the axial load and the rotation are applied together gradually until the desired values are reached. In the second stage of the analysis, the horizontal displacement is gradually increased while maintaining the axial load and rotation value from the first stage constant. In contrast to the analysis described in the previous section for validation purposes, the applied axial load and horizontal displacement do not follow the nodal rotation.

## 2.6 Effect of Rubber Description on the FEA Results

As mentioned earlier, rubber-like materials are typically described by hyperelastic material models. The Neo-Hookean solid is the simplest hyperelastic material model. It assumes that the shear modulus is constant during the analysis. Past experimental tests, however, have shown that the shear modulus is not constant, particularly at large shear strain values [48]. Other hyperelastic models, using more coefficients, provide more accurate description, but they require experimental data from material

tests, such as uniaxial tension and/or shear tests, to determine the coefficients. The main objective of this section is to study the effect of the material model on the critical point. In addition to Neo-Hookean material, two other constitutive models are considered for the rubber material: the Mooney-Rivlin [48] and the Yeoh [49] models. The strain energy density function for the Mooney-Rivlin constitutive model is defined by [48]

$$W = C_{10}\left(\bar{I}_1 - 3\right) + C_{20}\left(\bar{I}_2 - 3\right) + \frac{1}{D_1}\left(J-1\right)^2 \tag{2.22}$$

where $\bar{I}_2$ is the second modified invariant of the Cauchy-Green deformation tensor. The Neo-Hookean model can be obtained from the Mooney-Rivlin model by setting $C_{20} = 0$ in Eq. (2.22), resulting in the strain energy function given by Eq. (2.21).

The Yeoh strain-energy density function for compressible material is written in terms of the first modified invariant, $\bar{I}_1$, only [45],

$$W = C_{10}\left(\bar{I}_1 - 3\right) + C_{20}\left(\bar{I}_1 - 3\right)^2 + C_{30}\left(\bar{I}_1 - 3\right)^3 + \sum_{i=1}^{3}\frac{1}{D_i}\left(J-1\right)^{2i} \tag{2.23}$$

where $D_i$ are material parameters that introduce compressibility.

As mentioned above, standard material tests are needed to determine the model parameters of the strain energy density function for the Neo-Hookean, Mooney-Rivlin and Yeoh models. Uniaxial tension test and pure-shear test results from Forni et al. [50] are used herein for this purpose. Fig. 4.7 shows the results of a uniaxial tension and a pure-shear test [50]. Values for the model parameters are obtained using the 'material evaluation' curve-fitting tool available in ABAQUS [45]. Table 2.1 shows the resulting values. A value of 2000 MPa was assumed for the bulk modulus, $K$, for

all constitutive models.

To study the effect of rotation, a circular bearing with geometry similar to that in Weisman and Warn [33] was modeled in 3D. The bearing had a radius $R = 76$ mm, with 20 rubber layers, each 3 mm thick, providing a total rubber thickness of 60 mm. The bearing included 19 steel shims, each 3 mm thick. The steel material was modeled using a bilinear isotropic material model with Young's modulus of 200 GPa and a Poisson's ratio of 0.3. A post–yield modulus of 2 percent of the initial modulus was specified. In order to study the effect of the material model choice, two cases were considered: (1) No rotation at the end plates, and (2) Rotation at the top end plate only, $\theta_h = 0.02$ rad. To provide confidence in the predictions of the FEA model using different material models, the bearing was first analyzed by the procedure discussed in Section 2.4, and the results of the FEA were examined against the analytical solution. Fig. 4.8 shows a comparison between the FEA predictions using different hyperelastic material models and the analytical solution results for the case of rotation at the top support only ($\theta_h = 0.02$ rad) under a constant average vertical stress, $\bar{p}$, in the range of 0 to 16 MPa. As can be seen, there is good agreement between the results of the three FEA and the analytical solution for $\bar{p}$ up to 13 MPa. At large values of $\bar{p}$, there is a notable difference between the analytical solution and the three FEA solutions. This difference may be attributed to the fact that the FEA model considers full nonlinearity effects in both geometry and material behavior, while the theoretical model considers only *partial* nonlinear geometric effects (e.g., it does not consider axial shortening). Furthermore, it is observed that all three material models provide similar results at low to medium $\bar{p}$ values, while for large $\bar{p}$ values, the difference between the results of the three material models become more pronounced.

The increased discrepancy among the predictions of the three material models as $\bar{p}$ increases is due to the assumptions each model makes on the behavior of the rubber at large deformations. The results presented in Fig. 4.8 provide confirmation that the FEA model can be used with reasonable confidence to study the behavior of the bearing in the range of $\bar{p}$ used in this study.

This concludes the model validation, which utilized the analysis procedure presented in Section 2.4. The results presented in this paper from this point forward are from FEA that follows the analysis procedure presented in Section 2.5.

Fig. 4.9 shows the stress contours (in MPa) for the $S_{33}$ component of Cauchy stress, which is oriented along the vertical direction. Note that in the FEA the bearing was sheared along direction 1. The contours are plotted for the middle rubber layer (tenth rubber layer from the bottom of the bearing) at $u/t_r = 1$ and the critical point, $u_{cr}/t_r$. The three material models discussed above were used to describe the behavior of the rubber. The average vertical stress ($\bar{p}$) was equal to 11.02 MPa, and the rotation at the top end plate ($\theta_h$) was 0.02 rad counterclockwise. Despite the fact that these three models use different descriptions of the material, at the same displacement level, $u/t_r = 1$ (left column), all models provide similar prediction for the stress, while at the critical point (right column), the stress distribution varies slightly between the different hyperelastic material models. There is an area that experiences tension, and this area is larger for the Yeoh material in comparison with the Neo-Hookean and Mooney-Rivlin materials; the reason being that the Yeoh material predicts larger critical displacement. The differences between the stress distribution predicted by the different constitutive models at the critical point can be attributed on the assumptions the models place on the shear modulus. The Neo-Hookean model assumes that the

shear modulus is constant during the analysis, while for the other two models, the shear modulus decreases with increasing shear strain [45]. The differences can be more pronounced at large values of shear strain.

Fig. 4.11 shows a vertical cross section through the center of the bearing, together with the axes indicating the orthogonal directions 1–2–3. Line segment AA runs along the top of the uppermost rubber layer (where the rubber meets the steel end plate), while BB runs along the top of the middle (tenth) rubber layer (where the rubber meets the steel shim above it); both segments are parallel to direction 1. These segments will be referred to hereinafter in discussing stresses along those paths.

Fig. 4.12 shows the variation of normalized normal stress $S_{33}/\bar{p}$ and normal strain $\epsilon_{33}$ along segment BB (i.e., from $x = 0$ to $x = 2R$) under a displacement of $u/t_r = 0$ (left) and $u/t_r = 1.5$ (right), for the different material models. The average vertical stress is $\bar{p} = 11.02$ MPa, and the support rotations are zero in all cases. As can be seen, the normal stress distributions predicted by different material models are nearly identical to one another under pure compression ($u/t_r = 0$), while the Mooney-Rivlin model predicts different $S_{33}/\bar{p}$ in comparison with the other two models at larger lateral displacement ($u/t_r = 1.5$). For example, $S_{33}/\bar{p}$ at $x = R$ is $-2.58$ for the Mooney-Rivlin model, while it is approximately $-2.43$ and $-2.45$ for the Yeoh and Neo-Hookean models, respectively. The figure shows that at $u/t_r = 1.5$, the rubber layer experiences tensile stress close to the edges. These tensile stresses in the triangular regions outside the overlapping area develop in order to equilibrate the unbalanced moment that is generated by shear displacement of the bearing. The maximum tensile stress $S_{33}$ is 2.32, 1.59 and 1.27 MPa for the Mooney-Rivlin, Neo-Hookean and Yeoh models, respectively. When the bearing was sheared, the difference

between the results for $\epsilon_{33}$ is more pronounced than for $S_{33}/\bar{p}$. For example, the largest value of $|\epsilon_{33}|$ is 0.85, 0.82 and 0.79 for the Mooney-Rivlin, Neo-Hookean and Yeoh material models, respectively. Fig. 4.13 shows normalized shear stress $S_{13}/G$ and shear strain $\gamma_{13}$ distributions along segment BB. Under the pure compression case ($u/t_r = 0$), both the shear stress $S_{13}$ and shear strain $\gamma_{13}$ distributions are insensitive to the material model choice. $S_{13}/G$ is slightly different at the large lateral displacement ($u/t_r = 1.5$) for different material models, while the shear strain distributions predicted by different material models are close to each other. The same results were observed when the support rotations were not zero (not shown here). In general, it can be concluded that the material model choice does not affect the stress and strain distributions at low lateral displacements, but it can begin to have a noticeable effect at larger horizontal displacements. This conclusion is in agreement with the earlier observation that the differences between the predictions of the various material models become more pronounced when the bearing undergoes a large shear displacement.

Fig. 4.14 shows the effect of rotation at the top of the bearing on (a) the normalized critical displacement, $u_{cr}/t_r$, and (b) the normalized critical shear force, $F_{cr}/GA$, for the three constitutive models. The vertical axis plots the average vertical stress, which remains constant, for a given analysis. In the legend, 'R' denotes the case with 0.02 rad counterclockwise rotation at the top, and 'NR' denotes the case with no rotation. As can been seen, the choice of constitutive model affects the results, especially for the low values of critical pressure where the critical displacement is high. Following the earlier discussion, differences between the prediction of different constitutive models should be expected to be more pronounced at larger lateral

displacement, where the assumption of constant shear modulus (Neo-Hookean) loses its validity. This difference is more noticeable on the $\bar{p}_{cr}$ versus $F_{cr}/GA$ graph. It is interesting to note that the 0.02 rad counterclockwise rotation results in only a very small decrease in the critical displacement; however, it significantly increases the critical shear force.

## 2.7 Effect of Rotation on Stress and Strain Distributions

In order to study the effect of rotation on stress and strain distributions, the aforementioned bearing model with the Mooney-Rivlin material description for the rubber was analyzed under a constant vertical load (corresponding to $\bar{p} = 11.02$ MPa). Fig. 2.13 shows the deformation of the rubber layers at the cross section shown in Fig. 4.11 at different displacements ($u/t_r = u_o/t_r,\ 1,\ u_{cr}/t_r$) for different rotation angles at the top of the bearing ($\theta_h = 0, +0.02, -0.02$ rad, where the convention for positive rotation is counterclockwise). The leftmost column shows the deformed shapes at the end of the *first* state of the analysis. These deformed shapes indicate that the simultaneous application of rotation and vertical load in the first analysis stage causes the top surface of the bearing, which is not constrained laterally, to sway sideways. The horizontal displacement value at the end of the first stage of the analysis is herein referred to as *Initial Displacement* and denoted by $u_o$. $u_o$ can be positive or negative depending on the direction of the rotation. Positive (counterclockwise) rotation results in a negative initial displacement, and negative rotation in positive initial displacement. The effect of the rotation is obvious from the onset of the second

stage of the analysis ($u_o/t_r$) where, depending on the direction of the rotation, one end of the bearing moves down, while the other moves up, with respect to the position of the center of the rubber layer (i.e., $x = R$). The effect of rotation on various stress and strain distributions as the lateral displacement is increased is discussed next.

Fig. 2.14 shows the variation of normalized normal stress $S_{33}/\bar{p}$ (where $\bar{p} = 11.02$ MPa) in the rubber along line segments AA and BB (see Fig. 4.11) for $u/t_r = u_o/t_r$, 0, 1, and $u_{cr}/t_r$ and $\theta_h = 0, +0.02, +0.04$ rad. At the initial lateral displacement ($u_o/t_r$), the effect of rotation is more pronounced in the middle rubber layer (line segment BB). For example, the maximum compressive value of $S_{33}/\bar{p}$ in the top rubber layer is 1.50, 1.58 and 1.70 for $\theta_h = 0, +0.02, +0.04$ rad, respectively, whereas the corresponding values in the middle rubber layer are 1.50, 1.72 and 2.05. Moreover, the rotation changes the location where $S_{33}/\bar{p}$ attains its maximum value. The shift in the location of the maximum value caused by rotation is more pronounced in the middle rubber layer.

Especially important in this figure is the effect of rotation on the maximum tensile stresses, which are important in elastomeric bearings due to concerns for cavitation in the rubber and for debonding at the rubber–steel interface. The counterclockwise rotation of the top plate causes an increase in compression at the left side of the bearing and a decrease at the right side. Even at low lateral displacements, if the rotation is very large, it is possible for the stretching at the right side of the bearing to overcome the compression induced by the axial load and causes $S_{33}$ to be tensile. This, however, was not observed under the realistic values of average compressive stress and rotation angles used in this study. As the lateral displacement increases (see plots for $u/t_r = 1$ and $u_{cr}/t_r$ in Fig. 2.14), however, tensile stresses develop on the right side of bearing.

These tensile stresses are larger closer to the top of the bearing (segment AA) than the middle (segment BB), and they are appreciably exacerbated by the application of rotation. At $u/t_r = 1$, the maximum tensile value of $S_{33}$ at the top rubber layer is 2.46, 3.41 and 4.61 MPa for $\theta_h = 0, +0.02, +0.04$ rad, respectively, and it increases to 6.17, 6.91 and 7.72 MPa (for the same rotation values) at the critical displacement. These tensile stresses are large and in fact exceed the $3G$ negative pressure limit proposed by Gent [51] for the onset of cavitation. Previous studies report conflicting conclusions regarding how lateral displacement affects the cavitation strength of elastomeric bearings. For example, Kelly [52] cites experimental tests where bearings experienced tension that far exceeded the $3G$ cavitation limit, while Kumar et al. [53] concluded from their experimental tests that cavitation strength decreases with increasing lateral displacement. It is noted here that the hyperelastic models used in the present study do not include damage characterization, such as cavitation. The description of cavitation damage within hyperelastic constitutive models used in FEA is very complex and goes beyond the scope of this study. Nonetheless, the notable increase in maximum tensile stress $S_{33}$ caused by rotation as the bearing is sheared is a cause of concern. This observation, in conjunction with the conflicting observations of previous studies [52,53], calls for further studies to elucidate how the cavitation phenomenon manifests itself in elastomeric bearings under combined loading that includes rotation.

In the middle rubber layer (bottom row in Fig. 2.14), as expected, the compressive stress in the central portion of the bearing (i.e., the so-called overlapping area) increase with increasing lateral displacement. At larger displacement levels, as was the case for the top layer, tensile stresses develop. The *relative* increase in maximum

tensile stress $S_{33}$ due to rotation is larger in the middle layer than in the top layer; however, the numerical value of the maximum tensile stress in the middle layer is smaller than that in the top layer.

Fig. 2.15 shows the contours of shear strain $\gamma_{13}$ at the cross section shown in Fig. 4.11 for $\theta_h = 0$, +0.02 and +0.04 rad and different lateral displacement levels. The strain contour plots are plotted in the undistorted shape of the bearing. As can be seen, regardless of the rotation angle, for $u/t_r = u_o/t_r$ and 0, the peak shear strain occurs at the top and bottom outer edges of the rubber layers. Rotation at the top of the bearing results in a significant increase in the peak value of $\gamma_{13}$. For example, 0.02 and 0.04 rad rotation result in a 34 and 58 percent increase, respectively. Similarly, rotation increases the peak value of $\gamma_{13}$ at larger lateral displacement levels, although the percentage increase relative to the case of no rotation is smaller because the lateral displacement of bearing causes an additional shear strain that is fairly uniform throughout the rubber layer. At $u_{cr}/t_r$, the peak value of $\gamma_{13}$ is 2.29, 2.71 and 2.98 for $\theta_h = 0$, +0.02 and +0.04 rad, respectively.

Finally, it is interesting to examine how average vertical stress, $\bar{p}$, affects the stress distribution. Fig. 2.16 shows the variation of normal stress $S_{33}$ along line segment AA, shown in Fig. 4.11, at $u_o/t_r$ (top row) and $u_{cr}/t_r$ (bottom row) under $\bar{p} = 8.26$ and 11.02 MPa for various levels of rotation. Similar overall observations to those made above for $\bar{p} = 11.02$ MPa can be made about the shape of the stress distribution under $\bar{p} = 8.26$ MPa. At $u_o/t_r$ the larger $\bar{p}$ value of the two causes a larger peak compressive stress $S_{33}$. At $u_{cr}/t_r$, the larger $\bar{p}$ value results in a smaller peak tensile stress. For example, under zero support rotation, the peak tensile stress at the critical displacement is 7.85 and 6.17 MPa for $\bar{p} = 8.26$ and 11.02 MPa, respectively.

On the other hand, for a given support rotation angle, an increase in $\bar{p}$ seems to have a negligible effect on the peak compressive stress at the critical displacement.

## 2.8 Effect of Rotation on the Critical Point

In order to study the effect of rotation on the critical point, the aforementioned bearing model with the Mooney-Rivlin material description for the rubber was analyzed under a constant vertical load (corresponding to $\bar{p} = 8.26$ MPa). Fig. 2.17 presents normalized shear force–displacement curves (from the second stage of loading) for different values of rotation ($-0.04$ to $+0.04$ rad) at the top of the bearing. The figure shows the initial displacement, $u_o$, that corresponds to $F/GA = 0$, which was discussed earlier. $u_o$ increases in magnitude with larger rotation, and it can be positive or negative depending on the rotation direction. The load–displacement curves show that the tangent stiffness is nearly constant for most of the displacement range except near the critical point, where it drops to zero, and beyond which it becomes negative. At displacements less than the critical point, the amount of the rotation does not seem to affect the tangent stiffness of the bearing. These observations on the tangent stiffness, together with the fact that a positive rotation causes a negative initial displacement, explain why at any given lateral displacement $u/t_r$ (below the critical point), the force is larger under positive rotation than under zero rotation. Similarly, under negative rotation the force is lower than under zero rotation at a given $u/t_r$. The figure also shows that rotation has a minimal effect on the lateral displacement at the critical point but can affect the critical shear force. For instance, rotation of $+0.04$ rad increases the critical shear force by 13 percent, as compared to the zero rotation case, while rotation of $-0.04$ rad decreases it by approximately

15 percent. The critical displacement, on the other hand, is decreased by only 3.4 percent for +0.04 rad rotation, and increased by 1.2 percent for −0.04 rad rotation.

Fig. 2.18 shows the effect of rotation on the horizontal behavior of the bearing under different values of average vertical stress ($\bar{p} = 5.5$, 8.26 and 11.02 MPa). Two support rotation cases were considered: rotation at the top, and rotation at the top and bottom of the bearing. The value of the rotation varies from 0 to 0.04 rad. The figure shows that increasing the pressure can increase the initial displacement $u_o$ (for the same rotation value). The reason for this increased initial displacement is because, under rotation, a component of the vertical load acts as a shear force in the bearing, resulting in a horizontal displacement; the larger axial load (or average vertical stress), the larger that lateral displacement. Under large pressure, this initial displacement can be appreciable. For example, under a pressure of $\bar{p} = 11.02$ MPa, a 0.02 rad rotation at the top of the bearing results in an initial displacement of $u/t_r = 0.19$. As expected, the critical shear force decreases with increasing $\bar{p}$. The increased separation between load–displacement curves with larger $\bar{p}$, suggests that the relative effect of rotation is more pronounced. The case of rotation at the top and bottom (both counterclockwise) is more significant in the sense that it causes larger value of initial displacement than the first case with rotation at the top only. Also, the shear force at the critical point is larger for the case with rotation at both supports.

Fig. 2.19 shows the effect of rotation on the critical point of the bearing under different values of $\bar{p}$ (5.5, 8.26, 9.64, 11.02 and 12.40 MPa) for the same two support rotation cases. As can be seen, the rotation does not significantly affect the critical displacement for either case. Only a very slight decrease is observed with increasing

counterclockwise rotation. However, the rotation increases the critical shear force, particularly for the case of rotation at the top and bottom. To summarize, the case of rotation at both the top and bottom support can be more important than the other case.

## 2.9 Elastomeric Seismic Isolation Bearings: Case Studies

Up to this point, this paper has focused on elastomeric bearing configurations with low values of first and second shape factor, $S$ and $S_2$, respectively, the latter of which is defined for circular bearings as the ratio of the bearing diameter to the total thickness of rubber layers. Previous studies on stability of elastomeric bearings also focused on bearing designs with $S$ and $S_2$ values that were in the order of what was used in this study, e.g. [21,24,29,32,33]. Emphasis was given to such bearing designs because stability considerations become especially important for slender bearings with low shape factor layers. In most modern base-isolation applications, it is common to use bearings with fairly large values of $S$ and $S_2$. Elastomeric bearing manufacturers market such bearing designs in an effort to avoid stability concerns up to a practical lateral displacement design limit (e.g., $3t_r$). While bearing designs with large $S$ and $S_2$ values are the norm in modern seismic isolation applications, bearings with low to intermediate $S$ and $S_2$ are still widely available and offer certain advantages in specific applications, such as the potential to provide isolation in both the horizontal and vertical directions [54,55]; consequently, the instability potential of these bearing designs requires investigation.

In Sections 5 through 7, a bearing with $S = 12.66$ and $S_2 = 2.53$ was considered. Both shape factor values for that bearing can be considered to be on the low end for a modern seismic isolation bearing. This section examines the stability limits of five bearing designs with $S$ and $S_2$ values varying from 15 to 30 and 2.50 to 4.375, respectively. These five designs can be considered to fall within the low to intermediate $S$ and $S_2$ range. Table 2.2 lists details of the five bearings. All five bearings are annular in shape with inner diameter of 100 mm, 32 rubber layers (with $G = 0.9$ MPa and $K = 2000$ MPa), each 5 mm thick. Bearing 3 is a Bridgestone Corp. design [56].

The last three columns of Table 2.2 list the critical displacement, $u_{cr}/t_r$, corresponding to $\theta_h = 0$, $+0.02$ and $+0.04$ rad, when the bearings are subjected to $\bar{p} = 7.95$ MPa. Table 2.3 presents the results for the same five bearings but subjected to $\bar{p} = 10.61$ MPa. The values of critical displacement listed in Tables 2.2 and 2.3 demonstrate that rotation has a negligible effect in all cases. With regard to shape factor values, Montuori et al. [34] concluded that bearings with $S = 20$ and $S_2$ greater than 3.6, under the pressure used in practical design (8 MPa), do not experience any instability for $u/t_r < 3$. The $u_{cr}/t_r$ results for Bearing 5 shown in Tables 2.2 and 2.3 confirm this observation. The results from Tables 2.2 and 2.3 show that for bearings with lower values of $S_2$ than in [34] (i.e., $S_2 < 3.6$), the critical displacement is in fact less than $3t_r$, regardless of the value of $S$ or $\theta_h$. For example, Bearing 3 with $S = 20$ and $S_2 = 3.12$ reaches its critical lateral displacement at $u/t_r = 2.28$, 2.25 and 2.23 under rotation of 0, $+0.02$ and $+0.04$ rad, respectively. These values are lower than what is typically targeted in a base isolation design. Therefore, although rubber bearings with low to intermediate $S$ and $S_2$ values may be well used in seismic

isolation applications, their stability cannot be taken for granted, and care must be taken to ensure that the total maximum displacement of the isolator considered in design falls below the critical lateral displacement limit.

## 2.10 Conclusions

This study followed a 3D finite element approach to investigate the behavior of elastomeric bearings under combined applied loading, which included vertical load, horizontal displacement and rotation. First, the finite element model was validated against the results of an analytical solution under relatively low lateral displacement. Various rotation cases at the top and bottom supports of the bearing were considered. Subsequently, the paper studied the effect of the constitutive model choice (Neo-Hookean, Mooney-Rivlin and Yeoh hyperelastic material models) for the rubber. The paper then investigated the effect of rotation on stress and strain distributions, the load–displacement behavior, and the critical point of elastomeric bearings. The main observations of the study (based on a bearing with $S = 12.66$ and $S_2 = 2.53$) are as follows:

- The material model selection influences the critical point, particularly when the critical pressure is low, where the critical shear strain is large. It was shown that using different material models does not affect the stress and strain distributions at zero lateral displacement but can have a noticeable effect at large lateral displacement.

- Rotation has a more pronounced effect on the stress and strain distributions at smaller lateral displacement levels than larger ones. The simultaneous action

of rotation and axial load was observed to cause an initial lateral displacement that can change the lateral behavior of the bearing.

- For a given average vertical stress, and at displacements less than the critical point, the amount of the rotation does not seem to affect the tangent stiffness. Because the tangent stiffness is fairly constant and positive rotation causes negative initial displacement, at a given displacement, the shear force is larger under positive rotation than under no rotation—and smaller under negative rotation than under no rotation. At large displacements, near the critical value, the tangent stiffness decreases at a different rate depending on the support rotation angle.

- In general, support rotation has a minimal effect on the critical displacement, but it affects the critical shear force.

- A larger average vertical stress $\bar{p}$, for a given rotation value, results in a larger initial lateral displacement. As expected, the tangent stiffness and the critical shear force decrease with increasing $\bar{p}$. The increased separation between load–displacement curves with increased $\bar{p}$ suggests that the relative effect of rotation becomes more pronounced.

The last section of the paper concluded that for bearings with first and second shape factor in the 15 to 22.5 and 2.5 to 3.44 range, respectively, the instability point occurs at displacement less than $3t_r$, but again rotation has negligible effect on the critical displacement. In contrast, the bearing with $S = 30$ and $S_2 = 4.375$ experiences instability at displacement larger than $3t_r$.

As the first systematic FEA study of its kind on the behavior of rubber bearings under combined compression, lateral displacement and support rotation, the support rotation value was kept constant during the shearing of the bearing. Future studies need to investigate the effect of the more complex case where rotation varies as the lateral displacement increases.

## 2.11 References

[1] Stanton JF, Roeder CW. Elastomeric bearings design, construction, and materials. *NCHRP Report 248*. National Cooperative Highway Research Program (NCHRP). Transportation Research Board, Washington, DC, 1982.

[2] Buckle IG, Constantinou MC, Diceli M, Ghasemi H. Seismic isolation of highway bridges. *Report MCEER-06-SP07*. Multidisciplinary Center for Earthquake Engineering Research. University at Buffalo, State University of New York, 2006.

[3] Konstantinidis D, Kelly JM, Makris N. Experimental investigation on the seismic response of bridge bearings. *Report EERC 2008-02*. Earthquake Engineering Research Center. University of California, Berkeley, 2008.

[4] Constantinou MC, Kalpakidis I, Filiatrault A, Ecker Lay RA LRFD-based analysis and design procedures for bridge bearings and seismic isolators. *Report MCEER-11-0004*. Multidisciplinary Center for Earthquake Engineering Research. University at Buffalo, State University of New York, 2011.

[5] Naeim F, Kelly JM. *Design of seismic isolated structures: from theory to practice*. New York, NY: John Wiley & Sons, 1999.

[6] Constantinou MC, Whittaker AS, Kalpakidis Y, Fenz DM, Warn GP. Performance of seismic isolation hardware under service and seismic loading. *Report MCEER-07-0012*. Multidisciplinary Center for Earthquake Engineering Research. University at Buffalo, State University of New York, 2007.

[7] Kelly JM, Konstantinidis D. *Mechanics of rubber bearings for seismic isolation and vibration isolation.* Chichester: John Wiley & Sons, 2011.

[8] Kelly JM. *Earthquake-resistant design with rubber*, 2nd ed. London: Springer-Verlag Telos, 1997.

[9] Buckle IG, Kelly JM. Properties of slender elastomeric isolation bearings during shake table studies of a large-scale model bridge deck. ACI Special Publication 1986; 94: 247–270.

[10] Koh CG, Kelly JM. Effects of axial load on elastomeric isolation bearings. *Report UCB/EERC-86/12*. Earthquake Engineering Research Center. University of California, Berkeley, 1987.

[11] Chalhoub MS, Kelly JM. Effect of bulk compressibility on the stiffness of cylindrical base isolation bearings. International Journal of Solids and Structures 1990; 26(7):743–760.

[12] Stanton JF, Roeder CW, Mackenzie-Helnwein P, White C, Kuester C, Craig B. Rotation limits for elastomeric bearings. *Report NCHRP 596*. National Cooperative Highway Research Program (NCHRP). Transportation Research Board, Washington, DC, 2008.

[13] Ohsaki M, Miyamura T, Kohiyama M, Yamashita T, Yamamoto M, Nakamura, N. Finite-element analysis of laminated rubber bearing of building frame under seismic excitation. Earthquake Engineering & Structural Dynamics 2015; 44(11): 1881–1898.

[14] Crowder AP, Becker TC. Preliminary study on the behaviour of a column-top isolation system. In: Proc. 11th Canadian Conference on Earthquake Engineering, Victoria, BC, 21–24 July 2015.

[15] Haringx JA. On highly compressible helical springs and rubber rods and their application for vibration-free mountings. Philips Research Reports 1948; 13(6): 401–449.

[16] Gent AN. Elastic stability of rubber compression springs. Journal of Mechanical Engineering Science 1964; 6(4): 318–326.

[17] Stanton JF, Scroggins G, Taylor A, Roeder CW. Stability of laminated elastomeric bearings. Journal of Engineering Mechanics 1990; 116(6): 1351–1371.

[18] Buckle IG, Liu H. Stability of elastomeric seismic isolation systems. Seminar on Seismic Isolation, Passive Energy Dissipation and Control. Applied Technology Council (ATC), Redwood City, CA, 1993; 293305.

[19] Buckle IG, Nagarajaiah S, Ferrell K. Stability of elastomeric isolation bearings: experimental Study. Journal of Structural Engineering 2002; 128(1): 3–11.

[20] Cardone D, Perrone G. Critical load of slender elastomeric seismic isolators: an experimental perspective. Engineering Structures 2012; 40: 198–204.

[21] Sanchez J, Masroor A, Mosqueda G, Ryan KL. Static and dynamic stability of elastomeric bearings for seismic protection of structures. Journal of Structural Engineering 2013; 139(7): 1149–1159.

[22] Koh CG, Kelly JM. A simple mechanical model for elastomeric bearings used in base isolation. International Journal of Mechanical Sciences 1988; 30(12): 933–943.

[23] Koo G, Lee J, Yoo B, Ohtori Y. Evaluation of laminated rubber bearings for seismic isolation using modified macro-model with parameter equations of instantaneous apparent shear modulus. Engineering Structures 1999; 21(7): 594–602.

[24] Nagarajaiah S, Ferrell F. Stability of elastomeric seismic isolation bearings. Journal of Structural Engineering 1999; 125(9): 946–954.

[25] Iizuka M. A macroscopic model for predicting large-deformation behaviors of laminated rubber bearings. Engineering Structures 2000; 22(4): 323–334.

[26] Yamamoto S, Kikuchi M, Ueda M, Aiken ID. A mechanical model for elastomeric seismic isolation bearings including the influence of axial load. Earthquake Engineering & Structural Dynamics 2009; 38(2): 157–180.

[27] Kikuchi M, Nakamura T, Aiken ID. Three-dimensional analysis for square seismic isolation bearings under large shear deformations and high axial loads. Earthquake Engineering & Structural Dynamics 2010; 39(13): 1513–1531.

[28] Han X, Warn GP. Mechanistic model for simulating critical behavior in elastomeric bearings. Journal of Structural Engineering 2014; 139(12): 04014140.

[29] Vemuru VSM, Nagarajaiah S, Masroor A, Mosqueda G. Dynamic lateral stability

of elastomeric seismic isolation bearings. Journal of Structural Engineering 2014; 140(8): A4014014.

[30] Vemuru VSM, Nagarajaiah S, Mosqueda G. Coupled horizontal–vertical stability of bearings under dynamic loading. Earthquake Engineering & Structural Dynamics 2016; 45(6): 913–934.

[31] S JC, Kelly JM. Finite element analysis of the stability of multilayer elastomeric bearings. Engineering Structures 1984; 6(3): 162–174.

[32] Warn GP, Weisman J. Parametric finite element investigation of the critical load capacity of elastomeric strip bearings. Engineering Structures 2011; 33(12): 3509–3515.

[33] Weisman J, Warn GP. Stability of elastomeric and lead-rubber seismic isolation bearings. Journal of Structural Engineering 2012; 128(2): 215–223.

[34] Montuori GM, Mele G, Marrazzo G, Brandonisio G, De Luca A. Stability issues and pressure–shear interaction in elastomeric bearings: the primary role of the secondary shape factor. Bulletin of Earthquake Engineering 2016; 14(2): 569–597.

[35] Nguyen HH, Tassoulas JL. Directional effects of shear combined with compression on bridge elastomeric bearings. Journal of Bridge Engineering 2009; 15(1): 73–80.

[36] Mordini A, Strauss A. An innovative earthquake isolation system using fiber reinforced rubber bearings. Engineering Structures 2008; 30(10): 2739–2751.

[37] Toopchi-Nezhad H, Tait MJ, Drysdale RG. Bonded versus unbonded strip fiber reinforced elastomeric isolators: Finite element analysis. Composite Structures 2011; 93(2): 850–859.

[38] Osgooei PM, Tait MJ, Konstantinidis D. Finite element analysis of unbonded square fiber-reinforced elastomeric isolators (FREIs) under lateral loading in different directions. Composite Structures 2014; 113: 164–173.

[39] Osgooei PM, Tait MJ, Konstantinidis D. Three-dimensional finite element analysis of circular fiber-reinforced elastomeric bearings under compression. Composite Structures 2014; 108: 191–204.

[40] Van Engelen NC, Osgooei PM, Tait MJ, Konstantinidis D. Experimental and finite element study on the compression properties of Modified Rectangular Fiber-Reinforced Elastomeric Isolators (MR-FREIs). Engineering Structures 2014; 74: 52–64.

[41] Osgooei PM, Van Engelen NC, Konstantinidis D, Tait MJ. Experimental and finite element study on the lateral response of modified rectangular fiber-reinforced elastomeric isolators (MR-FREIs). Engineering Structures 2015; 85: 293–303.

[42] Al-Anany Y, Tait MJ. A numerical study on the compressive and rotational behaviour of fiber reinforced elastomeric isolators (FREI). Composite Structures 2015; 133: 1249–1266.

[43] Osgooei PM, Konstantinidis D, Tait MJ. Variation of the vertical stiffness of strip-shaped fiber-reinforced elastomeric isolators under lateral loading. Composite Structures 2016; 144: 177–184.

[44] Konstantinidis D, Rastgoo Moghadam S. Compression of unbonded rubber layers taking into account bulk compressibility and contact slip at the supports. International Journal of Solids and Structures 2016; 87: 206–221.

[45] Dassault Systèmes Simulia Corp. ABAQUS/CAE Version 6.10-1, Providence, RI, 2010.

[46] Karbakhsh Ravari A, Othman IB, Ibrahim ZB, Ab-Malek K. P-$\Delta$ and end rotation effects on the influence of mechanical properties of elastomeric isolation bearings. Journal of Structural Engineering 2012; 138(6): 669–675.

[47] Chang C. Modeling of laminated rubber bearings using an analytical stiffness matrix. International Journal of Solids and Structures 2002; 39(24): 6055–6078.

[48] Bathe KJ. *Finite Element Procedures.* New York, NY: Prentice Hall, 1995.

[49] Yeoh O. Some forms of the strain energy function for rubber. Rubber Chemistry and Technology 1993; 66(5): 754–771.

[50] Forni M, Martelli A, Dusi A. Implementation and validation of hyperelastic finite element models of high damping rubber bearings. Constitutive Models for Rubber 1999; 1: 237–247.

[51] Gent AN. Cavitation in rubber: a cautionary tale. Rubber Chemistry and Technology 1990; 63(3): 49–53.

[52] Kelly JM. Tension buckling in multilayer elastomeric bearings. Journal of Engineering Mechanics 2003; 129(12): 1363–1368.

[53] Kumar M, Whittaker AS, Constantinou MC. Experimental investigation of cavitation in elastomeric seismic isolation bearings. Engineering Structures 2015; 101: 290–305.

[54] Aiken ID, Kelly JM, Tajirian FF. Mechanics of low shape factor elastomeric seismic isolation bearings. *Report UCB/EERC–89/13*. Earthquake Engineering Research Center. University of California, Berkeley, 1989.

[55] Tajirian FF, Kelly JM, Aiken ID, Veljovich W. Elastomeric bearings for three-dimensional seismic isolation. Proceedings of the 1990 ASME Pressure Vessels and Piping Conference, Nashville, TN, 17–21 June 1990.

[56] Bridgestone, Inc. Base isolation manual. Bridgestone Engineered Products Company, Inc., Nashville, TN, 1999.

Table 2.1: Model parameters for the constitutive models.

| Material Model | $C_{10}$ (MPa) | $C_{20}$ (MPa) | $C_{30}$ (MPa) | $D_1$ ($MPa^{-1}$) |
|---|---|---|---|---|
| Neo-Hookean | 0.4500 | - | - | 0.001 |
| Mooney-Rivlin | 0.3904 | 0.0600 | - | 0.001 |
| Yeoh | 0.4682 | $-0.0188$ | 0.0018 | 0.001 |

Table 2.2: Critical displacement, $u_{cr}/t_r$, for five bearing designs under an average vertical stress of $\bar{p} = 7.95$ MPa.

| | | | $u_{cr}/t_r$ | | |
|---|---|---|---|---|---|
| | | | $\theta_h = 0$ | $\theta_h = +0.02$ | $\theta_h = +0.04$ |
| Bearing | $S$ | $S_2$ | (rad) | (rad) | (rad) |
| 1 | 15.0 | 2.50 | 1.55 | 1.53 | 1.50 |
| 2 | 17.5 | 2.81 | 1.80 | 1.76 | 1.77 |
| 3 | 20.0 | 3.12 | 2.28 | 2.25 | 2.23 |
| 4 | 22.5 | 3.44 | 2.58 | 2.56 | 2.52 |
| 5 | 30.0 | 4.375 | 3.68 | 3.63 | 3.60 |

Table 2.3: Critical displacement, $u_{cr}/t_r$, for five bearing designs under an average vertical stress of $\bar{p} = 10.61$ MPa.

| | | | $u_{cr}/t_r$ | | |
|---|---|---|---|---|---|
| | | | $\theta_h = 0$ | $\theta_h = +0.02$ | $\theta_h = +0.04$ |
| Bearing | $S$ | $S_2$ | (rad) | (rad) | (rad) |
| 1 | 15.0 | 2.50 | 1.35 | 1.31 | 1.29 |
| 2 | 17.5 | 2.81 | 1.60 | 1.56 | 1.54 |
| 3 | 20.0 | 3.12 | 2.03 | 2.02 | 2.00 |
| 4 | 22.5 | 3.44 | 2.31 | 2.29 | 2.27 |
| 5 | 30.0 | 4.375 | 3.36 | 3.32 | 3.29 |

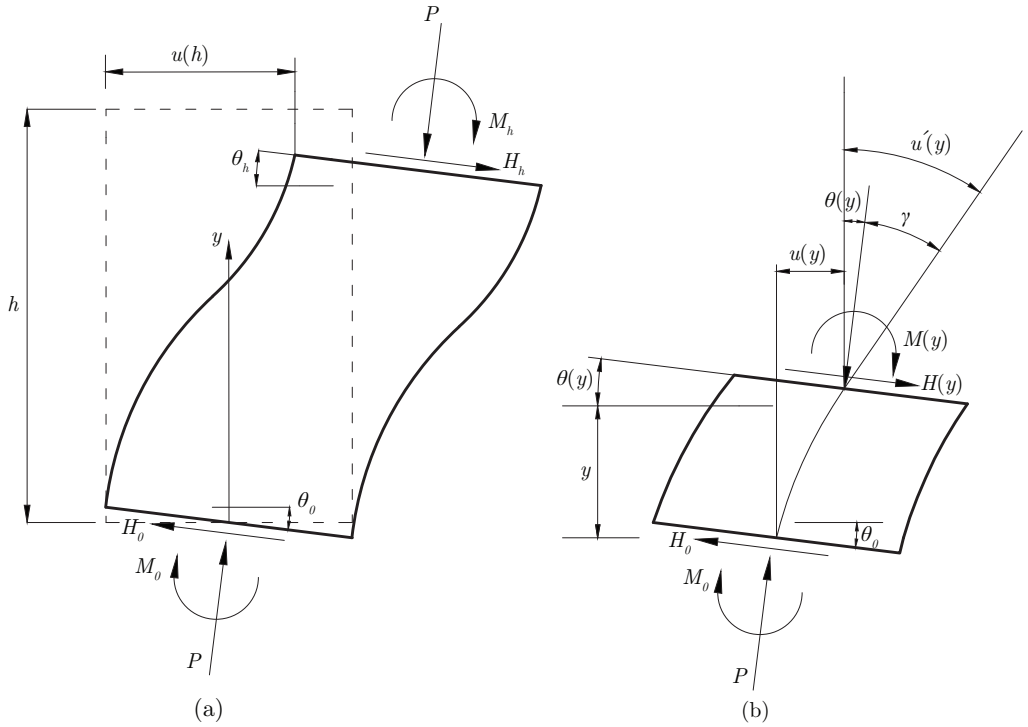


Figure 2.1: Deformed elastomeric bearing including rotation boundary conditions (a) Full bearing, (b) portion of the bearing below cut at elevation $y$.

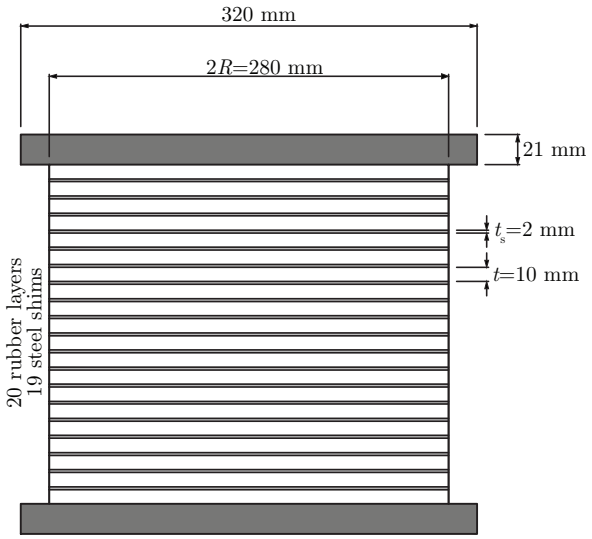


Figure 2.2: Geometry of the circular elastomeric bearing.

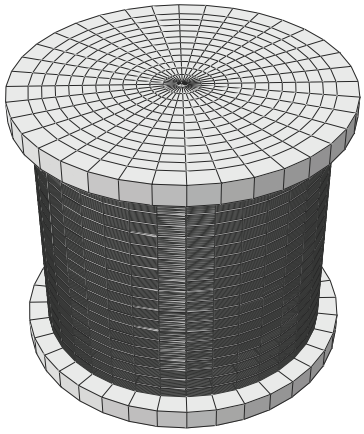

Figure 2.3: Finite Element mesh of the circular bearing.

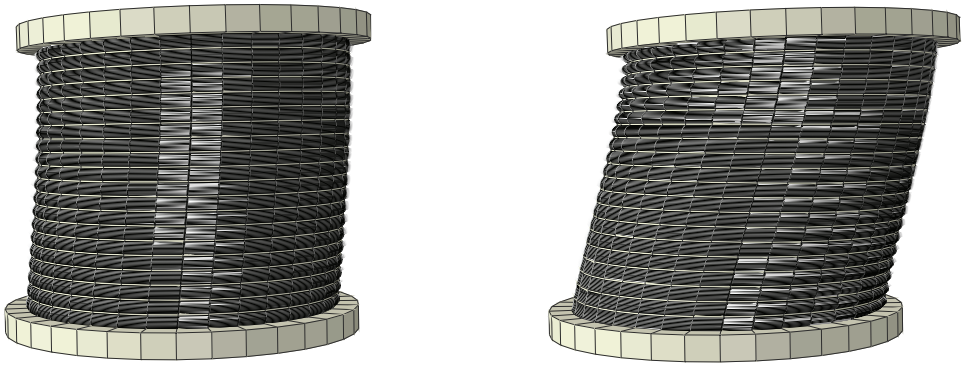


Figure 2.4: Deformed shape of the bearing ($P = 200$ kN, $H_0 = 5$ kN, $\theta_h = 0.02$ rad and $\theta_0 = 0$ rad) at the (a) First stage, (b) Second stage of the analysis.

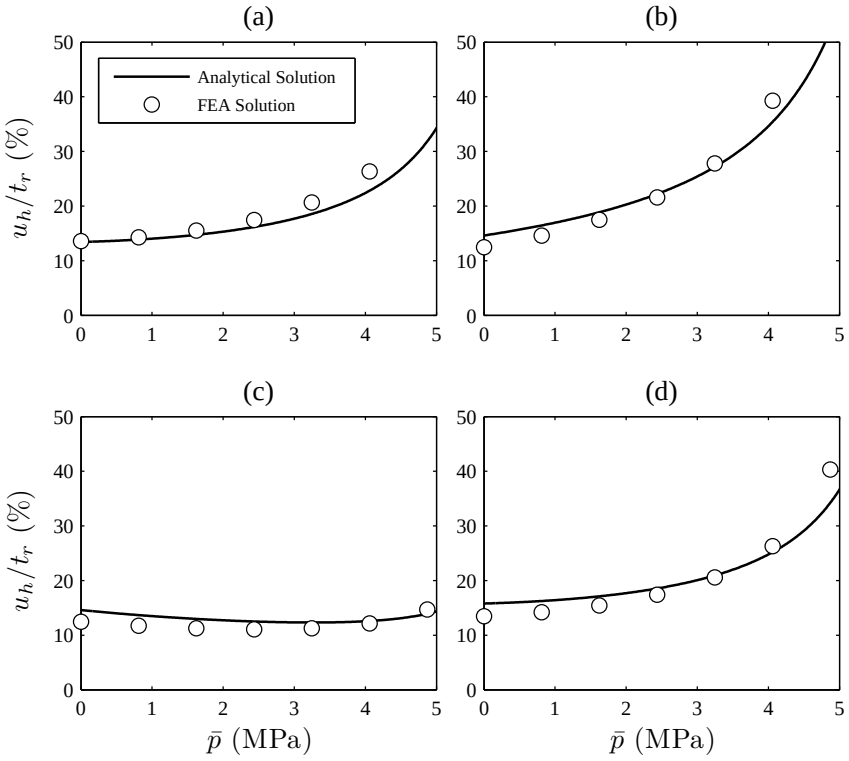


Figure 2.5: Comparison between FEA and analytical solution results ($H_0 = 5$ kN): (a) No rotation at the top or bottom of the bearing, (b) Rotation at the top of the bearing only ($\theta_h = 0.02$ rad), (c) Rotation at the bottom of the bearing only ($\theta_0 = 0.02$ rad), (d) Rotation at the top and bottom of the bearing ($\theta_h = \theta_0 = 0.02$ rad).

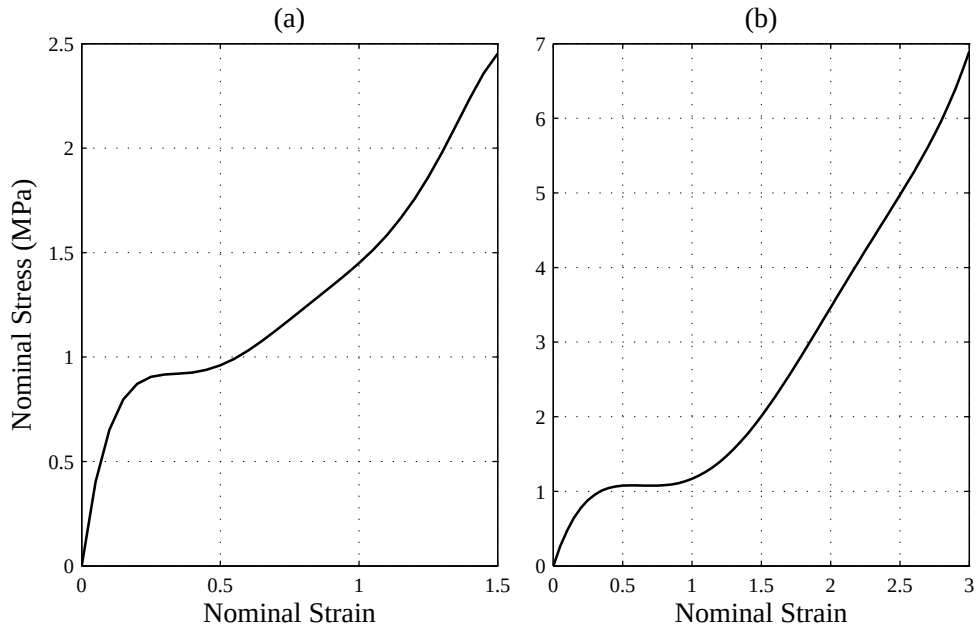


Figure 2.6: Material test results: (a) Uniaxial tension test, (b) Pure-shear test [50].

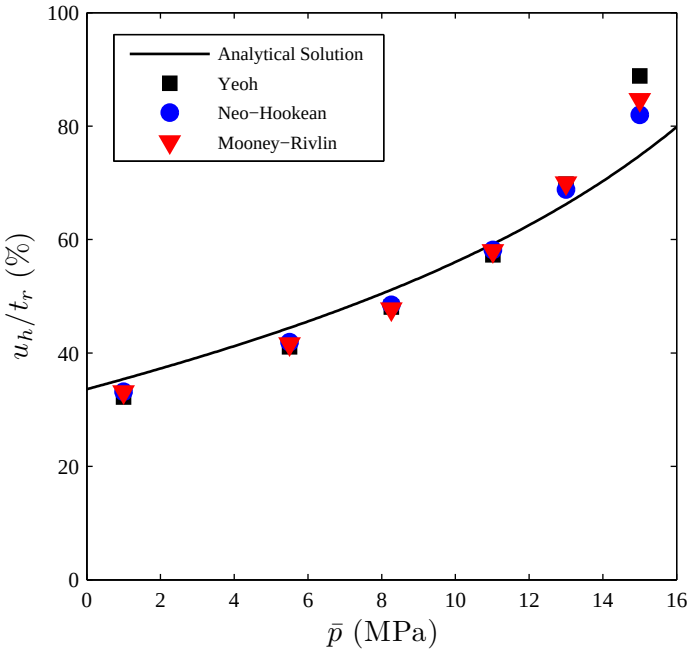


Figure 2.7: Comparison between FEA predicted by different hyperelastic material models and the analytical solution results ($H_0 = 5$ kN, $\theta_h = 0.02$, and $\theta_0 = 0.00$ rad).

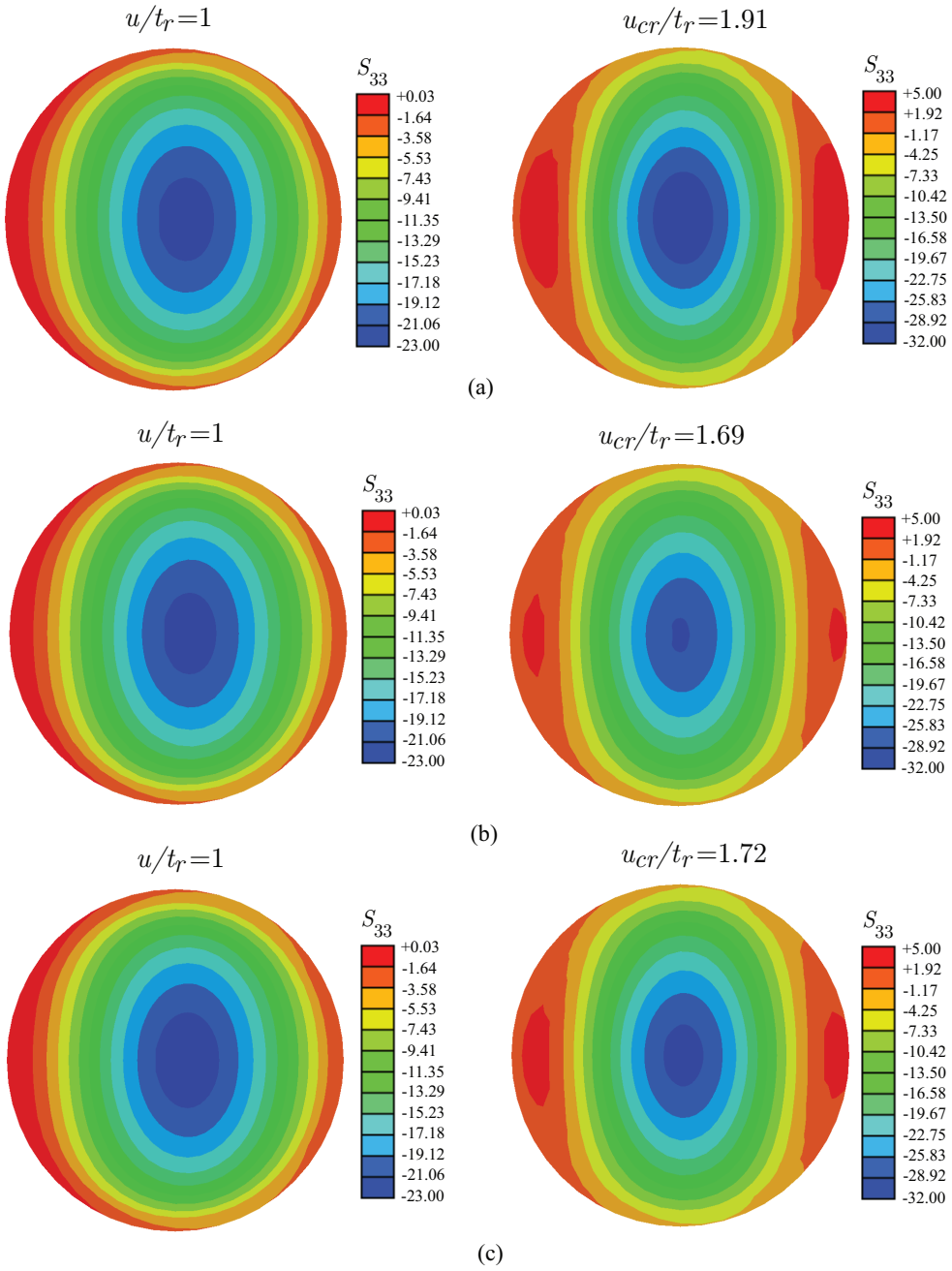


Figure 2.8: Stress contours (in MPa) for the tenth rubber layer of the bearing at $u/t_r = 1$ (left) and critical point (right), ($\bar{p} = 11.02$ MPa, $\theta_h = 0.02$ rad) (a) Yeoh (b) Neo-Hookean (c) Mooney-Rivlin.

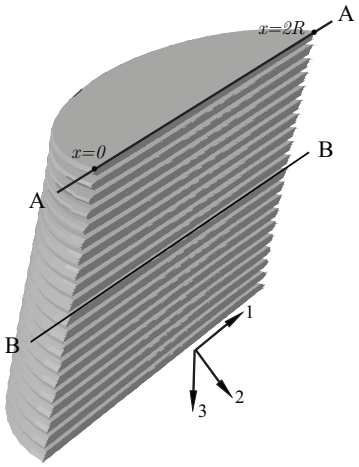


Figure 2.9: Definition of segments AA and BB in the bearing.

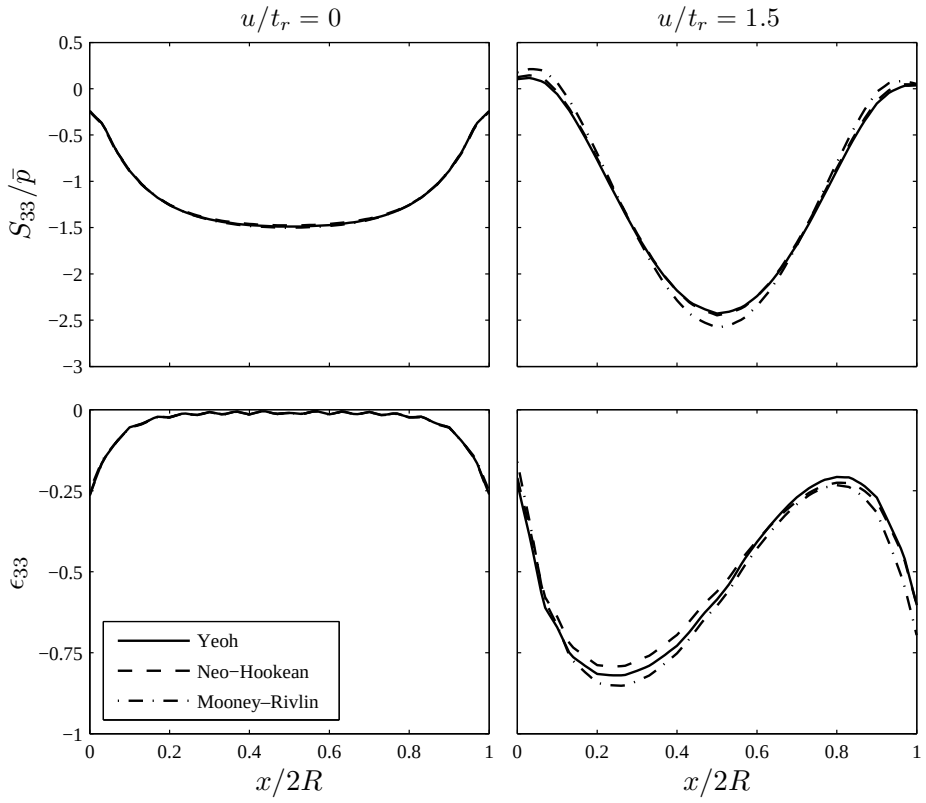


Figure 2.10: Variation of $S_{33}/\bar{p}$, and $\epsilon_{33}$ along segment BB at displacement $u/t_r = 0$ and 1.5 for different material models, under zero support rotations and $\bar{p} = 11.02$ MPa.

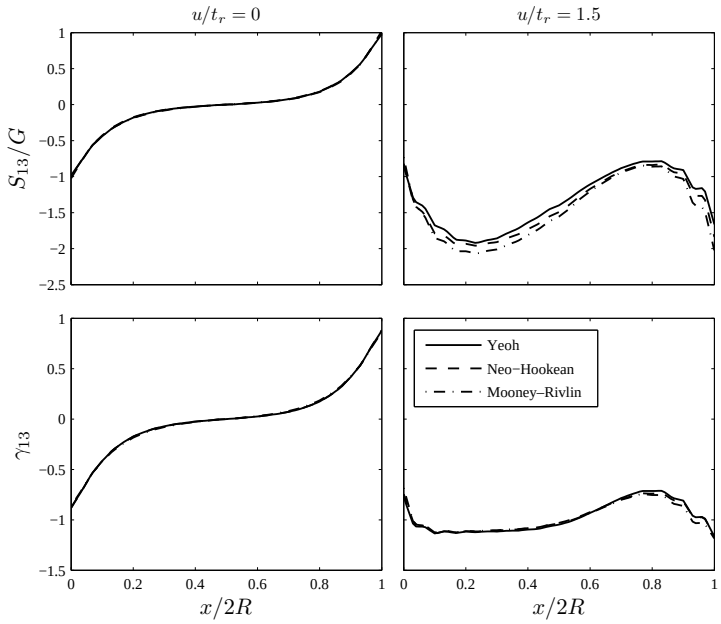


Figure 2.11: Variation of $S_{13}/G$, and $\gamma_{13}$ along segment BB at displacement $u/t_r = 0$ and 1.5 for different material models, under zero support rotations and $\bar{p} = 11.02$ MPa.

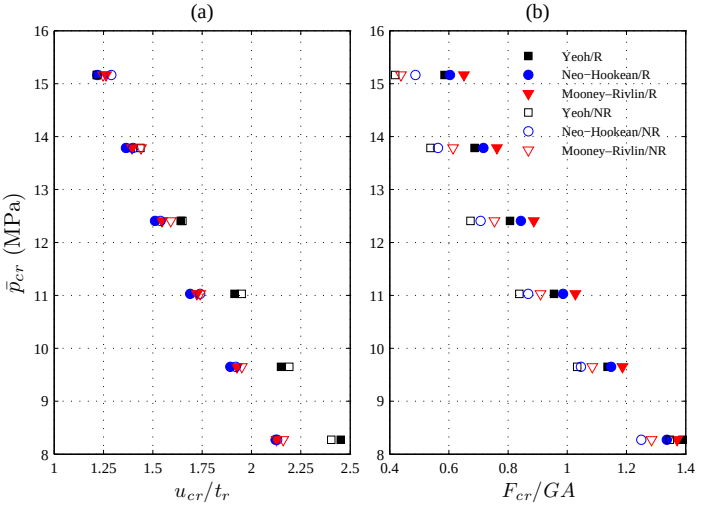


Figure 2.12: Effect of rotation at the top of the bearing on the critical point for (a) critical displacement, and (b) critical horizontal force, as predicted by different hyperelastic material models (R: with 0.02 rad counterclockwise rotation at the top, NR: no rotation).

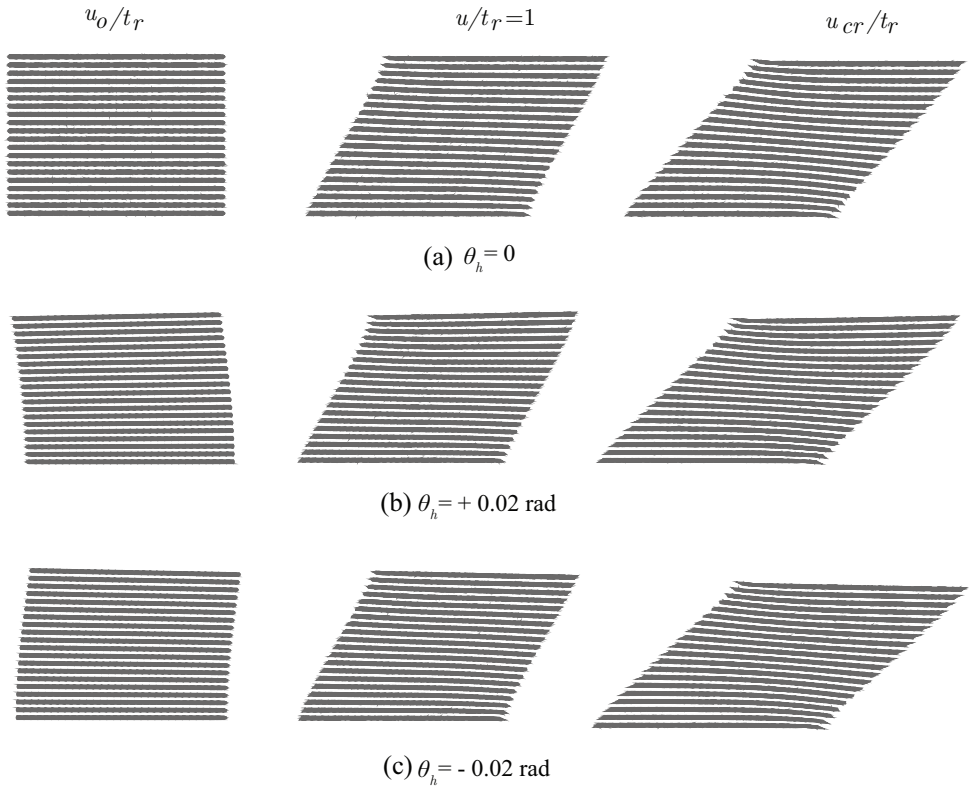


Figure 2.13: Deformation of the rubber layers at the cross section shown in Fig. 4.9 at different horizontal displacement levels ($u/t_r = u_o/t_r$, 1, $u_{cr}/t_r$), for different rotation angles at the top: (a) $\theta_h = 0$ (for which, $u_o/t_r = 0$ and $u_{cr}/t_r = 1.74$), (b) $\theta_h = +0.02$, ($u_o/t_r = -0.19$ and $u_{cr}/t_r = 1.72$), and (c) $\theta_h = -0.02$ rad ($u_o/t_r = 0.19$, $u_{cr}/t_r = 1.76$). $\bar{p} = 11.02$ MPa for all cases.

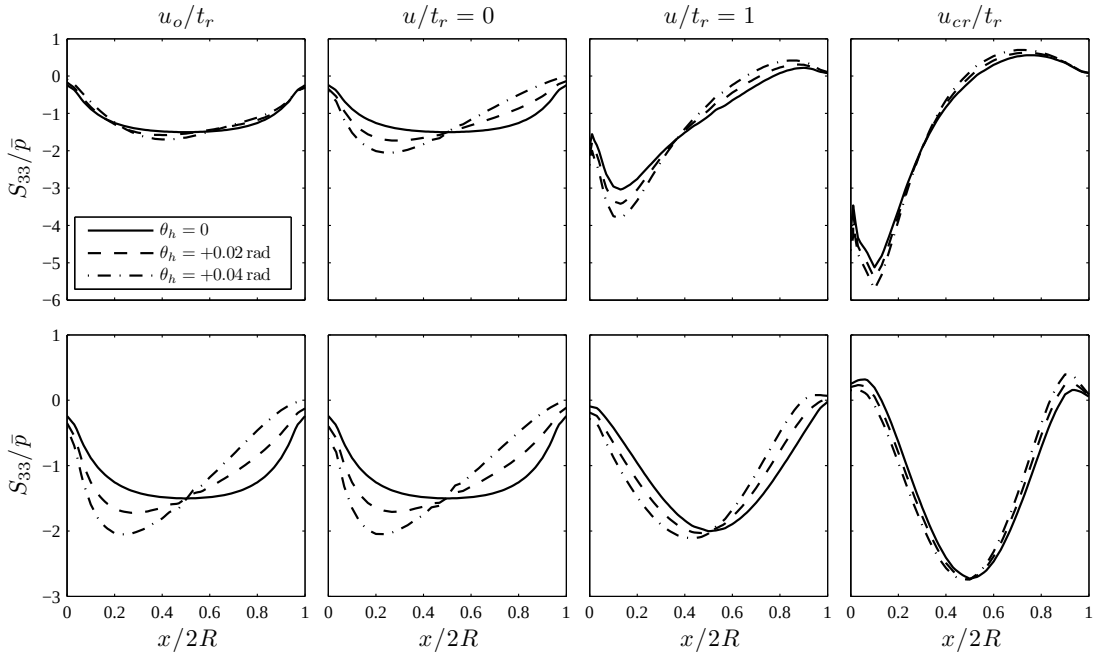


Figure 2.14: Variation of normalized normal stress $S_{33}/\bar{p}$ in the rubber layers along line segments AA (top row) and BB (bootom row) for $u/t_r = u_o/t_r$, 0, 1, $u_{cr}/t_r$, and $\theta_h = 0$ (for which, $u_o/t_r = 0$ and $u_{cr}/t_r = 1.74$), 0.02 rad ($u_o/t_r = -0.19$ and $u_{cr}/t_r = 1.72$), and 0.04 rad ($u_o/t_r = -0.39$ and $u_{cr}/t_r = 1.70$). $\bar{p} = 11.02$ MPa for all cases.

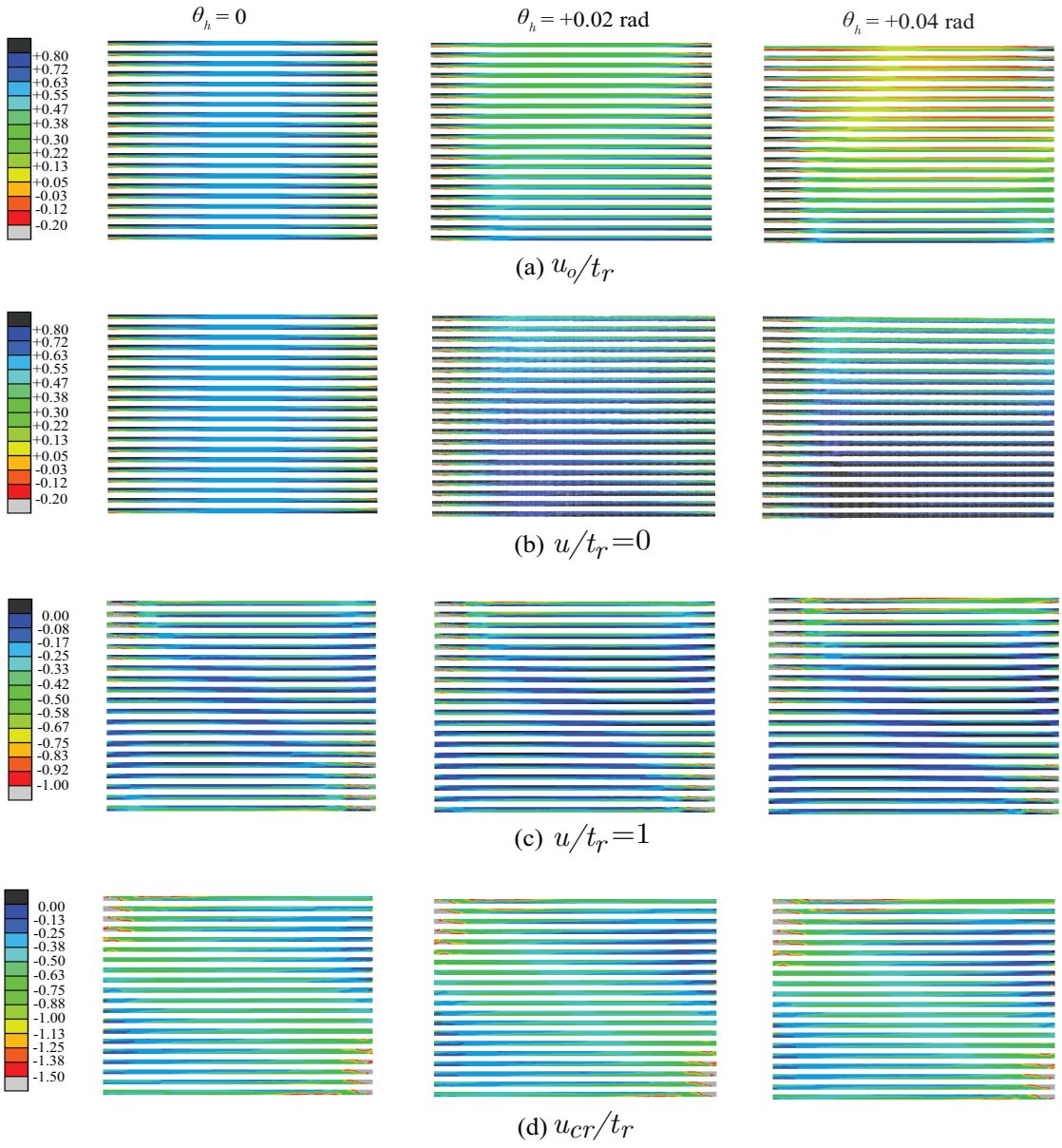


Figure 2.15: Contours of shear $\gamma_{33}$ at the cross section shown in Fig. 4.9 in the undistorted configuration of the rubber layers for (a) $u/t_r = u_o/t_r$, (b) $u/t_r = 0$ (c) $u/t_r = 1$, (d) $u/t_r = u_{cr}/t_r$, and $\theta_h = 0$ (for which, $u_o/t_r = 0$ and $u_{cr}/t_r = 1.74$), 0.02 rad ($u_o/t_r = -0.19$ and $u_{cr}/t_r = 1.72$), and 0.04 rad ($u_o/t_r = -0.39$ and $u_{cr}/t_r = 1.70$). $\bar{p} = 11.02$ MPa for all cases.

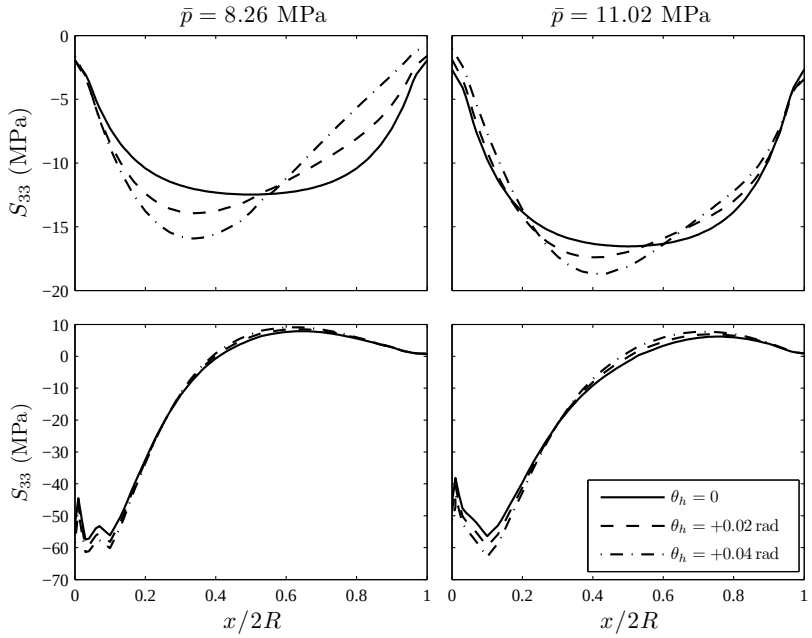


Figure 2.16: Variation of normal stress $S_{33}$ along line segment AA at $u_o/t_r$ (top row) and $u_{cr}/t_r$ (bottom row) under $\bar{p} = 8.26$ MPa for $\theta_h = 0$ ($u_o/t_r = 0$, $u_{cr}/t_r = 2.16$), $\theta_h = 0.02$ ($u_o/t_r = -0.13$, $u_{cr}/t_r = 2.12$) and $\theta_h = 0.04$ rad ($u_o/t_r = -0.28$, $u_{cr}/t_r = 2.08$), and $\bar{p} = 11.02$ MPa for $\theta_h = 0$ ($u_o/t_r = 0$, $u_{cr}/t_r = 1.74$), $\theta_h = 0.02$ ($u_o/t_r = -0.19$, $u_{cr}/t_r = 1.72$) and $\theta_h = 0.04$ rad ($u_o/t_r = -0.39$, $u_{cr}/t_r = 1.70$).

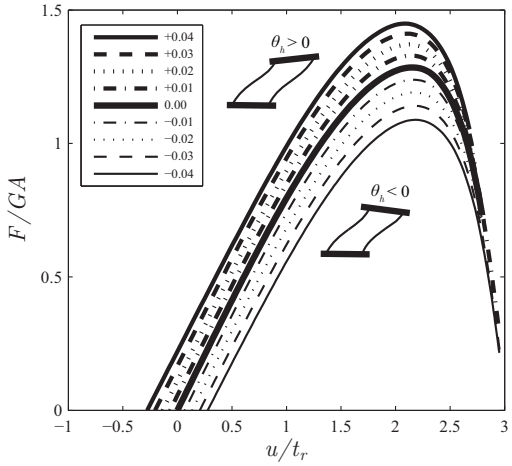


Figure 2.17: Normalized shear force–lateral displacement for different values of rotation at the top of the bearing ($-0.04$ to $+0.04$ rad, where the positive convention for rotation is counterclockwise) under an average vertical stress of $\bar{p} = 8.26$ MPa.

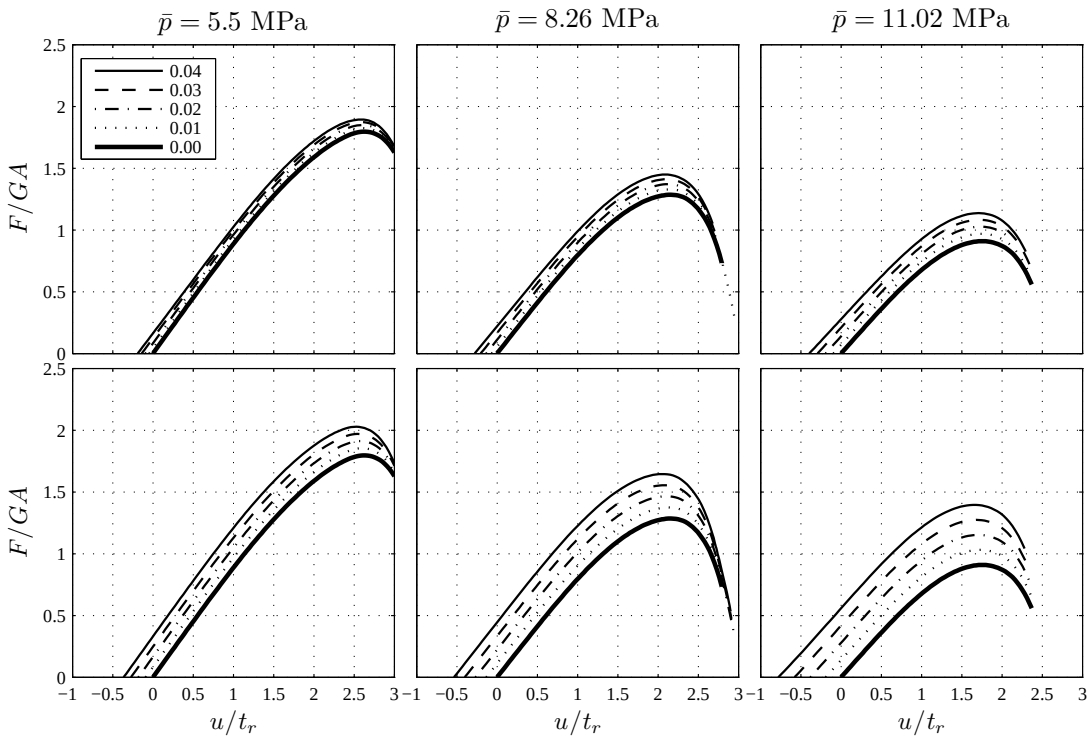


Figure 2.18: Effect of rotation (0 to 0.04 rad) on the lateral behavior of the bearing under different average vertical stress values for two cases: rotation at the top (top row), and rotation at the top and bottom (bottom row) of the bearing.

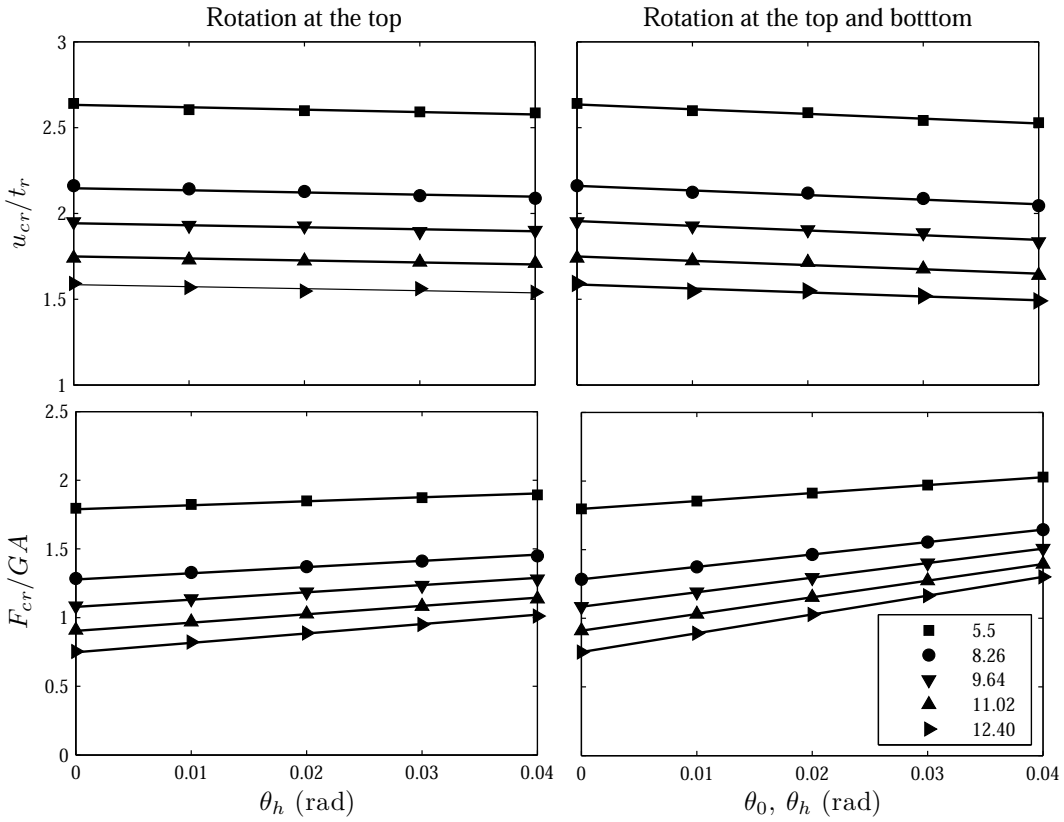


Figure 2.19: Effect of rotation on the critical point of the bearing under different average vertical stress values (5.5, 8.26, 9.64, 11.02 and 12.40 MPa) for two cases: rotation at the top and rotation at the top and bottom.

# Chapter 3

# Study of the Horizontal Behavior of Elastomeric Bearings by Simple Mechanical Models Including the Effect of Support Rotation

Rastgoo Moghadam S, Konstantinidis D. Study of the horizontal behavior of elastomeric bearings by simple mechanical models including the effect of support rotation. Submitted to *Engineering Structures*.

## 3.1 Abstract

Past studies have shown that the lateral behavior of a laminated elastomeric bearing is affected by axial load. Various mechanical models have been proposed to capture the lateral behavior of elastomeric bearings including the effect of horizontal–vertical coupling. These studies have characterized the effect of vertical load on the lateral stiffness and the lateral stability limit under the assumption that the bearing displaces horizontally and vertically only while the supports do not rotate. In this study, three existing models are considered: the Nagarajaiah–Ferrell, Iizuka, and Han–Warn models. First, these three models are evaluated by comparing their predictions with results of Finite Element Analysis (FEA), assuming no rotation at the supports. The models are subsequently modified to incorporate support rotation. The modified models are evaluated using results from FEA under prescribed rotation values. In order to investigate the effect of bearing aspect ratio on the results, bearings with different second shape factors (2, 4 and 6) are considered. The results show that these models cannot accurately predict the lateral force at the instability (critical) point; defined as the displacement at which the tangent stiffness becomes zero. Depending on the axial load and rotation value, the models underestimate or overestimate the lateral force at the critical point. Nevertheless they predict the displacement at the critical point with an acceptable accuracy. In general, it was found that the Han–Warn and Iizuka models provide more accurate predictions than the Nagarajaiah–Ferrell model. To improve the existing models, this paper proposes a new model, referred herein as Proposed Model (PM), that includes the effect of rotation on the lateral response. This model is used to find the lateral stability limit and the results are compared against those from FEA. It is shown that the PM can predict the lateral behavior of

elastomeric bearings more accurately than existing models.

## 3.2 Introduction

Seismic isolation using elastomeric bearings is one of the most effective and popular earthquake protection techniques, especially in the U.S. and Japan. In buildings, traditional practice places the isolation system at the foundation level and calls for the construction of rigid diaphragms above and below. The flexural rigidity of these diaphragms prevents the isolators from experiencing rotations. Recently, creative isolation designs have been introduced that reduce or eliminate these costly rigid diaphragms and in some cases move the isolation level higher up the structure. Another growing application of isolation is high-rise buildings, especially in Japan. In these innovative designs, aside from vertical and relative lateral displacements, the isolators can also experience rotations at their supports, as shown in a recent study by Oshaki et al. [1].

When an elastomeric bearing is subjected to a large lateral displacement, the full axial load is carried through by the overlapping region between the top and bottom surfaces [2]. As the overlapping area decreases with increasing lateral displacement, there is a concern with the stability of the bearing. The combination of axial load and horizontal displacement affects the bearing's stability limit. Previous studies introduced mechanical models [3-13] to examine the stability of elastomeric bearings under the assumption that the bearing only sheared horizontally and only displaced vertically, while the supports did not rotate. The increasing use of elastomeric bearings in high-rise buildings, mid-story or column-top isolation applications, as well as in bridge applications where bearings are expected to experience rotations, calls for an

improved understanding and characterization of the behavior of elastomeric bearings under combined loading that includes rotation.

Recent studies aimed to investigate the effect of rotation on the lateral behavior of bearings experimentally or numerically. Crowder and Becker [14] experimentally studied column-top isolation in a retrofit application and showed that, in the case of flexible columns, the endplate rotation due to the columns flexibility causes appreciable reduction in the lateral stiffness of the bearing. Ishii et al. [15] extended the previous model by Yamamoto et al. [8] to account for the effect of rotation on the horizontal behavior of elastomeric bearings. It was shown that end rotations do not affect the critical displacement. Using 3D FEA, Rastgoo Moghadam and Konstantinidis [16] confirmed that rotation does not significantly affect the critical displacement but noted that rotation can decrease or increase the critical shear force, depending on the rotation direction. It was concluded that imposing rotation at the supports, depending on the rotation value and axial force, can appreciably influence the lateral behavior of a rubber bearing. Another FEA study by Kalfas et al. [17] showed that when a bearing is subjected to axial and horizontal load and the endplate is allowed to rotate, the development of local tensile stresses changes the stiffness and damping ratio.

Various studies on the stability of laminated elastomeric bearings, assuming no rotation of the top/bottom supports, involved quasi-static and dynamic tests of bearings with different shape factors (defined for a single rubber layer as the ratio of loaded area to force-free area), second shape factors (defined for a bearing as the ratio of diameter/width to total thickness of rubber), geometric shapes, and rubber materials [10,18-25]. Some of the salient conclusions of these experimental studies

are:

1. The axial load capacity decreases when the bearing is displaced laterally [10,19-25].

2. The lateral stiffness of the bearing decreases with increasing axial load [10,19-25].

3. In lead-core bearings, the lead core does not have a significant effect on the critical capacity when the bearing is laterally deformed [24].

4. The method recommended by code (known as the overlapping area method) to estimate critical capacity is overly conservative [22-25], especially for slender bearings when the horizontal displacement is equal to the bearing diameter/width [22,24].

5. Quasi-static and dynamic test results agree, confirming that quasi-static tests can reliably determine the instability of elastomeric bearings [25].

6. Dynamic tests revealed that bearing can still sustain loads beyond the static critical load without observing any problem in the superstructure [10,25], but this conclusion is based on a limited number of tests [10]. It should be noted that most of design codes for elastomeric bearings do not allow the bearing to experience lateral displacements beyond the critical load capacity.

The use of FEA to study the stability of rubber isolators has become increasingly popular over the past few years. The first study on the stability of elastomeric bearings using FEA was conducted by Simo and Kelly [26]. The study used two-dimensional constitutive equations together with two-dimensional finite elasticity, extended to large displacements of the constitutive equations for an isotropic solid. A parametric study by Warn and Weisman [27] on the effect of geometry on the critical load of rubber bearings using 2D FEA showed that the bearing width and the individual

rubber layer thickness are more important parameters than the number of rubber layers. Weisman and Warn [24] showed that the axial load capacity of an elastomeric bearing does not improve by using a lead core in the bearing. Montuori et al. [28] studied the effect of the second shape factor on the stability of elastomeric bearings. It was shown that for bearings with second shape factors ranging from 1.5 to 6.2 the lateral behavior and stability of the bearings are related to the value of second shape factor.

While finite element models are indispensable for developing a good understanding of the behavior of elastomeric bearings, both at the global and local level, they are computationally much costlier and less practical than simple mechanical models. For this purpose, this study focuses on mechanical models capable of describing the lateral-vertical coupling and predicting instability in elastomeric bearings. The first two-spring simple mechanical model was proposed by Koh and Kelly [3], who used experimental results for natural rubber bearings to confirm that the model's accuracy. This model was improved by Koo et al. [4] by using an instantaneous apparent shear modulus instead of a constant shear modulus value. In this model, the shear modulus is a function of the shear strain and can be presented by a polynomial equation obtained by least-squares fitting of test results. The advantage of this modification is the elimination of imprecision associated with the constant shear modulus. Nagarajaiah and Ferrell [5] developed a nonlinear analytical model by extending the Koh–Kelly model to include large displacements. It was shown that this model is capable of predicting the instability point and that the critical load decreases with increasing lateral displacement. Iizuka [6] used the configuration of the Koh–Kelly

model, but the formulation was expanded by introducing finite deformation and nonlinear springs. The parameters of the nonlinear rotational and shear springs in the model are determined through experimental testing. Unlike previous models, the advantage of this model is that it can easily handle a variable axial force. The use of 2D series of vertical springs with a simple bilinear constitutive relationship along with a shear spring is the model proposed by Han and Warn [7]. The solution process to find the critical point based in the Han–Warn model is similar to the Iizuka model. In recent years, three-dimensional mechanical models have been proposed [8,9,15]. Although, based on comparison with experimental tests, these models are capable of predicting the lateral behavior of elastomeric bearings accurately, their complexity makes them difficult to use in practical applications.

Dynamic tests conducted by Vemuru et al. [10] showed that the stiffness of the bearings beyond the stability limit is larger than that predicted by quasi-static tests. As the Nagarajaiah-Ferrell model is based on quasi-static tests, the model cannot accurately predict the stiffness degradation beyond the stability point. Based on this observation, Vemuru et al. [10] proposed a new model by including higher order displacement terms in the stiffness of the rotational spring. The model is capable of characterizing the dynamic behavior of bearings more accurately than previous models, particularly beyond the instability point. In another study conducted by Vemuru et al. [11], vertical springs are introduced in the Nagarajaiah–Ferrell model to capture the vertical behavior of the bearings more accurately than in previous models. This model represents the coupled behavior of the bearing as a combination of reduction in vertical stiffness beyond the instability point and an increase in vertical displacement.

Forcellini and Kelly [12] modified the Koh–Kelly model to capture the tension buckling behavior of bearings. It was shown that the behavior of elastomeric bearings in tension is the 'mirror image' of those in compression. However, numerical and experimental investigations by Maureira et al. [13] showed that the the critical loads are higher in tension than in compression, particularly for bearings with low shape factor.

All aforementioned models assess the effect of vertical load on the stability of the elastomeric bearings under the assumption that the bearing experiences zero rotation at its supports. The first objective of this paper is evaluation of the existing models in the literature to capture the effect of rotation on the stability of elastomeric bearings. Three models are considered: Nagarajaiah–Ferrell [5], Iizuka [6], and Han–Warn [7]. The paper first summarizes each model and evaluates their performance by comparing their predictions to results of FEA assuming no rotation at the supports. To account for the effect of rotation, the models are extended, and their predictions are compared against FEA under prescribed rotation values. To study the effect of geometry on the performance of each model, bearings with different second shape factors were considered. In the last part of the study, a new macro model, referred to herein as the Proposed Model (PM), is introduced, and its performance in describing lateral behavior and predicting instability of rubber bearings is evaluated based on FEA results.

## 3.3 Existing Analytical Models

### 3.3.1 The Nagarajaiah–Ferrell Model

At least two mechanisms of deformation are needed in a simple mechanical model to represent the horizontal-vertical interaction and predict instability [29]. These mechanisms of deformation can be accommodated by shear and rotation springs as proposed first by Koh and Kelly [3] using linear springs. Nagarajaiah and Ferrell [5] later extended the formulation to include nonlinear springs. In the model shown in Fig. 3.1a, the model consists of two rigid tee-shaped elements, with total height of $h$ which are connected via frictionless rollers, a shear spring of nonlinear stiffness $K_s$ and two rotational springs of nonlinear stiffness $K_\theta$ connected to the top and bottom end plates. The top plate is free to move in the vertical and horizontal direction but is constrained from rotating. Under axial load $P$ and shear force $F$ the model includes the global horizontal displacement $u$ and vertical displacement $v$. These produce the local shear deformation $s$ that will be developed in the shear spring and the rotation $\theta$ concentrated in the two rotational springs which are identical. These local deformations ($s$,$\theta$) are associated with shear spring force $Q_s$ and rotational spring moment $M$. The compatibility and equilibrium equations of the model with nonlinear springs and nonlinear geometry are given by [5]

$$u = s\cos\theta + h\sin\theta \tag{3.1a}$$

$$v = s\sin\theta + h(1-\cos\theta) \tag{3.1b}$$

$$M = K_\theta\theta = Pu + F(h-v) \tag{3.1c}$$

$$Q_s = K_s s = P\sin\theta + F\cos\theta \tag{3.1d}$$

where, in Eq. (4.1d) [5],

$$K_s = \frac{GA_s}{h}\left[1 - C_s \tanh\left(s\right)\right] \tag{3.2}$$

where $G$ is the shear modulus of the rubber material, $A_s = A\left(h/t_r\right)$, where $A$ is the area in plan, $h$ is the total height of the bearing (rubber plus steel), and $t_r$ is the total height of rubber. $C_s$ is a dimensionless constant which can be estimated from experimental results if they are available, otherwise it [5] is suggested to assume a value of 0.325.

Additionally, in Eq. (4.1d) [5],

$$K_\theta = \frac{\pi^2 EI_s}{h}\left(1 - \frac{t_u - t}{D}s\right) \tag{3.3}$$

where $D$ is the bearing diameter, $t$ is the thickness of single rubber layer, and $t_u$ is the rubber layer of unit inch thickness (= 1). It is noted that in addition to $t_u$, the other variables inside the square brackets in Eqs. (4.2) and (4.3), i.e., $s$, $t$, and $D$, must be in inches. Also, $EI_s = EI_{eff}\left(h/t_r\right)$, where $EI_{eff}$ is the effective bending rigidity of a single rubber layer. For a circular bearing, assuming incompressible rubber, $EI_{eff} = E_c I/3$, where $E_c = 6GS^2$ is the compression modulus, $S = D/4t$ is the shape factor, and $I = \pi D^4/64$ is the area moment of inertia of a single rubber layer [29].

Vemuru et al. [10] showed that this model cannot predict stiffness degradation beyond the instability point and the experimental test revealed that bearings have further capacity beyond the critical point over that estimated by the model. In order to improve the model to address the drawback, Eq. (4.3) was modified by adding

higher order terms of $s$ [10]:

$$K_\theta = \frac{\pi^2 E I_s}{h}\left[1 - \frac{t_u - t}{D}s - C_{\theta 1}\left(\frac{s}{t_r}\right)^2 - C_{\theta 2}\left(\frac{s}{t_r}\right)^3\right] \tag{3.4}$$

where $C_{\theta 1}$ and $C_{\theta 2}$ are dimensionless parameters. The parameters are obtained based off of the response of the bearings to an earthquake excitation. Eqs. (4.1a)–(4.1d) for a given bearing subjected to axial force $P$ can be solved simultaneously using 'fsolve' in Matlab, which outputs the $F - u$ curve representing the lateral behavior of the bearing.

### 3.3.2 The Iizuka Model

The configuration of the Iizuka model [6] is similar to the Nagarajaiah–Ferrell model but the two rigid tee elements are replaced by a rigid column and two identical rotational springs are replaced by a single spring, as shown in Fig. 3.1b. The model assumes that the bending moment of the rotational spring, $M$, and the shear resistance of the shear spring, $Q_s$, are functions of axial load $P$, and rotational angle $\theta$, and shear deformation $s$; respectively $M = M(P, \theta)$, $Q_s = Q_s(s)$. Then Eq. (4.1) can be rewritten in the incremental form as follows [6]

$$\Delta u = h\cos\theta\Delta\theta + \cos\theta\Delta s - s\sin\theta\Delta\theta \tag{3.5a}$$

$$\Delta v = h\sin\theta\Delta\theta + \sin\theta\Delta s + s\cos\theta\Delta\theta \tag{3.5b}$$

$$\Delta M = u\Delta P + P\Delta u + (h - \Delta v)\Delta F - F\Delta v \tag{3.5c}$$

$$\Delta Q_s = \sin\theta\Delta P + P\cos\theta\Delta\theta + \cos\theta\Delta F - F\sin\theta\Delta\theta \tag{3.5d}$$

where

$$\Delta M = \frac{\partial M}{\partial P}\Delta P + \frac{\partial M}{\partial \theta}\Delta\theta \tag{3.6}$$

$$\Delta Q_s = \frac{dQ_s}{ds}\Delta s \tag{3.7}$$

Substituting Eqs. (4.6) and (4.7) into Eq. (4.5) and rearranging the equations as suggested in Han et al. [30], the incremental equilibrium and compatibility equations in a stepwise procedure for step $i$ can be obtained as

$$\begin{bmatrix} {}_i(\Delta\theta) \\ {}_i(\Delta s) \\ {}_i(\Delta v) \\ {}_i(\Delta F) \end{bmatrix} = \begin{bmatrix} h\sin{}_i\theta + {}_i s\cos{}_i\theta & \sin{}_i\theta & -1 & 0 \\ h\cos{}_i\theta - {}_i s\sin{}_i\theta & \cos{}_i\theta & 0 & 0 \\ {}_i(dM/d\theta) & 0 & {}_iF & {}_iv - h \\ P\cos{}_i\theta - {}_iF\sin{}_i\theta & -{}_i(dQ_s/d\theta) & 0 & \cos{}_i\theta \end{bmatrix}^{-1} \begin{bmatrix} 0 \\ 1 \\ P \\ 0 \end{bmatrix} \Delta u \tag{3.8}$$

The incremental response quantities ($\Delta\theta$, $\Delta s$, $\Delta v$ and $\Delta F$) for a given bearing under the axial force, $P$, and incremental lateral displacement, $\Delta u$, at the step $i$ are added to the current step to find the response values at the next step $(i+1)$. This procedure can be continued until the critical point at which $dF/du$ in the $F-u$ curve becomes zero; however the procedure can be pursued beyond the critical point to find the post-critical behavior of the bearing. In order to avoid an ill-conditioned matrix for solving Eq. (4.8) in the first step ($s = 0$), the solution derived by the Nagarajaiah–Ferrell model can be used [6], or linear spring properties can be assumed [30] for the first step. Then ${}_1\theta$ and ${}_1F$ in terms of ${}_1s$ can be obtained as

$${}_1\theta = \frac{GA_s + P}{P_E t_r}{}_1 s \tag{3.9}$$

$$ {}_1F = \frac{GA_sP_E - P^2}{P_Eh} {}_1s \tag{3.10} $$

where $P_E = \pi^2 EI_s/h^2$. ${}_1v$ and $\Delta u$ in terms of ${}_1s$ and ${}_1\theta$ are

$$ {}_1v = {}_1s \sin {}_1\theta + h(1 - \cos {}_1\theta) \tag{3.11} $$

$$ \Delta u = {}_1s \cos {}_1\theta + h \sin {}_1\theta \tag{3.12} $$

To find the relation for the rotational spring, an individual rubber layer assuming bilinear elastic behavior with zero post-cavitation stiffening as shown in Fig. 3.2a is considered. This layer is assumed bonded to the rigid plates, and it is subjected to axial force and bending moment. Stress on the cross section varies linearly in compression and in tension until the cavitation limit, $\sigma_c$, is reached, beyond which, the stress is constant. The cavitation bending moment $M_c$ can be obtained from [6]

$$ M_c = 2Z\left(\sigma_c + \bar{p}\right) \tag{3.13} $$

where $Z$ is elastic section modulus of bonded rubber area ($= \pi D^3/32$ for a circular bearing), $\bar{p}$ is average vertical stress ($= P/A$) and $\sigma_c$ is the cavitation stress, set at a value of $3G$ [31]. The cavitation rotational angle can be calculated from [6]

$$ \theta_c = \frac{M_c}{\pi^2 EI_s/h} = \frac{2hZ\left(\sigma_c + \bar{p}\right)}{\pi^2 EI_s} \tag{3.14} $$

The tangential rotational stiffness, $dM/d\theta$, can be computed from

$$\frac{dM}{d\theta} = \begin{cases} \frac{\pi^2 EI_s}{h} & (\theta \leq \theta_c) \\ \frac{\pi^2 EI_s/h}{\left[1+\frac{r}{3}\left(\frac{\theta}{\theta_c}-1\right)\right]^{\left(\frac{1+r}{r}\right)}} & (\theta > \theta_c) \end{cases} \tag{3.15}$$

where $r$ is a dimensionless parameter which controls the resisting moment after the cavitation bending moment is achieved. Iizuka [6] recommended a value between 1.2 and 3.5. Finally, the tangential shear stiffness, $dQ_s/ds$, is [6]

$$\frac{dQ_s}{d\theta} = \frac{GA_s}{h}\left[1 + s_1\left(1+s_2\right)\left(\frac{s}{t_r}\right)^{s_2}\right] \tag{3.16}$$

where $s_1$ and $s_2$ are dimensionless parameters which control the starting point and intensity of hardening in the rubber material. $s_1$ can be varied between 0.0068 and 0.01, and $s_2$ is equal to 3. In this study, $s_1 = 0.01$, $s_2 = 3$ and $r = 2$. Han et al. [30] showed that the instability point based on the Iizuka model is insensitive to $s_1$ and $s_2$; therefore they suggested that the $dQ_s/ds$ can be assumed constant (equal to $GA_s/h$) over the shearing deformation.

### 3.3.3 The Han–Warn Model

Han and Warn [7] replaced the rotational spring with a series of parallel vertical springs, as shown in Fig. 3.1c. The behavior of these springs is similar to the rotational spring in the Iizuka model (see Fig. 3.2a). The cross section is discretized into individual springs, similar to the fiber-element model. This means that each vertical spring (numbering of the springs begins from the left side of the cross section) represents a portion of the cross section and is located in the center of that portion.

The number of springs, $n$, should be large enough to obtain a converged solution for all axial loads for a given bearing (at least 12 [7]). In the present study, $n = 30$ is used for all bearings. A stepwise incremental analysis similar to the Iizuka approach is used (using Eqs. (4.9)–(4.12) for the first step and Eq. (4.8) for the $i$th step). The differential quantity $dM/d\theta$ can be obtained at step $i$ by

$$_i\left(\frac{dM}{d\theta}\right) = \frac{_iM - _{i-1}M}{_i\theta - _{i-1}\theta} \tag{3.17}$$

The vertical spring should satisfy the equilibrium equations [7]:

$$P = \sum_j \sigma_{s_j} A_j \tag{3.18}$$

$$_iM = \sum_j \sigma_{s_j} A_j \left(d_{s_j} + x\right) \tag{3.19}$$

and compatibility equation [7]:

$$\frac{\epsilon_{s_1} l_s}{d_{s_1} + x} = \frac{\epsilon_{s_2} l_s}{d_{s_2} + x} = ... = \frac{\epsilon_{s_j} l_s}{d_{s_j} + x} = ... = \frac{\epsilon_{s_n} l_s}{d_{s_n} + x} = \theta \tag{3.20}$$

where $\epsilon_{s_j}$ is strain of the $j$th vertical spring element, $\sigma_{s_j}$ is the stress in the $j$th vertical spring element which follows the loading path in Fig. 3.2a, or

$$\sigma_{s_j} = \begin{cases} E_c \epsilon_{sj} \ \ (\epsilon_{sj} \leq \epsilon_c) \\ \sigma_c \qquad \left(\epsilon_{s_j} > \epsilon_c\right) \end{cases} \tag{3.21}$$

where $\epsilon_c = \sigma_c / E_c$, $A_j$ is the area of the $j$th vertical spring element, $d_{s_j}$ is the distance between the centre of the $j$th vertical spring and the center of the bearing cross

section, $x$ is the distance between the neutral axis and the center of the bearing cross section, and $l_s$ is the initial length of the vertical spring element which is calculated by [7]

$$\frac{E_c}{l_s}\sum_j A_j d_{s_j}^2 = \frac{\pi^2 E I_{eff}}{t_r} \tag{3.22}$$

The tangential shear stiffness $dQ_s/ds$ is given by

$$\frac{dQ_s}{d\theta} = \frac{GA}{t_r}\left[1 - C_s \tanh\left(\frac{u}{t_r}\right)\right] \tag{3.23}$$

Kumar et al. [32] investigated the effect of cavitation on the behavior of rubber bearings and found experimentally that the post-cavitation stiffness is not zero, but can be represented by [32]

$$\sigma = \sigma_c\left[e^{k_c t_r\left(\epsilon_{s_j} - \epsilon_c\right)} + \frac{1}{k_c t_r}\left(e^{k_c t_r\left(\epsilon_{s_j} - \epsilon_c\right)} - 1\right)\right] \tag{3.24}$$

where $k_c$ is a cavitation parameter which describes the post-cavitation variation of tensile stiffness. This parameter for a given bearing can be obtained by calibration with experimental data. Eq. (3.24) is plotted in Fig. 3.2b. The effect of post-cavitation stiffness on the results using the Han–Warn model will be discussed later.

## 3.4 Modifying Existing Analytical Models to Account for Support Rotation

As discussed earlier, the aforementioned models are not capable of predicting the lateral behavior of an individual bearing when it is subjected to the support rotations.

Rastgoo Moghadam and Konstantinidis [16] have shown that the simultaneous application of vertical load and rotation at one of the bearing's supports causes the bearing to shear even in the absence of an applied horizontal load. In that analysis, it was assumed that the surface which is subjected to rotation is not constrained laterally. In reality, however, the superstructure and/or substructure restrict the supports of the bearing from freely displacing laterally relative to each other; therefore rotation induces a horizontal force to the bearing. This force is added to the shear force which is produced by external horizontal displacement. Moreover, the authors have shown that the critical displacement is not sensitive to the rotation angle, but the shear force corresponding to the critical point is affected appreciably [16].

Han et al. [30] have shown that the Nagarajaiah–Ferrell and Iizuka models are more sensitive to the nonlinear behavior of the rotational spring than the properties of the shear spring. Based on this finding, it is assumed that the support rotation affects the rotation angle $\theta$ only. Thus, $\theta$ should be modified to account for the support rotation. Letting $\theta_t$ and $\theta_b$ represent the applied rotation at the top and bottom supports, respectively, with counterclockwise being the positive convention, the compatibility and equilibrium equations (Eq. (4.1)) are modified as follows,

$$u = s\cos\left(\theta - \theta_t - \theta_b\right) + h\sin\left(\theta - \theta_t - \theta_b\right) \tag{3.25a}$$

$$v = s\sin\left(\theta - \theta_t - \theta_b\right) + h\left(1 - \cos\left(\theta - \theta_t - \theta_b\right)\right) \tag{3.25b}$$

$$M = \frac{K_\theta}{2}\left(\theta - \theta_t\right) + \frac{K_\theta}{2}\left(\theta - \theta_b\right) = Pu + F\left(h - v\right) \tag{3.25c}$$

$$Q_s = K_s s = P\sin\left(\theta - \theta_t - \theta_b\right) + F\cos\left(\theta - \theta_t - \theta_b\right) \tag{3.25d}$$

In order to use the Nagarajaiah–Ferrell model, Eqs. (3.25a) to (3.25d) can be solved

simultaneously. The Nagarajaiah–Ferrell model includes two rotational springs, one on each support of the bearing (see fig Fig. 3.1a); consequently, it is easy to apply different rotation cases: top only, bottom only, and the top and bottom simultaneously.

The finite-difference format of Eq. (3.25) is similar to Eq. (4.5). In order to modify the Iizuka and Han–Warn models and add the initial lateral force (due to rotation), the force in the first step, ${}_1F$, which is obtained by Eq. (4.10), should be modified. It should be noted that the modification discussed here, is only valid for the case of rotation at the top or bottom only. These two cases are similar to each other due to the inherent symmetry in geometry. Assuming linear spring in the first step, as discussed in Section 2.2 and replacing $\theta$ with $\theta - \theta_t$, ${}_1F$ is obtained from,

$$ {}_1F = \frac{{}_1s\,(GA_sP_E - P^2) - (PP_Eh\theta_t)}{P_Eh - P_E\theta_t\,{}_1s} \tag{3.26} $$

In order to use the Iizuka and Han–Warn models, Eqs. (3.26) and (4.8) can be used for the first step and subsequent, respectively. The results based off of these modifications will be discussed in Section 5.

## 3.5 Finite Element Analysis

One of the objectives of this study is to evaluate the performance of the simple mechanical models. This is done by comparing their predictions to results of FEA. This section provides a summary of the finite element approach followed. A comprehensive discussion of the approach, including validation using an available analytical solution

presented by Karbakhsh Ravari et al. [33] is presented in [16] to facilitate the evaluation of the mechanical models. Three-dimensional circular bearing models were developed in ABAQUS [34]. In the 3D finite element model, the rubber was discretized with a combination of 8-node linear brick, hybrid, constant pressure (C3D8H) and 6-node linear triangular prism, hybrid, constant pressure elements (C3D6H). The steel materials including shims and end plates were discretized with 8-node linear brick, incompatible modes elements (C3D8I).

The Neo-Hookean hyperelastic material was used to model the rubber. This material model is defined by two parameters, $C_{10}$ and $D_1$, which for consistency with a linear elastic material are related to the shear modulus, $G$, and the bulk modulus, $K$, through $C_{10} = G/2$, $D_1 = 2/K$. For the compressible Neo-Hookean model used in this study, the strain energy function is [35]:

$$W = C_{10}\left(\bar{I}_1 - 3\right) + \frac{1}{D_1}\left(J - 1\right)^2 \tag{3.27}$$

where $\bar{I}_1$ is the the first modified invariant of the deviatoric part of the Cauchy-Green deformation tensor, and $J$ is the elastic volume ratio. The steel material was modeled using a bilinear isotropic material model with a Young's modulus of 200 GPa and a Poisson's ratio of 0.3. A post-yield modulus of 2 percent of the initial modulus was specified.

In the model, all nodes at the top end plate were constrained to a point located at the centroid of the end plate and the boundary conditions were assigned to this point. The control node was free to move vertically and laterally in one direction, and in the case of rotation this node can rotate in the specified direction. Similar to the top end plate, all nodes at the bottom end plate were constrained to a control

node. This point was restrained in all degrees of freedom except for rotation. The analysis was performed in two stages: during the first stage, both axial load and rotations were imposed gradually until the desired values were reached. In the second stage of the analysis, the horizontal displacement was gradually increased while maintaining the axial load and rotation value from the first stage constant. The analysis included nonlinear geometry, large displacements, and large strains. The incremental nonlinear analysis was conducted using an updated Lagrangian formulation and Newton-Raphson iteration method.

In the analysis results, the critical point is defined as the point where the shear force reaches a maximum value in the shear force–lateral displacement curve. Beyond this point, the tangential lateral stiffness becomes negative. To obtain this point the Constant Axial Force Method [24] is used. In this method, the accuracy of which was experimentally confirmed by Sanchez et al. [25], the lateral displacement and shear force associated with the critical point are determined from the shear force–lateral displacement curve for a given constant axial load, $P$. The loading history in the FEA involves applying the axial load first, and then applying the horizontal displacement incrementally until the horizontal tangential stiffness becomes zero.

## 3.6 Evaluation of Existing Models

In this study different bearings were considered to compare the predictions of the aforementioned analytical models against FEA results. Table 3.1 shows details of the bearings used in this study. Bearing 1 is similar to the bearing tested by Weisman and Warn [24]; Bearing 2 is similar to the one studied by Vemuru et al. [10]; and Bearings 3 to 5 are similar to bearings in Montuori et al. [28].

Fig. 3.3 shows the lateral behavior of Bearing 1 obtained using the mechanical models and FEA under different average pressure ($\bar{p} = P/A$ = 5.5, 8.26 and 11.02 MPa). The Han–Warn model results are in good agreement with the FEA results, particularly for the intermediate pressure, which is in the order used in practical design. In all three cases, the Nagarajaiah–Ferrell model predicts a lower shear force, $F$, while the Iizuka model predicts larger values. As can be seen, the initial horizontal stiffness predicted by the Han–Warn and Iizuka models are close to the FEA results, while the Nagarajaiah–Ferrell model underestimates the horizontal stiffness, especially under the large pressure ($\bar{p}$ =11.02 MPa). For example, the initial horizontal stiffness is 224, 246, 238 and 171 N/mm for Bearing 1 under $\bar{p}$ =8.26 MPa predicted by FEA, the Iizuka, the Han–Warn, and the Nagarajaiah–Ferrell models, respectively. If the critical points are extracted from a multitude of lateral load–displacement curves like the ones shown in Fig. 3.3, under different values of constant $\bar{p}$, graphs showing (a) $P_{cr}$ versus $u_{cr}$, and (b) $P_{cr}$ versus $F_{cr}$, can be generated, as shown in Fig. 3.4. The figure shows that the analytical model results are in fair to good agreement with the FEA results in terms of the critical displacement, $u_{cr}$, while there are significant differences among the predictions of the models in estimating the critical shear force $F_{cr}$. For example, the critical displacement is 130, 123, 122 and 121 mm for Bearing 1 under $\bar{p}$ =8.26 MPa (corresponding to $P_{cr}$ = 150 kN in Fig. 3.4) predicted by the Finite Element Model (FEM), the Iizuka, the Han–Warn and the Nagarajaiah–Ferrell models, respectively. The values for $F_{cr}$, however, exhibit significant scatter; specifically, they are 21, 26, 21 and 14 kN, respectively. Moreover, Fig. 3.4 shows that the Iizuka model predicts the largest critical force.

Coefficient $C_s$ in Eq. (4.2) in the Nagarajaiah–Ferrell model is based on the

average of many tests. This value can be determined accurately for a specific bearing by calibration with experimental data. Vemuru et al. [10] conducted experimental tests on two identical bearing specimens (Bearing 2), and they determined $C_s$ to be 0.282 and 0.332 for the first and second bearing, respectively. Fig. 3.5 shows the lateral force-displacement curve for the Nagarajaiah–Ferrell model using different values of $C_s$ in Eq. (4.2). Also shown are the results using Eq. (4.4) proposed by Vemuru et al. [10] for the rotational stiffness and $C_s = 0.282$. $C_{\theta 1}$ and $C_{\theta 2}$ are $-0.1045$ and 0.0158, respectively [10]. These values are the average values of the four bearings. The figure shows that the effect of $C_s$ on the critical displacement is negligible, which means that the shear spring as represented by Eq. (4.2) does not have a significant influence on the critical displacement. This finding is in agreement with observations in Han et al. [30]. However, the value of $C_s$ does affect the critical shear force. Unlike the shear spring, the rotational spring has a major effect on the critical point [30]. Fig. 3.5 shows that using Eq. (4.4), proposed by Vemuru et al. [10], increases the value of critical shear force significantly. For instance, in terms of critical shear force the modification proposed by Vemuru et al. [10] with $C_s = 0.282$ provides 81 %, 73 % and 14.7 % error with reference to the experimental results presented in [10] for Bearing 2 under pressure of 4.30, 6.54 and 8.56 MPa, respectively. By comparison, the errors are 9 %, 20 % and 18 % for the Nagarajaiah–Ferrell model using $C_s = 0.282$. Nevertheless, the error decreases with increasing pressure using the Eq. (4.4). In terms of critical displacement, the error is 17 %, 12.5 % and $-32$ % using Eq. (4.4), while it is 29 %, $-25$ % and $-37$ % using the Nagarajaiah–Ferrell model for Bearing 2 under the same pressures. The modification factor proposed by Vemuru et al. [10] aimed to improve the agreement between the dynamic tests

and the Nagarajaiah–Ferrell model beyond the critical point. In comparison with the monotonic test, however, this modification does not necessarily enhance the results.

The simple bilinear elastic model with zero post-cavitation stiffness in the Han–Warn model can be replaced by Eq. (3.24) [32] to account for the effect of post-cavitation hardening in the rubber material. Fig. 3.6 shows the behavior of the rubber using equation Eq. (3.24) for different values of $k_c t_r$ for Bearings 1 and 3. In this study, $k_c t_r$ was selected so that the slope of the post-cavitation $\sigma$–$\epsilon$ behavior is similar to the experimental tests shown in [32]. Fig. 3.7 shows the results using the bilinear behavior shown in Fig. 3.6 in the Han–Warn model for Bearings 1 and 3. As can be seen, varying the post-cavitation behavior does not have a noticeable influence on the lateral behavior up to the instability point but has a noticeable effect on the post-critical behavior. In fact, $k_c$ controls how the lateral stiffness degrades beyond the critical point. This can improve a drawback of previous models noted experimentally by Vemuru et al. [10]: namely that the degradation beyond the critical point is less than predicted by previous models, particularly in dynamic tests.

Fig. 3.8 shows the effect of rotation ($\theta_t$ = 0.02 and 0.04 rad) on the lateral behavior of Bearing 1 under different pressures values (5.5, 8.26 and 11.02 MPa) using the modified analytical models (to account for the effect of rotation) and the FEM. As can be seen, the results of the modified Han–Warn model are in fairly good agreement with the FEA results at both rotation values (0.02 and 0.04 rad), especially for low and medium pressure values (5.5 and 8.26 MPa). As discussed in Section 3, under non-zero support rotation, the lateral force is not zero at zero displacement; i.e. the initial force. In terms of initial force, all modified analytical models predict a larger value than predicted by the FEM. This difference is more pronounced when

the axial load is increased. For example, the initial force is 1.8, 3.0, 3.0 and 3.67 kN for Bearing 1 under $\bar{p} = 8.26$ MPa and $\theta_t$ =0.02 rad using the FEM, the Han–Warn, the Iizuka, and the Nagarajaiah–Ferrell model, respectively, while these values are 2.3, 4.0, 4.0 and 4.6 kN for the bearing under the same rotation angle but $\bar{p} = 11.02$ MPa.

Fig. 3.9 compares the critical points predicted by the modified analytical models and FEM for Bearing 1 under different rotation values. The critical shear force values vary significantly depending on the rotation value and pressure, with larger values of pressure and rotation resulting in larger deviation between the predictions of the modified analytical models and the FEA results. Unlike the critical force, there is relatively good agreement between the results for critical displacement, especially for lower value of pressure and rotation. For example, $F_{cr}$ is 23, 31, 27 and 18 kN for Bearing 1 under $\bar{p} = 8.26$ MPa (corresponding to $P_{cr} = 150$ kN) and $\theta_t$ =0.03 rad as predicted by FEA, the Iizuka, the Han–Warn, and the Nagarajaiah–Ferrell models, respectively; while the corresponding values for $u_{cr}$ are 127, 126, 125 and 121 mm.

In order to evaluate the mechanical models for bearings with different second shape factors, Bearings 3–5 were considered. As shown in Table 3.1, these three bearings have different second shape factor ($S_2 = 2$, 3, and 4), achieved by a different number of layers, but otherwise share identical properties. Figs. 3.10 and 3.11 show the lateral behavior of the bearings under different pressures for top-support rotations of 0.02 and 0.04 rad, respectively. Figs. 3.12 and 3.13 show the corresponding critical points for the bearings under rotation of 0.02 and 0.04 rad, respectively, ($\bar{p}_{cr}$ varying from 5 to 10 MPa). It should be noted that the Iizuka model could not converge for Bearing 5 ($S_2 = 4$). Since the Iizuka model is sensitive to the parameter $r$, changing

$r$ could result in convergence. To investigate this, the parameter $r$ was increased, and the Iizuka model converged but provided grossly inconsistent results. Therefore, these results are not presented in Figs. 3.10 to 3.13. It seems that the Iizuka model cannot appropriately capture the lateral behavior of the bearing with a large second shape factor, and parameter $r$ should be adjusted accordingly to improve the results. It is interesting to note that regardless of the rotation angle, the predictions obtained by the modified Nagarajaiah–Ferrell and Han–Warn models are getting close to each other with increasing $S_2$, especially for the critical shear force (See Figs. 3.12 and 3.13 for Bearing 5). Regardless of the rotation angle, in general, the Iizuka model predicts larger lateral force (see Figs. 3.10 and 3.11 for Bearings 3 and 4), especially for the larger bearing (Bearing 4). However, all models provide similar values for the initial force.

## 3.7 Proposed Model

In the previous section, the three modified analytical models were evaluated, and the benefits and drawbacks of each model were discussed. In this section a new macro model referred to here as the *Proposed Model* (PM), based on the observations made through the evaluation of the selected models, is presented. Similar to the Han–Warn model, the PM includes a shear spring with behavior described by Eq. (3.23). The model consists of one series of vertical springs at the top support and another at the bottom (see Fig. 3.14). These two series of vertical springs make it feasible to apply rotation at the top only, and at the top and bottom simultaneously. The procedure is similar to the Han–Warn model using stepwise incremental analysis (Eq. (4.8)). The differential quantity $dM/d\theta$ can be calculated at step $i$ by Eq. (4.17). At step $i$,

the following equilibrium (Eqs. 3.28 to 3.30) and compatibility equations (Eqs. 3.31 and 3.32) must be satisfied,

$$P = \sum_j \sigma_{s_j} A_{j_t} = \sum_j \sigma_{s_j} A_{j_b} \tag{3.28}$$

$$_iM_t = \sum_j \sigma_{s_j} A_{j_t} d_{s_j} \tag{3.29}$$

$$_iM_b = \sum_j \sigma_{s_j} A_{j_b} d_{s_j} \tag{3.30}$$

$$\frac{\epsilon_{s_{1t}} l_s}{d_{s_{1t}} + x_t} = \frac{\epsilon_{s_{2t}} l_s}{d_{s_{2t}} + x_t} = ... = \frac{\epsilon_{s_{jt}} l_s}{d_{s_{jt}} + x_t} = ... = \frac{\epsilon_{s_{nt}} l_s}{d_{s_{nt}} + x_t} = \theta - \delta\theta_t \tag{3.31}$$

$$\frac{\epsilon_{s_{1b}} l_s}{d_{s_{1b}} + x_b} = \frac{\epsilon_{s_{2b}} l_s}{d_{s_{2b}} + x_b} = ... = \frac{\epsilon_{s_{jb}} l_s}{d_{s_{jb}} + x_b} = ... = \frac{\epsilon_{s_{nb}} l_s}{d_{s_{nb}} + x_b} = \theta - \delta\theta_b \tag{3.32}$$

where subscripts $t$ and $b$ in the equations indicate the case of rotation at the top and bottom, respectively. The total moment in the vertical top and bottom springs $_iM$ is equal to $_iM = {}_iM_t + {}_iM_b$. $\delta\theta_t$ and $\delta\theta_b$ are rotation increment values applied gradually at each step:

$$\delta\theta_t = \frac{i\,\theta_t}{(u_{max}/\Delta u)\, m_2} \tag{3.33}$$

$$\delta\theta_b = \frac{i\,\theta_b}{(u_{max}/\Delta u)\, m_2} \tag{3.34}$$

where $u_{max}$ is the target horizontal displacement that the bearing is displaced in the horizontal direction. $m_2$ is a modification factor to adjust the maximum force at the critical displacement. This value is preferably obtained by visual calibration with experimental data or FEA results. $m_2$ is selected based on the level of axial load. If FEA or experimental results are not available, it is recommended that $m_2$ is selected between $-2.5$ and $+2.5$ (but $m_2$ cannot be between 1 and -1), and for a bearing

under average pressure load used in practice, let's say 8 to 10 MPa, $m_2$ can be +2. Negative values of $m_2$ are used to increase the lateral force to adjust with the FEA or experimental results, while positive values decrease the lateral force. For example, $F_{cr}$ for Bearing 1 under pressure 8.26 MPa and $\theta_t = 0.04$ rad, using $m_2 = 4, 2, -2, -4$ in the PM, is 24.3, 23.7, 25.5, and 25.1 kN, respectively, while the FEM predicts 23.6 kN. To get the two curves obtained by the PM and the experimental or FEA results as close to each other as possible, it is recommended that $m_2$ is selected +2 in the first try. Then, comparison between $F_{cr}$ obtained by the PM and the experimental test or FEA helps the user to adjust the value for $m_2$.

To enhance the prediction beyond the critical point, $\sigma_{s_j}$ follows the behavior shown in Fig. 3.2b (Eq. (3.24)), which incorporates post-cavitation stiffness. Similar to the Han–Warn or Iizuka model, the first-step values for ${}_1\theta$, ${}_1v$, and $\Delta u$ are obtained by Eqs. (4.9), (4.11) and (4.12), while the first step lateral force is calculated by

$$ {}_1F = \frac{{}_1s\left(GA_sP_E - P^2\right) - \left(PP_Eh\frac{\theta_t+\theta_b}{m_1}\right)}{P_Eh - P_E\frac{\theta_t+\theta_b}{m_1}{}_1s} \tag{3.35} $$

where $m_1$ is a modification factor to adjust the initial force at zero lateral displacement; $m_1 = 2$ for rotation at the top only, and $m_1 = 1$ for rotation at the top and bottom. It is assumed that the initial force for the case of rotation at the top and bottom is twice as much as the initial force for the the case of rotation at the top only.

The FEA in this study is considered the criterion for evaluating the accuracy of new mechanical model; however, cavitation in the rubber is not considered in the FEM. Therefore, it may be argued that the results of the PM model, which considers

the post-cavitation behavior, and those of FEM should not be directly compared. However, Fig. 3.7 showed that the effect of cavitation is observed only beyond the critical point. Therefore, the authors believe that the evaluation of the PM based on a comparison with FEM results up to the critical point is fair. As such, to evaluate the PM model, the comparison is limited up to the critical point, although results in subsequent figures include the post-stability response.

Fig. 3.15 shows the comparison of shear force–lateral displacement results between the PM and the FEM for Bearing 1 under the pressure of 5.5, 8.26, and 11.02 MPa for rotations of 0.02 and 0.04 rad at the top only. The results show that there is a very good agreement between the PM and the FEM, especially for the low and moderate pressure values (5.5 and 8.26 MPa). Comparison between the results obtained by the three modified analytical models for Bearing 1, as shown in Fig. 3.8, with the PM results (Fig. 3.15) shows that the new formulation with introduced modification factors ($m_1$ and $m_2$) increased the accuracy in the prediction of the critical shear force. In order to quantify this benefit, Table 3.2 shows a comparison of the error of the Nagarajaiah–Ferrell, Iizuka, and Han–Warn models and the PM in predicting $F_{cr}$ using for Bearing 1 under the different pressure values ($\bar{p}$ = 4.13 to 12.40 MPa) and rotation at the top ($\theta_t$ =0.01 to 0.04 rad). The percentage error is computed using

$$error_{F_{cr}} = \frac{F_{cr}^{\text{FEM}} - F_{cr}^{\text{Mechanical}}}{F_{cr}^{\text{FEM}}} \times 100 \tag{3.36}$$

where $F_{cr}^{\text{Mechanical}}$ and $F_{cr}^{\text{FEM}}$ are the critical shear force predicted by the mechanical models being evaluated and the FEM, respectively. Table 3.2 shows that PM provides lower value of error in most cases, especially under common service pressures (around 8–10 MPa [29]).

Fig. 3.16 compares the critical points obtained by PM and FEM for Bearing 1 under different axial loads and $\theta_t = 0.02$ rad, $\theta_b = 0$. It can be seen that the PM predicts both critical shear force and displacement with an acceptable error. The figure confirms the observation made in Fig. 3.15; namely that the agreement between the results decreases with increasing axial load.

The PM is also capable of describing the behavior of the bearing under the rotation at the top and bottom. Fig. 3.17 shows the comparison of the shear force–lateral displacement results between PM and FEM for Bearing 1 under $\bar{p} = 5.5$, 8.26, and 11.02 MPa for $\theta_t = \theta_b = 0.01$ and $\theta_t = \theta_b = 0.02$ rad. The PM and FEM are in good agreement with each other for the case of rotation both at top and bottom, albeit not as good as in the case of rotation only at the top support. Again, there is better agreement for the bearing under the low and moderate pressure values (5.5 and 8.26 MPa).

It was shown that with available experimental or FEA data (as was the case in this study), the PM using a calibrated value of $m_2$ can predict the lateral behavior of the bearings more accurately than the modified versions of the three available mechanical models. However, in the absence of experimental or FEA data, the recommended value for $m_2$ is based on averaging over different bearings, and therefore in some cases the PM may not necessarily provide improved results compared to one of the modified mechanical models.

Finally, although the performance of the PM compared to the three modified analytical models beyond the critical point was not evaluated, it is postulated that a finite post-cavitation hardening behavior in the PM would likely improve the results beyond the critical point. This assertion is based on the effect of post-cavitation

hardening on the results of the modified Han-Warn model, presented in Section 5. However, experimental results or FEA considering cavitation is needed to confirm this.

## 3.8 Conclusions

This paper investigated the use of simple mechanical models to account for the effect of support rotation on the lateral behavior of elastomeric bearings. First, three existing models (the Nagarajiah–Ferrel, Iizuak, and Han–Warn models) were modified to include support rotation in their formulations. Their performance was evaluated by comparing the predictions of these mechanical models for different bearings against the result of FEA. In summary, the following results were observed:

1) The Nagarajiah–Ferrel model predicts lower values of critical shear force than FEA regardless of rotation value. The difference is more significant for bearings under higher pressures.

2) In many cases, the Iizuka model overpredicts of shear force at the critical point; especially for bearings with a large second shape factor. Consequently, for the bearing with large second shape factor considered in this study, this model is not accurate.

3) In general, the Han–Warn model provides relatively good agreement with FEA. This model can be improved beyond the critical point using a bilinear elastic model with post-cavitation hardening for the rubber material.

4) While the critical shear force values predicted by the different analytical models exhibit significant dispersion, the predicted critical displacement values are close to the FEA results.

5) All modified mechanical models provide larger initial lateral force than the one

obtained by the FEM, especially for large pressures.

This study was the first attempt of its kind to modify currently available mechanical models to predict the lateral response and instability of elastomeric bearings subjected to simultaneous axial, shear, and rotation. A new mechanical model was proposed, aiming to more accurately account for the effect of rotation on the lateral behavior. It was shown that the proposed model (PM) is more accurate than the modified models in predicting the critical shear force. The improvement was achieved through the introduction of two modifications factors, which were calibrated to decrease the error between the PM and FEA results. Furthermore, post-cavitation hardening was considered in describing the rubber material in the PM. The results of future experimental tests or FEA studies that include cavitation in the rubber can be used to improve the post-critical behavior of the PM.

## Acknowledgements

The authors would like to gratefully acknowledge the financial support of the Natural Sciences and Engineering Research Council of Canada (NSERC).

## 3.9 References

[1] Ohsaki M, Miyamura T, Kohiyama M, Yamashita T, Yamamoto M, Nakamura N. Finite-element analysis of laminated rubber bearing of building frame under seismic excitation. Earthquake Engineering & Structural Dynamics. 2015;44(11):1881–1898.

[2] Kelly JM, Marsico MR. Stability and post-buckling behavior in nonbolted elastomeric isolators. Seismic Isolation and Protection Systems. 2010;1(1):41–54.

[3] Koh CG, Kelly JM. Effects of axial load on elastomeric isolation bearings. Report UCB/EERC-86/12. Earthquake Engineering Research Center, University of California, Berkeley; 1987.

[4] Koo G, Lee J, Yoo B, Ohtori Y. Evaluation of laminated rubber bearings for seismic isolation using modified macro-model with parameter equations of instantaneous apparent shear modulus. Engineering Structures. 1999;21(7):594–602.

[5] Nagarajaiah S, Ferrell F. Stability of elastomeric seismic isolation bearings. Journal of Structural Engineering. 1999;125(9):946–954.

[6] Iizuka M. A macroscopic model for predicting large-deformation behaviors of laminated rubber bearings. Engineering Structures. 2000;22(4):323–334.

[7] Han X, Warn GP. Mechanistic model for simulating critical behavior in elastomeric bearings. Journal of Structural Engineering. 2014;139(12):04014140.

[8] Yamamoto S, Kikuchi M, Ueda M, Aiken ID. A mechanical model for elastomeric seismic isolation bearings including the influence of axial load. Earthquake Engineering & Structural Dynamics. 2009;38(2):157–180.

[9] Kikuchi M, Nakamura T, Aiken ID. Three-dimensional analysis for square seismic isolation bearings under large shear deformations and high axial loads. Earthquake Engineering & Structural Dynamics. 2010;39(13):1513–1531.

[10] Vemuru VSM, Nagarajaiah S, Masroor A, Mosqueda G. Dynamic lateral stability of elastomeric seismic isolation bearings. Journal of Structural Engineering. 2014;140(8):A4014014.

[11] Vemuru VSM, Nagarajaiah S, Mosqueda G. Coupled horizontal–vertical stability of bearings under dynamic loading. Earthquake Engineering & Structural Dynamics. 2016;45(6):913–934.

[12] Forcellini D, Kelly JM. Analysis of the large deformation stability of elastomeric bearings. Journal of Engineering Mechanics. 2014;140(6):04014036.

[13] Maureira N, de la Llera J, Oyarzo C, Miranda S. A nonlinear model for multilayered rubber isolators based on a co-rotational formulation. Engineering Structures. 2017;131:1–13.

[14] Crowder AP, Becker TC. Effects of non-traditional isolator placement for seismic retrofit. Canadian Society of Civil Engineering, Resilient Infrastructure. London, ON, June 1–4, 2016.

[15] Ishii K, Kikuchi M, Nishimura T, Black CJ. Coupling behavior of shear deformation and end rotation of elastomeric seismic isolation bearings. Earthquake Engineering & Structural Dynamics. 2016;In press.

[16] Rastgoo Moghadam S, Konstantinidis D. Finite element study of the effect of support rotation on the horizontal behavior of elastomeric bearings. Composite Structures. 2017;163:474–490.

[17] Kalfas KN, Mitoulis SA, Katakalos K. Numerical study on the response of steel-laminated elastomeric bearings subjected to variable axial loads and development of local tensile stresses. Engineering Structures. 2017;134:346–357.

[18] Stanton JF, Scroggins G, Taylor A, Roeder CW. Stability of laminated elastomeric bearings. Journal of Engineering Mechanics. 1990;116(6):1351–1371.

[19] Buckle IG, Kelly JM. Properties of slender elastomeric isolation bearings during shake table studies of a large-scale model bridge deck. ACI Special Publication 1986;94:247–270.

[20] Aiken ID, Kelly JM, Tajirian FF. Mechanics of low shape factor elastomeric seismic isolation bearings. Report UCB/EERC-89/13. Earthquake Engineering Research Center, University of California, Berkeley; 1989.

[21] Buckle IG, Liu H. Experimental determination of critical loads of elastomeric isolators at high shear strain. NCEER Bulletin. 1994;8(3):1–5.

[22] Buckle IG., Nagarajaiah S, Ferrell K. Stability of elastomeric isolation bearings: experimental Study. Journal of Structural Engineering. 2002;128(1):3–11.

[23] Cardone D, Perrone G. Critical load of slender elastomeric seismic isolators: an experimental perspective. Engineering Structures. 2012;40:198–204.

[24] Weisman J, Warn GP. Stability of elastomeric and lead-rubber seismic isolation bearings. Journal of Structural Engineering. 2012;128(2):215–223.

[25] Sanchez J, Masroor A, Mosqueda G, Ryan KL. Static and dynamic stability of elastomeric bearings for seismic protection of structures. Journal of Structural Engineering. 2013;139(7):1149–1159.

[26] Simo JC, Kelly JM. Finite element analysis of the stability of multilayer elastomeric bearings. Engineering Structures 1984;6(3):162–174.

[27] Warn GP, Weisman J. Parametric finite element investigation of the critical load capacity of elastomeric strip bearings. Engineering Structures. 2011;33(12):3509–3515.

[28] Montuori GM, Mele G, Marrazzo G, Brandonisio G, De Luca A. Stability issues and pressure–shear interaction in elastomeric bearings: the primary role of the secondary shape factor. Bulletin of Earthquake Engineering. 2016;14(2):569–597.

[29] Kelly JM, Konstantinidis D. Mechanics of rubber bearings for seismic isolation and vibration isolation. Chichester: John Wiley & Sons; 2011.

[30] Han X, Kelleher CA, Warn GP, Wagener T. Identification of the controlling mechanism for predicting critical loads in elastomeric bearings. Journal of Structural Engineering. 2013;139(12):04013016.

[31] Gent AN. Cavitation in rubber: a cautionary tale. Rubber Chemistry and Technology. 1990;63(3):49–53.

[32] Kumar M, Whittaker AS, Constantinou MC. An advanced numerical model of elastomeric seismic isolation bearings. Earthquake Engineering & Structural Dynamics. 2014;43(13):1955-1974.

[33] Karbakhsh Ravari A, Othman IB, Ibrahim ZB, Ab-Malek K. P-$\Delta$ and end rotation effects on the influence of mechanical properties of elastomeric isolation bearings. Journal of Structural Engineering. 2012;138(6):669–675.

[34] Dassault Systèmes Simulia Corp. ABAQUS/CAE Version 6.10-1, Providence, RI, 2010.

[35] Bathe KJ. Finite Element Procedures. New York, NY: Prentice Hall, 1995.

Table 3.1: Properties of the bearings used in this study.

| | | | Bearing | | | | |
|---|---|---|---|---|---|---|---|
| Property | Symbol | Unit | 1 | 2 | 3 | 4 | 5 |
| Outside diameter | $D$ | mm | 152 | 165 | 400 | 400 | 400 |
| Inside diameter | $D_i$ | mm | – | 30 | – | – | – |
| Thickness of individual rubber layer | $t$ | mm | 3 | 3.2 | 5 | 5 | 5 |
| Thickness of individual steel shim | $t_s$ | mm | 3 | 3.5 | 2 | 2 | 2 |
| Number of rubber layers | $n_r$ | - | 20 | 25 | 40 | 27 | 20 |
| Shape factor | $S$ | - | 12.7 | 10.6 | 20 | 20 | 20 |
| Second shape factor | $S_2$ | - | 2.5 | 2.1 | 2 | 3 | 4 |
| Shear modulus | $G$ | MPa | 0.9 | 0.46 | 0.7 | 0.7 | 0.7 |

Table 3.2: Percentage error of the various mechanical models in predicting $F_{cr}$ (as computed by Eq. (3.36)) for Bearing 1 under different pressure values ($\bar{p} = 4.13$ to 12.40 MPa) and rotation at the top ($\theta_t = 0.01$ to 0.04 rad, $\theta_b = 0.00$ rad).

| | $\bar{p}$ (MPa) | | | | | | |
|---|---|---|---|---|---|---|---|
| | 4.13 | 5.51 | 6.89 | 8.26 | 9.64 | 11.02 | 12.40 |
| $error_{F_{cr}}$ | $\theta_t = 0.01$ rad | | | | | | |
| Nagarajaiah–Ferrell | +37 | +33 | +31 | +28 | +26 | +24 | +22 |
| Iizuka | −9 | −13 | −19 | −26 | −34 | −44 | −56 |
| Han-Warn | +18 | +12 | +4 | −5 | −16 | −29 | −44 |
| Proposed Model (PM) | +18 | +8 | +6 | −1 | −10 | −20 | −32 |
| | $\theta_t = 0.02$ rad | | | | | | |
| Nagarajaiah–Ferrell | +36 | +31 | +27 | +24 | +20 | 1 + 7 | +14 |
| Iizuka | −11 | −15 | −21 | −29 | −38 | −45 | −60 |
| Han–Warn | +16 | +10 | +1 | −8 | −20 | −33 | −49 |
| Proposed Model (PM) | +18 | +7 | +7 | 0 | −7 | −17 | −26 |
| | $\theta_t = 0.03$ rad | | | | | | |
| Nagarajaiah–Ferrell | +33 | +29 | +24 | +20 | +15 | +10 | +4 |
| Iizuka | −12 | −17 | −24 | −32 | −41 | −52 | −64 |
| Han–Warn | +15 | +8 | −1 | −12 | −24 | −38 | −54 |
| Proposed Model (PM) | +17 | +6 | +6 | 0 | −4 | −16 | −20 |
| | $\theta_t = 0.04$ rad | | | | | | |
| Nagarajaiah–Ferrell | +32 | +27 | +21 | +15 | +10 | +3 | −4 |
| Iizuka | −14 | −19 | −27 | −35 | −45 | −55 | −68 |
| Han–Warn | +13 | +5 | −4 | −15 | −28 | −42 | −58 |
| Proposed Model (PM) | +16 | +6 | +6 | +1 | −5 | −11 | −14 |

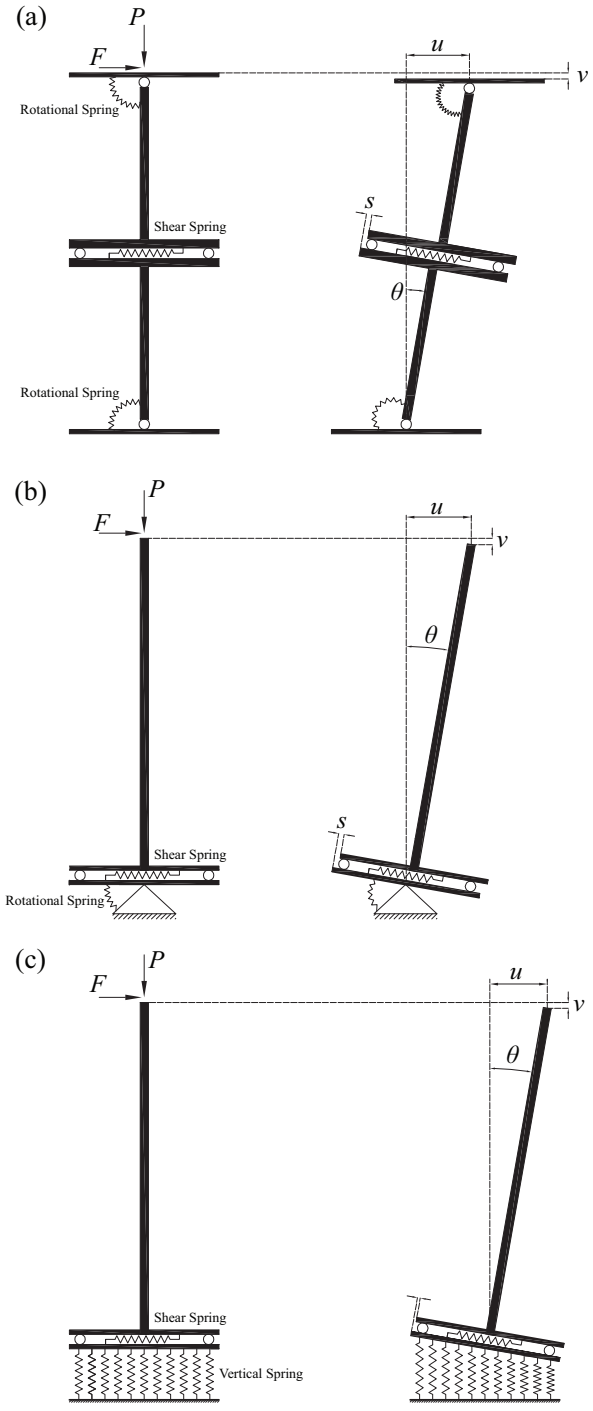


Figure 3.1: Illustration of the mechanical models in the laterally undeformed and deformed shape: (a) Nagarajaiah–Ferrell, (b) Iizuka, (c) Han–Warn.

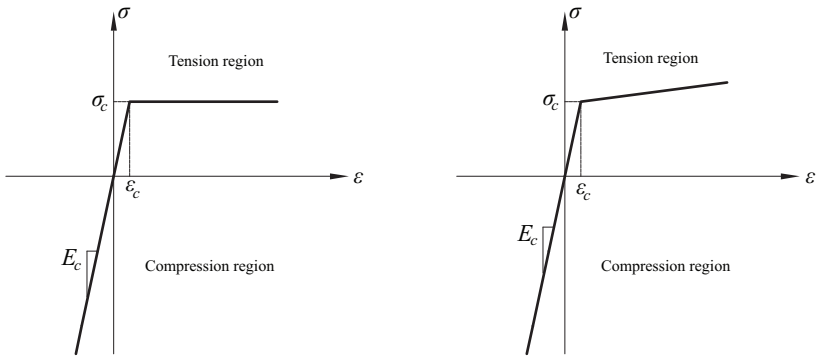


Figure 3.2: Bilinear elastic model for the rubber material used in the analytical model (a) with zero post-cavitation stiffness (Eq. (3.21)), (b) with non-zero post-cavitation stiffness (Eq. (3.24)).

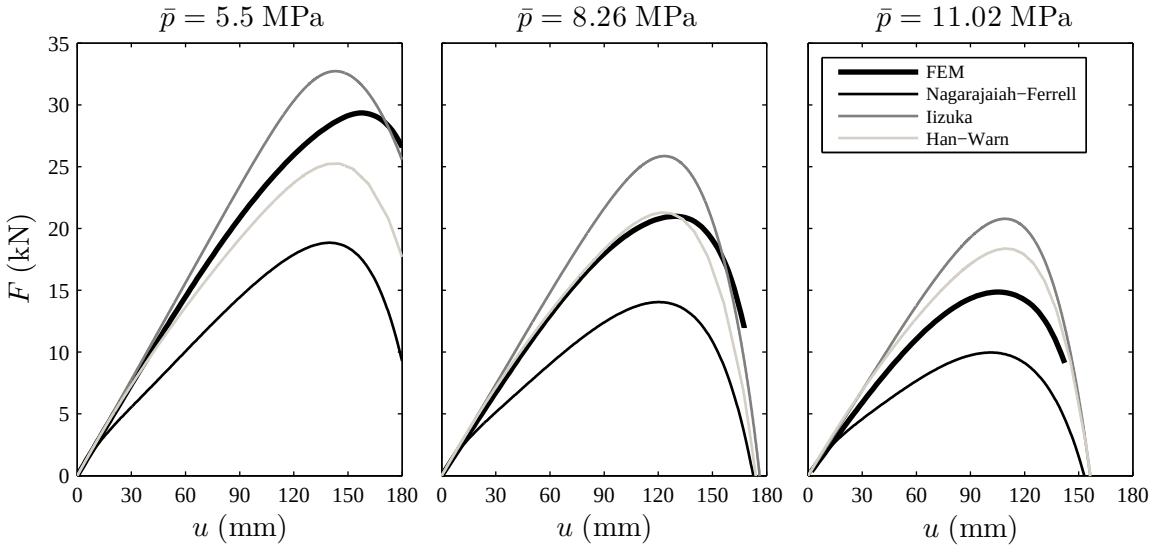


Figure 3.3: Shear force–lateral displacement results for the finite element model (FEM) of Bearing 1 and the three analytical models (Nagarajaiah–Ferrell, Iizuka, and Han–Warn) under $\bar{p} = 5.5$, 8.26 and 11.02 MPa.

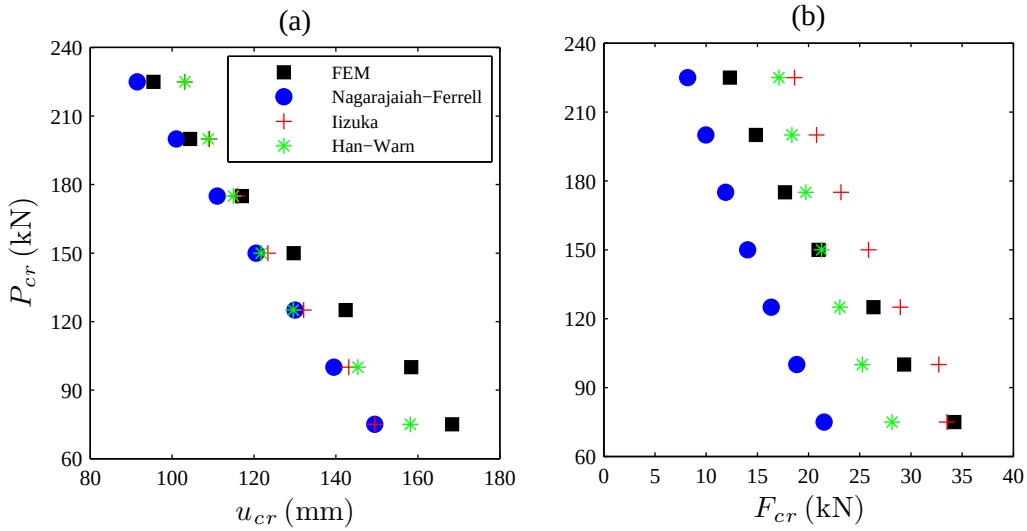


Figure 3.4: Critical points as predicted by the FEM and the three analytical models for Bearing 1: (a) $P_{cr}$ vs $u_{cr}$, (b) $P_{cr}$ vs $F_{cr}$.

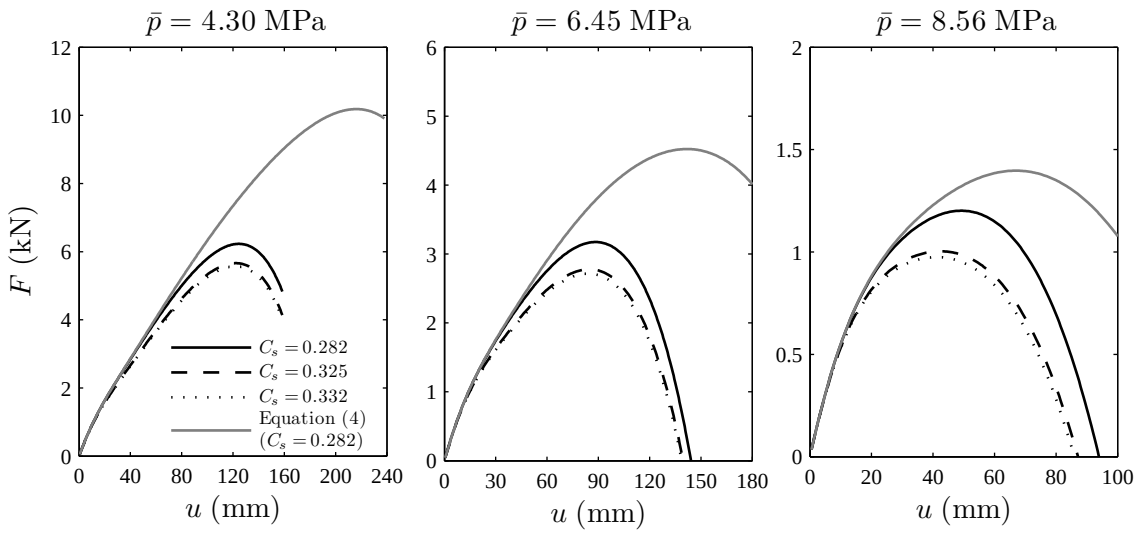


Figure 3.5: Shear force–lateral displacement results for the Nagarajaiah–Ferrell model (using three different values of $C_s$) and the modification proposed by Vemuru et al. [10] with $C_s = 0.282$ (Eq. (4.4)) for Bearing 2 under $\bar{p} = 4.30$, 6.45 and 8.56 MPa.

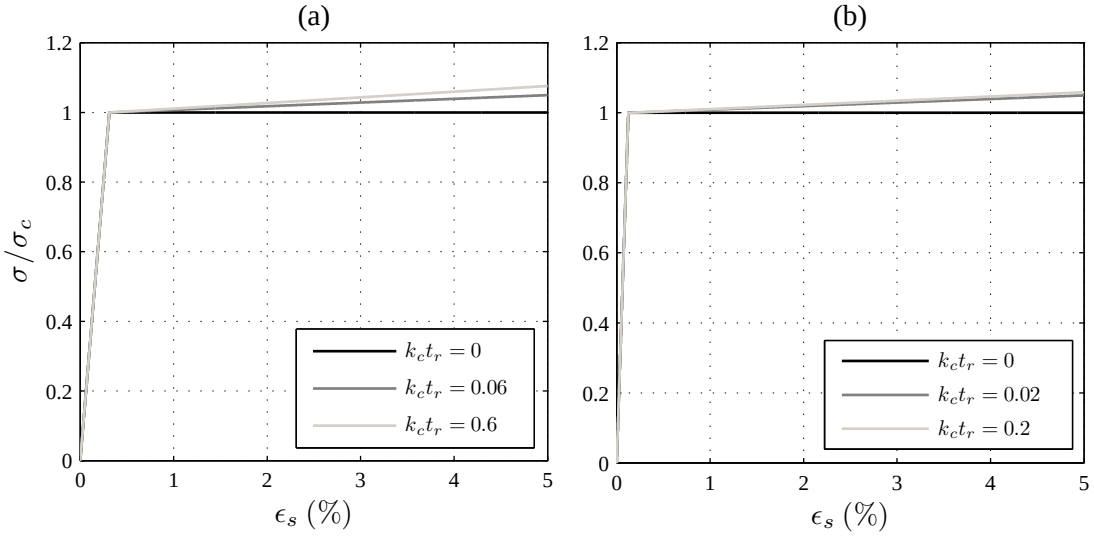


Figure 3.6: Bilinear elastic model for the rubber material in tension with post–cavitation hardening for different values of $k_c t_r$ using Eq. (3.24) for (a) Bearing 1 and (b) Bearing 3.

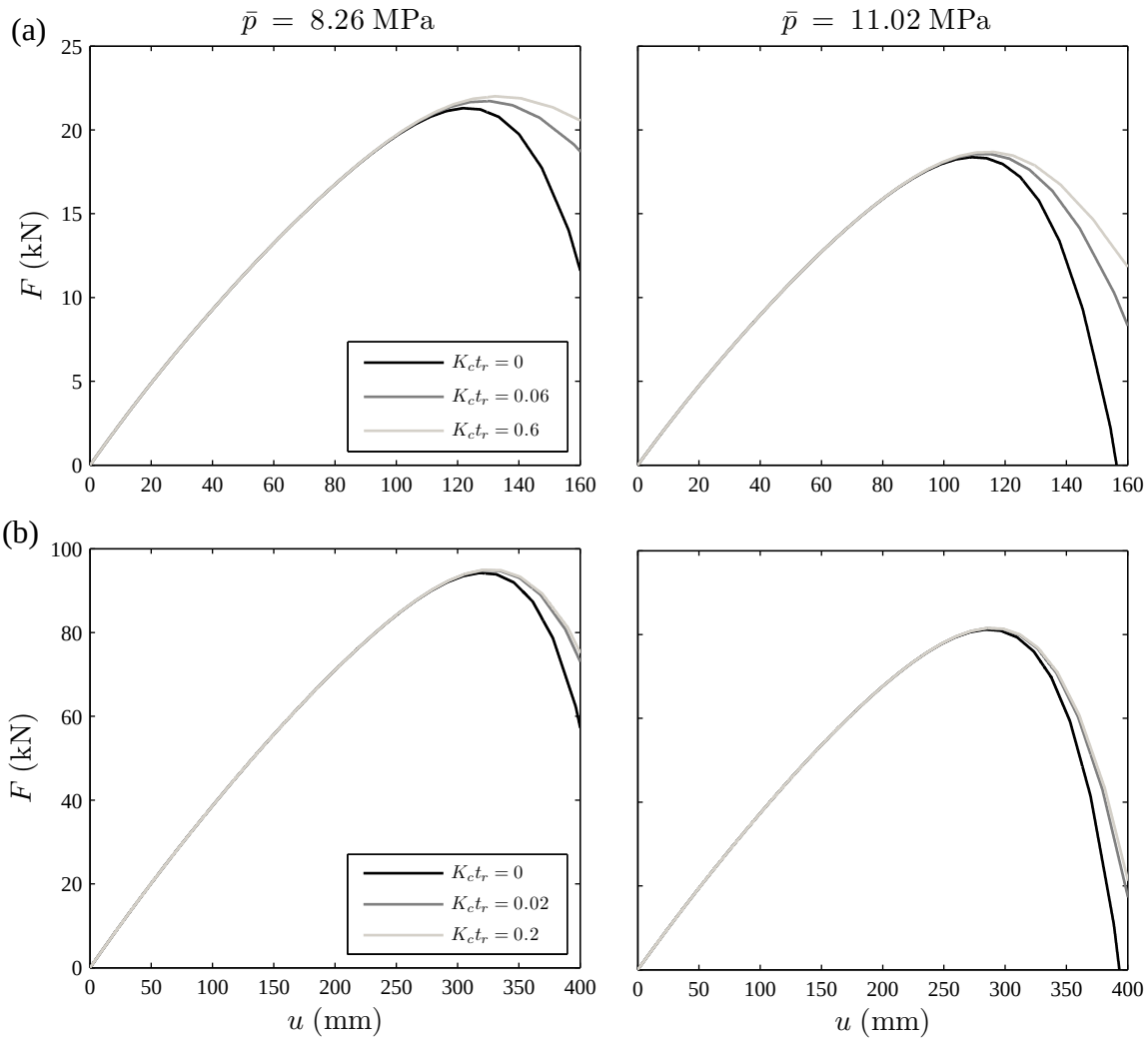


Figure 3.7: Shear force–lateral displacement results using the Han–Warn model with vertical springs characterized by Eq. (3.24) with different values of $k_c t_r$ for (a) Bearing 1 and (b) Bearing 3, under pressure of $\bar{p} = 8.26$ and 11.02 MPa.

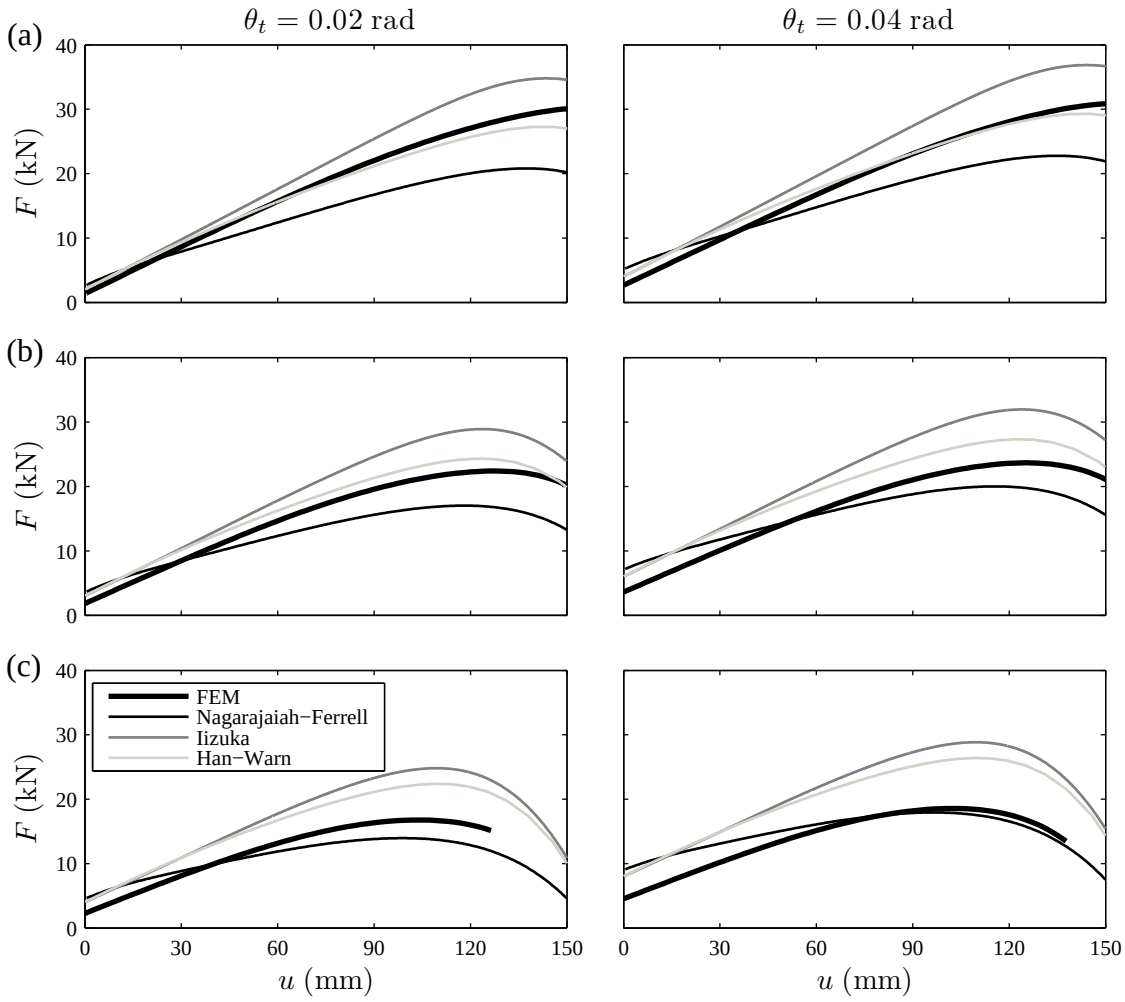


Figure 3.8: Comparison of shear force–lateral displacement curves obtained using the FEM and the three modified analytical models for Bearing 1 under top-support rotation of $\theta_t = 0.02$ rad (left) and $\theta_t = 0.04$ rad (right), and pressure of (a) 5.5, (b) 8.26, and (c) 11.02 MPa.

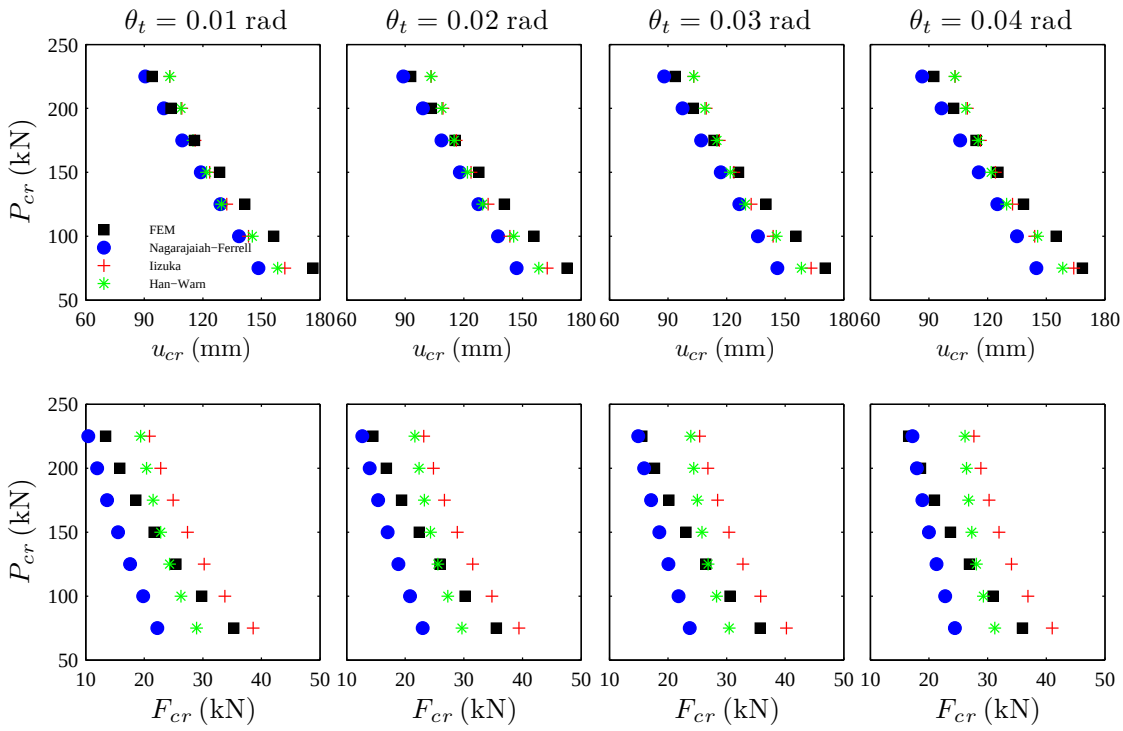


Figure 3.9: Comparison of critical points obtained by the FEM and the three modified analytical models for Bearing 1 ($\theta_t = 0.01$, 0.02, 0.03 and 0.04 rad, $\theta_b = 0.00$ rad).

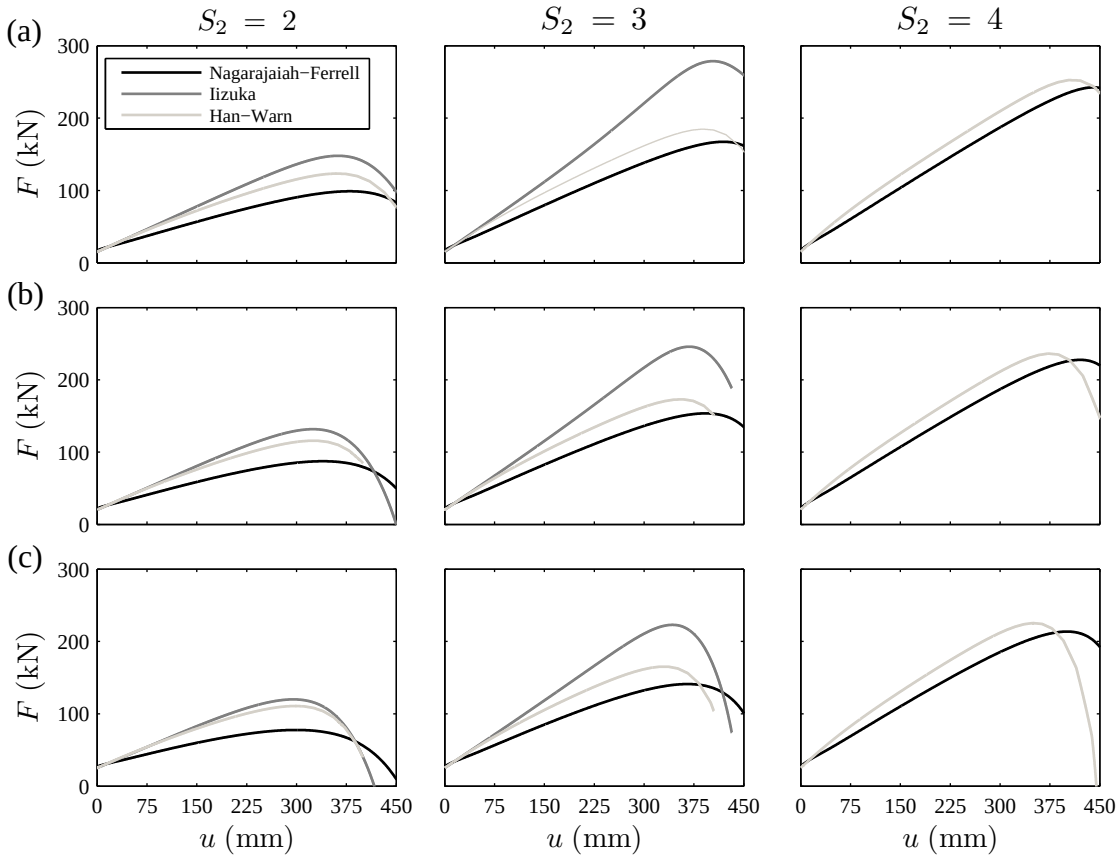


Figure 3.10: Comparison of shear force–lateral displacement curves obtained using the FEM and the three modified analytical models for $\theta_t = 0.02$ rad for Bearing 3 ($S_2 = 2$), Bearing 4 ($S_2 = 3$) and Bearing 5 ($S_2 = 4$) under pressure of (a) 5.5, (b) 8.26, and (c) 11.02 MPa.

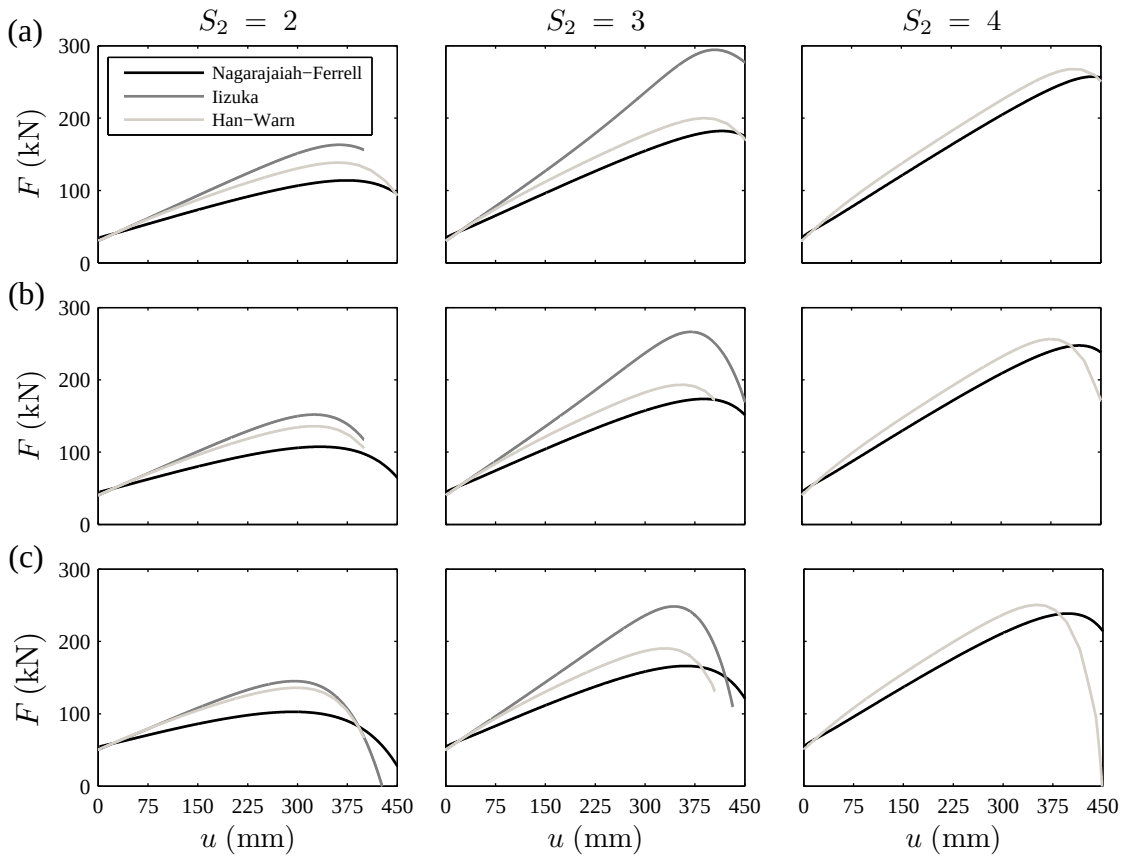


Figure 3.11: Comparison of shear force–lateral displacement curves obtained using the FEM and the three modified analytical models for $\theta_t = 0.04$ rad for Bearing 3 ($S_2 = 2$), Bearing 4 ($S_2 = 3$) and Bearing 5 ($S_2 = 4$) under pressure of (a) 5.5, (b) 8.26, and (c) 11.02 MPa.

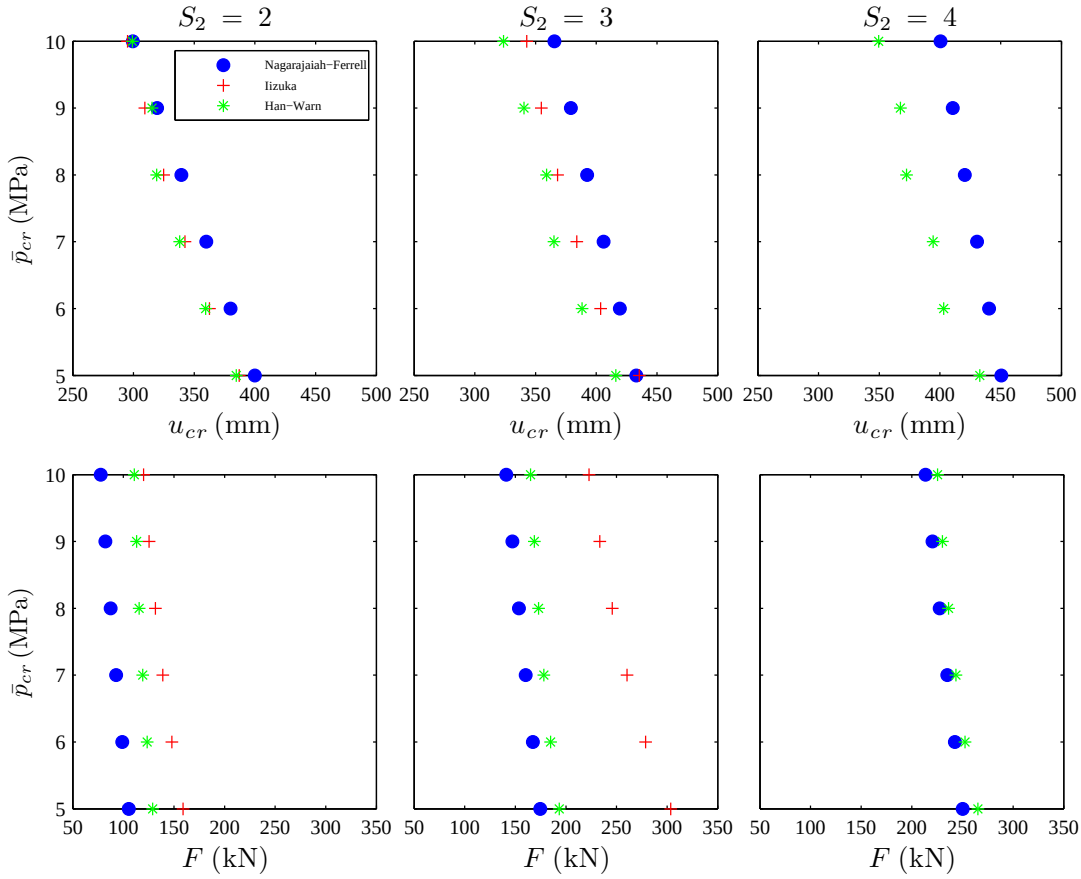


Figure 3.12: Critical points obtained using the FEM and the three modified analytical models for $\theta_t = 0.02$ rad for Bearing 3 ($S_2 = 2$), Bearing 4 ($S_2 = 3$) and Bearing 5 ($S_2 = 4$).

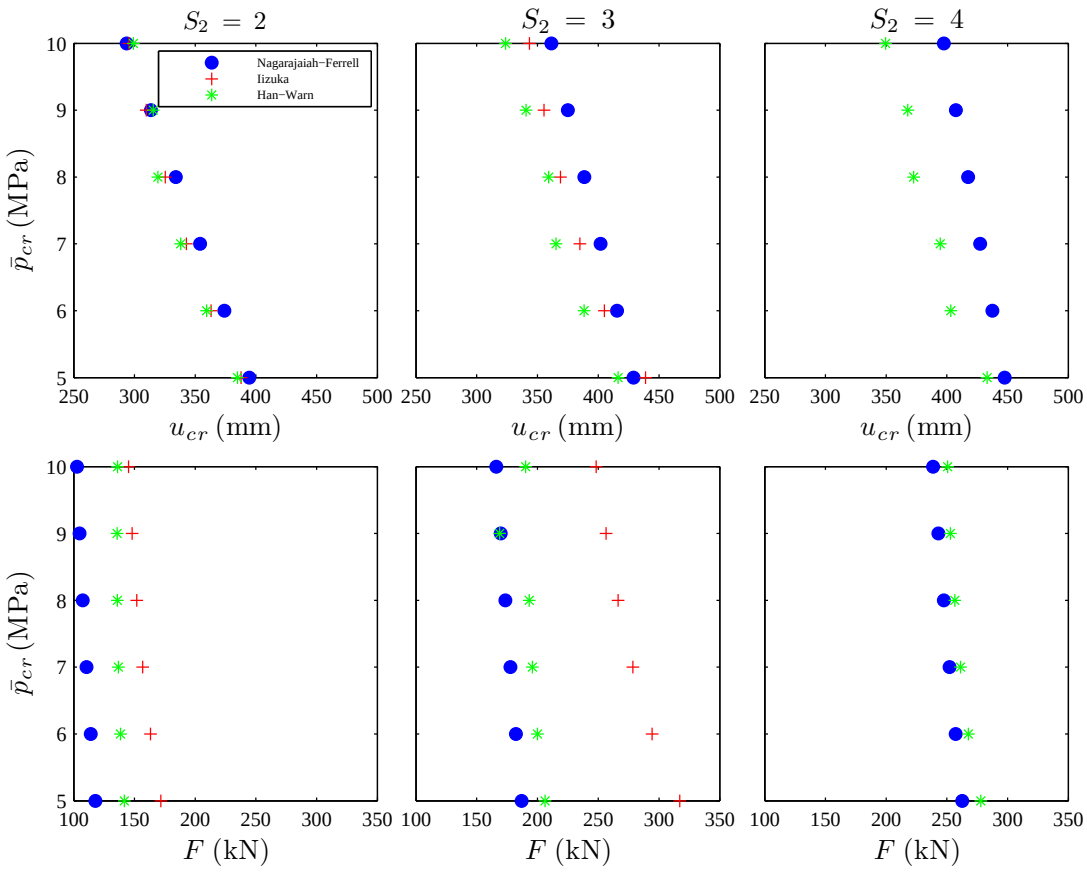


Figure 3.13: Critical points obtained using the FEM and the three modified analytical models for $\theta_t = 0.04$ rad for Bearing 3 ($S_2 = 2$), Bearing 4 ($S_2 = 3$) and Bearing 5 ($S_2 = 4$).

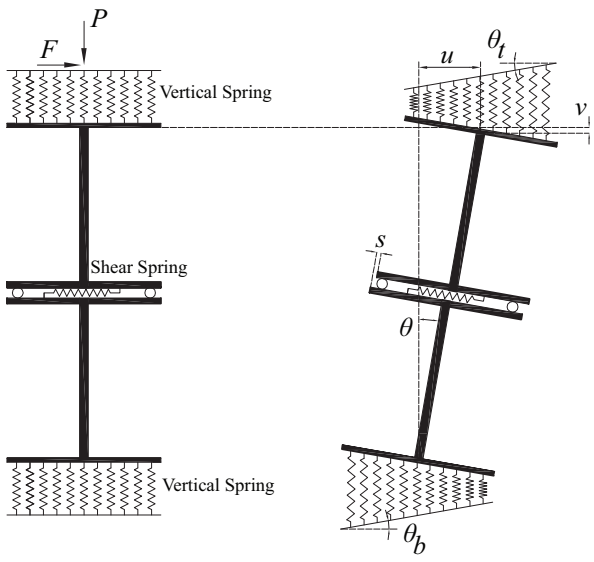


Figure 3.14: Illustration of the Proposed Model (PM) in the laterally undeformed and deformed shape ($\theta_t$ and $\theta_b$ as shown are positive).

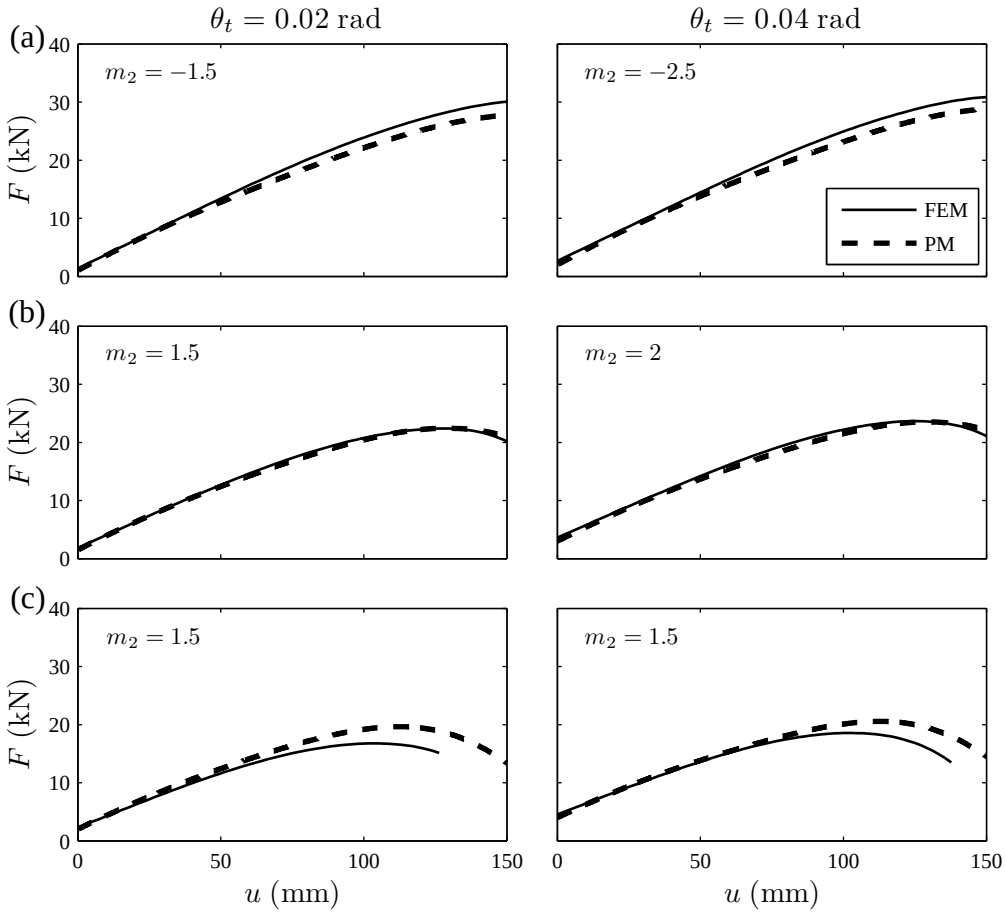


Figure 3.15: Comparison of shear force–lateral displacement curves obtained using the FEM and PM for Bearing 1 under rotation at the top only ($\theta_t = 0.02$ or 0.04 rad, $\theta_b = 0.00$ rad) and pressure of (a) 5.5, (b) 8.26, and (c) 11.02 MPa ($m_1 = 2$, $k_c t_r = 0.06$).

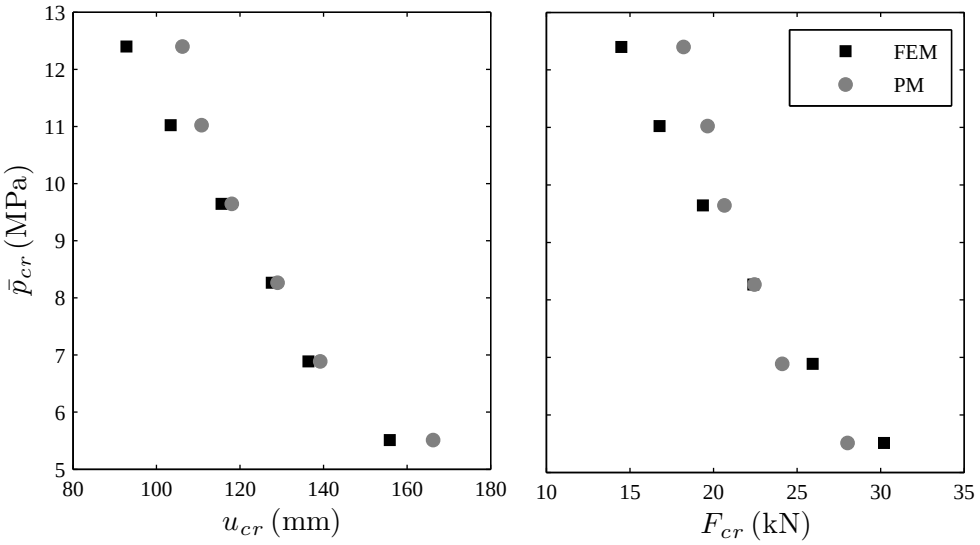


Figure 3.16: Comparison of critical points obtained by PM and FEM for Bearing 1 ($\theta_t = 0.02$ rad, $\theta_b = 0.00$ rad, $m_1 = 2$, $k_c t_r = 0.06$).

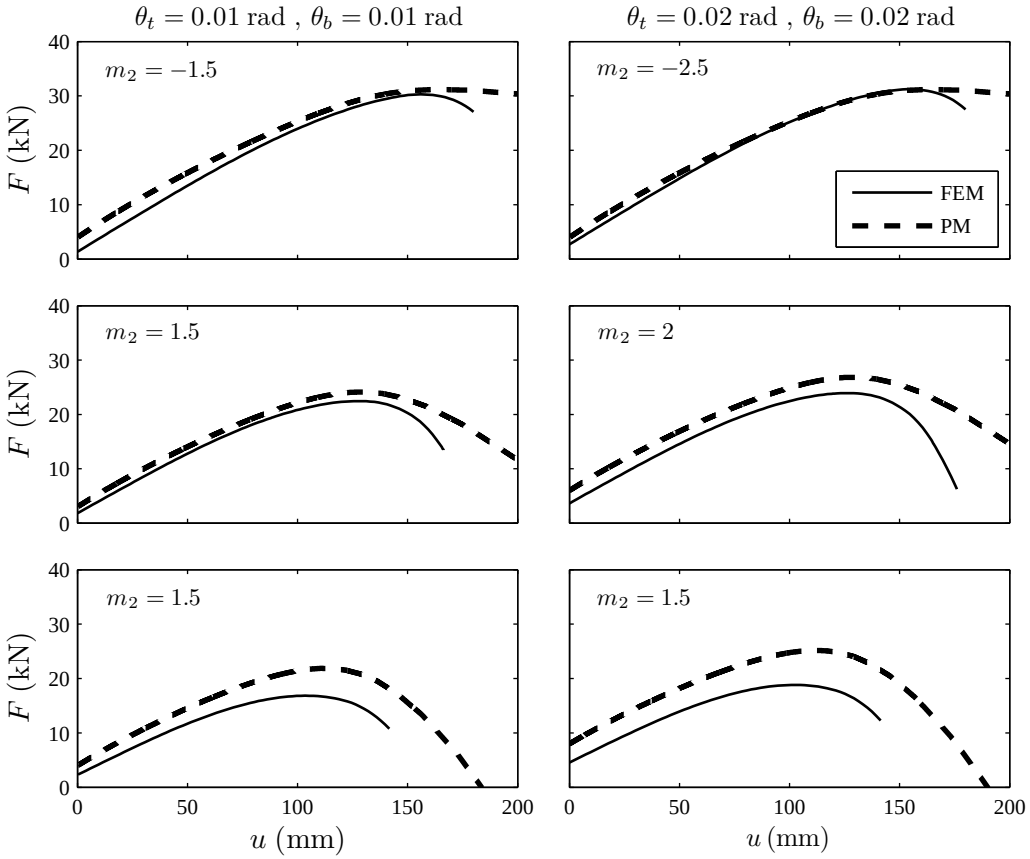


Figure 3.17: Comparison of shear force–lateral displacement curves obtained using the FEM and PM for Bearing 1 under rotation at both the top and bottom ($\theta_t = \theta_b = 0.01$ rad and $\theta_t = \theta_b = 0.02$) and pressure of (a) 5.5, (b) 8.26, and (c) 11.02 MPa ($m_1 = 1$, $k_c t_r = 0.06$).

# Chapter 4

# Experimental and Analytical Studies on the Horizontal Behavior of Elastomeric Bearings Under Support Rotation

Rastgoo Moghadam S, Konstantinidis D. Experimental and analytical studies on the horizontal behavior of elastomeric bearings under support rotation. Will be Submitted to *Journal of Structural Engineering*.

## 4.1 Abstract

Elastomeric seismic isolation bearings are among the most common earthquake protective devices in use. In traditional practice, due to the flexural rigidity of the superstructure and substructure above and below the isolation layer, the support surfaces at the top and bottom of elastomeric bearings experience negligible rotations. Therefore, past studies have focused on the behavior of bearing under the assumption of zero top and bottom support rotation. However, in bridge applications, isolation of high-rise buildings and mid-height isolation, it is possible for elastomeric bearings to experience rotation. The main objective of this study is to experimentally investigate the effect of support rotation on the lateral behavior of elastomeric bearings. For this purpose, experimental tests of a 1/4-scale circular isolator with a shape factor of 20 and second shape factor of 4 were conducted. Two experimental procedures were employed. The first investigated the behavior of the bearing under lateral quasi–static cyclic displacement, constant axial load and constant rotation. The cyclic test results showed that the rotation causes the hysteresis loops to shift up, and consequently the loops were not symmetric with respect to the zero point in the shear force–lateral displacement curve. The second procedure investigated the lateral behavior of the bearing through monotonic lateral displacement under constant axial load and rotation angle. The results of the tests are used to compare against Finite Element Analysis (FEA) results. There is a good agreement between the experimental result and the FEA results. Furthermore, the experimental results were used to evaluate a mechanical model proposed by the authors in another study. The experimental results showed that the mechanical model is able to simulate the effect of rotation on the lateral behavior of the bearing.

## 4.2 Introduction

Past studies [1-5] have shown that the combination of axial load and large horizontal displacement can decrease the axial load capacity of an individual bearing. These studies assumed that the isolator deformed vertically and horizontally without experiencing any rotation at the supports. A summary of experimental studies on elastomeric seismic isolation bearings in the literature is presented here. The reader interested in extensive review of numerical, and analytical studies on the subject is referred to [6-8]. Aiken et al. [2] carried out dynamic tests on low shape factor elastomeric seismic isolation bearings. The bearings varied in the elastomer (i.e., high damping, natural rubber), end plate connections (i.e., doweled, bolted). The tests included cyclic vertical loading, buckling tests and shear and tension failure tests. Stanton et al. [9] investigated the instability of elastomeric bearings theoretically and experimentally to account for the effect of axial shortening. To examine the effect of horizontal displacement on critical load, Buckle et al. [4] carried out a series of experimental tests on different bearings with low shape factor.

Cardone and Perrone [10] experimentally evaluated the critical behavior of a slender elastomeric bearing at different strain amplitudes, ranging from approximately 50 to 150 %. They showed that the critical load capacity is approximately 1.5 to 3.5 times more than the capacity predicted by current design procedures. Weisman and Warn [11] experimentally and numerically showed that the use of lead core in elastomeric bearings does not have a significant effect on the critical load of the tested bearings over the 150–280 percent range of shear strain. A Comprehensive experimental study on the stability of elastomeric bearings under quasi-static and dynamic loading test method was carried out by Sanchez et al. [12]. They confirmed the

observation made by Weisman and Warn [11] about the effect of lead core on the critical load capacity of elastomeric bearings. Moreover, They showed that the result from quasi-static and dynamic tests are in a relatively good agreement.

Koh and Kelly [13] studied the dynamic behavior of elastomeric bearings taking into account the effect of axial load. They proposed a mechanical model capable of accounting for the reduction of the dynamic shear stiffness and the height reduction of bearings due to the $P - \Delta$ effect and they verified the accuracy of the model by conducting cyclic shear and static axial loadings tests on four bearings. Nagarajaiah and Ferrell [14] extended the model proposed by Koh and Kelly [13] to include large displacements. To improve the prediction of the stiffness degradation beyond the stability point, Vemuru et al. [15] modified the model proposed by Nagarajaiah and Ferrell [14]. In another study conducted by Vemuru et al. [16], the coupled horizontal–vertical behavior of elastomeric bearings subjected to dynamic loading was investigated and compared against a proposed analytical model. Iizuka [17] developed a model by introducing finite deformation and nonlinear springs into the model proposed by Koh and Kelly [13]. Recently, Hongping et al. [18] experimentally investigated the horizontal behavior of elastomeric bearings when the axial load is applied with an eccentricity and compared against a modified Iizuka model [17].

Use of elastomeric bearings in bridges is very common and was studied in different projects. Warn et al. [19] investigated the influence of lateral displacement on the vertical stiffness of elastomeric and lead–rubber bearings. Their results showed that the vertical stiffness decreased with increasing horizontal displacement. An extensive experimental study on the seismic response of unbonded elastomeric bridge bearings can be found in [20]. Warn and Whittaker [21] experimentally studied the effect of

vertical earthquake excitation on the response of an isolated bridge with rubber and lead–rubber bearings.

Burtscher and Dorfmann [22] investigated the effect of inclined steel shims on high damping rubber bearings by series of compression and shear tests. Their results showed that vertical stiffness reduces with increasing slope of the steel shims. The horizontal stiffness increased up to shear strains 100 percent, while for large shear strains, increasing the angle of the steel shims did not have a significant effect on the lateral stiffness of the bearings.

The studies discussed above did not consider rotation at the supports, which in many cases is a reasonable assumption. Conventional practice places the isolation system at the foundation level and calls for the construction of rigid diaphragms above and below the isolation layer. Consequently, these rigid diaphragms prevent the isolators from experiencing rotation. However, there are several scenarios where isolators do experience rotations, including in tall buildings [23], in mid-story isolation applications [24,25], in bridges [26,27], etc.

This study builds upon previous analytical studies by the authors [6,7] aimed at characterizing the effect of support rotation on the horizontal behavior and instability (i.e., the point at which the tangential lateral stiffness becomes zero) of elastomeric bearings. An investigation using 3D FEA [6] showed that the effect of rotation in the stress and strain distributions is most pronounced at low lateral displacements. Moreover, it was shown that, in general, support rotation does not significantly affect the critical displacement at the instability point, but it can decrease or increase the critical shear force. In another study, the authors [7] modified existing mechanical models that do not account for support rotation so as to include rotation. The mechanical

models were evaluated using 3D FEA, and were shown to model the behavior with accuracy varying from fairly good to poor. Furthermore, a new mechanical model was proposed to capture the rotation effects and estimate the force at the critical point (instability) with improved accuracy than the previous models.

This study investigates the effect of rotation on the horizontal behavior of elastomeric isolation bearings through a series of experimental tests. For this purpose, a bearing-testing machine was built at the Applied Dynamic Laboratory at McMaster University. The machine was able to shear the bearing monotonically and cyclically while the axial load and support rotation angle was maintained constant. A 1/4-scale circular isolator constructed by Bridgestone Inc. [28] was considered. Various quasi–static cyclic and monotonic tests up to 300 % shear strain under different values of the pressure and rotation angle were conducted. This paper presents the results of this experimental test program. The experimental results are compared to result of FEA on a 3D finite element model (FEM) of the bearing developed in ABAQUS [29]. Furthermore, the experimental test results are used to validate the mechanical model (MM) proposed by the authors in [7].

## 4.3 Experimental tests

### 4.3.1 Elastomeric Bearing Test Specimen

A 1/4-scale circular elastomeric bearing with diameter of 158 mm was used for all tests in the experimental program. It consisted of 20 rubber layers of 2 mm thickness, making the shape factor, $S$, equal to 20 and the second shape factor, $S_2$, (defined as the ratio of diameter to total rubber thickness) equal to 4. Table 4.1 lists additional

details of the bearing and properties of the low-damping natural rubber compound used. Montuori et al. [30] have shown that elastomeric bearings with a second shape factor larger than 4 do not experience any instability under 300 % shear strain. Consequently, it was expected that the bearing tested in this study will likely not experience instability. The low value of bulk modulus provides compressible rubber material, then in the FEA and mechanical model, the compressibility of rubber should be considered. The bearing included 2 mm of cover to protect the bearing from environmental factors. It was assumed that this cover does not affect the behavior of the bearing and it was not considered in the numerical studies.

### 4.3.2 Bearing-Testing Apparatus

A bearing-testing machine designed and constructed at the Applied Dynamic Laboratory, McMaster University [25], was modified for the purposes of the current study. Fig. 4.1 shows the the setup with the elastomeric bearing installed. Fig. 4.2 illustrates each part of the setup in detail. Table 4.2 lists all instruments and equipment used in the setup. As shown in Fig. 4.2, the setup included two vertical actuators (labeled actuator[1] in Fig. 4.2) pin-connected to the two reaction columns on the left and right side of the setup. In order to apply vertical loads, these actuators were connected to the loading beam through a pin connection to the load cells. In addition, a plate was welded to each end of the beam and, four threaded rods (in front and behind of the reaction columns) which bolted to each plate, went through both sides of the reaction columns. In a similar way, the other end of the rods were also bolted to plates on the opposite side of the reaction columns. On each side of the reaction columns, there was a machined plate bolted to the reaction columns and

a thin polyoxymethylene layer was placed between this plate and the welded plate section. This synthetic polymer layer provided high stiffness in the lateral direction, low friction, and acted as a sliding surface between the columns and the beam. This mechanism minimized the friction force to allow the loading beam to move vertically while preventing the beam from swaying in the lateral direction.

The loading beam was controlled by two separate controlling systems. The first that worked in displacement-mode was used to maintain the beam horizontal. Two linear potentiometers (LPs), on the left and right sides of the setup were used to control the vertical actuators. The difference between the LPs was used as feedback. The controller was designed in such a way that this difference maintained zero during the test. For example, if one of the actuators pushed the loading beam and tried to tilt the beam, the other one followed the first actuator to maintain the beam horizontal position. The second controller which worked in force-control was used to maintain a constant axial load applied on the bearing. The summation of the loads from each vertical actuator (received from each load cell) was used as feedback for the second controller. During the test, the second controller attempted to maintain the summation with the prescribed axial load. The aforementioned controllers worked separately but the performance of each controller affected the other one, possibly caused cyclic teetering of the loading beam. To avoid this, in the design of the system, the displacement controller was given higher priority than the other one. It means the response of the system to difference between two LPs was faster than the response to the second controller, ensuring any cyclic responses between the two controllers were decreased.

The beam was connected to the elastomeric bearing by the designed mechanism

shown in Fig. 4.3. The mechanism included a roller in the middle and and an actuator (labeled Actuator$^2$ in Fig. 4.2) on the right side. The roller was between two steel pieces which were shaped and polished to hold the roller properly. The two pieces prevented the roller from moving in the lateral direction, but, the roller was allowed to revolve. The top piece was welded to a plate, which was bolted to the loading beam, and the bottom piece was also welded to a plate which was bolted to the top end plate of the elastomeric bearing (see Fig. 4.2). As the stroke in the Actuator$^2$ comes out, it pushes the loading beam upward and tries to tilt it, but the displacement controller explained in the previous paragraph prevents any rotation. Below Actuator$^2$, the transfer of the load caused the top end plate of the elastomeric bearing to rotate. Actuator$^2$ was controlled by a hand pomp, and the applied load was increased until the rotation angle on the top of the bearing reached the desired value. To measure the rotation, an inclinometer was attached at the rear of the top plate of the bearing. Once the desired rotation angle was obtained, the position of the top plate of the bearing was maintained by tightening four bolts and turnbuckles at the front and back. The bolts worked as compression elements, while the turnbuckles worked as tension elements. The combination of turnbuckles and bolts prevented the top of the bearing from experiencing larger or smaller rotation than the prescribed angle, thus providing constant rotation on the top of the bearing during the test.

The bottom end plate of the elastomeric bearing was connected to a thick platen supported by four load cells, similar to those used to monitor the load in the vertical actuators. These load cells were used to monitor the total axial load. The load cells were connected to a plate, which acted as a table bolted to three linear sliders. The table constructed on a steel section built by four steel channel sections and stiffened

by steel plates. The table could move in one direction by a horizontal actuator (labeled Actuator$^3$ in Fig. 4.2) pin-connected to the left reaction column. A string Potentiometer was attached to the actuator to monitor the displacement of the table. In addition, this string Potentiometer was used to control the movement of the table in displacement control mode. The actuator was able to reach a stroke of $\pm$ 120 mm corresponding to 300 % shear strain in the elastomeric bearing. Each linear slider included two sliding blocks connected to the aforementioned steel section. The rails of the sliders were installed with very high precision to ensure that the table moved with very low friction force. Furthermore, the rails and blocks were lubricated before each test.

The data acquisition and controlling system worked separately. As it was discussed earlier, some of the instrumention was used for both the control system and measurements, consequently the signals from these instruments were divided into two signals by isolation circuits. The data acquisition was designed for a maximum sampling rate of 10 Hz, but this number could be changed based on the number of the channels used during a test. In this study the sampling rate was 1.75 Hz.

### 4.3.3 Test Protocol

Two experimental procedures were used in this study. The quasi–static cyclic displacement history shown in Fig. 4.4, was applied horizontally to the bottom of the bearing at a constant velocity of 1 mm/s. In the loading protocol, the bearing was first subjected to the full axial load desired and then the rotation was applied. This procedure was followed to ensure that the whole bearing was under compressive stress when it experienced the rotation. As result of this, tensile stresses produced by the

rotation could be subtracted from the compressive stress due to the axial load. Therefore, the bearing was still under compressive stress, however this stress was not even on the surface of the bearing. On the other hand, a very large rotation could produce large tensile stresses and possibly damage the bearing. In this study, to avoid subjecting the bearing to such possible damage (before applying the lateral displacement) the applied rotation angle values were very small, in conjunction with high axial loads. The following presents the step by step procedure for the cyclic test:

- Apply the desired axial load and maintain the load.
- Use the hand pump to apply the desired rotation angle. The rotation in all tests were clockwise and applied on the top of the bearing.
- Tighten the turnbuckles and bolts to maintain the rotation angle during the lateral displacement. To ensure that the rotation angle was kept constant during the test, the rotation angle was measured by an inclinometer attached to the top end plate of the bearing, noting that a margin of $\pm$ 5 % deviation was accepted.
- Apply the lateral displacement history as shown in Fig. 4.4.
- Loosen the turnbuckles, bolts, and hand pomp to release the rotation.
- Release the axial load.

The second procedure followed involved monotonic lateral displacement tests. These tests were conducted in a fashion similar to the cyclic test procedure except for the horizontal displacement history. In these tests, the lateral displacement was increased monotonically until the horizontal displacement reached 100 mm.

## 4.4 Review of Mechanical Model

This section reviews the formulation of the mechanical model used to attempt to characterize the experimentally observed behavior. Comparison between predictions of the model and experimental results will be presented later in the paper. The mechanical model is based on the model proposed by Han and Warn [31] but includes modifications to take into account support rotation and post-cavitation hardening, as proposed and discussed in detail by Rastgoo Moghadam and Konstantinidis in another study [7]. The discussion here gives an overview of the models; the interested reader is referred to [7] for more details.

The model consists of two series of vertical springs at the top and bottom as shown in Fig. 4.5. The cross section of the top and bottom of the bearing are discretized into vertical springs, each of which represents a strip of the cross section running in the direction normal to the page. In this study, the number of springs, $n$, was equal to 30. The procedure attempts simultaneously to solve four equations at each lateral displacement and rotation increment. The stepwise incremental analysis proposed by Iizuka [17] was used. The stepwise equation for step $i$ can be obtained as,

$$\begin{bmatrix} {}_i(\Delta\theta) \\ {}_i(\Delta s) \\ {}_i(\Delta v) \\ {}_i(\Delta F) \end{bmatrix} = \begin{bmatrix} h\sin{}_i\theta + {}_i s\cos{}_i\theta & \sin{}_i\theta & -1 & 0 \\ h\cos{}_i\theta - {}_i s\sin{}_i\theta & \cos{}_i\theta & 0 & 0 \\ {}_i(dM/d\theta) & 0 & {}_iF & {}_iv - h \\ P\cos{}_i\theta - {}_iF\sin{}_i\theta & -{}_i(dQ_s/d\theta) & 0 & \cos{}_i\theta \end{bmatrix}^{-1} \begin{bmatrix} 0 \\ 1 \\ P \\ 0 \end{bmatrix} \Delta u \qquad (4.1)$$

where $\theta$ and $s$ are local deformations, $u$ and $v$ are global deformations, $F$ is the horizontal force and $P$ is the vertical force applied on the bearing, as shown in Fig. 4.5. $h$ is the height of the bearing including the rubber and steel shims. $\Delta$ represents

the increment at each step. $dQ_s/d\theta$ and $dM/d\theta$ are the tangential shear stiffness and tangential moment stiffness, respectively. They can be obtained by [14]

$$\frac{dQ_s}{d\theta} = \frac{GA}{t_r}\left[1 - 0.325\tanh\left(\frac{u}{t_r}\right)\right] \tag{4.2}$$

and [31]

$$_i\left(\frac{dM}{d\theta}\right) = \frac{_iM - _{i-1}M}{_i\theta - _{i-1}\theta} \tag{4.3}$$

where $t_r$ is the total thickness of the rubber layers, $A$ is the cross sectional area of the bearing, $M$ is the total moment in the vertical top and bottom springs. At the first step, $_1s$ is assumed arbitrarily, yet small enough for convergence, but the stepwise equation can be ill-conditioned. Therefore, the following equations are used for $_1\theta$, $_1F$, $_1v$, and $\Delta u$ [7]

$$_1\theta = \frac{GA_s + P}{P_E t_r}{}_1s \tag{4.4}$$

$$_1F = \frac{_1s\left(GA_sP_E - P^2\right) - \left(PP_Eh\frac{\theta_t+\theta_b}{m_1}\right)}{P_Eh - P_E\frac{\theta_t+\theta_b}{m_1}{}_1s} \tag{4.5}$$

$$_1v = {}_1s\sin{}_1\theta + h(1 - \cos{}_1\theta) \tag{4.6}$$

$$\Delta u = {}_1s\cos{}_1\theta + h\sin{}_1\theta \tag{4.7}$$

where subscripts $t$ and $b$ indicate the case of the top and bottom of the bearing, respectively; $m_1$ is a modification factor to adjust the initial force at zero lateral displacement; equal to 2 for rotation at the top only and equal to 1 for rotation at the top and bottom; $A_s = A(h/t_r)$ is the shear area of the elastomeric bearing, $P_E$ is

the Euler load for the standard column [5],

$$P_E = \frac{\pi^2 EI_s}{h^2} \tag{4.8}$$

$EI_s$ is the bending rigidity of the rubber–steel composite system computed from $EIs = EI_{eff}(h/t_r)$, where $EI_{eff}$ is the effective bending rigidity of an individual rubber layer. The effective bending rigidity of a circular elastomeric bearing with compressible rubber is obtained from [5]

$$EI_{eff} = KI\left(1 - \frac{4}{\sqrt{\frac{48G}{K}}S}\frac{I_2\left(\sqrt{\frac{48G}{K}}S\right)}{I_1\left(\sqrt{\frac{48G}{K}}S\right)}\right) \tag{4.9}$$

where $I = \pi D^4/64$, $I_1$ is moment of inertia of the rubber layer, and $I_1$ and $I_2$ are the first and second order modified Bessel function of the kind, respectively.

Each series of vertical springs should satisfy the equilibrium and compatibility equations as follows [7]

$$P = \sum_j \sigma_{s_j} A_{j_t} = \sum_j \sigma_{s_j} A_{j_b} \tag{4.10}$$

$$_iM_t = \sum_j \sigma_{s_j} A_{j_t} d_{s_j} \tag{4.11}$$

$$_iM_b = \sum_j \sigma_{s_j} A_{j_b} d_{s_j} \tag{4.12}$$

$$\frac{\epsilon_{s_{1t}} l_s}{d_{s_{1t}} + x_t} = \frac{\epsilon_{s_{2t}} l_s}{d_{s_{2t}} + x_t} = ... = \frac{\epsilon_{s_{jt}} l_s}{d_{s_{jt}} + x_t} = ... = \frac{\epsilon_{s_{nt}} l_s}{d_{s_{nt}} + x_t} = \theta - \delta\theta_t \tag{4.13}$$

$$\frac{\epsilon_{s_{1b}} l_s}{d_{s_{1b}} + x_b} = \frac{\epsilon_{s_{2b}} l_s}{d_{s_{2b}} + x_b} = ... = \frac{\epsilon_{s_{jb}} l_s}{d_{s_{jb}} + x_b} = ... = \frac{\epsilon_{s_{nb}} l_s}{d_{s_{nb}} + x_b} = \theta - \delta\theta_b \tag{4.14}$$

$_iM$ can be obtained by summation of $_iM_t$ and $_iM_b$, $A_j$ is the area corresponding to the

$j$th vertical spring element, $d_{s_j}$ is the distance between the center of the $j$th vertical spring and the center of the bearing cross section, and $x$ is the distance between the neutral axis and the center of the bearing cross section. $\sigma_{s_j}$ and $\epsilon_{s_j}$ are the stress and strain in the $j$th vertical spring element, the relationship between which is as proposed by Kumar et al. [32],

$$\sigma_{s_j} = \begin{cases} E_c \epsilon_{sj} & (\epsilon_{sj} \leq \epsilon_c) \\ \sigma_c \left[ e^{k_c t_r (\epsilon_{s_j} - \epsilon_c)} + \frac{1}{k_c t_r} \left( e^{k_c t_r (\epsilon_{s_j} - \epsilon_c)} - 1 \right) \right] & (\epsilon_{s_j} > \epsilon_c) \end{cases} \tag{4.15}$$

where $\epsilon_c = \sigma_c / E_c$, and $\sigma_c$ is the cavitation stress which is assumed to be $3G$ [33], $k_c$ is the cavitation parameter which can be obtained by calibration with experimental data. This parameter controls the lateral force at large displacements. Since the experimental data on the behavior of rubber in tension was not available, in this study, $k_c t_r = 0.04$, assuming the slope of the post-cavitation $\sigma$–$\epsilon$ behavior is similar to the experimental tests shown in [32]. $E_c$ is the compression modulus, which can be obtained by Eq. (4.16) for the compressible rubber material [34],

$$E_c = K \left( 1 - \frac{2}{\sqrt{\frac{48G}{K}} S} \frac{I_1 \left( \sqrt{\frac{48G}{K}} S \right)}{I_0 \left( \sqrt{\frac{48G}{K}} S \right)} \right) \tag{4.16}$$

In Eqs. (13) and (14), $l_s$ is the initial length of vertical springs element (top and bottom) which is calculated by [31],

$$\frac{E_c}{l_s} \sum_j A_j d_{s_j}^2 = \frac{\pi^2 E I_{eff}}{t_r} \tag{4.17}$$

$\delta\theta_t$ and $\delta\theta_b$ are rotation increment values which are applied gradually. They are

obtained by

$$\delta\theta_t = \frac{i\,\theta_t}{(u_{max}/\Delta u)\,m_2} \tag{4.18}$$

$$\delta\theta_b = \frac{i\,\theta_b}{(u_{max}/\Delta u)\,m_2} \tag{4.19}$$

where $u_{max}$ is the target lateral displacement of the bearing. $m_2$ is a modification factor to adjust the critical force. Since the bearing in this study did not experience instability, this value was assumed to be equal 1. Moreover, for the purposes of this study $\theta_b = 0$ and $\theta_t$ was a prescribed value.

As comparison of the experimental results and predictions of the mechanical model is presented later in the paper. Before that, the FEM used in this study is presented next.

## 4.5 3D FEA Model

A three-dimensional FEM of the bearing was developed in ABAQUS [29]. Rastgoo Moghadam and Konstantinids [6] showed that the result of a 3D FEM in which nonlinearities in materials and geometry were considered were in good agreement with an analytical solution proposed by Karbakhsh Ravari et al. [35]. The rubber layers were discretized with a combination of 8–node linear brick, hybrid, constant pressure elements (C3D8H) and 6–node linear triangular prism, hybrid, constant pressure elements (C3D6H) [29]. The steel shims and end plates were discretized with 8-node linear brick, incompatible modes elements (C3D8I) [29].

In this model, the compressible Neo-Hookean material was used for the rubber. This material model is defined by two parameters, $C_{10}$ and $D_1$, which for consistency with a linear elastic material are related to the shear modulus, $G$, and the bulk

modulus, $K$, through $C_{10} = G/2$, $D_1 = 2/K$. For the compressible Neo-Hookean model used in this study, the strain energy function is [36]:

$$W = C_{10}\left(\bar{I}_1 - 3\right) + \frac{1}{D_1}\left(J-1\right)^2 \tag{4.20}$$

where $\bar{I}_1$ is the the first modified invariant of the deviatoric part of the Cauchy-Green deformation tensor, and $J$ is the elastic volume ratio. The steel material was modeled using a bilinear isotropic material model with a Young's modulus of 200 GPa and a Poisson's ratio of 0.3. A post-yield modulus of 2 percent of the initial modulus was specified.

In the FEA model, all nodes of the top end plate were constrained to a point (control node) located at the centroid of the end plate. The boundary conditions were assigned to this node. To simulate the support conditions of the experimental setup, the control node was free to move vertically and, in the case of rotation, this node could rotate in the specified direction. Similar to the top end plate, all nodes at the bottom end plate were constrained to a control node. This point could move laterally in one direction but was restrained in all other degrees of freedom. The analysis was performed in two stages: during the first stage, the axial load but also rotations were imposed gradually until the desired values were reached; and in the second stage of the analysis, the horizontal displacement of bottom support was gradually increased while maintaining the axial load and rotation value from the first stage constant. The analysis included nonlinear geometry, large displacements, and large strains. The incremental nonlinear analysis was conducted using an updated Lagrangian formulation and the Newton-Raphson iteration method. Fig. 4.6 shows the deformed shape of the bearing using FEA and the procedure that was explained.

## 4.6 Results and Discussion

### 4.6.1 Summary of Experimental Results

To check how well axial load remained constant during testing, the summation of loads applied by actuators (Actuator[1]) was monitored. Fig. 4.7a shows the variation of the average vertical stress, $\bar{p} = P/A$, versus the shear strain, $u/t_r$. It is an example to show how the axial load remained constant during testing. As can be seen, $\bar{p}$ remained the same during the test, and equals to 6 MPa. The applied rotation was also constant during the test. The mechanism that was designed to keep the rotation angle constant during the test was discussed in Section 2.2. $\theta_t$ was monitored during the test by an inclinometer and shown in Fig. 4.7b. $\theta_t$ was supposed to be 0.02 rad during the shown cyclic test. Fig. 4.7b shows that the rotation angle was approximately constant during the test, noting that the maximum error was less than 5 % which was deemed acceptable.

Table 4.3 shows the experimental tests conducted on the bearing and presented in this paper. The leftmost column shows the name of each test, where 'c' and 'm' indicate the cyclic and monotonic testing, respectively. Fig. 4.8 shows the deformation of the bearing during testing under $\bar{p} = 8$ MPa at different horizontal displacements ($u/t_r = 0$, 1.5, 2.5) for different rotation angles ($\theta_t = 0$, 0.03 rad, where the rotation is clockwise). As can be seen, the deformed shape of the bearing at $u/t_r = 0$ and zero rotation shows the bulging effect on the left and right side of the bearing equally, while at $\theta_t = 0.03$ rad the bulging on the right side is more pronounced than the left side of the bearing; i.e. the right side of the bearing experiences larger pressure. As the bearing is subjected to lateral displacement, the difference in bulging is less

noticeable.

Fig. 4.9 shows the results of cyclic tests on the bearing under $\bar{p} = 6$, 7 and 8 MPa for $\theta_t = 0.00$ and 0.03 rad. As can be seen, the hysteresis loops are symmetric for the case of zero rotation; i.e. the absolute values of maximum and minimum shear force are equal. When the bearing is subjected to rotation, however, the behavior is not symmetric. The loops shift up, and the difference between the maximum and minimum force is obvious in comparison with the zero rotation case. Moreover, this difference becomes more pronounced when the axial load was increased. For example, the rotation (0.03 rad) increased the maximum shear force by 9.46, 10.49, and 16.75 percent for the bearing under $\bar{p} = 6$, 7 and 8 MPa, respectively. Similar behavior was observed for tests under different values of rotation. Since the top plate of the bearing was fixed in the lateral direction when the axial load and rotation were applied, the rotation causes a horizontal force. Consequently the bearing experienced lateral force even before applying any horizontal displacement on the bottom plate. This explains the reason for the shift in the hysteresis. This force referred to herein as the *Initial Force* can be noticed easily in the monotonic testing, which will be discussed later.

To ensure that the bearing was not damaged during each test, the monotonic test under zero rotation and $\bar{p} = 6$ MPa was selected as a benchmark (mp6r0 test in Table 4.3). This test was conducted periodically between tests, and the load–displacement curve was compared with that from the very first test to ensure that the two tests provided similar results. During the cyclic test in which the bearing was sheared up to $u/t_r = 3$, $\bar{p} = 9$ MPa, and $\theta_t = 0$ rad, as it is shown in Fig. 4.10, it was noticed that the second cycle, in the negative direction, was slightly different than the first one. It was suspected that the bearing was damaged during this test with excessive

lateral displacement. Therefore, the test was stopped and the bearing was removed from the setup to conduct visual inspection. Fig. 4.11 shows the bearing after the test. The surface of the bearing showed very large bulging near the top and bottom of the bearing. This bulging was permanent and visible even under zero vertical load. It should be noted that it was not clear where/what the damage was because of the presence of the cover, intended to protect the bearing from environmental factors.

In order to check whether that bearing was still usable after this test, the benchmark monotonic test under zero rotation and $\bar{p} = 6$ MPa was conducted. Fig. 4.12 shows the behavior of the bearing before and after the likely occurrence of damage. As can be seen, the curve corresponding to the latest test deviates from the benchmark curve, indicating a different initial stiffness. The authors believe that the combination of large axial load and excessive lateral displacement caused internal damage to the the bearing. However, the bearing was used to continue other tests under larger axial load. Following each test, the bearing was tested based on the new benchmark test and the results were compared with the 'After Damage' curve shown in Fig. 4.12. Comparison with the 'After Damage' curve showed no notable difference in the response. This suggests that the damage did not propagated further during additional experimental tests. It should be noted that the results presented in this paper are based on the experimental tests before the bearing was damaged.

### 4.6.2 Comparison with Analytical Results

Fig. 4.13 shows the comparison of the FEA results with the cyclic testing results under $\bar{p} = 6$, 7 and 8 MPa for $\theta_t = 0.00$, 0.01, and 0.02 rad. To obtain the FEA results in both positive and negative displacement, the bearing was sheared in both directions

separately. As can be seen, the FEA results predicted the initial lateral stiffness of the bearing with good accuracy. The FEA curve passes through approximately the middle of the loops, but as the rotation increases, the FEA curve touches the upper portion of the experimental loops. Moreover, in all the cases shown in Fig. 4.13, the FEA curves begin to deviate from the loops in large lateral displacements ($u/t_r > 2$). In addition, in this range of displacement, the stiffness predicted by FEA decreased (particularly for $\bar{p} = 8$ MPa). This could be a consequence of the modeling with Neo-Hookean material in which the shear modulus is constant. Past experimental tests [36], however, have shown that the shear modulus is not constant, especially at large shear displacement. Moreover, the stiffening in the actual rubber at large lateral displacement, as a consequence of the phenomenon known as strain-induced crystallization, could be another reason. As in the case of the experimental results, the FEA curve shifted up as the rotation value increased.

Fig. 4.14 compares the FEM and MM results with the monotonic testing results under $\bar{p} = 6$, 7 and 8 MPa for $\theta_t = 0.00$, 0.01 and 0.03 rad. As can be seen, the results in estimating the initial lateral stiffness are in a relatively good agreement. Moreover, the figure shows that there is a good agreement between the results in predicting the initial force due to the rotation. For example, the initial force for the bearing under $\bar{p} = 6$ MPa and $\theta_t = 0.01$ rad is 1.00, 0.82, and 0.68 kN predicted by the experimental test, FEA, and MM, respectively and it increases to 2.36, 1.90, and 1.86 kN for $\theta_t = 0.03$ rad. Following the previous discussion about the strain-induced crystallization, as the bearing experiences larger shear displacement, the experimental curve shows stiffening while the FEM and MM did not show this stiffening up to $u/t_r = 2.5$. Fig. 4.14 also shows that there is a good agreement between the results

in predicting the initial lateral stiffness. For example, the initial stiffness for the bearing under $\bar{p} = 6$ MPa and zero rotation is 203, 163, and 182 N/mm predicted by the experimental test, FEA, and MM, respectively and it decreases to 182, 140, and 177 N/mm for $\bar{p} = 8$ MPa. These values for the bearing under $\bar{p} = 8$ MPa and $\theta_t = 0.03$ rad are 162, 128, and 168 N/mm, respectively. It can be concluded that the rotation has a negligible effect on the initial stiffness, which is in agreement with the finding by Rastgoo Moghadam and Konstantinidis [6].

## 4.7 Conclusions

This study followed on experimental and analytical approach, including 3D FEA and analysis using a simple mechanical model, to investigate the behavior of elastomeric bearings under combined applied loading, which included vertical load, horizontal displacement and rotation. The paper described the experimental setup and controlling system used in this study. Two kinds of tests, quasi–static cyclic and monotonic tests were conducted on a 1/4-Scale bearing with the shape factor of 20 and second shape factor of 4. The experimental results using cyclic testing revealed that rotation causes the hysteresis loops to shift up. Increasing rotation angle and axial load accentuated this shifting. Finally, the bearing was tested under a large axial force and horizontal force and some evidence was provided that indicated the bearing might be damaged due the large axial force and/or horizontal displacement. A comparison between FEA and the cyclic test results showed that the FEA passes through approximately the middle of the hysteresis; however for the larger rotation and axial load, the FEA curve passes along the upper edge of the hysteresis loops. The results predicted by the mechanical model which was proposed by the authors in another study [7] and

summarized here were compared against the monotonic tests. The monotonic tests showed stiffening behavior in the rubber while the results from FEA and MM did not show the stiffening up to $u/t_r = 2.5$. However, both the FEM and Mechanical model predicted well the initial force due to the rotation.

## Acknowledgements

The authors would like to gratefully acknowledge the financial support of the Natural Sciences and Engineering Research Council of Canada (NSERC).

## References

[1] Buckle IG, Kelly JM. Properties of slender elastomeric isolation bearings during shake table studies of a large-scale model bridge deck. ACI Special Publication. 1986;94:247–270.

[2] Aiken ID, Kelly JM, Tajirian FF. Mechanics of low shape factor elastomeric seismic isolation bearings. Report UCB/EERC-89/13. Earthquake Engineering Research Center, University of California, Berkeley; 1989.

[3] Buckle IG, Liu H. Experimental determination of critical loads of elastomeric isolators at high shear strain. NCEER Bulletin. 1994;8(3):1–5.

[4] Buckle IG., Nagarajaiah S, Ferrell K. Stability of elastomeric isolation bearings: experimental Study. Journal of Structural Engineering. 2002;128(1):3–11.

[5] Kelly JM, Konstantinidis D. Mechanics of rubber bearings for seismic isolation and vibration isolation. Chichester: John Wiley & Sons; 2011.

[6] Rastgoo Moghadam S, Konstantinidis D. Finite element study of the effect of support rotation on the horizontal behavior of elastomeric bearings. Composite Structures. 2017;163:474–490.

[7] Rastgoo Moghadam S, Konstantinidis D. Study of the horizontal behavior of elastomeric bearings by simple mechanical models including the effect of support rotation. Submitted to Engineering Structures. 2017.

[8] Konstantinidis D, Rastgoo Moghadam S. Compression of unbonded rubber layers taking into account bulk compressibility and contact slip at the supports. International Journal of Solids and Structures. 2016;87:206–221.

[9] Stanton JF, Scroggins G, Taylor A, Roeder CW. Stability of laminated elastomeric bearings. Journal of Engineering Mechanics. 1990;116(6):1351–1371.

[10] Cardone D, Perrone G. Critical load of slender elastomeric seismic isolators: an experimental perspective. Engineering Structures. 2012;40:198–204.

[11] Weisman J, Warn GP. Stability of elastomeric and lead-rubber seismic isolation bearings. Journal of Structural Engineering. 2012;128(2):215–223.

[12] Sanchez J, Masroor A, Mosqueda G, Ryan KL. Static and dynamic stability of elastomeric bearings for seismic protection of structures. Journal of Structural Engineering. 2013;139(7):1149–1159.

[13] Koh CG, Kelly JM. Effects of axial load on elastomeric isolation bearings. Report UCB/EERC-86/12. Earthquake Engineering Research Center, University of California, Berkeley; 1987.

[14] Nagarajaiah S, Ferrell F. Stability of elastomeric seismic isolation bearings. Journal of Structural Engineering. 1999;125(9):946–954.

[15] Vemuru VSM, Nagarajaiah S, Masroor A, Mosqueda G. Dynamic lateral stability of elastomeric seismic isolation bearings. Journal of Structural Engineering. 2014;140(8):A4014014.

[16] Vemuru VSM, Nagarajaiah S, Mosqueda G. Coupled horizontal–vertical stability of bearings under dynamic loading. Earthquake Engineering & Structural Dynamics. 2016;45(6):913–934.

[17] Iizuka M. A macroscopic model for predicting large-deformation behaviors of laminated rubber bearings. Engineering Structures. 2000;22(4):323–334.

[18] Hongping Z, Zixiang Z, Fangyuan Z, Hui L, Xuan D. Horizontal mechanical behavior of elastomeric bearings under eccentric vertical loading: Full-scale tests and analytical modeling. Construction and Building Materials. 2016;125:574–584.

[19] Warn GP, Whittaker AS, Constantinou MC. Vertical stiffness of elastomeric and lead–rubber seismic isolation bearings. Journal of Structural Engineering. 2007;133(9):1227–1236.

[20] Konstantinidis D, Kelly JM, Makris N. Experimental investigation on the seismic response of bridge bearings. Technical Report EERC 2008-02. Earthquake Engineering Research Center, University of California, Berkeley; 2008.

[21] Warn GP, Whittaker AS. Vertical earthquake loads on seismic isolation systems in bridges. Journal of Structural Engineering. 2008;134(11):1696–1704.

[22] Burtscher SL, Dorfmann A. Compression and shear tests of anisotropic high damping rubber bearings. Engineering Structures. 2004;26(13):1979–1991.

[23] Ohsaki M, Miyamura T, Kohiyama M, Yamashita T, Yamamoto M, Nakamura N. Finite-element analysis of laminated rubber bearing of building frame under seismic excitation. Earthquake Engineering and Structural Dynamics. 2015;44(11):1881–1898.

[24] Crowder AP. Investigating substructure flexibility in column–top isolation systems with elastomeric bearings. Master Thesis. McMaster University, Hamilton; 2016.

[25] Crowder AP, Becker TC. Effects of non-traditional isolator placement for seismic retrofit. Canadian Society of Civil Engineering, Resilient Infrastructure. London, ON, June 1–4, 2016.

[26] Constantinou MC, Kalpakidis I, Filiatrault A, Ecker Lay RA LRFD-based analysis and design procedures for bridge bearings and seismic isolators. Technical Report MCEER-11-0004. Multidisciplinary Center for Earthquake Engineering Research. University at Buffalo, State University of New York; 2011.

[27] Van Engelen NC, Konstantinidis D, Tait MJ. Shear strain demands in elastomeric bearings subjected to rotation. Journal of Engineering Mechanics. 2017;04017005.

[28] Bridgestone, Inc. Base isolation manual. Bridgestone Engineered Products Company, Inc., Nashville; 1999.

[29] Dassault Systèmes Simulia Corp. ABAQUS/CAE Version 6.10-1, Providence; 2010.

[30] Montuori GM, Mele G, Marrazzo G, Brandonisio G, De Luca A. Stability issues and pressure–shear interaction in elastomeric bearings: the primary role of the secondary shape factor. Bulletin of Earthquake Engineering. 2016;14(2):569–597.

[31] Han X, Warn GP. Mechanistic model for simulating critical behavior in elastomeric bearings. Journal of Structural Engineering. 2014;139(12):04014140.

[32] Kumar M, Whittaker A, Constantinou MC. An advanced numerical model of elastomeric seismic isolation bearings. Earthquake Engineering & Structural Dynamics. 2014;43(13):1955-1974.

[33] Gent AN. Cavitation in rubber: a cautionary tale. Rubber Chemistry and Technology. 1990;63(3):49–53.

[34] Chalhoub MS, Kelly JM. Effect of bulk compressibility on the stiffness of cylindrical base isolation bearings. International Journal of Solids and Structures. 1990;26(7):743–760.

[35] Karbakhsh Ravari A, Othman I,B Ibrahim ZB, Ab-Malek K. P-$\Delta$ and end rotation effects on the influence of mechanical properties of elastomeric isolation bearings. Journal of Structural Engineering. 2012;138(6):669–675.

[36] Bathe KJ. Finite Element Procedures. New York: Prentice Hall; 1995.

Table 4.1: Properties of the bearing used in this study.

| Property | Symbol | Unit | Value |
|---|---|---|---|
| Diameter | $D$ | mm | 158 |
| Thickness of individual rubber layer | $t$ | mm | 2.0 |
| Thickness of individual steel shim | $t_s$ | mm | 1.0 |
| Number of rubber layers | $n_r$ | - | 20.0 |
| Shape factor | $S$ | - | 20 |
| Second shape factor | $S_2$ | - | 4.0 |
| Shear modulus | $G$ | MPa | 0.4 |
| Bulk modulus | $K$ | MPa | 1200 |

Table 4.2: Instrumention and equipment used in the experimental setup.

| Instrument | Company | Model |
|---|---|---|
| Load cell | Interface | 1020 |
| Actuator[1] | Shur–Lift | 4x18 Utility |
| Actuator[2] | Enerpac | RSM-500 |
| Actuator[3] | Shur–Lift | 2.5x12 Implement |
| Inclinometer | Measurement Specialties | NS-5/DMG2-U |
| Data Acquisition | Agilent | 34970A |
| Control System | MTS | FlexTest GT |

Table 4.3: Experimental tests conducted on the rubber bearing.

| Test | $\bar{p}$ (MPa) | $u_{max}/t_r$ | $\theta_t$ (rad) |
|---|---|---|---|
| cp6r0 | 6 | 2.5 | 0.00 |
| cp6r1 | 6 | 2.5 | 0.01 |
| cp6r2 | 6 | 2.5 | 0.02 |
| cp6r3 | 6 | 2.5 | 0.03 |
| mp6r0 | 6 | 2.5 | 0.00 |
| mp6r1 | 6 | 2.5 | 0.01 |
| mp6r2 | 6 | 2.5 | 0.02 |
| mp6r3 | 6 | 2.5 | 0.03 |
| cp7r0 | 7 | 2.5 | 0.00 |
| cp7r1 | 7 | 2.5 | 0.01 |
| cp7r2 | 7 | 2.5 | 0.02 |
| cp7r3 | 7 | 2.5 | 0.03 |
| mp7r0 | 7 | 2.5 | 0.00 |
| mp7r1 | 7 | 2.5 | 0.01 |
| mp7r2 | 7 | 2.5 | 0.02 |
| mp7r3 | 7 | 2.5 | 0.03 |
| cp8r0 | 8 | 2.5 | 0.00 |
| cp8r1 | 8 | 2.5 | 0.01 |
| cp8r2 | 8 | 2.5 | 0.02 |
| cp8r3 | 8 | 2.5 | 0.03 |
| mp8r0 | 8 | 2.5 | 0.00 |
| mp8r1 | 8 | 2.5 | 0.01 |
| mp8r2 | 8 | 2.5 | 0.02 |
| mp8r3 | 8 | 2.5 | 0.03 |
| mp9r0 | 9 | 3 | 0.00 |

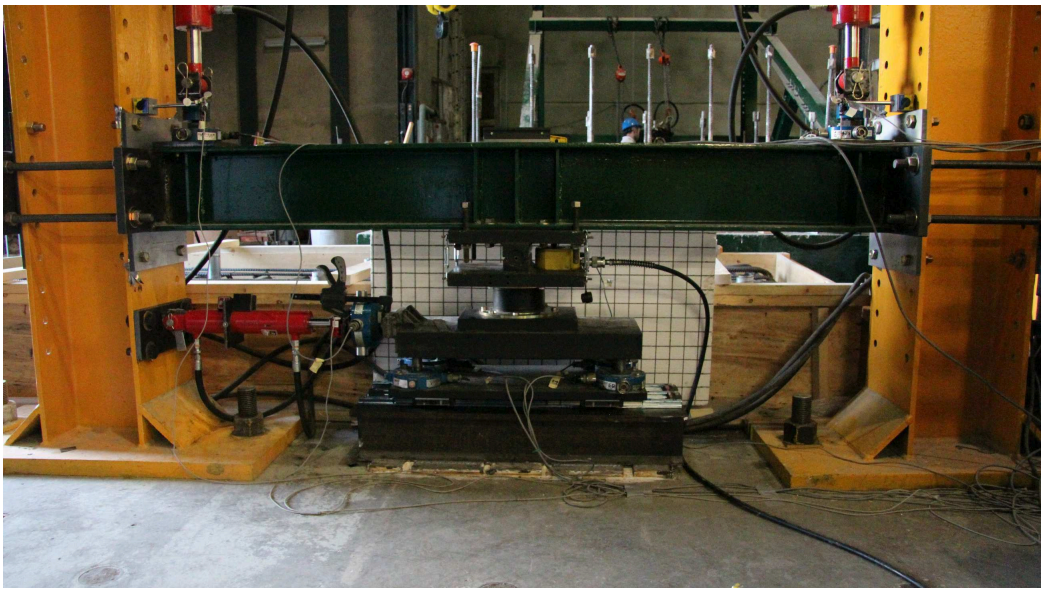

Figure 4.1: Completed setup with the elastomeric bearing installed.

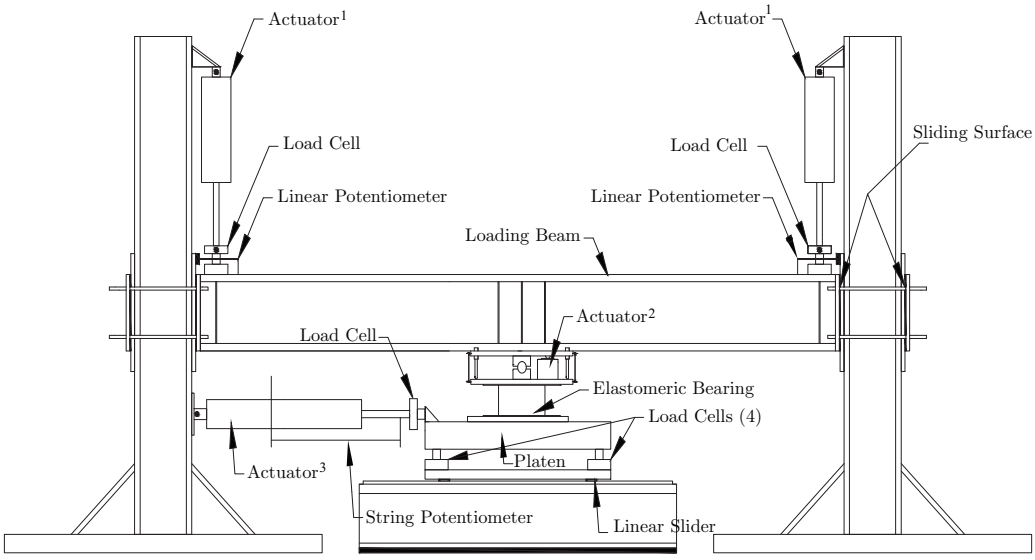


Figure 4.2: Schematic of the experimental setup.

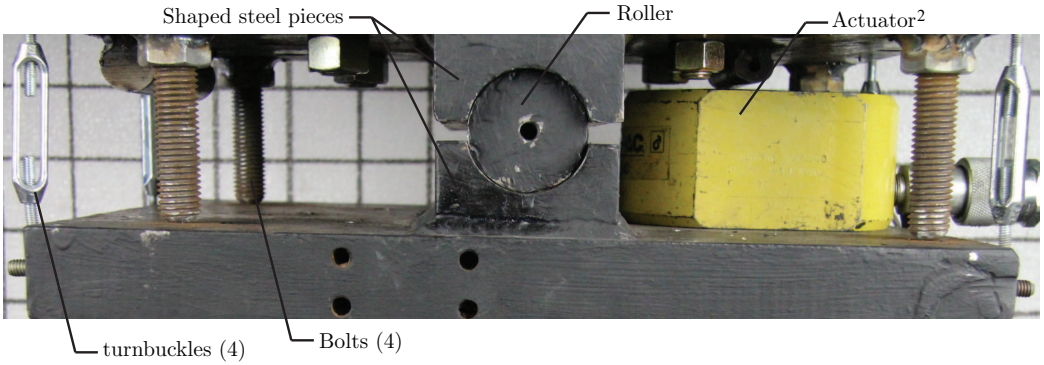


Figure 4.3: Designed mechanism to apply the rotation on the top of the elastomeric bearing.

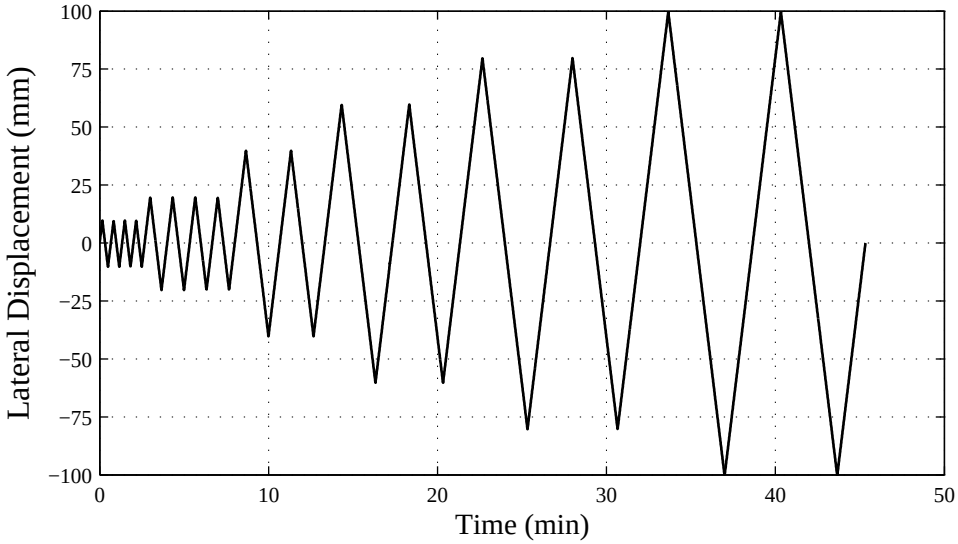


Figure 4.4: Lateral displacement history used for cyclic test.

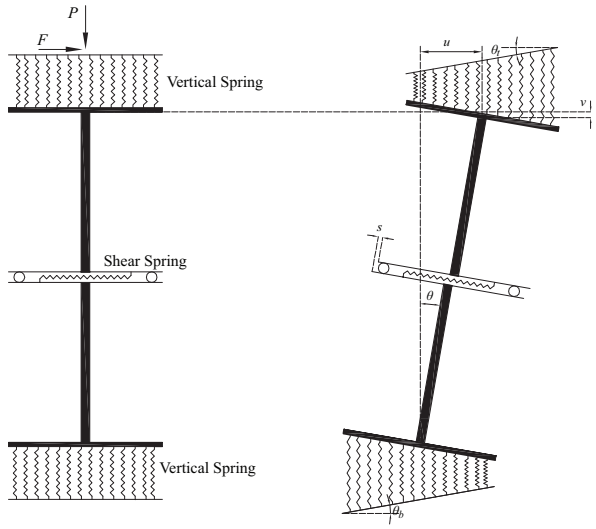


Figure 4.5: Illustration of the Mechanical Model (MM) in the laterally undeformed and deformed shape.

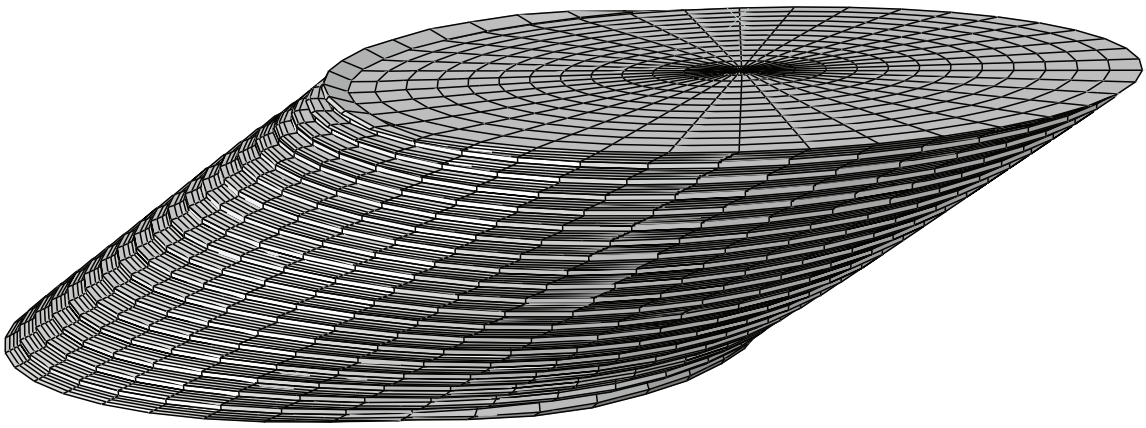

Figure 4.6: Deformed shape of the bearing using FEA.

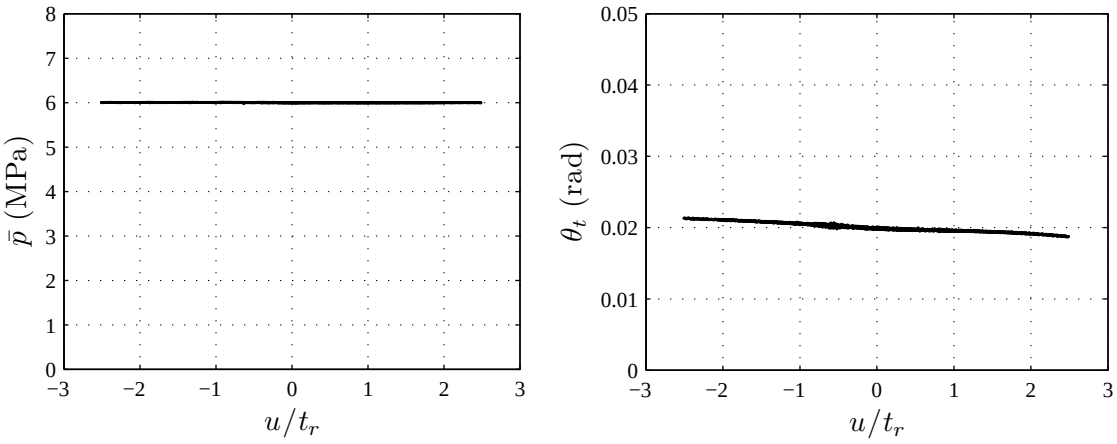


Figure 4.7: Variation of (a) the average vertical stress ($\bar{p}$), and (b) the applied rotation on the top of the bearing ($\theta_t$) versus the shear strain ($u/t_r$).

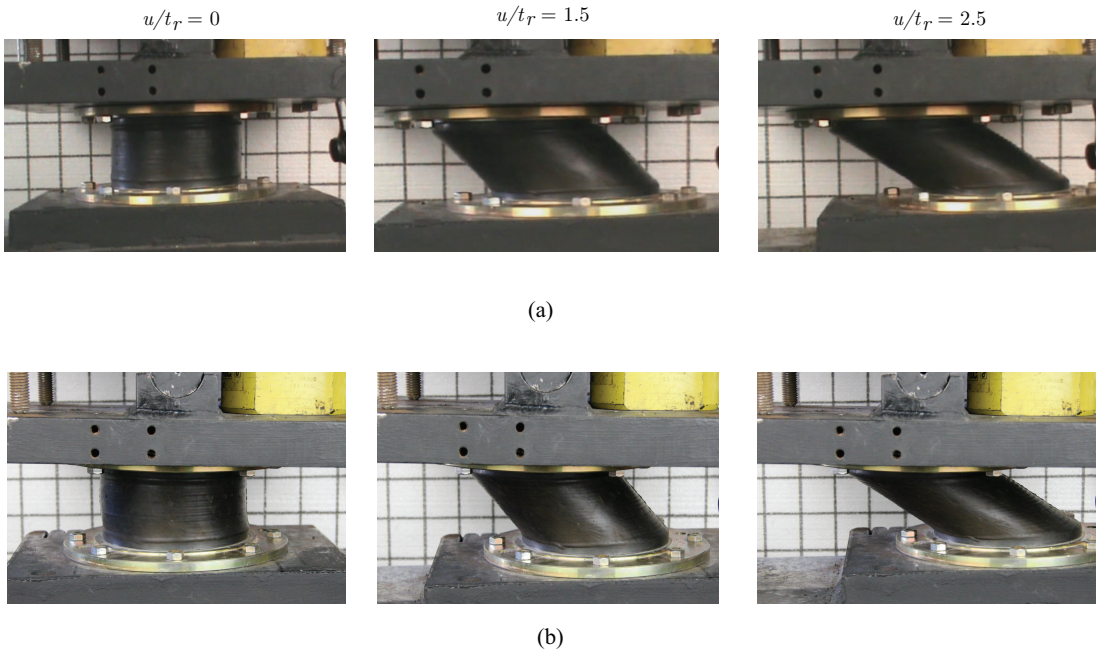


Figure 4.8: Snapshot photographs of the bearing at different displacement levels taken during two tests: (a) $\theta_t = 0.00$ and (b) $\theta_t = 0.03$ rad ($\bar{p} = 8$ MPa in both tests).

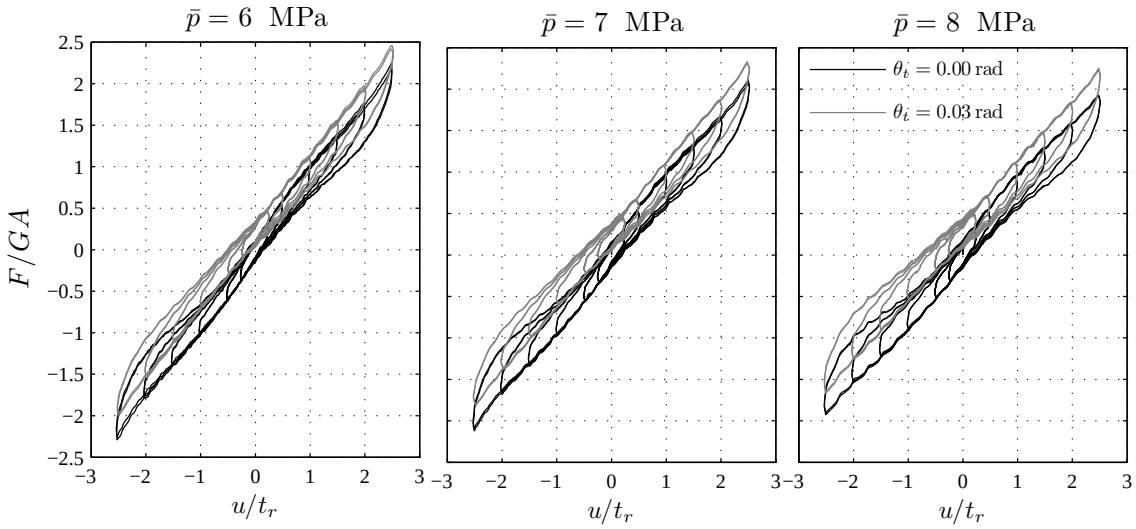


Figure 4.9: Cyclic testing on the bearing under $\bar{p} = 6$, 7 and 8 MPa for $\theta_t = 0.00$ and 0.03 rad.

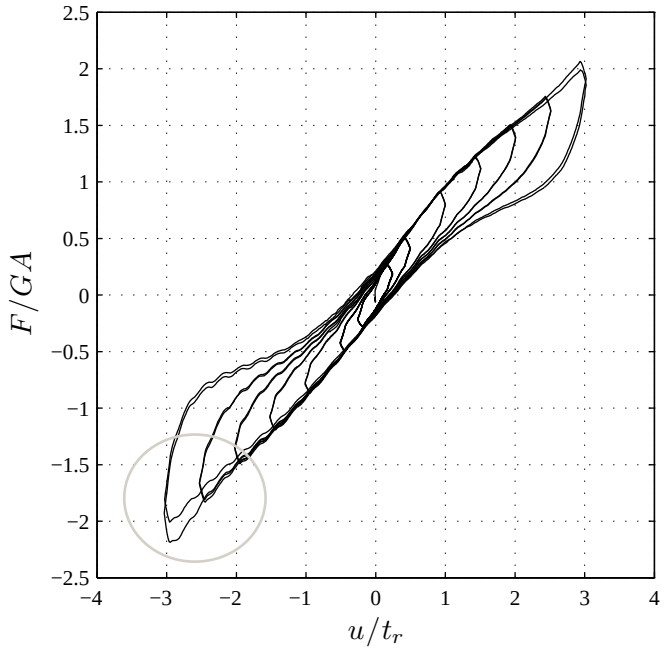


Figure 4.10: Cyclic testing on the bearing under $\bar{p} = 9$ MPa for $\theta_t = 0.00$ rad.

Figure 4.11: Photograph taken after a test with $u/t_r = 3$ and under $\bar{p} = 9$ MPa. Excessive rubber bulging is apparent on the top and bottom of the bearing, indicating likely damage in the interior.

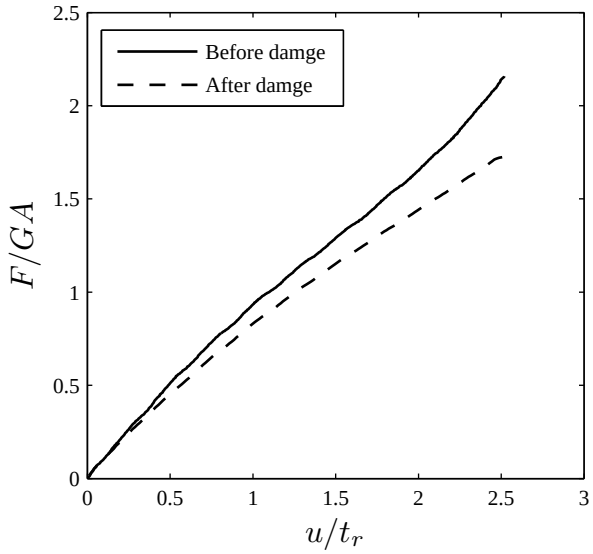


Figure 4.12: Comparison of the behavior of the bearing obtained from benchmark tests ($\theta_t = 0$ rad, $\bar{p} = 6$ MPa) conducted before and after the damage observed under the test with $u/t_r = 3$, $\theta_t = 0$ rad, and $\bar{p} = 9$ MPa.

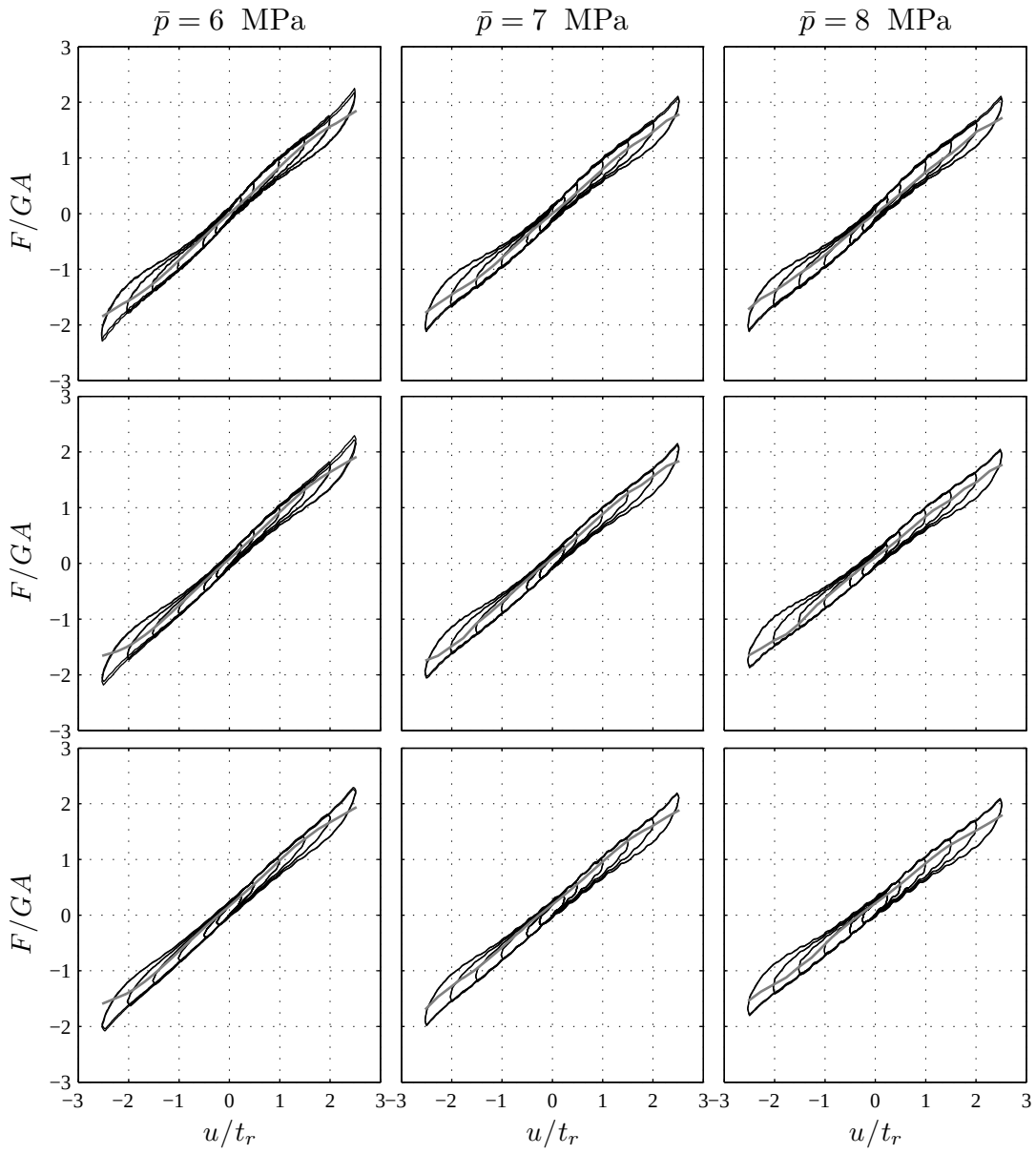


Figure 4.13: Comparison of the FEA results with the cyclic testing results under $\bar{p} = 6$, 7 and 8 MPa for $\theta_t = 0.00$ rad (top row), 0.01 rad (middle row), and 0.02 rad (bottom row).

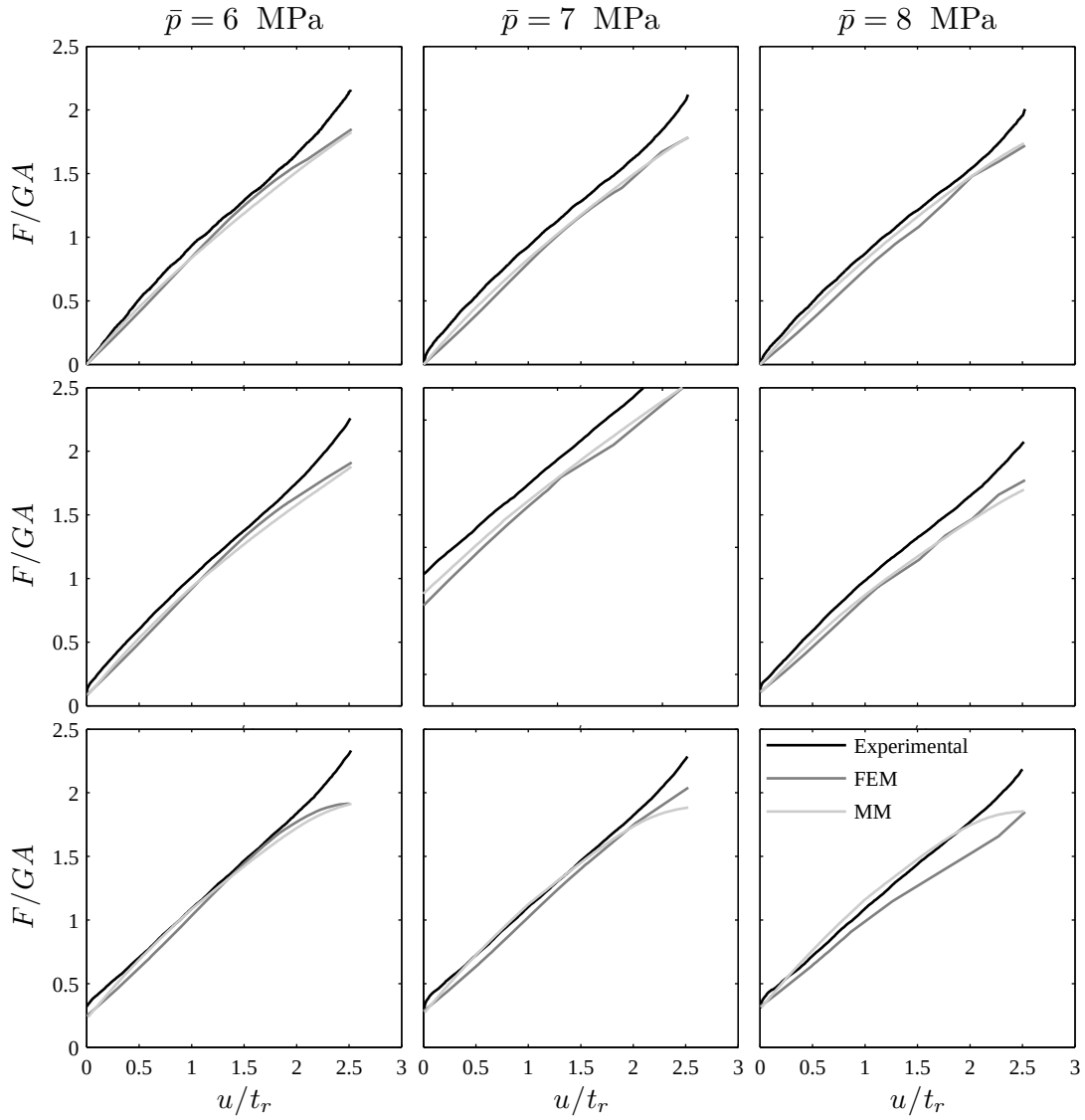


Figure 4.14: Comparison of the monotonic testing results with the FEM and MM results under $\bar{p} = 6$, 7 and 8 MPa for $\theta_t = 0.00$ rad (top row), 0.01 rad (middle row), and 0.03 rad (bottom row).

# Chapter 5

# Compression of Unbonded Rubber Layers Taking into Account Bulk Compressibility and Contact Slip at the Supports



Konstantinidis D, Rastgoo Moghadam S. Compression of unbonded rubber layers taking into account bulk compressibility and contact slip at the supports. *International Journal of Solids and Structures*, 2016; 87: 206–221.

## 5.1 Abstract

The behavior of rubber layers under pure compression has been investigated to considerable extent in the literature. The most widely used approach is the so-called *pressure solution*, which is based on several assumptions, most notably that the stress state is dominated by the hydrostatic pressure. Other approaches have also been considered, but for nearly incompressible material and thin layers their predictions are very similar to those of the pressure solution. Nearly all past studies on the subject have focused on rubber layers that are bonded to either rigid or flexible supports (or reinforcement). Unreinforced (i.e., single layer) rubber pads are often installed as unbonded, i.e., without steel end plates connecting them to their top and bottom supports. In an unbonded application, rubber pads rely solely on friction to develop shear resistance along the contact interfaces. This shear resistance is necessary to provide the pad with an adequately large vertical stiffness. The effect of the frictional restraint along the top and bottom contact surfaces and the influence of partial slip have received very little attention. In this paper, we present a theoretical analysis for the behavior of an unbonded rubber layer, including the effects of the elastomer's bulk compressibility and the contact slip at the supports. Results of a finite element analysis are also presented and shown to be in good agreement with the results of the theoretical analysis.

## 5.2 Introduction

Rubber bearings are used in a broad range of engineering applications, including buildings, bridges, storage tanks, railways, etc. Early applications date back to mid-nineteenth century when 50-mm thick rubber mats were installed to reduce railway vibration on the Britannia and Conwy Bridges in Wales (Ab-Malek and Roberts, 2013). Over time, the use of rubber bearings grew and extended to various new applications; most notably, they are currently used widely to accommodate deformations associated with thermal expansion/contraction, traffic loads and construction misalignment in bridges (Stanton and Roeder, 1982; Constantinou et al., 2011), to isolate equipment and structures from vibration and shock (Snowdon, 1979), and to seismically isolate structures (Naeim and Kelly, 1999; Constantinou et al., 2007; Kelly and Konstantinidis, 2011).

The first attempt to predict the compression stiffness of a rubber layer bonded to rigid supports was made by Rocard (1937) using an energy approach. Further developments were made by Gent and Lindley (1959) who derived expressions for the compressive stiffness of long-strip and circular elastic layers bonded to rigid plates, assuming incompressible material. Gent and Meinecke (1970) extended the analysis and presented an expression for the compression modulus of a square-shape elastic layer. Lindley (1979) applied the energy method to extend the theory for incompressible material to compressible elastic layers.

The approach widely used to estimate the compression stiffness of rubber layers bonded to rigid supports originates from the work of Gent and Lindley (1959) and has since come to be known as the *pressure solution*. The pressure solution is based on four assumptions (two kinematic and two on the state of stress): (i) points on a vertical line

before deformation lie on a parabola after loading (*parabolic bulging*); (ii) horizontal planes remain horizontal; (iii) the stress state is assumed to be dominated by the internal pressure, $p$ (which gives the solution its name), such that the normal stress components are all approximately equal to $-p$; and (iv) the in-plane shear stresses (in the plane parallel to the end supports) are negligible (Kelly and Konstantinidis, 2011). Although it was first used for incompressible material, it was later extended to include bulk compressibility effects. Expressions for the compression stiffness of rubber layers including compressibility have been developed for rubber layers with various geometries: circular (Chalhoub and Kelly, 1990), annular (Constantinou et al., 1992), infinite-strip (Chalhoub and Kelly, 1991), square (Koh and Kelly, 1989; Kelly, 1997), rectangular (Koh and Lim, 2001; Kelly and Konstantinidis, 2011).

Various efforts have been made to remove the assumptions of the pressure solution. For instance, Koh and Kelly (1989) used only the two kinematic assumptions of the pressure solution (i.e., removing the normal stress assumption) and a variable transformation method to develop solutions for the compression modulus of a square layer bonded to rigid supports. The same approach was applied by Koh and Lim (2001) to a rectangular layer. Tsai and Lee (1998) proposed an approach that eliminated the normal stress assumption and used *mean* pressure, instead, to derive expressions for infinite-strip, circular and square elastic layers bonded to rigid supports. Tsai (2005) applied this approach to a rectangular layer, developing a single series solution for the compression modulus.

Papoulia and Kelly (1996) followed an approach using the minimum potential energy and Hellinger–Reissner variational principles to estimate the compression modulus of nearly incompressible elastic layers. Pinarbasi et al. (2006) developed an

analytical solution based on a modified version of the Galerkin method for the analysis of infinite-strip elastic layers bonded to rigid supports. The order of the theory is based on the number of shape functions considered in the displacement expansions. The method was applied to circular and annular layers in Pinarbasi et al. (2008). The formulations in these studies are applicable to elastic material with a broad range of Poisson's ratio, but they converge to the pressure solution for large values of Poisson's ratio (or large bulk-to-shear modulus ratio), especially for layers with larger shape factor, $S$ (defined as the ratio of the loaded area to the load-free area that is free to bulge) (Papoulia and Kelly, 1996). Therefore, the pressure solution provides accurate results for rubber layers with, say, $S > 5$ (Kelly, 1997).

The aforementioned studies developed solutions for the compression modulus of rubber layers under the assumption that the layers are bonded to *rigid* supports. Osgooei et al. (2014) showed that these solutions, developed for single layers, provide accurate estimates of the compression stiffness of a multilayer rubber bearing reinforced with steel shims by treating the layers as springs in series. The development of fiber-reinforced laminated rubber bearings has prompted various investigations on the compressive behavior of rubber layers bonded to axially *flexible* supports, representing the fiber reinforcement. To achieve this, Kelly (1999) proposed a pressure solution approach whereby the assumed displacement field is modified to include the stretch of the reinforcement. The approach was used, assuming incompressible material, to develop solutions for infinite-strip-shaped Kelly (1999), circular-shaped (Tsai and Kelly, 2001) and rectangular-shaped (Tsai and Kelly, 2001, 2002) layers. The effect of bulk compressibility was later included to develop solutions for rubber layers bonded to flexible supports for different geometries: infinite strip (Kelly, 2002; Kelly

and Takhirov, 2002), rectangular (Angeli et al., 2013; Kelly and Van Engelen, 2015), annular (Pinarbasi and Okay, 2011), and circular (Kelly and Calabrese, 2013). (Tsai, 2004, 2006) relaxed the normal stress assumption of the pressure solution to develop solutions for infinite strip and circular elastic layers bonded to flexible reinforcement. The compression stiffness of a laminated rubber bearing was estimated by taking into account the fact that layers in the middle portion of the bearing will extend laterally more than those closer to the top and bottom supports through the introduction of an assumed parabolic shape. Pinarbasi and Mengi (2008) extended the approach presented in (Pinarbasi et al., 2006) to infinite-strip-shaped elastic layers bonded to extensible reinforcement.

In all these studies, aimed at quantifying the compressive characteristics of rubber layers, it is assumed that the layers are bonded to either rigid or flexible reinforcement. The intent is usually to provide the compression modulus of a layer, which can then be used to compute the compressive stiffness of a laminated steel- or fiber-reinforced rubber bearing. The resulting solutions are appropriate for bearings that are bonded to steel end plates, as is the case almost always for seismic isolators. However, rubber bearings are very commonly used in unbonded applications. Under unbonded boundary conditions, the friction between the rubber and the top and bottom supports of the bearing is responsible for the development of shear stresses under pure compressive load. These surface shear stresses, $\tau_s$, increase outwardly towards the edges of layer, while the pressure, $p$, decreases. If the rubber–support interfaces are characterized by Coulomb friction with coefficient of friction $\mu$, the surface shears are limited to$\tau_s \leqslant \mu p$, which means that at some point slip must occur. Although friction in rubber is relatively high, smooth support surfaces or the introduction of

some level of lubrication, either intentionally or accidentally, can reduce the frictional restraint along the support–rubber interfaces, resulting in slip and a reduction in the compression modulus. Kelly and Konstantinidis (2009) investigated the effect of slip on the compression properties of a single rubber layer restrained by friction along its top and bottom supports, as well as on a rubber layer bonded to a rigid support on one end (representing a steel shim) but restrained by friction on the other. The study focused on infinite-strip-shaped layers of incompressible rubber and concluded that slip can significantly reduce the compression modulus of the layer. later that, this conclusion has been confirmed by Rastgoo Moghadam and Konstantinidis (2014) using Finite Element method. For unbonded multilayer rubber bearings, especially with only a few layers, this can in turn result in an appreciable reduction in the overall vertical stiffness of the bearing.

Various analytical and experimental studies (Gent and Lindley, 1959; Koh and Kelly, 1989; Kelly and Konstantinidis, 2011) have pointed out that consideration of the bulk compressibility of the elastomer in the compression analysis of rubber layers can have a significant effect on the pressure distribution, the maximum shear strain which is developed by the constraint of the rigid supports on the top and bottom of the bonded rubber layer, and the compression modulus, especially for bearings with large shape factor (Kelly and Konstantinidis, 2011; Van Engelen et al., 2016). This paper presents a theoretical analysis of the compression behavior of strip and circular rubber layers taking into account bulk compressibility and contact slip at the supports. Fig. 5.1 shows a photograph of a typical thin rubber pad. The analysis presented herein is for a single-layer pad restrained by Coulomb friction at the top and bottom supports, while the compressive behavior of a friction-restrained multilayer

bearing with compressible material will be investigated in a future study. Although the description of a rubber–steel or rubber–concrete interface by a simple Coulomb friction model may not be entirely accurate (Konstantinidis et al., 2008), it makes the problem amenable to theoretical investigation. Finally, the paper presents results of a finite element analysis and compares them against the predictions of the theoretical solution.

## 5.3 Compression of a Rubber Layer Bonded to Rigid Supports

In this section, we briefly review the compression of a rubber layer bonded to rigid supports, as several parts of the theory will be used later in dealing with the unbonded layer. The rubber is assumed to behave as a linear elastic material, and bulk compressibility is included in the analysis. A pressure solution approach is followed, the kinematic and stress assumptions of which have been stated in the Introduction, and further details can be found in (Kelly, 1997). We consider an arbitrarily shaped pad of thickness $t$ and position a Cartesian coordinate system, $(x, y, z)$, with the origin at mid-height of the layer. Under the assumptions of the pressure solution, the displacements $\mathbf{u} = (u, v, w)$ in the coordinate directions are

$$u(x, y, z) = u_0(x, y)\left(1 - \frac{4z^2}{t^2}\right) \tag{5.1a}$$

$$v(x, y, z) = v_0(x, y)\left(1 - \frac{4z^2}{t^2}\right) \tag{5.1b}$$

$$w(x, y, z) = w(z) \tag{5.1c}$$

For compressible material, $\nabla \cdot \mathbf{u} = \epsilon_{xx} + \epsilon_{yy} + \epsilon_{zz} = -p/K$, where $\epsilon_{xx} = \partial_x u$, $\epsilon_{yy} = \partial_y v$, $\epsilon_{zz} = \partial_z w$ [where the $\partial$ denotes partial derivative with respect to the subscripted variable], $p$ is pressure, and $K$ is the bulk modulus. This leads to

$$\partial_x u + \partial_y v + \partial_z w = (\partial_x u_0 + \partial_y v_0)\left(1 - \frac{4z^2}{t^2}\right) + w' = -p/K \tag{5.2}$$

where the prime denotes ordinary derivative. When integrated through the thickness $(-t/2, t/2)$, this gives

$$\partial_x u_0 + \partial_y v_0 = \frac{3}{2}\left(\epsilon_c - p/K\right) \tag{5.3}$$

where $\Delta$ is the change of thickness of the pad (with $\Delta > 0$ indicating compression), and $\epsilon_c = \Delta/t$ is the compression strain.

The complete equilibrium equations in Cartesian coordinates are

$$\partial_x \sigma_{xx} + \partial_y \tau_{xy} + \partial_z \tau_{xz} = 0 \tag{5.4a}$$

$$\partial_x \tau_{yx} + \partial_y \sigma_{yy} + \partial_z \tau_{yz} = 0 \tag{5.4b}$$

$$\partial_x \tau_{zx} + \partial_y \tau_{zy} + \partial_z \sigma_{zz} = 0 \tag{5.4c}$$

Under the assumptions of the pressure solution, the stress state is dominated by the pressure, $p$. The normal stressed deviate from $-p$ only by terms of order $t^2/l^2$, i.e., $\sigma_{xx} \approx \sigma_{yy} \approx \sigma_{zz} \approx -p(1 + \mathrm{O}(t^2/l^2))$, where $l$ is a characteristic length in the $x$-$y$ plane. The shear stress components $\tau_{xz}$ and $\tau_{yz}$ are of order $(t/l)p$. The in-plane shear stress $\tau_{xy}$ is of order $(t^2/l^2)p$ and thus negligible in this analysis. Under these

assumptions, the first two equations reduce to

$$\partial_z \tau_{xz} = \partial_x p \tag{5.5a}$$

$$\partial_z \tau_{yz} = \partial_y p \tag{5.5b}$$

For a linear elastic material, $\tau_{xz} = G\gamma_{xz}$ and $\tau_{yz} = G\gamma_{yz}$, where $G$ is the shear modulus. Since $\gamma_{xz} = \partial_z u + \partial_x w$ and $\gamma_{yz} = \partial_z v + \partial_y w$,

$$\tau_{xz} = -\frac{8G}{t^2} z u_0 \tag{5.6a}$$

$$\tau_{yz} = -\frac{8G}{t^2} z v_0 \tag{5.6b}$$

or, from Eq. (5.5),

$$\partial_x p = -\frac{8G}{t^2} u_0 \tag{5.7a}$$

$$\partial_y p = -\frac{8G}{t^2} v_0 \tag{5.7b}$$

Differentiating the first of these equations with respect to $x$, the second with respect to $y$, and adding the two resulting equations gives

$$\nabla^2 p = \partial_{xx} p + \partial_{xy} p = -\frac{8G}{t^t} \left(\partial_x u + \partial_y v\right) \tag{5.8}$$

and substituting Eq. (5.3) into this expression gives the Helmholtz equation with imaginary wavenumber:

$$\nabla^2 p - \lambda^2 p = -\lambda^2 K \epsilon_c \tag{5.9}$$

where $\lambda^2 = 12G/(Kt^2)$. The Dirichlet boundary condition $p = 0$ on the edges of the

pad completes the system for $p(x, y)$.

For an infinitely long strip pad of width $2b$, as shown in Fig. 5.2(a), Eq. (5.9) reduces to $p'' - \lambda^2 p = -\lambda^2 K\epsilon_c$, which with $p(x = \pm b) = 0$ gives

$$p(x) = K\epsilon_c \left(1 - \frac{\cosh(\lambda x)}{\cosh(\lambda b)}\right) \tag{5.10}$$

Integrating $p$ over the area of the pad (considering a unit depth), $A = 2b$ gives the compressive force $P$

$$P = 2K\epsilon_c b \left(1 - \frac{1}{\lambda b}\tanh(\lambda b)\right) \tag{5.11}$$

The *compressive modulus* of the rubber layer, defined as $E_c = P/(A\epsilon_c)$, is

$$E_c = K \left(1 - \frac{1}{\lambda b}\tanh(\lambda b)\right) \tag{5.12}$$

In terms of the shape factor, $S$ ($= b/t$ for an infinite strip), we have $\lambda b = \sqrt{\frac{12G}{K}}S$, and Eq. (5.12) can be expressed as

$$E_c = K \left(1 - \frac{\tanh\left(\sqrt{\frac{12G}{K}}S\right)}{\sqrt{\frac{12G}{K}}S}\right) \tag{5.13}$$

At this point, it would be useful to investigate the behavior along the upper and lower surfaces, $z = \pm t/2$. With reference to Fig. 5.3, integration of Eq. (5.5a) through the thickness of the layer gives

$$\tau_s = -\frac{t}{2}p' = \frac{\lambda t}{2}K\epsilon_c \frac{\sinh(\lambda x)}{\cosh(\lambda b)} \tag{5.14}$$

which increases monotonically with $x$. On the other hand, Eq. (5.10) suggests that

the $p$ decreases with increasing $x$. If the constraint were controlled only by friction, that is by $\tau_s \leqslant \mu p$ where $\mu$ is friction coefficient, at some point slip would occur. For incompressible material, the equality of $\tau_s$ and $\mu p$ would give (Kelly and Konstantinidis, 2009)

$$\frac{x}{b} = \sqrt{1 + \frac{1}{4\mu^2 S^2}} - \frac{1}{2\mu S} \tag{5.15}$$

and for compressible material,

$$\frac{\lambda t}{2\mu} \frac{\sinh(\lambda x)}{\cosh(\lambda b)} = 1 - \frac{\cosh(\lambda x)}{\cosh(\lambda b)} \tag{5.16}$$

An important quantity in the design of rubber pads is the maximum shear strain that results due to by the rigid constraint at the top and bottom of the layer. The surface shear, given by Eq. (5.14), with the assumption of linear elastic material, gives the variation of shear strain (neglecting sign) along $z = \pm t/2$

$$\gamma = \epsilon_c \sqrt{\frac{3K}{G}} \frac{\sinh\left(\sqrt{\frac{12G}{K}} S \frac{x}{b}\right)}{\cosh\left(\sqrt{\frac{12G}{K}} S\right)} \tag{5.17}$$

from which it can be seen that the peak occurs at $x = b$ and is equal to

$$\gamma_{max} = \epsilon_c \sqrt{\frac{3K}{G}} \tanh\left(\sqrt{\frac{12G}{K}} S\right) \tag{5.18}$$

The peak strain occurring at $x = b$ is an inconsistency of the pressure solution. In reality, the peak strain occurs just before the free edge, and $\gamma$ very rapidly drops to zero at the free edge.

For a circular pad (as shown in Fig. 5.2(b)) with radius, $R$, and thickness, $t$,

under pure compression, the pressure is a function of the radial distance $r$ only, and Eq. (5.9) becomes

$$p'' + \frac{1}{r}p' - \lambda^2 p = -\lambda^2 K \varepsilon_c \tag{5.19}$$

which, with finite $p(r=0)$ and $p(r=R)=0$, gives

$$p\left(r\right) = K\epsilon_c \left(1 - \frac{I_0\left(\lambda r\right)}{I_0\left(\lambda R\right)}\right) \tag{5.20}$$

where $I_0$ is the zeroth-order modified Bessel function of the first kind. Integrating $p$ over the area of the pad gives the compression force $P$:

$$P = K\epsilon_c \pi R^2 \left(1 - \frac{2}{\lambda R}\frac{I_1\left(\lambda R\right)}{I_0\left(\lambda R\right)}\right) \tag{5.21}$$

where $I_1$ is the first-order modified Bessel function of the first kind. The compression modulus in terms of the shape factor $S$ ($= R/(2t)$ for a circular layer) is

$$E_c = K\left[1 - \frac{2}{\sqrt{\frac{48G}{K}}S}\frac{I_1\left(\sqrt{\frac{48G}{K}}S\right)}{I_0\left(\sqrt{\frac{48G}{K}}S\right)}\right] \tag{5.22}$$

The shear strain along $z = \pm t/2$, is given by

$$\gamma = \epsilon_c \sqrt{\frac{3K}{G}}\frac{I_1\left(\sqrt{\frac{48G}{K}}S\frac{r}{R}\right)}{I_0\left(\sqrt{\frac{48G}{K}}S\right)} \tag{5.23}$$

from which it can be seen that the peak shear strain occurs at $r = R$ and is equal to

$$\gamma_{max} = \epsilon_c \sqrt{\frac{3K}{G}} \frac{I_1\left(\sqrt{\frac{48G}{K}} S\right)}{I_0\left(\sqrt{\frac{48G}{K}} S\right)} \tag{5.24}$$

## 5.4 Compression of an Infinite-Strip Rubber Layer with Surface Slip

The analysis follows a pressure solution approach where the originally assumed displacement field, given by Eq. (5.1), is supplemented by an additional term $u_1$ that is constant through the thickness of the layer and is intended to account for the slip (see Fig. 5.4). The assumed displacement field is

$$u(x,z) = u_0(x)\left(1 - \frac{4z^2}{t^2}\right) + u_1(x) \tag{5.25a}$$

$$w(x,z) = w(z) \tag{5.25b}$$

where $u_1(x) = 0$ for $0 \leqslant x \leqslant x_1$, with $x_1$ being the location where slip starts.

For this displacement field, $\epsilon_{xx} + \epsilon_{yy} + \epsilon_{zz} = -p/K$ leads to

$$u_0' + \frac{3}{2}u_1' = \frac{3}{2}\left(\epsilon_c - \frac{p}{K}\right) \tag{5.26}$$

From Eq. (5.7),

$$p' = -\frac{8G}{t^2}u_0 \tag{5.27}$$

Where there is no slip, i.e., $0 \leqslant x \leqslant x_1$, $u_1(x) = 0$. Substitution of Eq. (5.26) into the derivative of Eq. (5.27) gives an ordinary differential equation for pressure with

solution

$$p\left(x\right) = K\epsilon_c\left[1 - B\cosh\left(\lambda x\right)\right] \tag{5.28}$$

where $B$ is a constant to be determined.

For the region where slip occurs, $x_1 \leqslant x \leqslant b$, $\tau_s = \mu p$ and $\tau_s = -(t/2)p'$ give

$$p' + \frac{2\mu}{t}p = 0 \tag{5.29}$$

The solution of this equation is $p(x) = Ce^{-\frac{2\mu}{t}x}$, where $C$ is a constant of integration computed from the boundary condition at the edge of the layer: $p(b) = E_0\epsilon_c$, where $E_0 = \frac{9KG}{3K+G}$. For most thin bonded layers, this is completely negligible since $E_0$ is around two orders of magnitude smaller than $E_c$ (Kelly and Konstantinidis, 2009, 2011), and thus $p = 0$ is used around the edges of the layer. In this case of a layer with partial slip, the form of the solution necessitates the use of the non-zero boundary condition. Letting $\eta = \frac{3}{3+G/K}$, then $p(b) = 3G\eta\epsilon_c$, and

$$p(x) = 3G\eta\epsilon_c e^{\frac{2\mu}{t}(b-x)} \tag{5.30}$$

At $x = x_1$, $p(x)$ and $p'(x)$ are continuous. From Eq. (5.28), for $0 \leqslant x \leqslant x_1$

$$p' = -K\epsilon_c B\lambda\sinh\left(\lambda x\right) \tag{5.31}$$

and from Eq. (5.30), for $x_1 \leqslant x \leqslant b$

$$p' = -3G\eta\epsilon_c\frac{2\mu}{t}e^{\frac{2\mu}{t}(b-x)} \tag{5.32}$$

At $x = x_1$, $p'(x_1^-) = p'(x_1^+)$ gives

$$B = 3\frac{G}{K}\frac{\eta}{\lambda}\frac{1}{\sinh(\lambda x_1)}\frac{2\mu}{t}e^{\frac{2\mu}{t}(b-x_1)} \tag{5.33}$$

and $p(x_1^-) = p(x_1^+)$ gives

$$B = \frac{1}{\cosh(\lambda x_1)}\left[1 - \frac{3G}{K}\eta e^{\frac{2\mu}{t}(b-x_1)}\right] \tag{5.34}$$

Equating Eq. (5.33) and Eq. (5.34), and recognizing that $\eta \approx 1$, gives

$$\frac{2\mu}{\sqrt{\frac{12G}{K}}}\coth\left(\frac{\sqrt{\frac{12G}{K}}}{2\mu}2\mu S\frac{x_1}{b}\right) + 1 = \frac{K}{3G}e^{2\mu S\frac{x_1}{b}}e^{-2\mu S} \tag{5.35}$$

Letting $\vartheta \equiv 2\mu S\frac{x_1}{b}$, $\rho \equiv \frac{2\mu}{\sqrt{\frac{12G}{K}}}$ and $\psi \equiv e^{2\mu s\frac{3G}{K}}$, then

$$\rho\coth\left(\frac{\vartheta}{\rho}\right) + 1 = \frac{e^{\vartheta}}{\psi} \tag{5.36}$$

Solution of Eq. (5.36) by numerical means provides the unknown $\vartheta$, from which $x_1$ is readily determined. In turn, the constant $B$ can be determined from Eq. (5.34), or in terms of the newly defined parameters:

$$B = \frac{1}{\cosh\left(\frac{\vartheta}{\rho}\right)}\left[1 - \psi e^{-\vartheta}\right] \tag{5.37}$$

Fig. 5.5 shows graphs for $x_1/b$ for values of $\mu$ ranging between 0.1 and 1.0; for $S$ = 10, 20, 30, and 40; and $K/G$ = 1000, 2000, 5000, and 10,000. It can be seen that $x_1/b$ is highly sensitive to the shape factor, especially for low to intermediate

values of $\mu$. For example, for a layer with shape factor of 10, about 3/4 of the layer would be slipping, while for one with a shape factor of 40, only about 1/3. For low friction coefficient values, most of the layer is slipping. It is interesting to note that even for a large friction coefficient, say $\mu = 1.0$, an appreciable portion of the layer is experiencing slip, especially for lower shape factors; e.g., for $S = 10$ and $\mu = 1.0$, $x_1/b$ is approximately 0.85.

Fig. 5.6 shows the effect of bulk compressibility on $x_1/b$. As expected, it can be seen that as $K/G$ increases, the curves saturate to the curve representing the incompressible case investigated by Kelly and Konstantinidis (2009). For layers with larger shape factor values, the effect of compressibility becomes more pronounced, manifested by the increased separation between curves.

The pressure distribution in the layer is given by

$$p(x) = K\epsilon_c \left[1 - B\cosh\left(\lambda x\right)\right]; \quad 0 \leqslant x \leqslant x_1 \tag{5.38a}$$

$$p(x) = 3G\eta\epsilon_c e^{\frac{2\mu}{t}(b-x)}; \quad x_1 \leqslant x \leqslant b \tag{5.38b}$$

Fig. 5.7 plots the pressure distribution from Eq. (5.38), normalized with respect to the average pressure in a fully bonded incompressible layer ($= 4GS^2\epsilon_c$), for rubber with $K/G = 4000$ and different values of $\mu$, ranging between 0.1 and 1.0, together with the pressure distribution for a fully bonded layer, given by Eq. (5.10). The graphs are plotted for $S = 10$, 20, 30, and 40. It can be seen that slip results in a reduction in peak pressure. This reduction becomes more pronounced for lower shape factor; while for large shape factor, the pressure distribution becomes insensitive to the friction coefficient for $\mu > 0.3$. The bold curves in Fig. 5.7 show the evolution

of $x_1/b$: the intersection of the bold curve with the a pressure distribution curve corresponding to a specific $\mu$ value indicates the location where slip initiates. The figure suggests that even for very large values of $\mu$, a small portion of the layer close to the edges is slipping.

The shear strain along $z = \pm t/2$ is given by

$$\gamma(x) = \tfrac{Kt}{2G}\epsilon_c B\lambda \sinh(\lambda x); \quad 0 \leqslant x \leqslant x_1 \tag{5.39a}$$

$$\gamma(x) = 3\eta\epsilon_c \mu e^{\frac{2\mu}{t}(b-x)}; \quad x_1 \leqslant x \leqslant b \tag{5.39b}$$

Fig. 5.8 plots the shear strain distribution from Eq. (5.39), normalized with respect to the maximum shear strain in a fully bonded incompressible layer ($= 6S\epsilon_c$), for rubber with $K/G = 4000$; $S = 10$, 20, 30, and 40, and different values of $\mu$ ranging between 0.1 and 1.0, together with the shear strain distribution of a fully bonded layer, given by Eq. (5.17)(dashed line). It can be seen that the shear strain in the unbonded pad attains its maximum at the location where slip initiates, given by

$$\gamma_{max} = 3\eta\epsilon_c \mu e^{2\mu S(1-x_1/b)} \tag{5.40}$$

and then decreases in the slip region. The figure illustrates that slip causes a reduction in the maximum shear strain, which is more pronounced for lower values of $S$. Fig. 5.9 shows the effect of bulk compressibility on the normalized maximum shear strain, $\gamma_{max}/6S\epsilon_c$. It is evident that compressibility results in a significant reduction in maximum shear strain, especially for higher shape factors. It is noted that $\gamma_{max}$ becomes insensitive for compressible layers with larger values of $S$ and $\mu$. Consequently, for unbonded strip-shaped layers with $S \geqslant 20$, $K/G \leqslant 5000$, and $\mu \geqslant 0.6$,

Eq. (5.18) can be used to obtain a reasonably accurate estimate of $\gamma_{max}$ for design purposes.

The compression modulus is computed from $E_c = P/(2b)$, where

$$P = 2\left\{\int_0^{x_1} K\varepsilon_c\left(1 - B\cosh\left(\lambda x\right)\right)dx + \int_{x_1}^{b} 3G\eta\varepsilon_c e^{\frac{2\mu}{t}(b-x)}dx\right\} \tag{5.41}$$

leading to

$$E_c = K\left\{\frac{x_1}{b} - \frac{B}{\sqrt{\frac{12G}{K}}S}\sinh\left(\sqrt{\frac{12G}{K}}S\frac{x_1}{b}\right) + \frac{3G\eta}{K}\frac{1}{2\mu S}\left[e^{2\mu S\left(1-\frac{x_1}{b}\right)} - 1\right]\right\} \tag{5.42}$$

Fig. 5.10 plots the ratio of the compression moduli of the unbonded layer and bonded layers for values of $\mu$ between 0.1 and 1.0 and $S$ = 10, 20, 30, and 40, and $K/G$ = 1000, 2000, 5000, and 10,000. The compression modulus of bonded layer is computed using Eq. (5.13). The figure shows that the introduction of a frictional constraint described by a Coulomb model, rather than assuming that the rubber layer is rigidly bonded to its supports, can result in a dramatic decrease in the compression modulus of the layer, regardless of the value of $K/G$. A substantially larger drop in compression modulus (compared to the bonded case) is noted for layers with low shape factor, especially for low to intermediate values of the friction coefficient; e.g., for $S$ = 10, $\mu$ = 0.4 and $K/G$ = 2000, the compression modulus is 40% that of the bonded layer. Fig. 5.11 shows the compression modulus ratio for different values of $K/G$. Layers with large shape factor are more sensitive to variations in $K/G$, with more compressible material resulting is lower reduction of the compression modulus relative to bonded case. For example, for $S$ = 40 and $\mu$ = 0.4, the compression modulus is reduced only by about 10% for $K/G$ = 1000, while for incompressible

material it is reduced by about 35%.

To illustrate the error in estimating the compression modulus of a thin rubber pad by ignoring the possibility of partial slip, we consider a single-layer rubber pad with $G = 1.0$ MPa, $K = 2000$ MPa, $S = 20$, and the Caltrans-recommended value of $\mu = 0.4$ for rubber–concrete surfaces (Caltrans, 1994). In this case, the bulk modulus predicted assuming a fully bonded layer would overestimate $E_c$ by more than 50%.

## 5.5 Compression of a Circular Rubber Layer with Surface Slip

The approach used for an unbonded infinite-strip layer is followed for the circular pad of radius $R$. In this case the displacement field is

$$u(r,z) = u_0(r)\left(1 - \frac{4z^2}{t^2}\right) + u_1(r) \tag{5.43a}$$

$$w(r,z) = w(z) \tag{5.43b}$$

where $u_1(r) = 0$ for $0 \leqslant r \leqslant r_1$, with $r_1$ indicating the radial distance at which slip initiates. The three normal strains are then given by

$$\epsilon_r = \partial_r u = u_0'\left(1 - \frac{4z^2}{t^2}\right) + u_1' \tag{5.44a}$$

$$\epsilon_\theta = \frac{u}{r} = \frac{u_0}{r}\left(1 - \frac{4z^2}{t^2}\right) + \frac{u_1}{r} \tag{5.44b}$$

$$\epsilon_z = w' \tag{5.44c}$$

Therefore, $\epsilon_r + \epsilon_\theta + \epsilon_z = -\frac{p}{K}$ integrated through the thickness of the layer, gives

$$\frac{1}{r}\left(ru_0\right)' + \frac{3}{2}\frac{1}{r}\left(ru_1\right)' = \frac{3}{2}\left(\epsilon_c - \frac{p}{K}\right) \tag{5.45}$$

The equations of stress equilibrium in polar coordinates are

$$\frac{\partial \sigma_r}{\partial r} + \frac{\partial \tau_{rz}}{\partial z} + \frac{\sigma_r - \sigma_\theta}{r} = 0 \tag{5.46a}$$

$$\frac{\partial \tau_{rz}}{\partial r} + \frac{\partial \sigma_z}{\partial z} + \frac{\tau_{rz}}{r} = 0 \tag{5.46b}$$

which with the assumption that the normal stresses are all equal to the $-p$ and $\tau_{rz} = G\gamma_{rz} = -\frac{8G}{t^2} z u_0$, give

$$p' = -\frac{8G}{t^2} u_0 \tag{5.47}$$

Over $0 \leqslant r \leqslant r_1$, $u_1 = 0$, and Eq. (5.45) and Eq. (5.47) give

$$p(r) = K\epsilon_c \left[1 - BI_0\left(\lambda r\right)\right] \tag{5.48}$$

Equating $\tau_s = \mu p$ and $\tau_s = -(t/2)p'$ leads to the same equation as for an infinite strip pad,

$$p' + \frac{2\mu}{t} p = 0 \tag{5.49}$$

with solution $p(r) = Ce^{-\frac{2\mu}{t}r}$, where $C$ is computed from the boundary condition $p(R) = 3G\eta\epsilon_c$, resulting in

$$p(r) = 3G\eta\epsilon_c e^{\frac{2\mu}{t}(R-r)} \tag{5.50}$$

From Eq. (5.48), for $0 \leqslant r \leqslant r_1$,

$$p'(r) = -K\epsilon_c B\lambda I_1(\lambda r) \tag{5.51}$$

and from Eq. (5.50), for $r_1 \leqslant r \leqslant b$,

$$p'(r) = -3G\eta\epsilon_c \frac{2\mu}{t} e^{\frac{2\mu}{t}(R-r)} \tag{5.52}$$

Continuity in $p'$ at $r = r_1$ gives

$$B = 3\frac{G}{K}\frac{\eta}{\lambda}\frac{1}{I_1(\lambda r_1)}\frac{2\mu}{t}e^{\frac{2\mu}{t}(R-r_1)} \tag{5.53}$$

while continuity in $p$ gives

$$B = \frac{1}{I_0(\lambda r_1)}\left[1 - \frac{3G}{K}\eta e^{\frac{2\mu}{t}(R-r_1)}\right] \tag{5.54}$$

We proceed in a similar fashion to the infinite strip pad. Eq. (5.53) and Eq. (5.54), with $\eta = 1$, give

$$\frac{2\mu}{\sqrt{\frac{12G}{K}}}\frac{I_0\left(\sqrt{\frac{12G}{K}}\frac{2\mu S\frac{r_1}{R}}{\mu}\right)}{I_1\left(\sqrt{\frac{12G}{K}}\frac{2\mu S\frac{r_1}{R}}{\mu}\right)} + 1 = \frac{K}{3G}e^{4\mu S\frac{r_1}{R}}e^{-4\mu S} \tag{5.55}$$

With $\vartheta \equiv 2\mu S\frac{r_1}{R}$, $\rho \equiv \frac{2\mu}{\sqrt{\frac{12G}{K}}}$ and $\psi \equiv e^{4\mu s}\frac{3G}{K}$, Eq. (5.55) becomes

$$\frac{\rho I_0\left(\frac{2\vartheta}{\rho}\right)}{I_1\left(\frac{2\vartheta}{\rho}\right)} + 1 = \frac{e^{2\vartheta}}{\psi} \tag{5.56}$$

Solution of Eq. (5.56), provides $\vartheta$, and thus $r_1/R$. $B$ can be determined from Eq.

(5.53), which can expressed as

$$B = 3\frac{G}{K}\frac{2\mu}{\sqrt{\frac{12G}{K}}\, I_1\left(2\sqrt{\frac{12G}{K}}S\frac{r_1}{R}\right)}\frac{e^{4\mu S\left(1-\frac{r_1}{R}\right)}}{} \tag{5.57}$$

Fig. 5.12 plots $r_1/R$ for values of $\mu$ ranging between 0.1 and 1.0; $S = 10$, 20, 30, and 40; and $K/G = 1000$, 2000, 5000, 10,000. Fig. 5.13 shows the effect of the bulk modulus (as $K/G$) on $r_1/R$ for different values of $S$ and $\mu$. Similar conclusions as for the case of an infinite-strip layer are drawn for the circular layer.

The pressure distribution is given by

$$p(r) = K\epsilon_c\left[1 - BI_0(\lambda r)\right]; \quad 0 \leqslant r \leqslant r_1 \tag{5.58a}$$

$$P(r) = 3G\eta\epsilon_c e^{\frac{2\mu}{t}(R-r)}; \quad r_1 \leqslant r \leqslant R \tag{5.58b}$$

Fig. 5.14 shows the pressure distribution of an unbonded circular layer, as described by Eq. (5.58), $K/G = 4000$; $S = 10$, 20, 30, and 40; and various values of $\mu$ between 0.1 and 1.0. The pressure is normalized by the average pressure in a fully-bonded, incompressible layer ($= 6GS^2\epsilon_c$). In addition, the pressure distribution for a fully bonded layer is shown. A significant reduction in peak pressure is observed with decreasing $\mu$. It can be seen from the figure that for large $S$ the sensitivity of the maximum pressure to variations in $\mu$ is lower.

The shear strain along $z = \pm t/2$ is given by

$$\gamma(r) = \tfrac{Kt}{2G}\epsilon_c B\lambda I_1(\lambda r); \quad 0 \leqslant r \leqslant r_1 \tag{5.59a}$$

$$\gamma(r) = 3\eta\epsilon_c\mu e^{\frac{2\mu}{t}(R-r)}; \quad r_1 \leqslant r \leqslant R \tag{5.59b}$$

The shear strain attains its maximum value at $r = r_1$, given by

$$\gamma_{max} = 3\eta\epsilon_c\mu e^{4\mu S(1-r_1/R)} \tag{5.60}$$

Fig. 5.15 shows the shear strain distribution given by Eq. (5.59), normalized by the maximum shear strain in a fully bonded incompressible circular layer ($= 6S\epsilon_c$), for $K/G = 4000$; $S = 10$, 20, 30, and 40; and different values of $\mu$ ranging between 0.1 and 1.0. Also shown is the shear strain distribution in a fully bonded circular layer (dashed line), given by Eq. (5.23). Similar to the observation made for the pressure distribution, the maximum shear strain becomes less sensitive to $\mu$ for larger values of $S$. Fig. 5.16 shows the effect of the bulk modulus (as $K/G$) on the maximum shear strain for different values of $S$ and $\mu$. It can be seen that $\gamma_{max}$ decreases significantly, with this decrease becoming more pronounced for layers with higher $S$. An interesting observation is that for layers with large $S$ values, although compressibility should be included in the analysis to realistically estimate $\gamma_{max}$, the value of $\gamma_{max}$ becomes insensitive for large $\mu$ values. Therefore, to simplify design, if $S \geqslant 20$, $K/G \leqslant 5000$, and $\mu \geqslant 0.5$, it is reasonably accurate to estimate $\gamma_{max}$ assuming that the layer is fully bonded, i.e., using Eq. (5.24).

$E_c$ is calculated by integrating the pressure over $0 \leqslant r \leqslant R$ to determine $P$ and then dividing by $A\epsilon_c$, giving

$$P = 2\pi\left[\int_0^{r_1} K\epsilon_c\left(1 - BI_0(\lambda r)\right) r dr + \int_{r_1}^{R} 3G\eta\epsilon_c e^{\frac{2\mu}{t}(R-r)} r dr\right] \tag{5.61}$$

and

$$E_c = 2K\Bigg\{\tfrac{1}{2}\left(\tfrac{r_1}{R}\right)^2 - B\left(\tfrac{r_1}{R}\right)\tfrac{1}{2\sqrt{\frac{12G}{K}}S} I_1\left(2\sqrt{\tfrac{12G}{K}}S\tfrac{r_1}{R}\right) + \tfrac{3G}{K}\tfrac{1}{(4\mu S)^2}\left[-4\mu S - 1 + e^{4\mu S\left(1-\frac{r_1}{R}\right)}\left(4\mu S\tfrac{r_1}{R}+1\right)\right]\Bigg\} \tag{5.62}$$

Fig. 5.17 shows the compression modulus ratio for values of $\mu$ between 0.1 and 1.0; $S = 10$, 20, 30, and 40, and $K/G = 1000$, 2000, 5000, and 10,000. The compression modulus of fully bonded pad, appearing in the denominator of the ratio, is based on Eq. (5.22). Fig. 5.18 shows the effect of bulk compressibility on the compression modulus.

## 5.6 Finite Element Analysis

The behavior of an unbonded rubber layer under pure compression was also investigated using the commercially available finite element analysis software MSC Marc (MSC Software, 2011). A rubber layer was discretized using quadrilateral plane-strain elements. Two horizontal rigid elements were defined at the top and bottom of the layer representing the supports. The details of using MSC Marc for modeling rubber bearings under compression have been discussed in Van Engelen et al. (2014); and references reported therein. The touching contact model was selected between the rubber layer and the supports. Based on this option, the nodal points of one surface are permitted to separate from those of the contacting surface in the normal direction. In the tangential direction, the contact is prescribed by a Coulomb friction model. To evaluate the effect of slip at the contact support, the coefficient of friction was varied from 0.1 to 1.0 with 0.1 increment. The rubber was modeled using the compressible Neo-Hookean hyperelastic constitutive model (Bathe, 1995; Bonet and Wood, 1997).

This material was selected for its simplicity and the fact that it behaves most closely to a linear elastic material for smaller strains. The strain energy density function of the compressible Neo-Hookean model is given by

$$W = C_{10}\left(\bar{I}_1 - 3\right) + \frac{1}{D_1}\left(\ln J\right)^2 \tag{5.63}$$

where $C_{10} = G/2$, $D_1 = 2/K$, $\bar{I}_1$ is the first reduced (or modified) invariant of the Cauchy–Green deformation tensor (deviatoric part only), and $J$ is the elastic volume ratio. In all analyses, it was assumed that $K/G = 5000$. Fig. 5.19 shows the finite element mesh of the rubber layer with $t = 10$ mm and $b = 100$, 200, and 300 mm, corresponding to shape factor $S = 10$, 20, and 30.

Fig. 5.20 shows the deformed shape of a layer with $S = 10$ and $\mu = 0.3$ for $0 \leqslant x \leqslant b$ under an average compressive stress of 2.0 MPa. It can be seen that the parabolic bulging of the layer increases from the center of the layer outwards and becomes maximum at the location where slip initiates ($x_1/b = 0.445$). From that point towards the edge of the layer, the parabolic bulging decreases, as the deformation is controlled by the slip.

The location where slip initiates was determined by monitoring the relative motion of nodes along the contact surfaces. Fig. 5.21 compares the location where slip initiates as determined by the finite element analysis (FEA) and by theoretical solution for unbonded infinite strip pad with shape factor of 10, 20, and 30. It can be seen that there is good agreement between the two, although in some cases the FEA predicts that slipping occurs over a larger portion of the pad, compared to the theoretical solution. Slight deviation between the results is observed for higher friction coefficient values. Fig. 5.22 shows the pressure distribution based on theoretical

and FEA. The difference between the predictions is more pronounced for the pressure distribution, especially for lower shape factor. However, Fig. 5.23, which shows the comparison modulus obtained by the two methods, shows good overall agreement, especially for low shape factor.

## 5.7 Conclusions

The behavior of rubber layers under pure compression has been the focus of a large number of studies. In these studies, the layer is assumed to be bonded to rigid or flexible supports (reinforcement). However, the effect of partial slip in a rubber pad that is installed in an unbonded applications, and relies solely on the friction between the rubber and the supports to keep it in place, has received very little attention. The effect of bulk compressibility in such an application has not been investigated in past studies. This paper investigated the behaviour of an unbonded rubber pad including the effect of compressibility and slip at the top and bottom supports. It was shown that slip can have a significant effect on the pressure distribution and compression modulus of the pad. It was observed that even for pads with high friction coefficient ($\mu = 1$), a portion of the pad (up to 15% for pads with shape factor of 10) close to the edge is experiencing slip. The compression modulus is more sensitive to variations in bulk modulus for layers with larger shape factor. However, the compression modulus of layers with high shape factor is closer to the value corresponding to the bonded case than for layers with low shape factor. The study showed that compressibility and slip can significantly reduce the maximum shear strain in unbonded layers. However, for unbonded rubber layers with typical bulk-modulus-to-shear-modulus ratio values and large values of shape factor and $\mu$, the maximum shear strain becomes insensitive

to variations in $\mu$. Consequently, the paper presented various conditions under which the maximum shear strain in an unbonded layer (strip or circular) can be estimated with reasonable accuracy using the solution that corresponds to a fully bonded layer. Finally, the paper presented results from a finite element analysis study on the compression behavior of three rubber pads with shape factor 10, 20, and 30. The results of the finite element investigation are in good overall agreement with the predictions of the theoretical solution.

This paper focused on the compression of a unreinforced, unbonded rubber pad (i.e., a single layer experiencing symmetric slip on its top and bottom surface). The theoretical analysis in this study is not applicable to unbonded layers with different friction coefficient values on the top and bottom supports or to unbonded multilayer rubber bearings. In such a bearing, the frictional constrain is only applies to the surface of the topmost and bottommost layers that are in contact with the supports. These problem involve unsymmetrical boundary conditions that are substantially more complex and will be investigated in future publications.

## 5.8 References

Ab-Malek, K., Roberts, A.D. (2013). *From Pelham to Penang : Natural Rubber Bearing Development for Civil Engineering.* Malaysian Rubber Board.

Angeli, P., Russo, G., Paschini, A. (2013). Carbon fiber-reinforced rectangular isolators with compressible elastomer: analytical solution for compression and bending. *International Journal of Solids and Structures.* 50(22), 3519–3527.

Bathe, K.-J. (1995). *Finite Element Procedures.* New York, US: Prentice Hall.

Bonet, J., Wood R.D. (1997). *Nonlinear continuum mechanics for finite element analysis*. Cambridge University Press, UK: Cambridge.

Caltrans (1994). Bridge Memo to Designers. Section 7: Bridge Bearings. California Department of Transportation, Sacramento, California.

Chalhoub, M.S., Kelly, J.M. (1990). Effect of bulk compressibility on the stiffness of cylindrical base isolation bearings. *International Journal of Solids and Structures.* 26(7), 743–760.

Chalhoub M.S., Kelly J.M. (1991). Analysis of infinite-strip-shaped base isolator with elastomer bulk compression. *Journal of Engineering Mechanics (ASCE).* 117(8), 1791–1805.

Constantinou, M.C., Kartoum, A., Kelly, J.M. (1992). Analysis of compression of hollow circular elastomeric bearings. *Engineering Structures.* 14(2): 103–111.

Constantinou, M.C., Kalpakidis, I., Filiatrault, A., Ecker Lay, R.A. (2011). LRFD-based analysis and design procedures for bridge bearings and seismic isolators. *Technical Report MCEER-11-0004.* Multidisciplinary Center for Earthquake Engineering Research. University at Buffalo, State University of New York.

Constantinou, M.C., Whittaker, A.S., Kalpakidis, Y., Fenz, D.M., Warn, G.P. (2007). Performance of seismic isolation hardware under service and seismic loading. *Technical Report MCEER-07-0012.* Multidisciplinary Center for Earthquake Engineering Research. University at Buffalo, State University of New York.

Gent, A.N., Lindley P.B. (1959). The compression of bonded rubber blocks. *Proceedings of the Institution of Mechanical Engineers.* 173(3), 111–122.

Gent, A.N., Meinecke E.A. (1970). Compression, bending and shear of bonded rubber blocks. *Polymer Engineering and Science.* 10(2), 48–53.

Kelly, J.M. (1997). *Earthquake-Resistant Design with Rubber*. 2nd ed. London: Springer-Verlag Telos.

Kelly, J.M. (1999). Analysis of fiber-reinforced elastomeric isolators. *Journal of Seismology and Earthquake Engineering.* 2(1), 19–34.

Kelly, J.M. (2002). Seismic isolation systems for developing countries. *Earthquake Spectra.* 18(3), 385–406.

Kelly, J.M., Calabrese, A. (2013). Analysis of fiber-reinforced elastomeric isolators including stretching of reinforcement and compressibility of elastomer. *Ingegneria Sismica.* 30(3), 5–14.

Kelly, J.M., Konstantinidis, D. (2009). Effect of friction on unbonded elastomeric bearings. *Journal of Engineering Mechanics.* 135(9), 953–960.

Kelly, J.M., Konstantinidis, D. (2011). *Mechanics of Rubber Bearings for Seismic Isolation and Vibration Isolation*. Chichester, UK: John Wiley & Sons.

Kelly, J.M., Takhirov S.M. (2002). Analytical and Experimental Study of Fiber-Reinforced Strip Isolators. *Technical Report PEER 2002/11.* Pacific Earthquake Engineering Research Center, University of California, Berkeley.

Kelly, J.M., Van Engelen, N.C. (2015). Single Series Solution for the Rectangular Fiber-Reinforced Elastomeric Isolator Compression Modulus. *Technical Report PEER 2015/03.* Pacific Earthquake Engineering Research Center. University of California, Berkeley.

Koh, C.G., Kelly, J.M. (1989). Compression stiffness of bonded square layers of nearly incompressible material. *Engineering Structures.* 11(1), 9–15.

Koh, C.G., Lim, H.L. (2001) Analytical solution for compression stiffness of bonded rectangular layers. *International Journal of Solids and Structures.* 38(3), 445–455.

Konstantinidis, D., Kelly, J. M., Makris, N. (2008). Experimental investigation on the seismic response of bridge bearings. *Technical Report EERC 2008-02.* Earthquake Engineering Research Center. University of California, Berkeley.

Lindley, P.B. (1979). Compression moduli for blocks of soft elastic material bonded to rigid end plates. *Journal of Strain Analysis for Engineering Design.* 14(1), 11–16.

MSC Software (2011). *MSC Marc and Mentat.* [computer software]. Santa Ana, California: MSC Software Corporation.

Naeim, F., Kelly, J.M. (1999) *Design of Seismic Isolated Structures: From Theory to Practice.* New York: John Wiley & Sons.

Osgooei, P.M., Tait, M.J., Konstantinidis, D. (2014). Three-dimensional finite element analysis of circular fiber-reinforced elastomeric bearings under compression. *Composite Structures.* 108, 191–204.

Papoulia, K.D., Kelly, J.M. (1996). Compression of bonded blocks of soft elastic material: variational solution. *Journal of Engineering Mechanics.* 122(2), 163–170.

Pinarbasi, S., Mengi, Y. (2008). Elastic layers bonded to flexible reinforcements. *International Journal of Solids and Structures.* 45(3), 794–820.

Pinarbasi, S., Okay, F. (2011). Compression of hollow-circular fiber-reinforced rubber bearings. *Structural Engineering and Mechanics.* 38(3), 361–384.

Pinarbasi, S., Akyuz, U., Mengi, Y. (2006). A new formulation for the analysis of elastic layers bonded to rigid surfaces. *International Journal of Solids and Structures.* 43(14-15), 4271–4296.

Pinarbasi, S., Mengi, Y., Akyuz, U. (2008). Compression of solid and annular circular discs bonded to rigid surfaces. *International Journal of Solids and Structures.* 45(16), 4543–4561.

Rastgoo Moghadam, S., Konstantinidis, D. (2014). The effect of slip on the compressive behavior of unbonded rubber pads: a Finite Element approach. *Proceedings of the 10th National Conference in Earthquake Engineering.* Earthquake Engineering Research Institute, Anchorage, AK.

Rocard Y. (1937). Note sur le calcul des propriétés élastique des supports en caoutchouc adhérent. *Le Journal de Physique et le Radium.* 8, 197–203.

Snowdon, J.C. (1979). Vibration isolation: use and characterization. *The Journal of the Acoustical Society of America.* 66(5), 1245–1274.

Stanton, J.F., Roeder, C.W. (1982). Elastomeric bearings design, construction, and materials. *NCHRP Report 248.* National Cooperative Highway Research Program (NCHRP). Transportation Research Board, Washington, DC.

Tsai, H.-C. (2004). Compression stiffness of infinite-strip bearings of laminated elastic material interleaving with flexible reinforcements. *International Journal of Solids and Structures.* 41(24), 6647–6660.

Tsai, H.-C. (2005). Compression analysis of rectangular elastic layers bonded between rigid plates. *International Journal of Solids and Structures.* 42(11-12), 3395-3410.

Tsai, H.-C. (2006). Compression stiffness of circular bearings of laminated elastic material interleaving with flexible reinforcements. *International Journal of Solids and Structures.* 43(11), 3484–3497.

Tsai, H.-C., Kelly, J.M. (2001). Stiffness Analysis of Fiber-Reinforced Elastomeric Isolators. *Technical Report PEER 2001/05.* Pacific Earthquake Engineering Research Center. University of California, Berkeley.

Tsai, H.-C., Kelly, J.M. (2002). Stiffness analysis of fiber-reinforced rectangular seismic isolators. *Journal of Engineering Mechanics.* 128(4), 462–470.

Tsai, H.-C., Lee C.-C. (1998). Compressive stiffness of elastic layers bonded between rigid plates. *International Journal of Solids and Structures.* 35(23), 3053-3069.

Van Engelen, N.C., Osgooei, P.M., Tait, M.J., Konstantinidis, D. (2014). Experimental and finite element study on the compression properties of Modified Rectangular Fiber-Reinforced Elastomeric Isolators (MR-FREIs). *Engineering Structures.* 74, 52–64.

Van Engelen N.C., Tait, M.J., Konstantinidis, D. (2016). Development of design code oriented formulas for elastomeric bearings including bulk compressibility and reinforcement extensibility. *Journal of Engineering Mechanics* (in press).

Figure 5.1: Unbonded rubber pad.

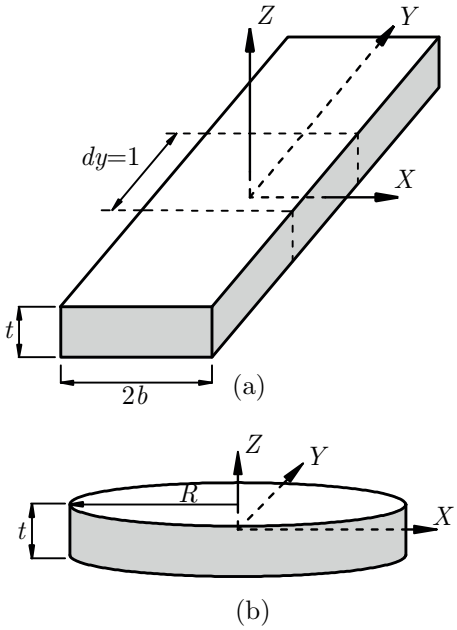


Figure 5.2: (a) Infinite strip pad of width $2b$, and (b) Circular pad of radius $R$.

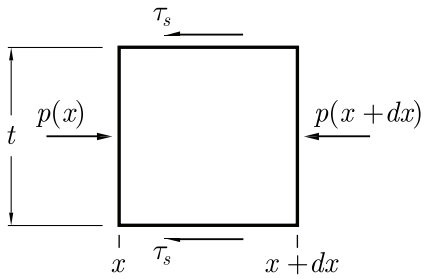


Figure 5.3: Definition of surface shears.

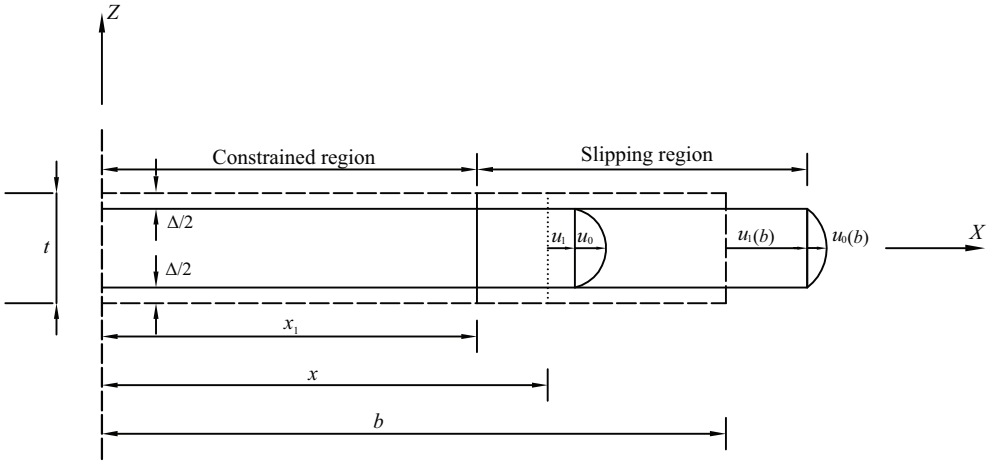


Figure 5.4: Deformation of a rubber layer with slip on the top and bottom surfaces.

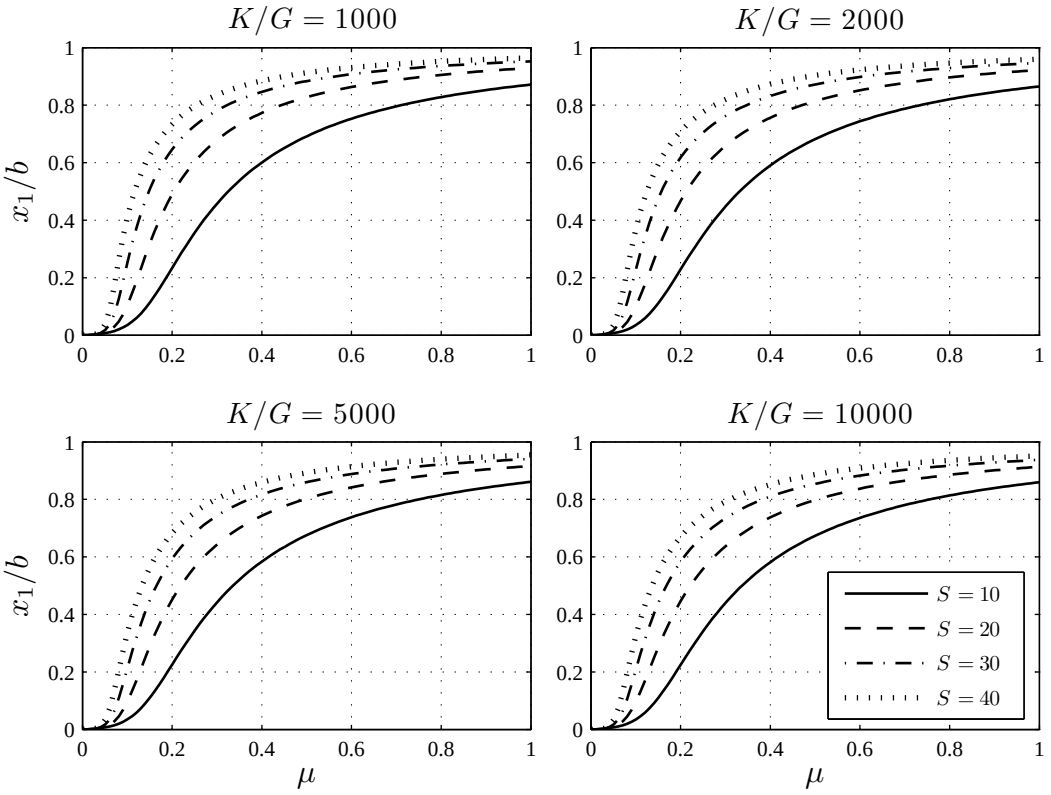


Figure 5.5: Location where slip initiates for an unbonded infinite-strip pad.

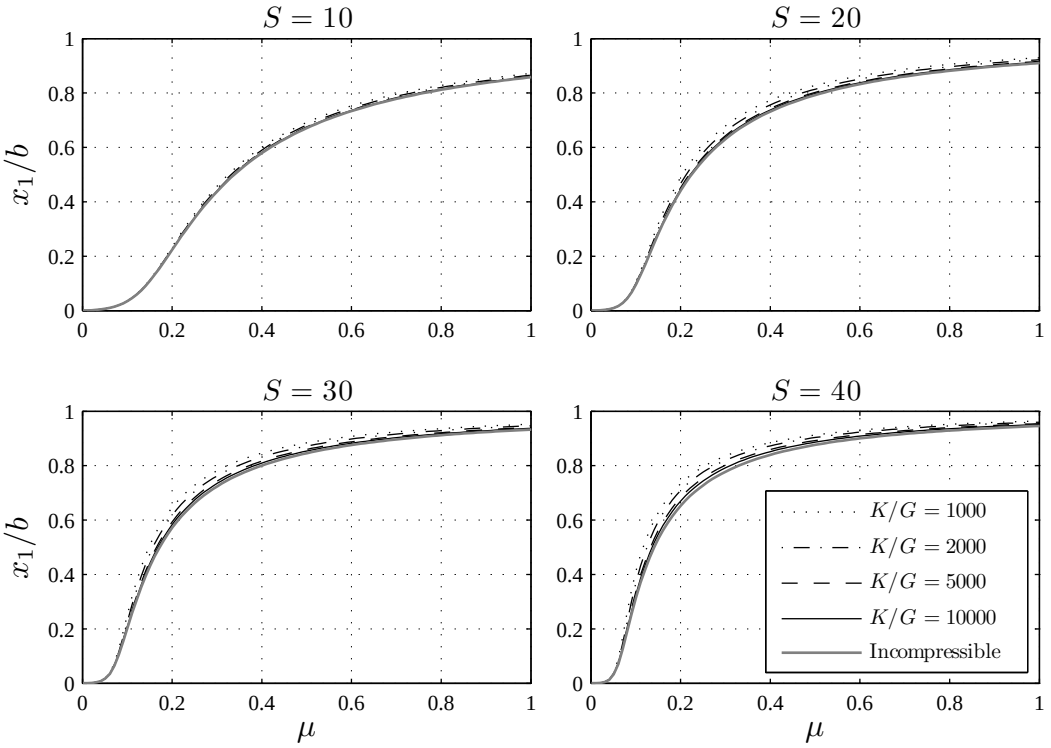


Figure 5.6: Effect of the bulk modulus on the location where slip initiates in an unbonded infinite-strip pad.

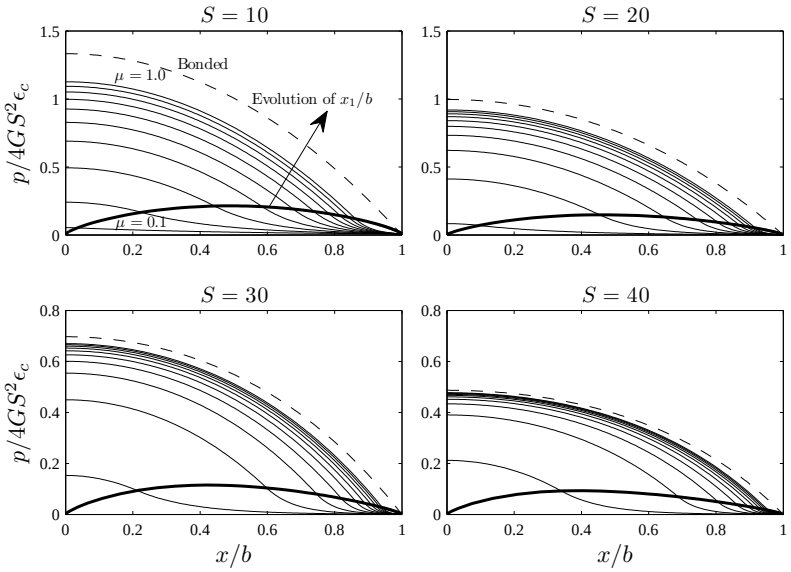


Figure 5.7: Pressure distribution of an unbonded infinite strip pad with $S = 10$, 20, 30, and 40; and $K/G = 4000$.

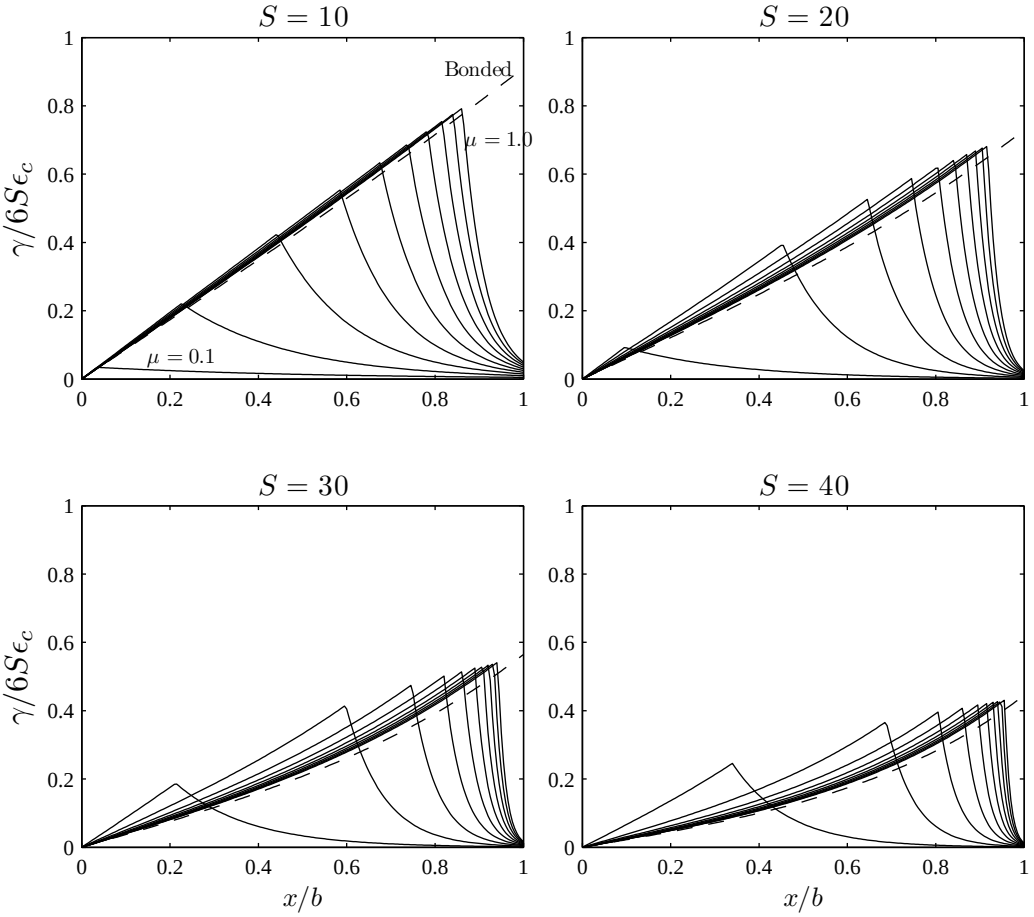


Figure 5.8: Shear strain distribution at the top or bottom of an unbonded infinite strip pad with $S = 10$, 20, 30, and 40; and $K/G = 4000$.

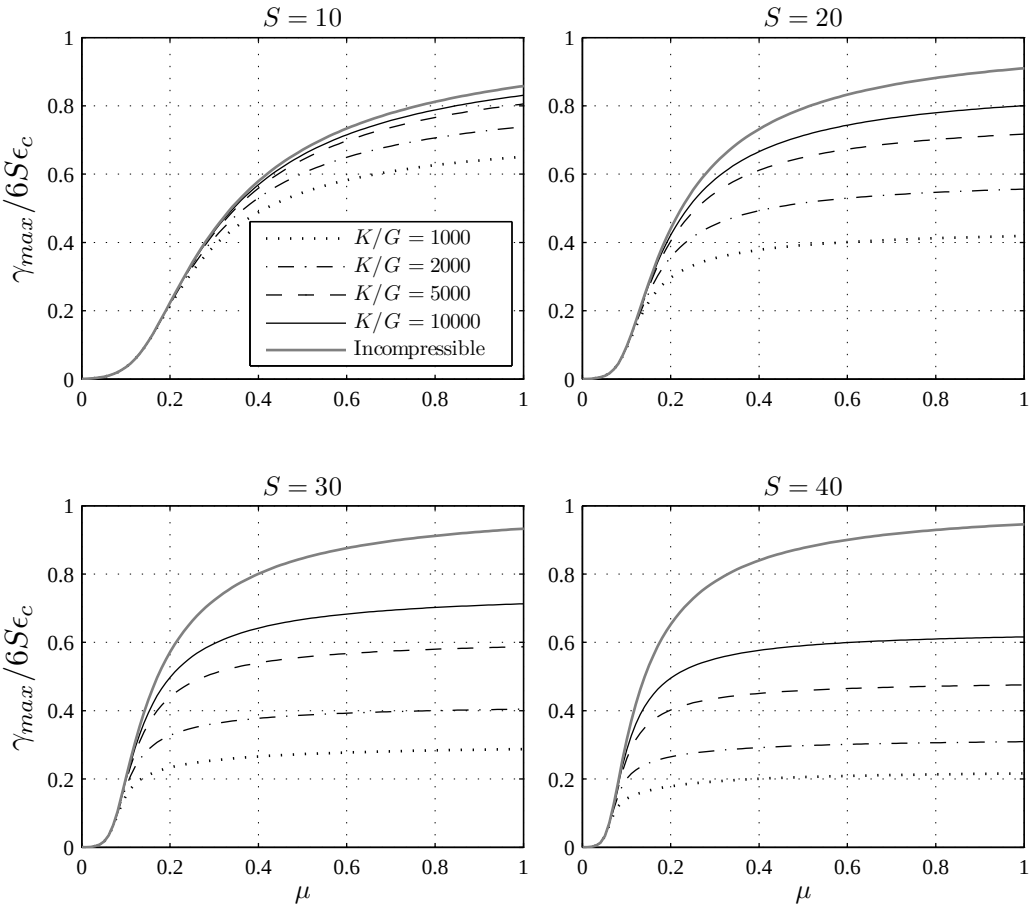


Figure 5.9: Effect of the bulk modulus on the maximum shear strain in an unbonded infinite-strip pad.

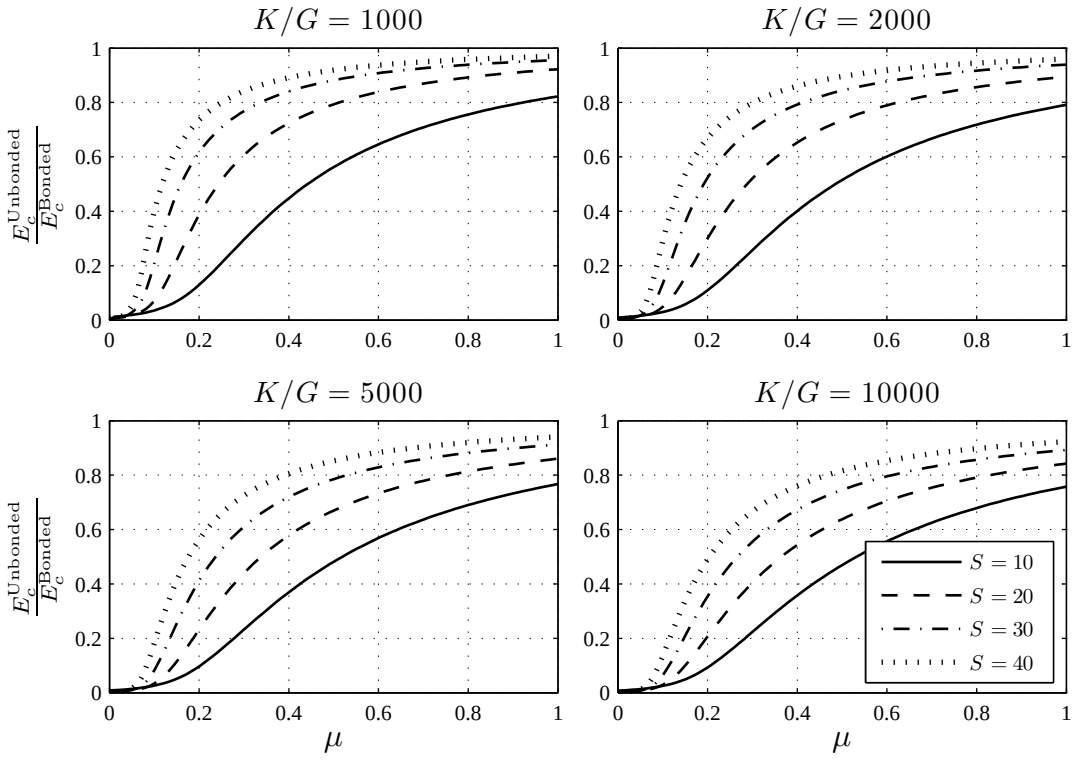


Figure 5.10: Unbonded–to–bonded compression modulus ratio for an infinite-strip layer.

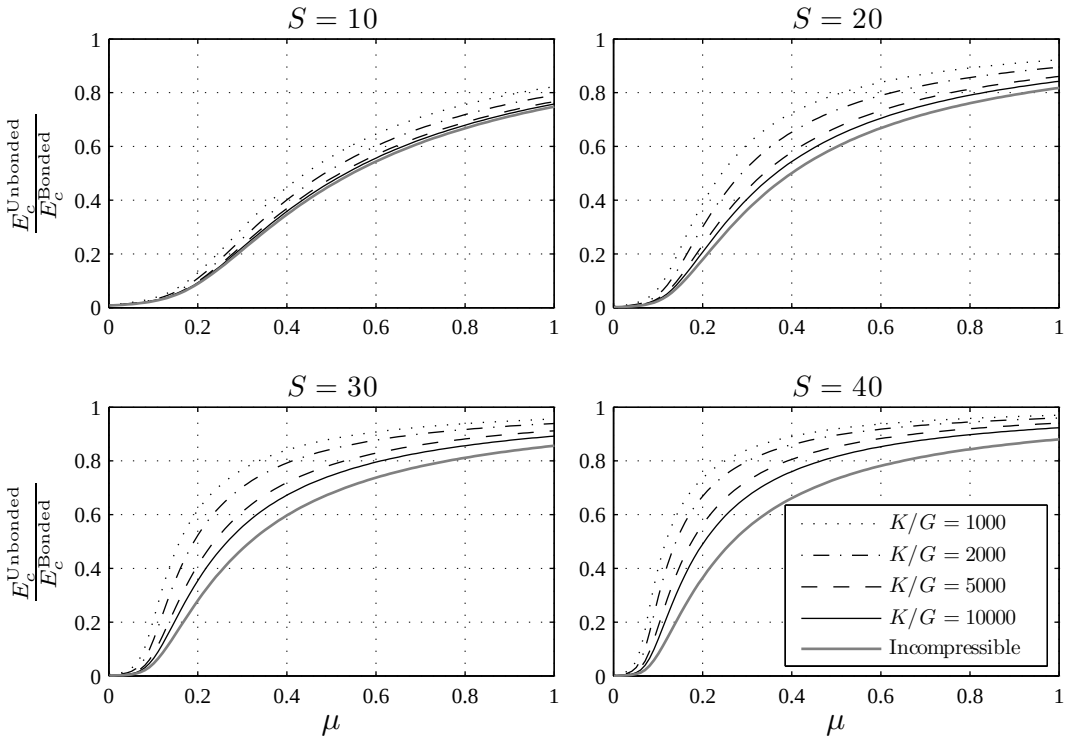


Figure 5.11: Effect of compressibility on the compression modulus of an unbonded infinite-strip layer.

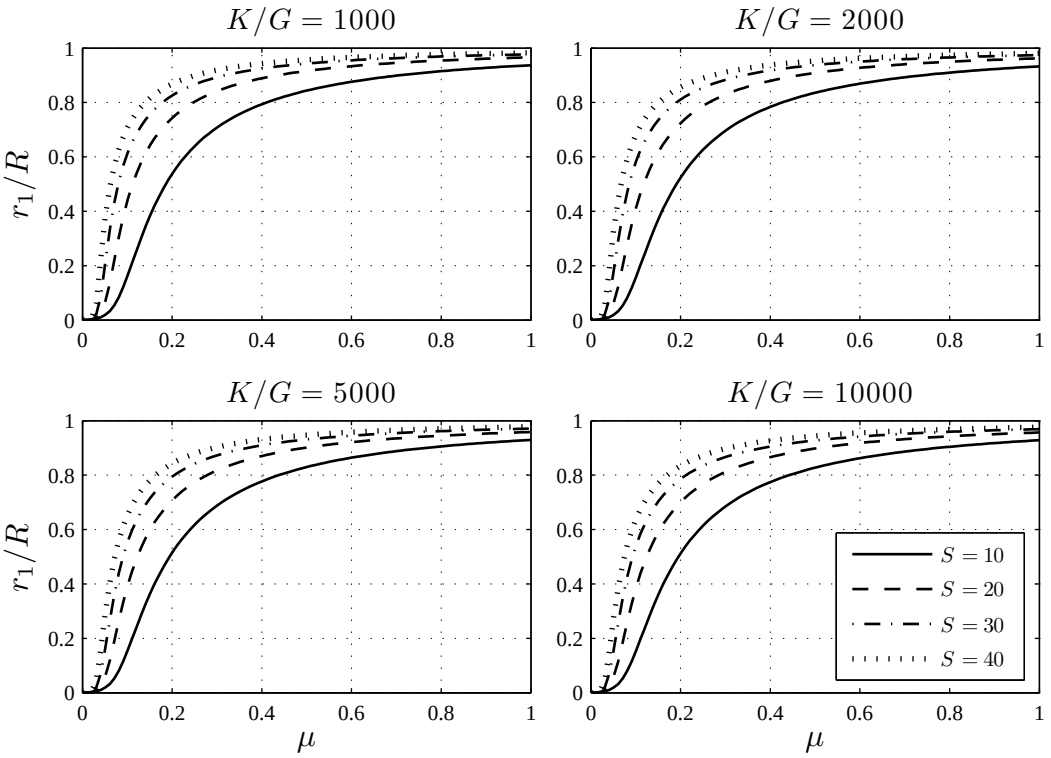


Figure 5.12: Location where slip initiates in a circular pad.

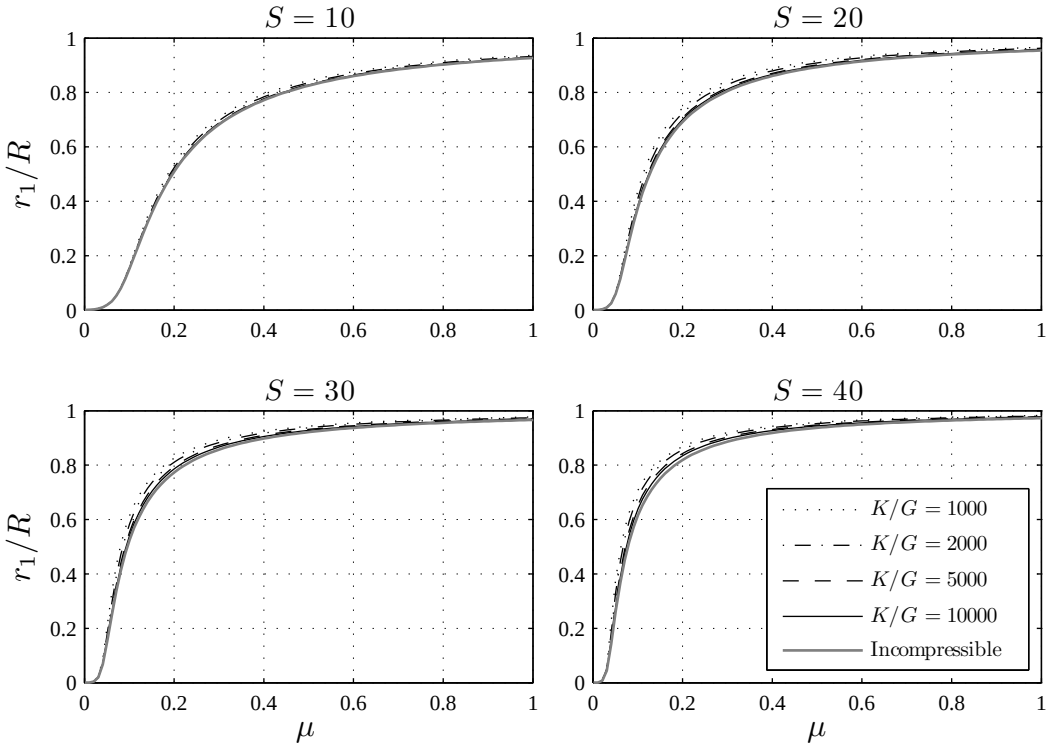


Figure 5.13: Effect of bulk modulus on the location where slip initiates in a circular pad.

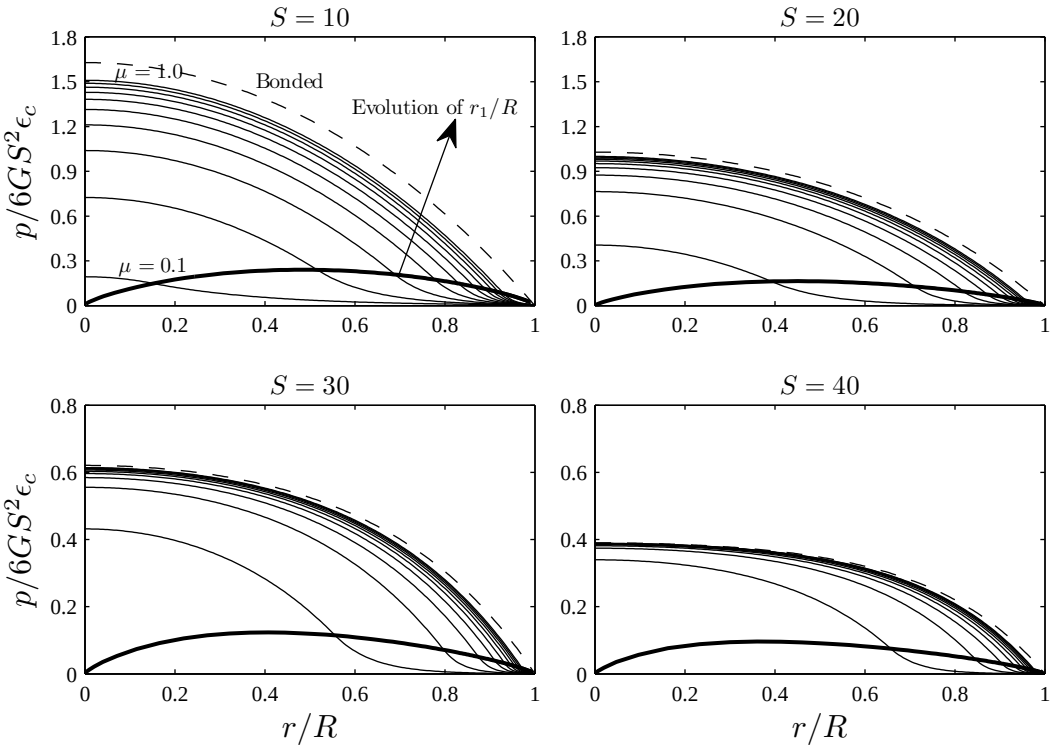


Figure 5.14: Pressure distribution of a circular pad with $K/G = 4000$ and $S = 10$, 20, 30, and 40.

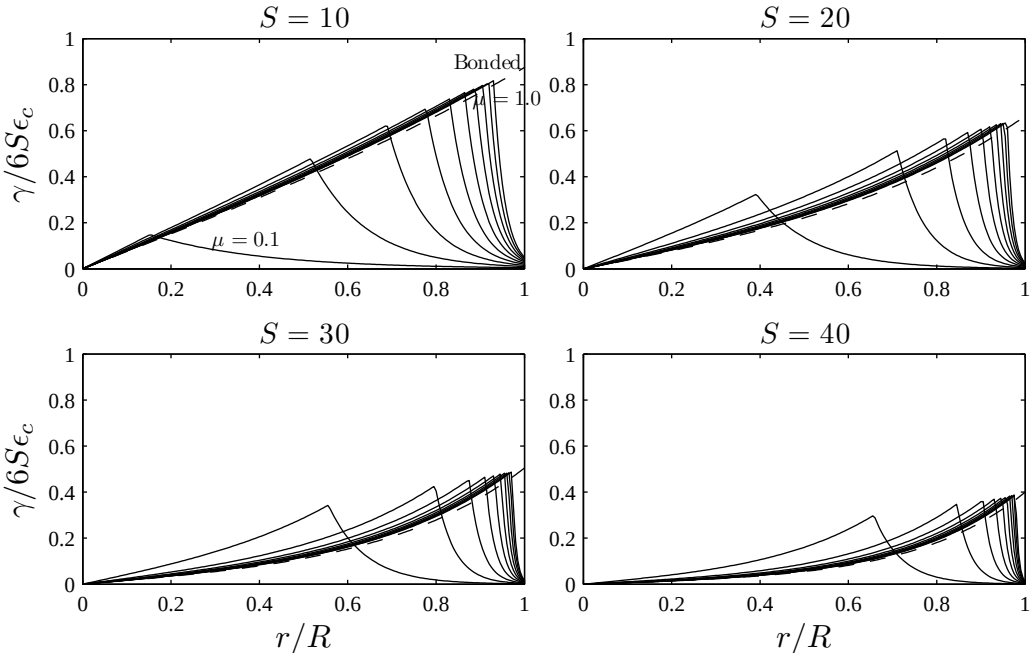


Figure 5.15: Shear strain distribution at the top or bottom of an unbonded circular pad with $S = 10$, 20, 30, and 40; and $K/G = 4000$.

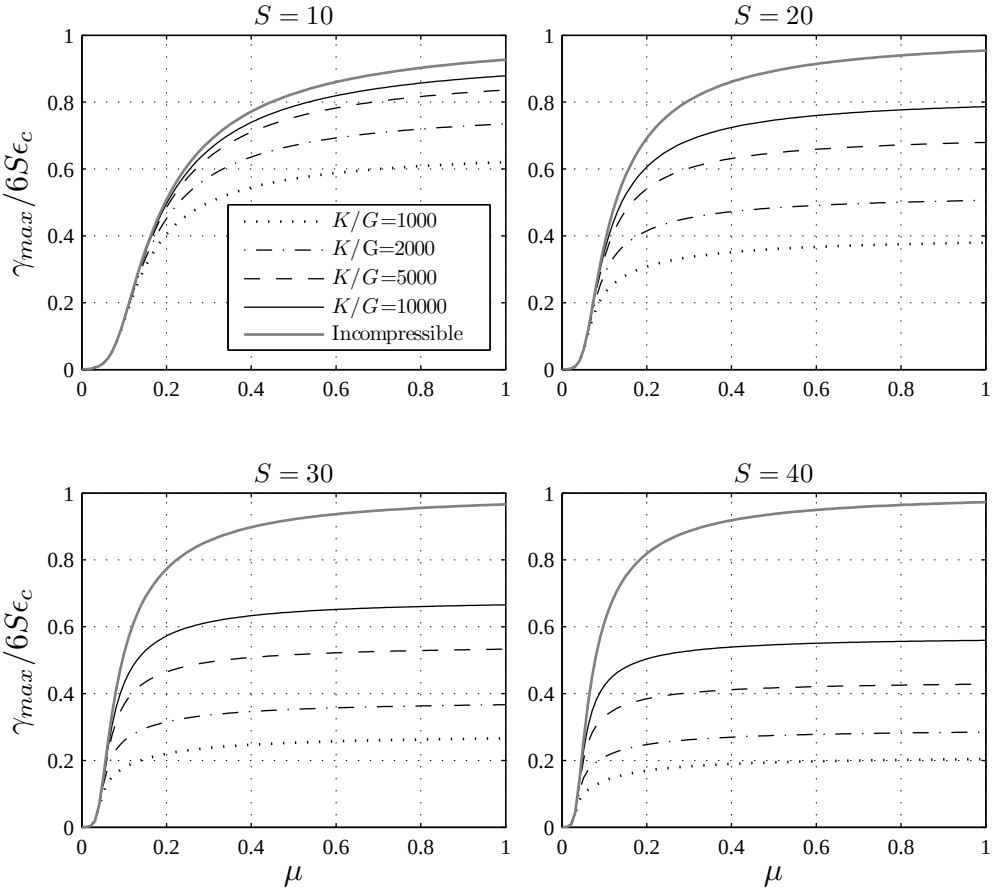


Figure 5.16: Effect of the bulk modulus on the maximum shear strain in an unbonded circular pad.

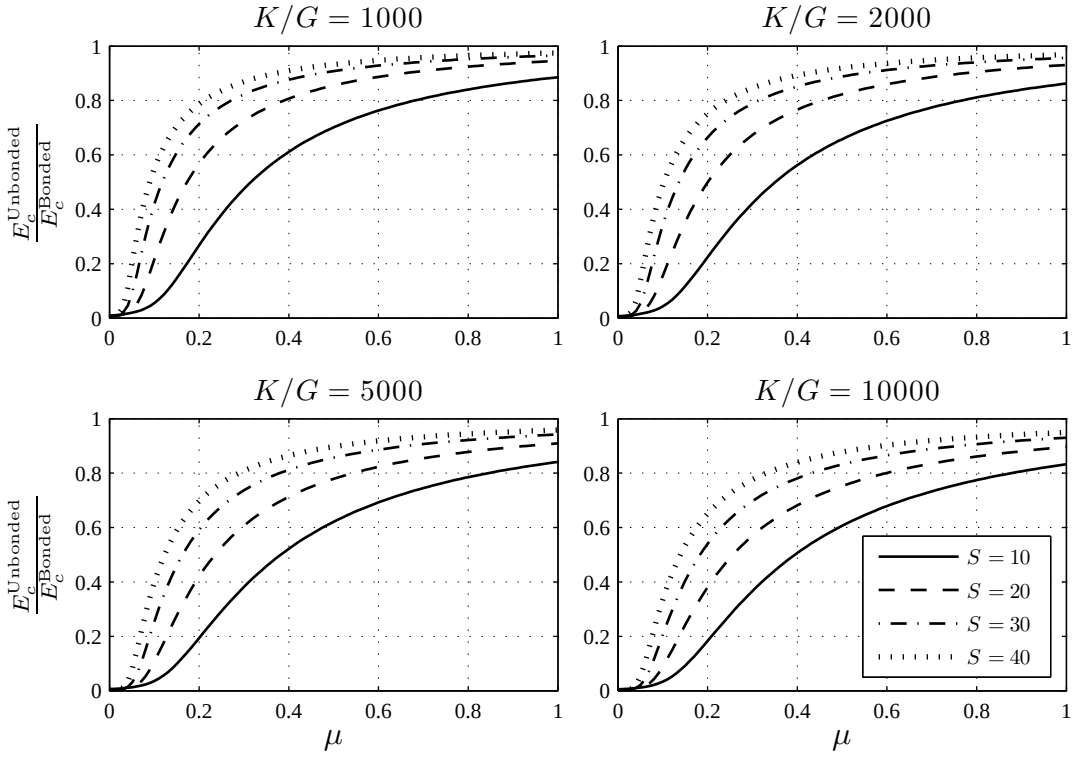


Figure 5.17: Normalized compression modulus for unbonded circular pad.

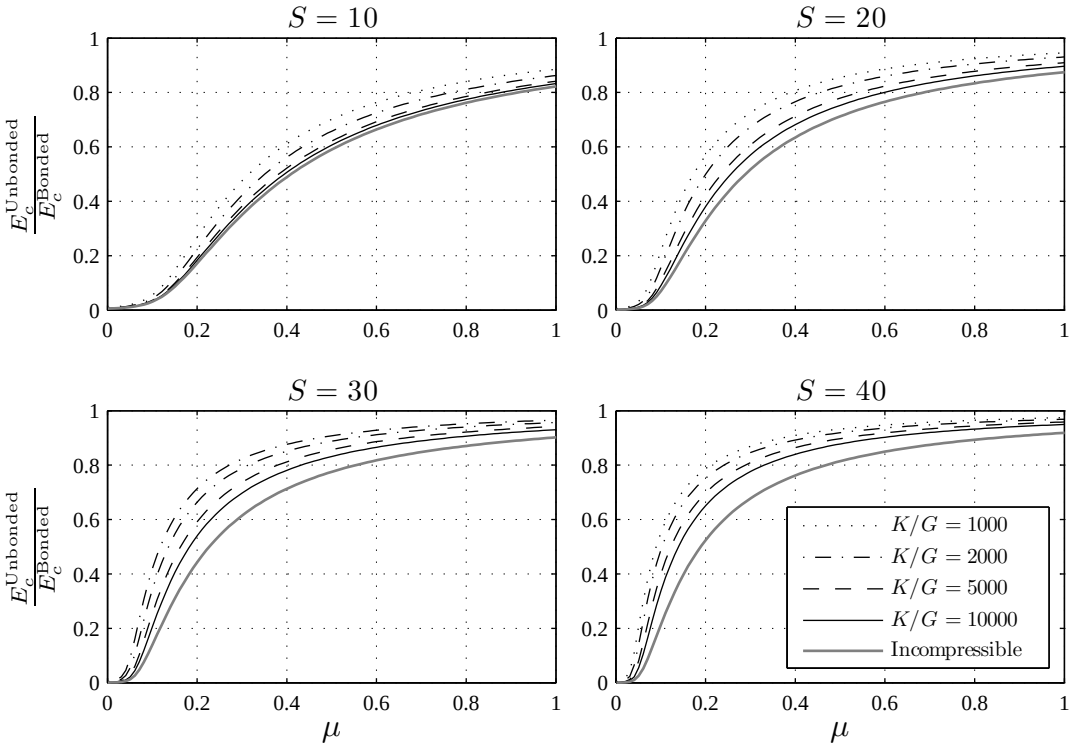


Figure 5.18: Effect of compressibility on the compression modulus of an unbonded circular pad.

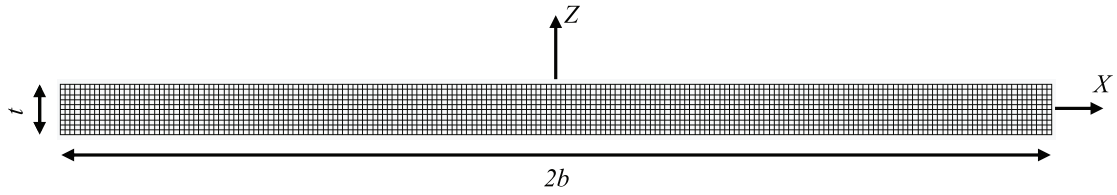


Figure 5.19: Finite element mesh of a rubber layer with $S = 10$.

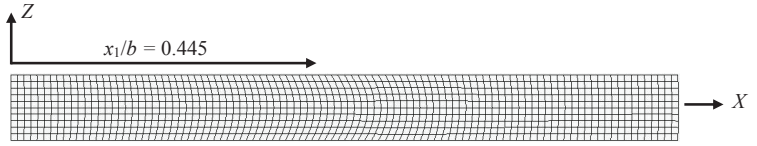


Figure 5.20: The deformed shape of a rubber layer ($S = 10$, $K/G = 5000$, and $\mu = 0.3$) under an average compressive stress of 2.0 MPa.

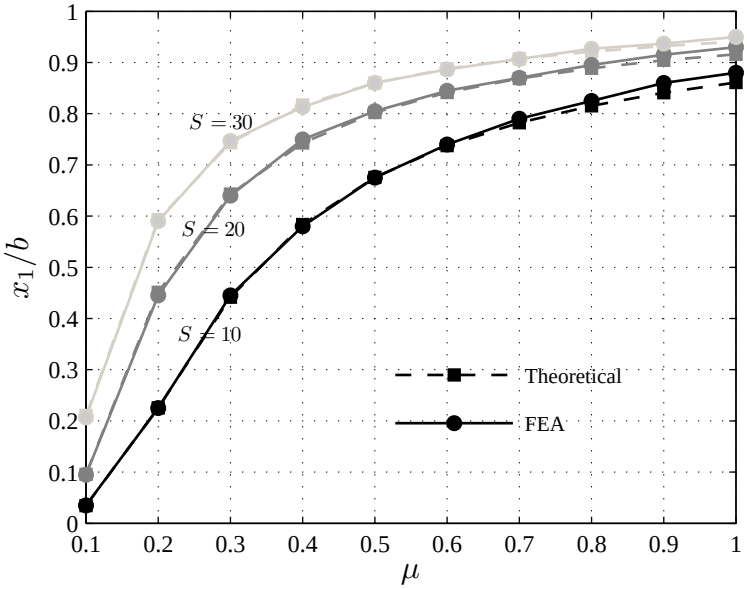


Figure 5.21: Location where slip initiates in unbonded infinite strip pad based on theoretical and finite element analysis (FEA) [$K/G = 5000$].

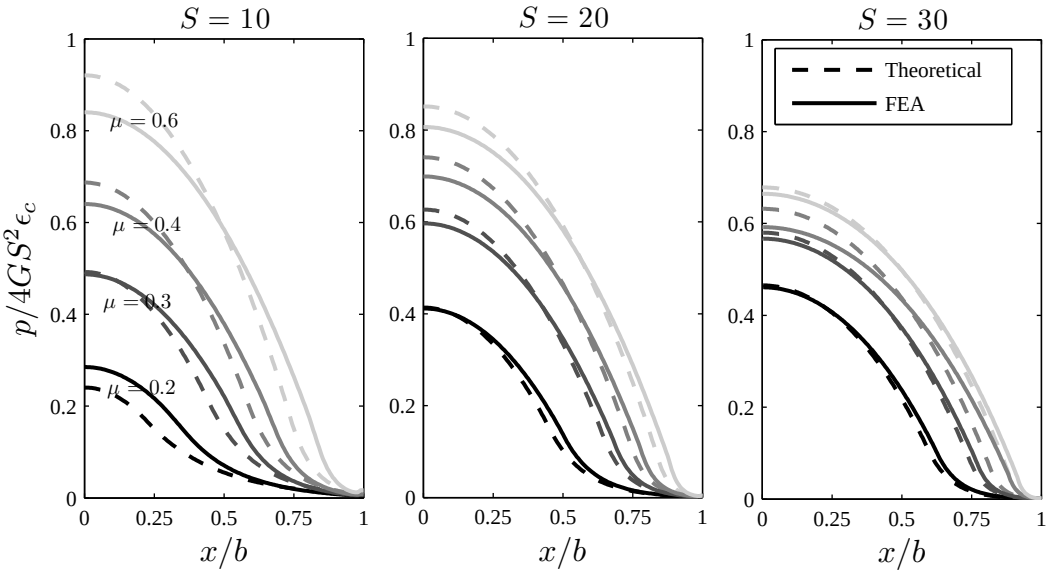


Figure 5.22: Pressure distribution of an unbonded infinite strip pad based on theoretical and finite element analysis (FEA) [$K/G = 5000$].

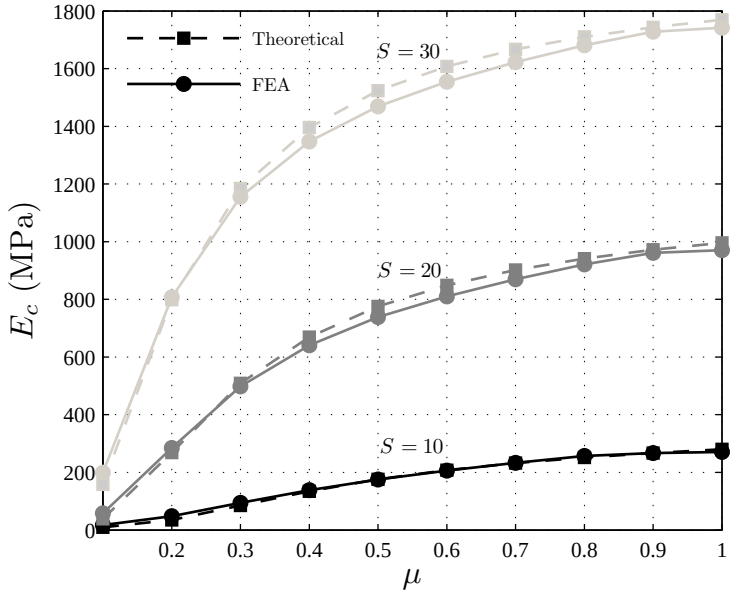


Figure 5.23: Compression modulus of an unbonded infinite strip pad based on theoretical and finite element analysis (FEA) $[K/G = 5000]$.

# Chapter 6

# Conclusions and Recommendations

## 6.1 Summary

Most studies in the available literature aimed to model the behavior of elastomeric bearings under combined vertical and lateral forces only, without considering rotation at the supports. The assumption of zero rotation at the supports is often valid due to the existence of rigid elements above/below the isolation layer. However, recent applications have shown that this assumption is not accurate for tall buildings (Oshaki et al., 2015), mid-story isolation systems (Murakami et al., 2000; Crowder, 2016), and bridges (Constantinou et al., 2011). The first objective of this thesis was to evaluate the effect of rotation at the supports using three approaches: finite element analysis, mechanical models, and experimental studies.

Unbonded bearings do not feature thick steel end plates. Shear forces are transferred from the bearing to the superstructure and substructure by the frictional force that develops along the rubber–to–concrete or rubber–to–steel interface. The second objective of this thesis was to investigate the effects of the elastomer's bulk compressibility and the contact slip at the supports on an unbonded rubber layer using theoretical solution and FEA.

## 6.2 Finite Element Analysis

In this study, 3D finite element analyses of a laminated rubber bearing were conducted to validate the model against results of an existing analytical solution (Karbakhsh Ravari et al., 2012), which is applicable for studying the behavior of elastomeric bearings before the instability point. To validate the model, four boundary conditions were considered: (1) no rotation at the top and bottom supports of the bearing, (2)

rotation only at the top support, (3) rotation only at the bottom support, and (4) rotation at both the top and bottom supports of the bearing. It was shown that the finite element model can reliably capture the effect of rotation on the horizontal behavior of the bearing.

The study evaluated the effect of the constitutive model selection for the rubber. The Neo-Hookean, Mooney-Rivlin, and Yeoh hyperelastic material models were considered to describe the rubber layers of a bearing. The results showed that material model selection influences the critical point, especially when the critical pressure is low where the critical shear strain is large. Furthermore, it was shown that using different material models does not affect the stress and strain distributions at zero lateral displacement, but that it can have a pronounced effect at large horizontal displacement.

The study then focused on the effect of rotation on stress and strain distributions and the load–displacement behavior of elastomeric bearings. It was shown that rotation has a more pronounced effect on the stress and strain distributions at smaller lateral displacement levels than larger ones. For a given average vertical stress, and at displacements less than the critical point, the amount of the rotation does not seem to affect the tangent stiffness. Because the tangent stiffness is fairly constant and positive rotation (counterclockwise) causes negative initial displacement, at a given displacement, the shear force is larger under positive rotation than under no rotation—and smaller under negative rotation than under no rotation. At large displacements near the critical value, the tangent stiffness decreases at a different rate depending on the support rotation angle. It was noted that, in general, support

rotation has a minimal effect on the critical displacement, but it does affect the critical shear force. Moreover, as expected, the tangent stiffness and the critical shear force decrease with increasing pressure. The relative effect of rotation becomes more pronounced with increased pressure.

## 6.3 Mechanical Models

finite element modeling is a complicated and time consuming process. In order to simplify the analysis, simple mechanical models (the Nagarajiah-Ferrell (Nagarajaiah and Ferrell, 1999), the Iizuka (Iizuka, 2000), and the Han-Warn (Han and Warn, 2014)) which are reliable were considered to capture the behavior of elastomeric bearings under axial–horizontal–rotation loading. First, these three models were evaluated by comparing their predictions with results of FEA, assuming no rotation at the supports. Then, the models were modified to account for the effect of rotation. The modified models were then evaluated using results from FEA under prescribed rotation values for the elastomeric bearing with shape factors of 12.67. In order to investigate the effect of geometry on the results, bearings with different second shape factor (2, 4 and 6) were considered. The following results were observed:

- The Nagarajiah-Ferrel model predicts lower values of force at the critical point than FEA, regardless of rotation value. The difference is more significant for bearings under higher pressures.

- In many cases, the Iizuka model provides very large values of force at the critical point, particularly for bearings with a large second shape factor. Consequently, this model is not accurate for bearings with a large second shape factor; although

this needs to be investigated with more elastomeric bearings.

- In general, the Han-Warn model provides relatively good agreement with FEA. This model can be improved beyond the critical point using a bilinear elastic model with post-cavitation hardening for the rubber material.

- Unlike the dispersion of the results using different models, the mechanical models predict the displacement at the critical point with a good agreement with FEA.

- All modified mechanical models provide larger initial lateral force than the one obtained by the FEM, especially for large pressures.

To eliminate the drawbacks and weaknesses of the existing models, this study proposed a new model that includes the effect of rotation on the lateral response. This model was used to predict the lateral stability limit, and the results were compared against those from FEA. It was shown that the new model can predict the lateral behavior of elastomeric bearings more accurately than existing models (their modified versions).

## 6.4 Experimental Studies

To ensure that the FEA and proposed simple mechanical models were reliable and accurate, an experimental setup was built at Applied Dynamic Laboratory, McMaster University. Chapter 4 provided detailed information about the setup and its limitations. A 1/4–scale circular isolator with the shape factor of 20 and second shape factor of 4 was considered. Two kinds of experimental testing, quasi–static cyclic

and monotonic tests, were conducted on a given bearing. The experimental results using cyclic testing revealed that the hysteresis loops shift up due to the rotation. Furthermore, this shifting, depending on the axial force and rotation angle, can be different. The FEA results compared with the cyclic testing showed that the FEA curve passes through approximately the middle of the loops, however, for the larger rotation, the FEA curve touches the upper portion of the experimental loops. The proposed mechanical model was compared against the experimental results. The monotonic tests showed stiffening behavior in the rubber, while the results from FEA and the mechanical model did not show any stiffening.

## 6.5 Closed-Form Solution for Unbonded Rubber Pads

In the last part of the thesis, the effect of friction on unbonded pads under axial loads was investigated. The study investigated the behavior of an unbonded rubber pad including the effect of compressibility and slip at the top and bottom supports. It was shown that slip can have a significant effect on the pressure distribution, compression modulus, and shear strain of the pad. The compression modulus is more sensitive to variations in bulk modulus for layers with larger shape factor. However, the compression modulus of layers with high shape factor is closer to the value corresponding to the bonded case than for layers with low shape factor. The study showed that compressibility and slip can significantly decrease the maximum shear strain in unbonded layers. However, for unbonded rubber layers with typical bulk-modulus-to-shear-modulus ratio values and large values of shape factor and friction

coefficient, the maximum shear strain becomes less sensitive to variations in friction coefficient. Consequently, the study presented various conditions under which the maximum shear strain in an unbonded layer (strip or circular) can be estimated with reasonable accuracy using the solution that corresponds to a fully bonded layer. Moreover, the FEA results were in a relatively good agreement with the predictions of the theoretical solution.

## 6.6 Recommendations for Future Study

Though this study tried to evaluate and model the effect of support conditions on the behavior of elastomeric bearings, there are still areas that call for further investigations:

- The support rotation value was kept constant during the shearing of the bearing. Future studies need to investigate the effect of the more complex case where rotation varies as the lateral displacement increases.

- This study did not consider dynamic effects on the lateral behavior and stability of the bearings. The damping effects of elastomeric bearings should be added to the model, and time history analysis can be performed on different structural systems and compared with the case where the isolators do not experience.

- This study assumes that the top plate of the bearing is fixed or free to move when it is subjected to the rotation and axial load simultaneously. Consequently, the bearing experiences initial displacement when the bearing is free to move, or initial force in the case that the bearing is fixed. In reality, however, due to the stiffness of the superstructure, the top plate is not either totally fixed or free

to move. It is recommended that the stiffness of the superstructure is added to the analytical models.

- This study was focused on an individual bearing. The effect of rotation on the lateral behavior and stability of a group of bearings in a given building would be another recommendation.

- The closed-from solution in Chapter 5 is not applicable to unbonded layers with different friction coefficient values on the top and bottom supports or to unbonded multilayer rubber bearings. In such a bearing, the frictional constrain is only applies to the surface of the topmost and bottommost layers that are in contact with the supports. These problems involve unsymmetrical boundary conditions that are substantially more complex.

## 6.7 References

Constantinou, M.C., Kalpakidis, I., Filiatrault, A., Ecker Lay, R.A. (2011). LRFD-based analysis and design procedures for bridge bearings and seismic isolators. *Technical Report MCEER-11-0004.* Multidisciplinary Center for Earthquake Engineering Research. University at Buffalo, State University of New York.

Crowder A.P. (2016). Investigating substructure flexibility in column–top isolation systems with elastomeric bearings. Master Thesis. McMaster University, Hamilton.

Han X., Warn G.P. (2014). Mechanistic model for simulating critical behavior in elastomeric bearings. *Journal of Structural Engineering.* 139(12): 04014140.

Iizuka M. (2000). A macroscopic model for predicting large-deformation behaviors of laminated rubber bearings. *Engineering Structures*. 22(4): 323–334.

Karbakhsh Ravari A., Othman I.B., Ibrahim Z.B., Ab-Malek K. (2012). P-$\Delta$ and end rotation effects on the influence of mechanical properties of elastomeric isolation bearings. *Journal of Structural Engineering*. 138(6): 669–675.

Murakami K., Kitamura K., Ozaki H., Teramoto T. (2000). Design and analysis of a building with the middle-story isolation structural system. *12th World Conference of Earthquake Engineering*. Auckland, New Zealand, Jan 30–Feb 4.

Nagarajaiah S., Ferrell F. (1999). Stability of elastomeric seismic isolation bearings. *Journal of Structural Engineering*.125(9): 946–954.

Ohsaki M., Miyamura T., Kohiyama M., Yamashita T., Yamamoto M., Nakamura, N. (2015). Finite-element analysis of laminated rubber bearing of building frame under seismic excitation. *Earthquake Engineering & Structural Dynamics*. 44(11): 1881–1898.

# Appendix A

# Appendix

## A.1 Investigation on the effect of rotation using simplified method

The effect of rotation can be estimated approximately by transformation of coordinates (the coordinate system aligns with the bearing). It means the axial load is inclined at a slight angle, perpendicular to the bearing. Therefore, the initial force can be estimated by $P \sin \theta_t$. It is assumed that $\theta_t$ is small, then the initial force is computed by $P\theta_t$. The critical force using for the simplified method (SM) is assumed to deviate from the FEA value by $P\theta_t$. Tables A.1 and A.2 show the initial force and critical force for Bearing 1 (see Table 3.1) using the FEA and simplified method (SM) under different $\bar{p}$ values and $\theta_t = 0.02$ and 0.04 rad, respectively. The simplified method overestimates the initial force, especially for the large axial load. Furthermore, the error between the critical force predicted by SM and FEA is increased by increasing the axial load. This difference is due to the nonlinearity in the FEA which provides more accurate prediction.

Table A.1: Comparison between the FEA and simplified method (SM) ($\theta_t$=0.02 rad).

| | Initial Force (kN) | | | Critical Force (kN) | | |
|---|---|---|---|---|---|---|
| $\bar{p}$ (MPa) | FEA | SM | error(%) | FEA | SM | error (%) |
| 4.13 | 0.6 | 1.5 | 150 | 35 | 36 | 2.8 |
| 5.51 | 1.1 | 2.0 | 82 | 30 | 31 | 3.3 |
| 6.89 | 1.3 | 2.5 | 92 | 26 | 27 | 3.8 |
| 8.26 | 1.8 | 3.0 | 67 | 22 | 23 | 4.5 |
| 9.64 | 2.0 | 3.5 | 75 | 19 | 21 | 10.5 |
| 11.02 | 2.3 | 4.0 | 74 | 17 | 19 | 11.7 |
| 12.40 | 2.5 | 4.5 | 80 | 14 | 16 | 14.3 |

Table A.2: Comparison between the FEA and simplified method (SM) ($\theta_t$=0.04 rad).

| | Initial Force (kN) | | | Critical Force (kN) | | |
|---|---|---|---|---|---|---|
| $\bar{p}$ (MPa) | FEA | SM | error(%) | FEA | SM | error (%) |
| 4.13 | 1.4 | 3.0 | 114 | 36 | 38 | 5.5 |
| 5.51 | 2.7 | 4.0 | 48 | 31 | 33 | 6.4 |
| 6.89 | 3.0 | 5.0 | 67 | 27 | 29 | 7.4 |
| 8.26 | 3.6 | 6.0 | 67 | 24 | 26 | 8.3 |
| 9.64 | 4.0 | 7.5 | 88 | 21 | 24 | 14.3 |
| 11.02 | 4.5 | 8.0 | 78 | 19 | 22 | 15.8 |
| 12.40 | 5.0 | 9.0 | 80 | 17 | 20 | 17.6 |